IChF
Institute of Physical Chemistry PAS

PhD Dissertation

Unraveling the chemistry behind the biological activity of green silver nanocomposites

Neha Venkatesh Rangam

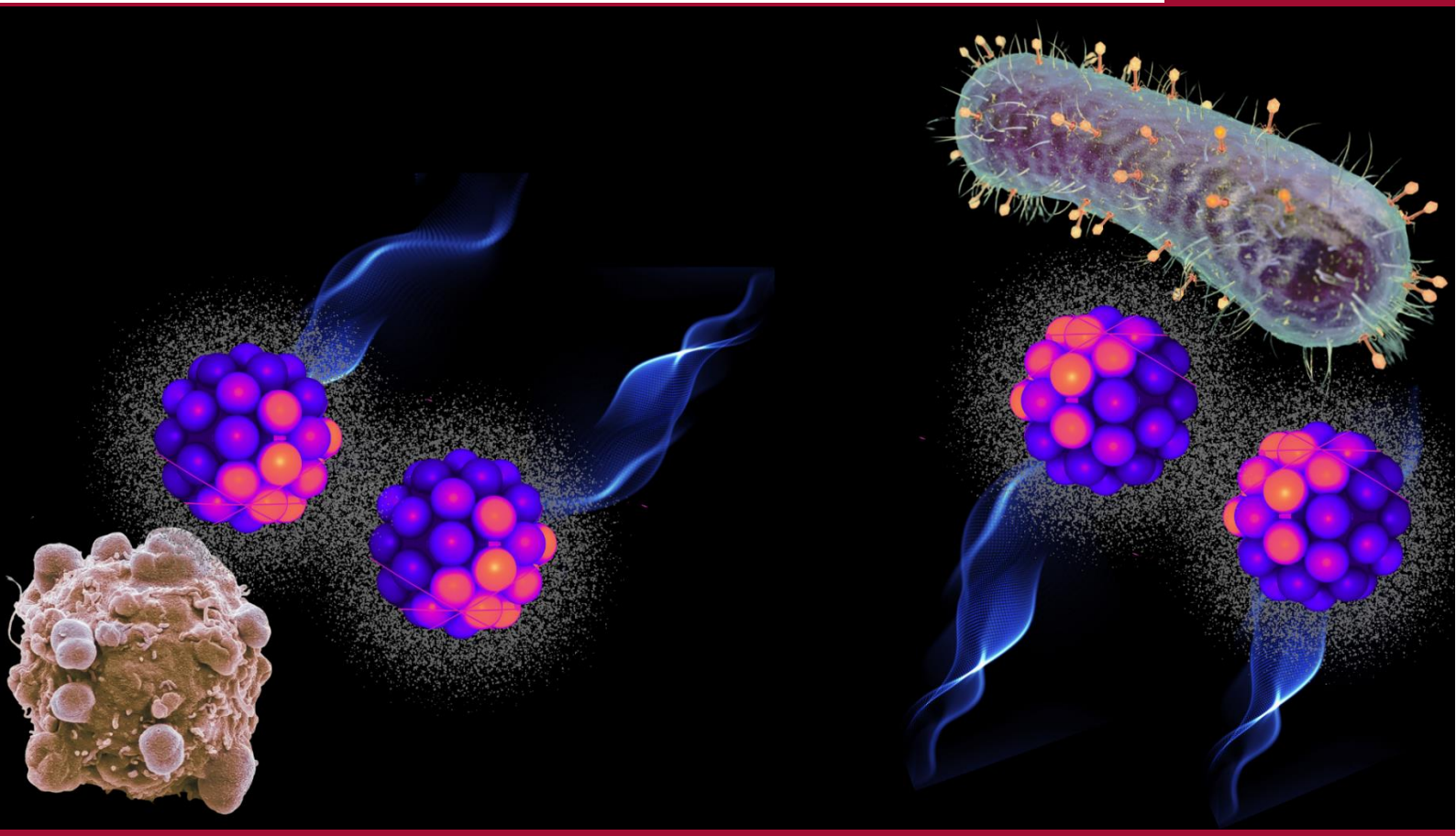

PhD Thesis

Unraveling the chemistry behind the biological activity of green silver nanocomposites

Neha Venkatesh Rangam

Supervisor: Dr. hab Beata Orłowska, Ph.D., D.Sc.

Auxiliary supervisor: Dr. László Kövér, Ph.D.

The thesis was prepared within the International Doctoral Studies in Chemistry at the Institute of Physical Chemistry of the Polish Academy of Sciences (Warsaw, Poland) in the Dynamics of nanocrystal structure induced by surface chemistry group in collaboration with Laboratory of Materials Science, Institute for Nuclear Research (ATOMKI) at the Hungarian Academy of Sciences (MTA), (Debrecen, Hungary).

Warsaw, April 2025

Declaration of originality

I declare that the research included within this thesis was carried out by myself or with support of others included in the acknowledgments.

I state that I have exercised care to ensure that the work is original and contains no previously published material or written by another person, except where citations have been made in the text. The content provided here does not violate any copyrights to the best of my knowledge.

I accept that the Polish Academy of Sciences has the right to use plagiarism detection software to ensure the legitimacy of the thesis.

I certify that no part of my thesis has been or will be submitted for obtaining a degree or diploma by the Institute of Physical Chemistry, Polish Academy of Science, or any other educational institution.

This thesis's copyright rests with the author, and no information derived from it may be published without the author's consent.

Warsaw, 1st April, 2025

Signature

Acknowledgements

This Ph.D. journey has been both inspiring and transformative, shaping me not only as a researcher but also as an individual. I am grateful to God for blessing me with the opportunity to walk this path and experience the beauty of learning and growth. It has been a long and challenging road, filled with both highs and lows, but each step has taught me valuable lessons about life.

I want to express my deepest gratitude to my family—my father (Venkatesh), my brother (Anuj), and my late mother (Vijayalaxmi)—whose unwavering support and love have been the foundation of my journey. Your encouragement and belief in me have guided me through every challenge and triumph in life. I am incredibly fortunate to have been surrounded by a wonderful circle of friends: Alcina, Nikhil, Vicky, Jyoti, Swaraj, Tanvi, Pallavi, Pradeep, and Daya. Your support, patience, and constant motivation have kept me going through this long and demanding journey. Especially to Alcina, I am endlessly grateful for standing by me through all the challenges, guiding me, encouraging me, and supporting me every step of the way. A special thanks to Alcina's mother (Henrita), uncle (Arulraj) and family, Ravi uncle, who welcomed me as one of their own and provided immense emotional support during difficult times. Your kindness and encouragement meant a lot to me.

I would like to express my sincere gratitude to my supervisor, Dr. hab. Beata Lesiak-Orłowska, for accepting me as a PhD student under her guidance. Your patience and constant support through every request and challenge I faced during this work have been inspiring. Thank you for teaching me the intricacies of X-ray Photoelectron Spectroscopy (XPS) and helping me analyze the spectra to gain expertise in XPS which has been invaluable throughout this research. I am thankful to my co-supervisors, Prof. László Kövér and Dr. József Tóth from the Institute for Nuclear Research (ATOMKI), Debrecen, Hungary, for supporting the project through funding, characterization experiments, and publications. I am grateful to Dr. László Kövér, for his insightful guidance and continuous support throughout my PhD journey. Your expertise and encouragement have significantly contributed to the progress of this work. I would also like to thank Dr. József Tóth for teaching me the operation of various commercial and home-built XPS instruments at ATOMKI and for providing XPS data. I would like to express my heartfelt gratitude to Prof. Dr. hab. Marek Tkacz for his kindness, guidance, and unwavering support from the very first day I arrived at the Institute. His generosity and encouragement made me feel truly welcomed in a foreign country.

I would like to express my sincere gratitude to Dr. Karina Kwapiszewska for allowing me to work in her biological laboratory and guiding me through the cytotoxicity analysis of nanocomposites. I am thankful to Dr. Karina Kwapiszewska, Dr. Marta Pilz, Dr. Grzegorz Bubak, and Dr. Faria Khan for their support with cytotoxicity assays and confocal microscopy experiments. My appreciation also extends to Dr. Artur Ruszczak, Dr. Ilona Paulina Foik, and Shakeel Ahmad for their assistance with antibacterial studies and data analysis of nanocomposites. I would like to acknowledge Dr. Martin Jonsson-Niedziółka and Dr. Marcin Hołdyński for granting access and support for the scanning electron microscopy (SEM) facility. I am grateful to Prof. Dr. hab. Zbigniew Kaszkur for his valuable assistance with X-ray diffraction (XRD) equipment and data analysis. My sincere thanks to Dr. Ilia Smirnov from the Dynamics of Nanocrystal Structure Induced by Surface Chemistry group for his constant support with X-ray fluorescence (XRF) and XRD experiments. I would also like to thank Dr. Paweł Borowicz from the Laboratory of Molecular Film Investigation for FT-IR spectra. My gratitude also goes to Dr. Magdalena Bonarowska from the Modern Heterogeneous Catalysis group for her invaluable guidance and for granting me access to the Brunauer-Emmett-Teller (BET) instrument. I am thankful to Dr. Agnieszka Wiśniewska from the Laboratory for Soft Matter Research for the collection of thermogravimetric data and for providing access and training on the UV-vis spectrophotometer and dynamic light scattering (DLS) instruments. I would like to emphasize the collaborative effort with Dr. Alcina, which played a crucial role in the successful development of this project. I would like to acknowledge Prof. Dr. hab. Adam Kubas for the Computer Graphics in Chemistry course, which laid the foundation for creating scientific illustrations during my Ph.D., including those presented in this thesis. My sincere thanks to Dr. Krzysztof R. Noworyta for his valuable guidance and support.

I am thankful to Dr. Grzegorz Trykowski from Nicolaus Copernicus University, Toruń, Poland, for providing the transmission electron microscopy (TEM) images of the nanocomposites. I am also grateful to Dr. Jarosław Grzegorz Sadło from the Institute of Nuclear Chemistry and Technology, Poland, for his guidance in Electron Spin Resonance (ESR) spectroscopy and for performing γ-irradiation on the nanocomposites. I am deeply grateful to Dr. Hab. Piotr Dłużewski from the Institute of Physics of the Polish Academy of Sciences, Warsaw, Poland, for granting me access to the HR-TEM equipment and offering invaluable training. My sincere thanks to Dr. Dorota Michałowska and Prof. Marek Ł. Roszko from the Institute of Agriculture and Food Biotechnology - State Research Institute, Warsaw, Poland, for their support in brewery waste analysis. I would also like to thank the Central Research Laboratory of the University of Life Sciences, Lublin, Poland, for performing the total organic content analysis of brewery by-products and product.

I would like to express my sincere gratitude to Prof. Shinji Kawasaki from Kawasaki & Ishii's Laboratory, Nagoya Institute of Technology (NITech), Japan, for granting access to the lab and providing invaluable training and guidance in the purification of single-walled carbon nanotubes, thermogravimetric analysis (TGA), N_2 adsorption spectroscopy, Brunauer-Emmett-Teller (BET) analysis, X-ray diffraction, and Raman spectroscopy. Finally, I am deeply grateful to all the collaborators, colleagues, and technical staff who have contributed to this work in one way or another. This journey would not have been possible without your support and guidance.

Funding

The present research was financed by the following funding organizations.

The European Union Horizon 2020 Research and Innovation Programme under the Marie Skłodowska-Curie grant agreement no. 711859 and the Polish Ministry of Science and Higher Education for implementing an international co-financed NaMeS project in the years 2017–2021.

Funded by the Horizon 2020 Framework Programme of the European Union

Ministry of Science and Higher Education

Republic of Poland

The Polish National Science Centre, OPUS 8 grant no. 2014/15/B/NZ/01011.

NATIONAL SCIENCE CENTRE
POLAND

List of scientific accomplishments

A. Publication included in the dissertation

3. A.J. Sudagar, **N.V. Rangam**, A. Ruszczak, P. Borowicz, J, Tóth, L. Kövér, D. Michałowska, M.Ł. Roszko, K.R. Noworyta, B. Lesiak, *Valorization of Brewery Wastes for the Synthesis of Silver Nanocomposites Containing Orthophosphate*. Nanomaterials 2021, 11, 2659, 25p., https://doi.org/10.3390/nano11102659.

4. **N.V. Rangam**, A.J. Sudagar, A. Ruszczak, P. Borowicz, J. Tóth, L. Kövér, D. Michałowska, M.Ł. Roszko, K.R. Noworyta, B. Lesiak, *Valorizing the Unexplored Filtration Waste of Brewing Industry for Green Silver Nanocomposite Synthesis*. Nanomaterials 2022, 12, 442, 26p., https://doi.org/10.3390/nano12030442.

5. **N. Rangam**, A. Sudagar, R. Koronkiewicz, P. Borowicz, J. Tóth, L. Kövér, D. Michałowska, M. Roszko, M. Pilz, K. Kwapiszewska, B. Lesiak-Orłowska, *Surface and composition effects on the biphasic cytotoxicity of nanocomposites synthesized using leaf extracts*, International Journal of Biological Macromolecules 2024, 276, 133723, 12p., https://doi.org/10.1016/j.ijbiomac.2024.133723.

6. **N. Rangam**, A. Sudagar**,** M. Pilz, K. Kwapiszewska, B. Lesiak-Orłowska, *Cytotoxic effects of nanocomposites synthesized using brewery wastes against human cell lines,* to be submitted (2025).

B. Other publications

1. A. Sudagar, **N. Rangam**, M. Bonarowska, A. Wisniewska, J. Sadło, J. Tóth, L. Kövér, G. Trykowski, W. Kutner, B. Lesiak-Orlowska, K.R. Noworyta, *Electrocatalytic oxygen reduction reaction on green-chemistry-synthesized silver nanocomposites and their antibacterial activity,* to be submitted (2025).

2. B. Lesiak-Orłowska, **N.V. Rangam**, N.K. Sahu, P. Jiricek, J. Houdkova, A. Atrei, *Surface chemical and electronic properties of functionalized Fe_3O_4 nanoparticles influencing their cytotoxicity*, Applied Surface Science 684 (2025) 161873, 14p., https://doi.org/10.1016/j.apsusc.2024.161873.

3. **N.V. Rangam**, Sh. Ahmad, R. Koronkiewicz, I.P. Foik, P. Borowicz, A. Wisniewska, M. Hołdyński, J. Tóth, L. Kövér, M.Ł. Roszko, B. Lesiak-Orłowska, A.J. Sudagar,

Bactericidal efficiency of silver nanocomposites obtained using Brewer's spent grains, Applied Surface Science 661 (2024) 159958, 11p., https://doi.org/10.1016/j.apsusc.2024.159958.

4. B. Lesiak, G. Trykowski, J. Tóth, S. Biniak, L. Kövér, **N. Rangam**, A. Malolepszy, L. Stobinski, *Effects of microwave treatment in a high pressure microwave reactor on graphene oxide reduction process – XRD, Raman spectroscopy, IR and electron spectroscopic studies*, Materials MPDI 14(19) (2021) 5728, 17p., https://doi.org/10.3390/ma14195728.

5. B. Lesiak, **N. Rangam**, P Jiricek, I Gordeev, J Tóth, L Kövér, M Mohai, P Borowicz. *Surface study of Fe_3O_4 nanoparticles functionalized with biocompatible adsorbed molecules*. In: VSR Rajasekhar Pullabhotla, editor. Prime Archives in Chemistry: 2nd Edition. Hyderabad, India: Vide Leaf 2021.

6. B. Lesiak, G. Trykowski, J. Tóth, S. Biniak, L. Kövér, **N. Rangam**, L. Stobinski, A. Malolepszy, *Chemical and structural properties of reduced graphene oxide – dependence on the reducing agent*, J. Material Sciences, online 2020, 56 (2021) 3738-3754, https://doi.org/10.1007/s10853-020-05461-1.

7. B. Lesiak, **N. Rangam**, P. Jiricek, I. Gordeev, J. Tóth, L. Kövér, M. Mohai, P. Borowicz, *Surface study of Fe_3O_4 nanoparticles functionalized with biocompatible adsorbed molecules*, Frontiers in Chemistry 7 (2019) 642, 16p., https://doi.org/10.3389/fchem.2019.00642.

8. B. Lesiak, L. Kövér, J. Tóth, J. Zemek, P. Jiricek, A, Kromka, **N. Rangam**, *C sp^2/sp^3 hybridisations in carbon nanomaterials – XPS and (X)AES study,* Applied Surface Science 452 (2018) 223-231, https://doi.org/10.1016/j.apsusc.2018.04.269.

C. Patent application

A. Sudagar, **N. Rangam**, P. Borowicz, J. Tóth, B. Lesiak, L. Kövér, *Sposób otrzymywania nanocząstek metalu oraz nanocząstki metalu* (*Method of obtaining metal nanoparticles and metal nanoparticles*). Patent application no P.435084 (2020); approved 2022.

D. Conference participations

1. B. Lesiak, **N**. **Rangam**, P. Jiricek, I. Gordeev, J. Tóth, L. Kövér, M. Mohai, "*Surface study of Fe_3O_4 nanoparticles functionalised with biocompatible adsorbed molecules."* Microsymposium organized at IPC PAS, Warsaw, Poland, 2019. (Poster presentation).
2. **N**. **Rangam**, G. Bubak, K. Kwapiszewska, B. Lesiak, J. Tóth, L. Kövér, L. Stobinski, A. Malolepszy, *Cytotoxicity of different nanocarbon materials tested on HeLa cells."* 1 and 2D Materials International Conference and Exhibition (1 & 2DM), January 29-30, Tokyo, Japan, 2019. (Poster presentation).
3. B. Lesiak, N**. Rangam**, P. Jiricek, I. Gordeev, J. Tóth, L. Kövér, M. Mohai, "*Surface study of Fe_3O_4 nanoparticles functionalised with biocompatible adsorbed molecules."* Asian Conference on Recent Advances in Science, Engineering and Technology, 26th May, 2019, Pune, India. (Poster presentation).
4. Lesiak, G. Trykowski, J. Toth, S. Biniak, L. Kover, **N**. **Rangam**, L. Stobiński, A. Małolepszy, *Effect of different chemical agents on reduction of graphene oxide (GO) and rGO structural and chemical properties – TEM, XRD, Raman, IR and surface electron spectroscopic studies.* Microsymposium IPC PAS, January, Warsaw, Poland, 2020. (Poster presentation).
5. N. Rangam, B. Lesiak, P. Jiricek, I. Gordeev, J. Tóth, L. Kövér, M. Mohai, "*Understanding the cytotoxic effect of surface grafted Fe_3O_4 nanoparticles for HeLa cells."* ICONSAT 2020, India, 2020. (Poster presentation).
6. A. Sudagar, N. Rangam, B. Lesiak, J. Tóth, L. Kövér, "*Industrial by-product mediated synthesis of nanoparticles containing orthophosphate*." ICONSAT 2020, India, 2020. (Poster presentation).
7. N. Rangam, B. Lesiak, P. Jiricek, I. Gordeev, J. Tóth, L. Kövér, M. Mohai, "*Understanding the cytotoxic effect of surface grafted Fe_3O_4 nanoparticles for HeLa cells*." Microsymposium IPC PAS, Warsaw, Poland, 2021. (Poster presentation).
8. N. Rangam, Lesiak, P. Jiricek, I. Gordeev, J. Tóth, L. Kövér, M. Mohai, "*Understanding the cytotoxic effect of surface grafted Fe_3O_4 nanoparticles for HeLa cells*." ESSONN 2021, European School on Nanoscience and Nanotechnologies, Grenoble, France, 2021. (Poster presentation).
9. A. Sudagar, N. Rangam, P. Borowicz, J. Tóth, B. Lesiak, L. Kövér, *Industrial by-product mediated synthesis of silver nanocomposites.* Microsymposium IPC PAS, Warsaw, Poland, 2021. (Poster presentation).

10. B. Lesiak-Orłowska, N.V. Rangam, N.K. Sahu, P. Jiricek, J. Houdkova, A. Atrei, "*Surface chemical and electronic properties of functionalized Fe_3O_4 nanoparticles influencing their cytotoxicity*." Microsymposium IPC PAS, Warsaw, Poland, 2024. (Poster presentation).
11. A. Sudagar, N.V. Rangam, B. Lesiak-Orłowska, *"Influence of surface properties of Ag nanocomposites resulting from green synthesis on the antibacterial activity."* 6th International Conference on Catalysis and Chemical Engineering, CCE-2022, Hybrid mode, San Francisco, USA, 22-26 February 2022. (Lecture).

E. Research visit and schools

1. Research visit to Laboratory of Materials Science, Institute for Nuclear Research (ATOMKI), Hungarian Academy of Sciences (MTA), Debrecen, Hungary, 27th – 30th November 2017. (Research topic: X-Ray photoelectron spectroscopy and electro spray techniques)
2. Research visit to Kawasaki and Ishii Laboratory, Nagoya Institute of Technology (NITech), Nagoya, Japan, November 2018 – April 2019. (Research topic: Purification of single walled carbon nanotubes and synthesis of C60 peapod)
3. Research visit to Institute of Physics, Polish Academy of Sciences (PAS), Warsaw, Poland, November 2019 – April 2020 (Research topic: HR-TEM of silver nanocomposites synthesized using different brewery wastes)
4. Research visit to Department of Chemistry of Materials Adsorption and Catalysis, Carbon Materials Application in Electrochemistry and Environmental Protection Research Group, and Faculty of Chemistry, Nicolaus Copernicus University, Torun, 12th – 18th January 2020. (Research topic: HR-TEM and FTIR measurements of 1D and 2D hybrid nanomaterials)
5. Research visit to Institute of Nuclear Chemistry and Technology, Warsaw, Poland, November 2020 – January 2022. (Research topic: Electro paramagnetic resonance spectroscopy of silver nanocomposites synthesized using different brewery wastes)
6. European School on Nanosciences and Nanotechnologies (ESONN'21), France, 23 August – 10 September 2021.

List of abbreviations

A

A549– Adenocarcinomic human alveolar basal epithelial cells

Ag– Silver

Ag^{+}– Silver ion

Ag_{met}–Metallic silver

AgCl– Silver chloride

$AgNO_3$– Silver nitrate

AgO– Silver peroxide

Ag_2O– Silver oxide

AgOH– Silver hydroxide

Ag_3PO_4– Silver phosphate

Al– Aluminium

AM– Acetoxymethyl

ATP– Adenosine triphosphate

Ar^{+}– Argon ion

Au– Gold

B

B– Boron

B– Beer

BE– Binding energy

BSG– Brewer's spent grains

BSY– Brewer's spent yeast

BW– Brewery waste

BW3– Brewery waste from stage 3 of brewing process

BW5– Brewery waste from stage 5 of brewing process

BW7– Brewery waste from stage 7 of brewing process

BW9– Brewery waste from stage 9 of brewing process

C

Ca– Calcium

CD– Conductive detection

CFU– Colony forming unit

Cl^-– Chlorine ion

C=O– Carbonyl group

C–OH– Hydroxyl group

C–OOH– Carboxylic group

CN– Charge neutralization

COVID-19– Corona virus disease 2019

CT scan– Computed tomography scan

Cu– Copper

D

DLS– Dynamic light scattering

DMEM– Dulbecco's modified eagle's medium

DMSO– Dimethyl sulfoxide

DNA– Deoxyribonucleic acid

DOX– Doxorubicin

E

E. coli– *Escherichia coli*

EC_{50}– Half maximal effective concentration

EDTA– Ethylenediamine tetraacetic acid

EDXRF– Energy dispersive x-ray fluorescence (spectroscopy)

EDXS– Energy-dispersive x-ray spectroscopy

EHT– Extra high tension

ESCA– Electron spectroscopy for chemical analysis

eV– Electron volt

F

FBS– Fetal bovine serum

FDA– U. S. Food and Drug Administration

Fe– Iron

FEG– Field emission gun

FITC– Fluorescein isothiocyanate

FRR– Fixed retarding ratio

FT-IR– Fourier transform infrared (spectroscopy)

FWHM– Full width at half-maximum

G

GSH– Glutathione

H

HAADF– High angle annular dark-field

HEK293– Human embryonic kidney 293 cells

HeLa– Cervical cancer named after Henrietta Lacks

HER2– Human epidermal growth factor receptor 2

HPO_4– hydrogen phosphate

$H_4P_4O_2$– Dioxide diphosphorus

HPLC– High-performance liquid chromatography

HPV– human papillomavirus

HR-TEM–High resolution transmission electron microscopy

H_2O– Water

H_2O_2– Hydrogen peroxide

I

IC_{50}– Half maximal inhibitory concentration

ICDD– International center for diffraction data

IMFP– Inelastic mean free path

IO– Iron oxide

IPA– India pale ale

IR– Infrared

K

K– Potassium

K^+– Potassium ion

L

LB– Lysogeny broth

LC_{50}– Half maximal lethal concentration

LE– Leaf extract

LE1– *Malus sylvestris L.* leaf extract

LE2– *Pinus sylvestris L.* leaf extract

LE3– *Sorbus aucuparia L.* leaf extract

LG– L-glutamine

LDH– Lactate dehydrogenase

M

MBC– Minimum bactericidal concentration

MCF-7– Breast cancer cell line named after Michigan cancer foundation-7

MDA-MB-231– Metastatic ductal adenocarcinoma mammary breast cancer cell line 231

Mg– Magnesium

MH– Mueller Hinton

MIC– Minimum inhibitory concentration

Mn– Manganese

MS– Mass spectrometry

MTT– [3–(4,5–Dimethylthiazol–2–yl)–2,5–Diphenyl tetrazolium Bromide]

MRI– Magnetic resonance imaging

N

N– Nitrogen

NAD^+– Nicotinamide adenine dinucleotide ion

NCI– National Cancer Institute

NH_2– Amino group

NH_3– Ammonia

NH_4^+– Ammonium ion

Ni– Nickel

NO_3^-– Nitrate ion

NP– Nanoparticle

O

O_2– Oxygen

O_2^-– Superoxide

OH^-– Hydroxide ion

ORR– Oxygen reduction reaction

P

P– Phosphorous

PCS– Photon correlation spectroscopy

PDT– Photo dynamic therapy

PEELS– Parallel electron energy loss spectrometer

PEG– Polyethylene glycol

pH– Potential of hydrogen

PI– Propidium iodide

PO_4^-– Phosphate ion

P_2O_7– Diphosphate

P_3O_{10}– Triphosphate

PO_3CH_3– Methyl phosphate

PS– Penicillin-streptomycin

PTT– Photo thermal therapy

PVP– Polyvinyl pyrrolidone

PXRD– Powder X-ray diffraction

R

RID– Refractometric detection

RIR– Reference intensity ratio

RNA– Ribonucleic acid

ROS– Reactive oxygen species

rpm– Revolutions per minute

RPMI– Roswell Park Memorial Institute

S

SEM– Scanning electron microscopy

SO_2– Sulfonyl

SO_3– Sulfonate

SO_4^{2-}– Sulfate ion

T

TC– Tissue culture

TEM– Transmission electron microscopy

TGA– Thermogravimetric analysis

TiO_2– Titanium dioxide

TOC– Total organic carbon

TRITC– Tetramethyl rhodamine isothiocyanate

U

UV-vis– Ultraviolet-visible (spectroscopy)

X

XPS– X-ray photoelectron spectroscopy

XRD– X-ray diffraction

Z

Zn– Zinc

ZnO– Zinc oxide

List of symbols

A

A– Absorbance

Å– Armstrong unit

$A_{control}$– Absorbance of spontaneous LDH activity

$A_{maximum}$–Absorbance of maximum LDH activity

A_{sample}– Absorbance of sample

$A_{490\ nm}$– Absorbance measured at wavelength 490 nm

$A_{540\ nm}$– Absorbance measured at wavelength 540 nm

$A_{680\ nm}$– Absorbance measured at wavelength 6800 nm

$A_{690\ nm}$– Absorbance measured at wavelength 690 nm

A1– Bottom limit (start point)

A2– Top limit (end point)

H

h1– Slope1

h2– Slope2

K

k– Retardation ratio

K_{α}– L → K electron transition

K_{β}– M → K electron transition

L

LOGx01– 1^{st} EC_{50}

LOGx02– 2^{nd} EC_{50}

P

p– Proportion

Special characters

θ– Diffraction angle

°– Degree

°C– Degree Celsius

μ– Micro

Abstract

Cancer continues to be a major global health challenge, claiming millions of lives each year and profoundly impacting individuals, families, and communities. Conventional therapies can have severe side effects and drug resistance, necessitating the development of more biocompatible and targeted treatment approaches. The burgeoning field of green nanotechnology has paved the way for sustainable and eco-friendly synthesis routes for metal nanocomposites. This approach not only minimizes hazardous byproducts but also enhances the biocompatibility and bioactivity of nanomaterials due to the presence of bioactive phytochemicals.

This dissertation investigates the green synthesis of silver nanocomposites utilizing brewery waste (**BW**) stages 5 (**BW5**), 7 (**BW7**), and 9 (**BW9**), as well as beer (**B**) (Chapter 3) and leaf extracts from *Malus sylvestris L.* (**LE1**), *Pinus sylvestris L.* (**LE2**) and *Sorbus aucuparia L.* (**LE3**) (Chapter 4) as natural reducing-oxidizing and stabilizing agents. The increasing accumulation of brewery waste poses significant environmental challenges due to the complexity of its disposal, thereby highlighting the urgent need for sustainable strategies to recycle these wastes into value-added materials. This research focussed on the potential of brewery waste in comparison to leaf extracts for the eco-friendly synthesis of silver nanocomposites through a simple and cost-effective "one-pot" approach.

The synthesized nanocomposites were thoroughly characterized using various analytical techniques including X-ray diffraction, energy-dispersive X-ray fluorescence spectroscopy, transmission electron microscopy, and scanning electron microscopy/ energy dispersive X-ray spectroscopy to determine their chemical composition and structural properties. The surface composition of these nanocomposites was studied using X-ray photoelectron spectroscopy. Their biocompatibility was assessed on Human Embryonic Kidney (HEK293) cells, while their cytotoxicity was evaluated against four cancer cell lines: cervical cancer (HeLa), lung cancer (A549), and breast cancer (MCF-7 and MDA-MB-231). The anticancer activity studies were achieved using live/dead assay, LDH assay and MTT assay. Further, the bactericidal activity of the nanocomposites was also tested on the bacterial strain *Escherichia coli*.

The chemical analysis using spectrophotometric and chromatographic methods revealed that both **BW** (Section 3.1) and **LE** extracts (Section 4.1) were rich in carbohydrates, polyphenols, fermentable sugars, sulfates, nitrogen, and phosphorus. The silver nanocomposites synthesized

using **BW** predominantly contained AgCl and Ag_3PO_4 as major phases, with a minor quantity of metallic silver (Section 3.2.1). In contrast, **LE**-derived nanocomposites primarily consisted of metallic silver with traces of AgCl (Section 4.2.1). All elements were uniformly distributed in the bulk of nanocomposites (Section 3.2.3 and 4.2.3). X-ray Photoelectron Spectroscopy (XPS) analysis confirmed the presence of silver, carbon, and oxygen as major elements on all the nanocomposites′ surfaces (Section 3.2.4 and 4.2.4). At the same time, trace amounts of chlorine and phosphorus were also detected in **BW**-based nanocomposites. Overall silver elemental content increased with increasing synthesis temperature from 25 to 80 ℃ for both **BW** and **LE** nanocomposites. The surface of **BW** nanocomposites consisted of a majority of silver (40–60 wt.%), carbon content ~20–40 wt.% and oxygen content ~10–15 wt.% while **LE** nanocomposites consist majorly of carbon (55–75 wt.%), oxygen ~15–25 wt.% and silver ~8–20 wt.%.

Cytotoxicity assays demonstrated a dose-dependent response, showing selective toxicity toward cancer cells (Section 3.3 and 4.3). A biphasic toxicity mechanism was observed across all nanocomposites: at lower concentrations (0–10 μg ml^{-1}), cell growth inhibition was predominant, while at higher concentrations (10–70 μg ml^{-1}), direct cell destruction occurred after achieving approximately 30-50% inhibition. Notably, nanocomposites synthesized at 25(±1) °C exhibited higher cytotoxicity, leading to increased cell death at lower concentrations compared to those synthesized at 80(±1) °C. All nanocomposites displayed higher toxicity against HeLa and A549 cells compared to MCF-7 and MDA-MB-231 cell lines. Half maximal inhibition concentrations (IC_{50}s) and half maximal lethal concentrations (LC_{50}s) values for **BW** nanocomposites is lower than that of **LE** nanocomposites, indicating **BW** nanocomposites are more effective regarding cytotoxicity to cancer cells than **LE** nanocomposites (Section 5.1). **BW** nanocomposites have more of silver content (mostly containing AgCl and Ag_3PO_4 acting as silver ion source), phosphorous and chlorine on surface as well as in the bulk, than **LE** nanocomposites. These possibly enable easier availability of Ag^+ ions for penetrating into cells, P and Cl toxicity to cells and improved overall cytotoxicity of **BW** nanocomposites in comparison to **LE** nanocomposites. Moreover, all nanocomposites showed biocompatibility to normal human cells HEK293 in the concentration range, where they exhibited cytotoxicity to cancerous cells (Section 3.3 and 4.3). The synthesis temperature of the **BW** and **LE** nanocomposites affected their properties and interactions with normal cells, with those synthesized at higher temperatures showing the improved compatibility. The highest anticancer activity was exhibited by **BW5Ag1** nanocomposite due to the larger content and small size of

Ag forms (Ag_{met}, AgCl and Ag_3PO_4) providing Ag^+ ions, presence of phosphorus, and a high saturated carbon content at the surface, as well as H_2O_2 ROS generated. The highest antibacterial activity was exhibited by **BW7Ag1** and **BW7Ag3** nanocomposites due to larger content of small size Ag_3PO_4 forms present and generated ROS (Section 3.4).

This research provides valuable insights into the role of green synthesis in enhancing the bioactivity of silver nanocomposites and highlights their potential as effective and eco-friendly therapeutic agents for cancer treatment and other biomedical applications.

Streszczenie

Rak nadal stanowi poważne globalne wyzwanie zdrowotne, pochłaniając miliony istnień ludzkich każdego roku i wywierając głęboki wpływ na jednostki, rodziny i społeczności. Konwencjonalne terapie mogą mieć poważne skutki uboczne i lekooporność, co wymaga opracowania bardziej biokompatybilnych i ukierunkowanych metod leczenia. Rozwijająca się dziedzina zielonej nanotechnologii utorowała drogę zrównoważonym i przyjaznym dla środowiska metodom syntezy nanokompozytów metalowych. Takie podejście nie tylko minimalizuje niebezpieczne produkty uboczne, ale także zwiększa biokompatybilność i bioaktywność nanomateriałów dzięki obecności bioaktywnych fitochemikaliów.

Niniejsza rozprawa dotyczy zielonej syntezy nanokompozytów srebra z wykorzystaniem odpadów browarniczych **(BW)** etapów **5** (**BW5**), **7** (**BW7**) i **9** (**BW9**), a także piwa (**B**) (Rozdział 3) i ekstraktów z liści *Malus sylvestris L.* (**LE1**), *Pinus sylvestris L.* (**LE2**) i *Sorbus aucuparia L.* (**LE3**) (Rozdział 4) jako naturalnych środków redukująco-utleniających i stabilizujących. Rosnąca akumulacja odpadów browarniczych stanowi poważne wyzwanie dla środowiska ze względu na złożoność ich utylizacji, podkreślając tym samym pilną potrzebę opracowania zrównoważonych strategii recyklingu tych odpadów w materiały o wartości dodanej. Badania te koncentrowały się na potencjale odpadów browarniczych w porównaniu z ekstraktami z liści w zakresie przyjaznej dla środowiska syntezy nanokompozytów srebra dzięki prostemu i opłacalnemu podejściu "jednonaczyniowemu".

Zsyntetyzowane nanokompozyty zostały dokładnie scharakteryzowane przy użyciu różnych technik analitycznych, w tym dyfrakcji rentgenowskiej, spektroskopii fluorescencji rentgenowskiej z dyspersją energii, transmisyjnej mikroskopii elektronowej oraz skaningowej mikroskopii elektronowej / spektroskopii rentgenowskiej z dyspersją energii, w celu określenia ich składu chemicznego i właściwości strukturalnych. Skład powierzchni tych nanokompozytów badano za pomocą rentgenowskiej spektroskopii fotoelektronów. Ich biokompatybilność oceniano na komórkach ludzkiej embrionalnej nerki (HEK293), natomiast ich cytotoksyczność oceniano wobec czterech linii komórek nowotworowych: raka szyjki macicy (HeLa), raka płuc (A549) i raka piersi (MCF-7 i MDA-MB-231). Badania aktywności przeciwnowotworowej przeprowadzono przy użyciu testu żywych/martwych komórek, testu

LDH i testu MTT. Ponadto przetestowano działanie bakteriobójcze nanokompozytów na szczepie bakterii *Escherichia coli*.

Analiza chemiczna metodami spektrometrycznymi i chromatograficznymi wykazała, że zarówno ekstrakty **BW** (Sekcja 3.1), jak i **LE** (Sekcja 4.1) były bogate w węglowodany, polifenole, cukry fermentacyjne, siarczany, azot i fosfor. Nanokompozyty srebra zsyntetyzowane przy użyciu **BW** zawierały głównie AgCl i Ag_3PO_4 jako podstawowe fazy, z niewielką ilością srebra metalicznego (Sekcja 3.2.1). Natomiast nanokompozyty pochodzące z **LE** składały się głównie ze srebra metalicznego ze śladowymi ilościami AgCl (Sekcja 4.2.1). Wszystkie pierwiastki były równomiernie rozmieszczone w masie nanokompozytów (Sekcja 3.2.3 i 4.2.3). Analiza metodą rentgenowskiej spektroskopii fotoelektronów potwierdziła obecność srebra, węgla i tlenu jako głównych pierwiastków na powierzchni wszystkich nanokompozytów (Sekcja 3.2.4 i 4.2.4). W tym samym czasie śladowe ilości chloru i fosforu wykryto również w nanokompozytach na bazie **BW**. Ogólna zawartość pierwiastków srebra zwiększała się wraz ze wzrostem temperatury syntezy z 25 do 80 °C zarówno dla nanokompozytów **BW**, jak i **LE**. Powierzchnia nanokompozytów **BW** składała się w większości ze srebra (40–60% wag.), węgla o zawartości ~20–40% wag. i tlenu o zawartości ~10–15% wag., podczas gdy nanokompozyty **LE** składają się głównie z węgla (55–75% wag.), tlenu ~15–25% wag. i srebra ~8–20% wag.).

Testy cytotoksyczności wykazały odpowiedź zależną od dawki, wykazując selektywną toksyczność w stosunku do komórek nowotworowych (Sekcje 3.3 i 4.3). We wszystkich nanokompozytach zaobserwowano dwufazowy mechanizm toksyczności: przy niższych stężeniach (0–10 μg ml^{-1}) dominowało zahamowanie wzrostu komórek, natomiast przy wyższych stężeniach (10–70 μg ml^{-1}) bezpośrednie zniszczenie komórek następowało po osiągnięciu około 30-50% zahamowania wzrostu. Warto zauważyć, że nanokompozyty syntetyzowane w temperaturze 25(±1) °C wykazywały wyższą cytotoksyczność, prowadząc do zwiększonej liczby śmierci komórek przy niższych stężeniach w porównaniu z tymi syntetyzowanymi w temperaturze 80(±1) °C. Wszystkie nanokompozyty wykazywały wyższą toksyczność wobec komórek HeLa i A549 w porównaniu z liniami komórkowymi MCF-7 i MDA-MB-231. Wartości połowy maksymalnego stężenia hamującego (IC50s) i połowy maksymalnego stężenia śmiertelnego (LC50s) dla nanokompozytów **BW** są niższe niż w przypadku nanokompozytów **LE**, co wskazuje, że nanokompozyty **BW** są bardziej skuteczne pod względem cytotoksyczności dla komórek nowotworowych niż nanokompozyty **LE** (Sekcja 5.1). Nanokompozyty **BW** mają wyższą zawartość srebra (głównie zawierają AgCl i

Ag_3PO_4 działających jako źródło jonów srebra), fosforu i chloru na powierzchni oraz w masie, niż nanokompozyty **LE**. Prawdopodobnie umożliwiają one łatwiejszy dostęp jonów Ag^+ przenikających do komórek, lepszą toksyczność P i Cl dla komórek oraz poprawę ogólnej cytotoksyczności nanokompozytów **BW** w porównaniu z nanokompozytami **LE**. Ponadto wszystkie nanokompozyty wykazywały biokompatybilność z normalnymi komórkami ludzkimi HEK293 w zakresie stężeń, w którym wykazywały cytotoksyczność dla komórek nowotworowych (Sekcja 3.3 i 4.3). Temperatura syntezy nanokompozytów **BW** i **LE** wpłynęła na ich właściwości oraz oddziaływania z normalnymi komórkami, przy czym te zsyntetyzowane w wyższych temperaturach wykazały lepszą biokompatybilność. Najwyższą aktywność przeciwnowotworową wykazywały nanokompozyty **BW5Ag1** ze względu na większą zawartość i mały rozmiar form Ag (Ag_{met}, AgCl i Ag_3PO_4) dostarczający jonów Ag^+, obecność fosforu i wysoką zawartość węgla nasyconego na powierzchni, a także generowany H_2O_2 ROS. Największą aktywność przeciwbakteryjną wykazywały nanokompozyty **BW7Ag1** i **BW7Ag3** ze względu na wyższą zawartość form Ag_3PO_4 o małych rozmiarach oraz generowany ROS (Sekcja 3.4).

Badania te dostarczają cennych informacji na temat roli zielonej syntezy w zwiększaniu bioaktywności nanokompozytów srebra i podkreślają ich potencjał jako skutecznych i przyjaznych dla środowiska środków terapeutycznych w leczeniu nowotworów oraz innych zastosowaniach biomedycznych.

Table of Contents

1. Introduction

1.1 Cancer

Cancer has been a subject of study since ancient times, with the earliest known description dating back to 3000 BC in Egypt. The term "cancer" originated from Greek and Roman physicians, signifying the crab-like appearance of tumors, which in Greek is "karkinos". The history of cancer research chronicles the discovery of its causes, ranging from cancerous growths found in dinosaur fossils to modern discussions of the difficulties encountered in understanding this complex disease. Today, cancer continues to be a significant global health issue, with increasing incidence and mortality rates, particularly affecting low- and middle-income countries. Despite remarkable progress in understanding the hallmarks of cancer development and treatment, the impact of this disease on individuals and healthcare systems remains profound. Ongoing efforts in cancer research and treatment aim to address these challenges and improve outcomes for patients worldwide [1]. The impact of cancer on health is multifaceted, involving risk factors, pathophysiology, patient education, mortality rates, and various healthcare measures aimed at prevention, early detection, and treatment [2, 3]. From the predictable genetic changes leading to pre-cancer discovered by Stanford Medicine researchers to the crucial role of basic science in revealing new ideas about cancer biology, the multifaceted impact of cancer on health is undeniable. This ongoing exploration of the historical, scientific, and societal dimensions of cancer reflects the relentless pursuit of prevention, detection, and treatment measures to combat this formidable disease [3]. Despite remarkable progress in understanding the hallmarks of cancer development and treatment, the impact of this disease on individuals and healthcare systems remains profound. Ongoing efforts in cancer research and treatment aim to address these challenges and improve outcomes for patients worldwide.

Cancer is a complex disease characterized by the uncontrolled division and survival of transformed cells [4]. It is not a single disease but rather a collection of more than 100 diseases [4], characterized by uncontrolled cell growth and spread with various causal mechanisms that share a common characteristic. Cancer cells grow uncontrollably and have the ability to spread to other parts of the body [5]. They differ from normal cells in several ways, including their ability to grow without signals, ignore signals to stop dividing or dying, invade nearby areas, and evade the immune system. Cancer can develop in different organs and tissues of the body. The development of cancer can be caused by genetic changes that affect the control of cell

growth and division, errors in cell division, damage to DNA from environmental factors, or inherited genetic changes. Each person's cancer has a unique combination of genetic alterations, and additional changes occur as the cancer progresses. Finding a cure for cancer remains a significant challenge [4].

Cancer is primarily caused by mutations, or alterations, in the DNA of cells [6]. Scientists suggest that a combination of genetic predisposition, environmental influences, and individual constitutional characteristics contribute to the development of cancer. It is the interplay between these factors that ultimately leads to the onset of the disease. These external factors causing DNA alterations are called carcinogens, increasing the risk of developing cancer. As individuals age, the likelihood of developing cancer also increases [6]. The external factors leading to different types of carcinogens are found in day-to-day life as listed in Figure 1.1.

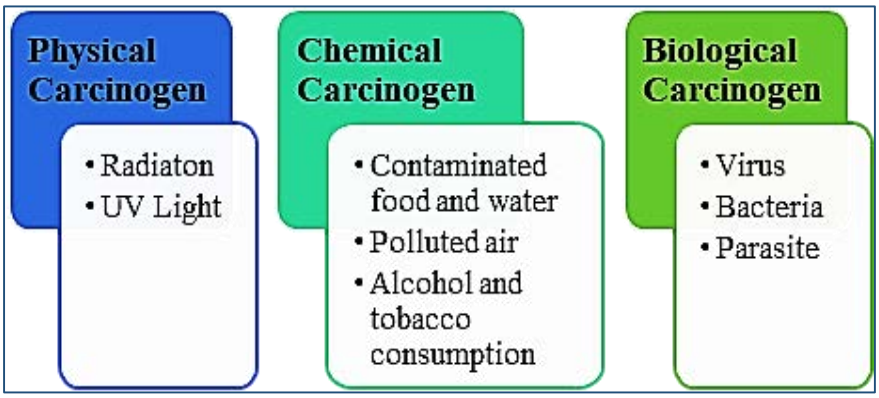

Figure 1.1 Different types of carcinogens.

1.1.1 Types of Cancer:

There are various types of cancer, each classified based on different criteria. Cancers can be categorized by the type of tissue or fluid from which they originate, as well as the specific location in the body, where they first develop. By site of origin, cancers can include breast cancer, lung cancer, prostate cancer, and more. They can also be classified by their histological or tissue types. The major categories of cancer based on tissue types are carcinoma, sarcoma, myeloma, leukemia, lymphoma, and mixed types as listed in Figure 1.2. Carcinomas are cancers that originate in the epithelial cells i.e., the cells lining the organs and tissues [7].

Sarcomas have their origins in connective and supportive tissues, encompassing a wide range of malignant diseases with diverse clinical presentations and natural histories [8]. Sarcoma is a type of cancer that specifically arises in supportive and connective tissues like bones, tendons, cartilage, muscle, and fat [7].

Myeloma originates in plasma cells of the bone marrow [7]. Plasma cell is a type of white blood cell responsible for producing antibodies that help the body fight infections. In myeloma, these

plasma cells become cancerous and multiply uncontrollably, crowding out the healthy blood cells in the bone marrow. This leads to a decrease in the production of red blood cells, white blood cells, and platelets, causing various symptoms like bone pain, fatigue, frequent infections, and anemia.

Leukemia affects blood cell production in the bone marrow [7]. It is characterized by the overproduction of abnormal white blood cells, which are responsible for fighting infections. These abnormal cells crowd out the healthy blood cells, leading to a weakened immune system and an inability to fight off infections.

Lymphomas are malignancies that affect the lymphatic system, an integral part of the immune system in vertebrates [7]. This complex organ system comprises a vast network of lymphatic vessels, lymph nodes, lymphoid organs, lymphoid tissues, and lymph fluid. Lymphomas specifically target these components and disrupt their normal function. As a result, the immune system's ability to protect the body from infections and foreign substances is compromised. Lymphomas can arise in various regions of the lymphatic system and manifest as tumors.

Mixed types of cancer have two or more components [6].

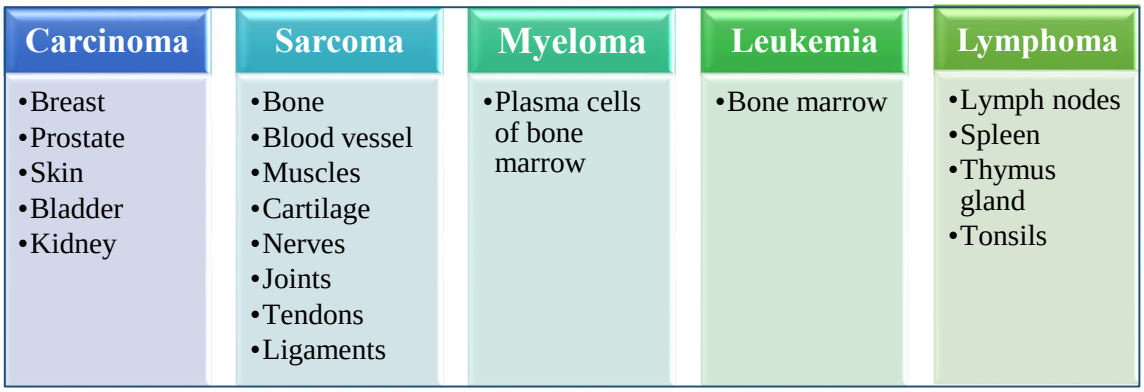

Figure 1.2 Different types of cancer.

1.1.2 Carcinoma

Carcinoma is a type of cancer that arises from epithelial cells, which are the cells that line the internal and external surfaces of the body. It is one of the most common types of cancer, accounting for a majority of cancer cases worldwide. Carcinomas can occur in various organs and tissues, including the skin, lungs, breast, prostate, colon, and pancreas, among others. The development of carcinoma is often associated with genetic mutations that disrupt the normal growth and function of epithelial cells. These mutations can be caused by various factors, such as exposure to carcinogens, genetic predisposition (inherited genetic changes), or chronic inflammation. Carcinoma typically begins with the transformation of a single abnormal cell, which then proliferates and forms a tumor. There are different subtypes of carcinoma, including

adenocarcinoma (develops in glands), squamous cell (skin) carcinoma, and transitional cell (kidney/ureter) carcinoma, each with its own characteristics and clinical features.

The diagnosis of carcinoma involves various methods, such as imaging tests, biopsies, and molecular profiling, to determine the extent of the disease and guide treatment decisions. Treatment options for carcinoma depend on several factors, including the stage and location of the cancer, as well as the patients' overall health. Common treatment modalities include surgery, radiation-, chemo-, targeted-, and immune-therapy. The choice of treatment aims to remove or destroy the cancer cells while minimizing damage to healthy tissues [9].

1.1.2.a Cervical cancer:

Cervical cancer is a type of cancer that originates in the cells of the cervix, the lower part of the uterus that connects to the vagina [10, 11]. The development of cervical cancer is typically slow, starting with changes in the cervical tissue called dysplasia. If left untreated, these abnormal cells can become cancerous and spread deeper into the cervix and surrounding areas [11]. The primary cause of cervical cancer is a long-lasting infection with certain types of human papillomavirus (HPV) [12]. It is important to undergo regular screening for cervical cancer to detect any abnormalities early on [11]. Diagnosis of cervical cancer involves various tests to determine the stage of the cancer. Treatment options are available depending on the extent of the cancer and may include surgery, radiation therapy, chemotherapy, or a combination of these approaches. It is worth noting that cervical cancer is rare in children [11]. The HeLa cell line, derived from the cervical tissue sample of Henrietta Lacks, is an immortal human cell line, developed in 1951 [13, 14]. These cells have the unique ability to continuously multiply outside of the human body, making them invaluable for scientific research and advancements. The HeLa cell line has played a crucial role in various medical breakthroughs, including the development of vaccines for diseases like polio and COVID-19. The cells are widely used in research to study disease mechanisms and test potential treatments [15].

1.1.2.b Breast cancer:

Breast cancer is a malignant cell growth that primarily affects women but can also occur in men [16]. It is the most common cancer diagnosed in women, accounting for more than 1 in 10 new cancer diagnoses each year [16]. The incidence of breast cancer increases with age, with the highest occurrence in women over the age of 50 [17]. Risk factors for breast cancer include age, gender, personal history of breast cancer, family history, and genetic factors [16]. It is usually discovered through routine screening or symptoms such as breast lumps or changes in breast shape or size. Early diagnosis is crucial for improved survival rates. In 2005, there

were an estimated 211,240 new cases of breast cancer in women and 1,690 new cases in men in the United States [17].

Breast cancer treatment involves a combination of treatments tailored to the type and stage of cancer. Surgery is often recommended, where the cancer is cut out. Systemic treatments like chemotherapy, targeted drug therapy, and immunotherapy may be used to shrink or kill cancer cells [18]. Radiation therapy, using x-rays or proton therapy, is also a common treatment for breast cancer. MDA-MB-231 and MCF-7 are both breast cancer cell lines that are commonly used in cancer research [19, 20]. However, they exhibit distinct characteristics and genetic differences. MDA-MB-231 cells are classified as a triple-negative breast cancer cell line, meaning they do not express estrogen receptors, progesterone receptors, or human epidermal growth factor receptor 2 (HER2) [19, 20]. These cells are highly aggressive and invasive, making them a valuable model for studying metastasis. Metastasis means that cancer has spread to a different part of body than where it originally started. Additionally, MDA-MB-231 cells have been shown to have a higher resistance to certain chemotherapeutic agents compared to other breast cancer cell lines [19, 20]. On the other hand, MCF-7 cells are estrogen receptor-positive, progesterone receptor-positive, and HER2-negative [20]. These cells are less aggressive and invasive compared to MDA-MB-231 cells. MCF-7 cells are commonly used to study hormone-responsive breast cancers and to evaluate the efficacy of endocrine therapies such as tamoxifen [21].

The genetic differences between these cell lines contribute to their distinct characteristics and make them valuable tools for studying different aspects of breast cancer [20, 21]. Sensitivity of these 2 cell lines depends on the drug used. MDA-MB-231 cells are metastatic so, in vitro cell migration/invasion assays are a very good indicator of the activity of these cells [21]. MCF-7 cells are not metastatic and can serve as a negative control in the in vitro cell migration/invasion assays.

1.1.2.c Lung cancer:

Lung cancer is the second most common cancer, accounting for about one out of five malignancies in men and one out of nine in women [22]. Lung cancer is a condition characterized by the uncontrolled growth of cells in the lungs [23]. It starts in the cells that make up the lungs and is not cancer that spreads to the lungs from other parts of the body [22, 23]. Smoking is the main cause of lung cancer, but it can also be caused by other types of tobacco, secondhand smoke, exposure to certain substances, gene mutations, or family history [22]. Diagnosis of lung cancer involves various tests, including imaging tests, sputum cytology,

and biopsies, which help determine the type of cancer and guide treatment decisions [22, 23]. Treatment for lung cancer may include surgery, chemotherapy, radiation therapy, targeted therapy, or a combination of these treatments [23].

A549 is the most commonly used human non-small cell lung cancer cell line for both basic research and drug discovery. The A549 cell line consists of alveolar basal epithelial cells. This cell line was first developed by D. J. Giard et al. in 1973 [24] by removing and culturing pulmonary carcinoma tissue from the explanted tumor of a 58-year-old Caucasian male. A549 cells are squamous and are responsible for the diffusion of water and electrolytes across the alveoli. When grown in vitro, these cells grow as a monolayer, adhering to the culture flask. These cells can synthesize lecithin and contain a high percentage of unsaturated fatty acids that are responsible for the maintenance of membrane phospholipids.

1.1.3 Cancer diagnosis and treatment

The diagnosis of cancer plays a crucial role in determining the most effective treatment options and improving patient outcomes [25-27]. Advances in diagnostic tools and methods have the potential to revolutionize cancer care [25]. These tools provide valuable information about the origin, stage, genetic factors, and treatment possibilities for a particular cancer. Precision medicine, in particular, relies on diagnostic tools that identify specific molecular alterations in tumors, enabling targeted therapies. However, accurately predicting a cancer's response to treatment can be challenging due to tumor heterogeneity and rapid molecular changes [25, 26]. Rapid molecular changes in cancer refer to the alterations that occur in the DNA, RNA, microRNAs, and proteins of cancer cells at a fast pace. These changes play a crucial role in the development and progression of the disease. The identification and analysis of these molecular changes have led to significant advancements in cancer diagnosis and treatment [26, 27]. By understanding these rapid molecular changes, researchers can develop innovative diagnostic tools and targeted therapies for personalized medicine. These tools can help detect cancer at an early stage, assess prognosis, and guide treatment decisions for better patient outcomes [26, 27]. Cancer diagnosis is a complex process that usually requires more than one test for diagnosis as listed in Figure 1.3a. Diagnostic procedures for cancer may include imaging, laboratory tests (such as tumor markers), tumor biopsy, endoscopic examination, surgery, or genetic testing. In some instances, repeated testing is necessary to confirm abnormal results or when a person's condition changes. Effective diagnostic testing is vital in the fight against cancer [28].

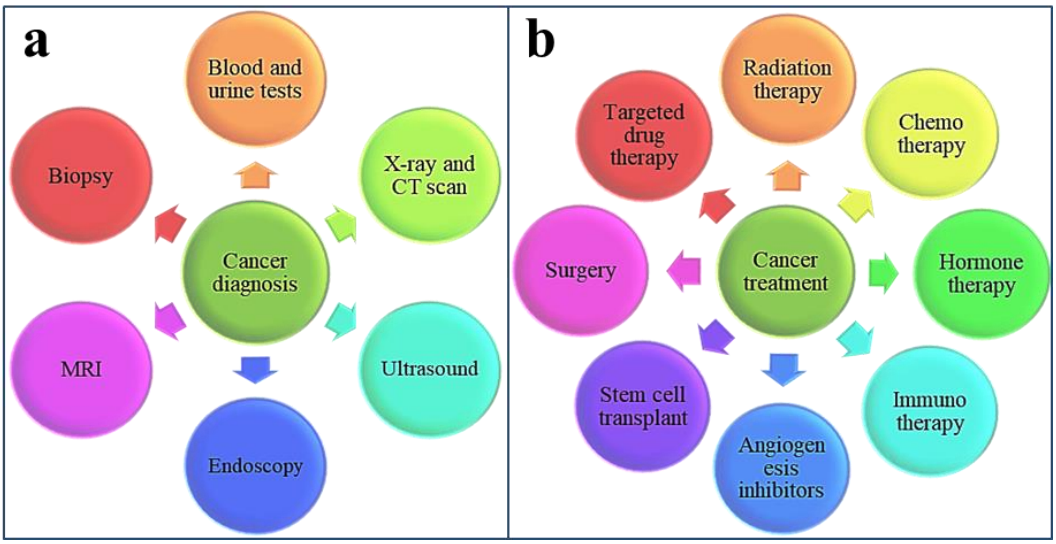

Figure 1.3 Different types of (a) cancer diagnosis and (b) cancer treatment.

Cancer is a complex and challenging disease requiring a variety of treatment approaches [29, 30]. Conventional cancer treatments such as surgery, chemotherapy, and radiotherapy are widely used (Figure 1.3b) [30]. The advantages and disadvantages of conventional cancer treatments are listed in Figure 1.4 [31]. Conventional treatments like surgery, chemotherapy, and radiation therapy have limitations in terms of efficacy and side effects [32, 33]. Surgery, while effective in removing localized tumors, may not be suitable for advanced stages of cancer. Chemotherapy can have severe side effects such as nausea, hair loss, and a weakened immune system, while radiation therapy can cause damage to surrounding tissues. Moreover, conventional treatments may not effectively target specific genetic alterations or mutations driving cancer growth [29, 32, 33]. Additionally, cancer cells can develop resistance to these treatments over time, leading to treatment failure. Furthermore, conventional treatments often lack specificity and fail to eliminate cancer stem cells, which can contribute to tumor recurrence [29]. These limitations highlight the importance of exploring new treatment approaches that provide better precision, efficacy, and fewer side effects. Therefore, new treatments are needed to overcome these challenges and improve patient outcomes [32].

Recent advancements in cancer therapies have led to new treatment options including stem cell therapy, targeted therapy, immunotherapy, and gene therapy [30, 32]. Moreover, ongoing research is exploring the development of safe and efficient cancer nanomedicines, like using nanoparticles, and natural antioxidants as a priority. With these new nanomedicine-based technologies in clinical trials, the hope is that these treatments will offer better outcomes and pave the way for a future, where cancer is no longer a global health problem.

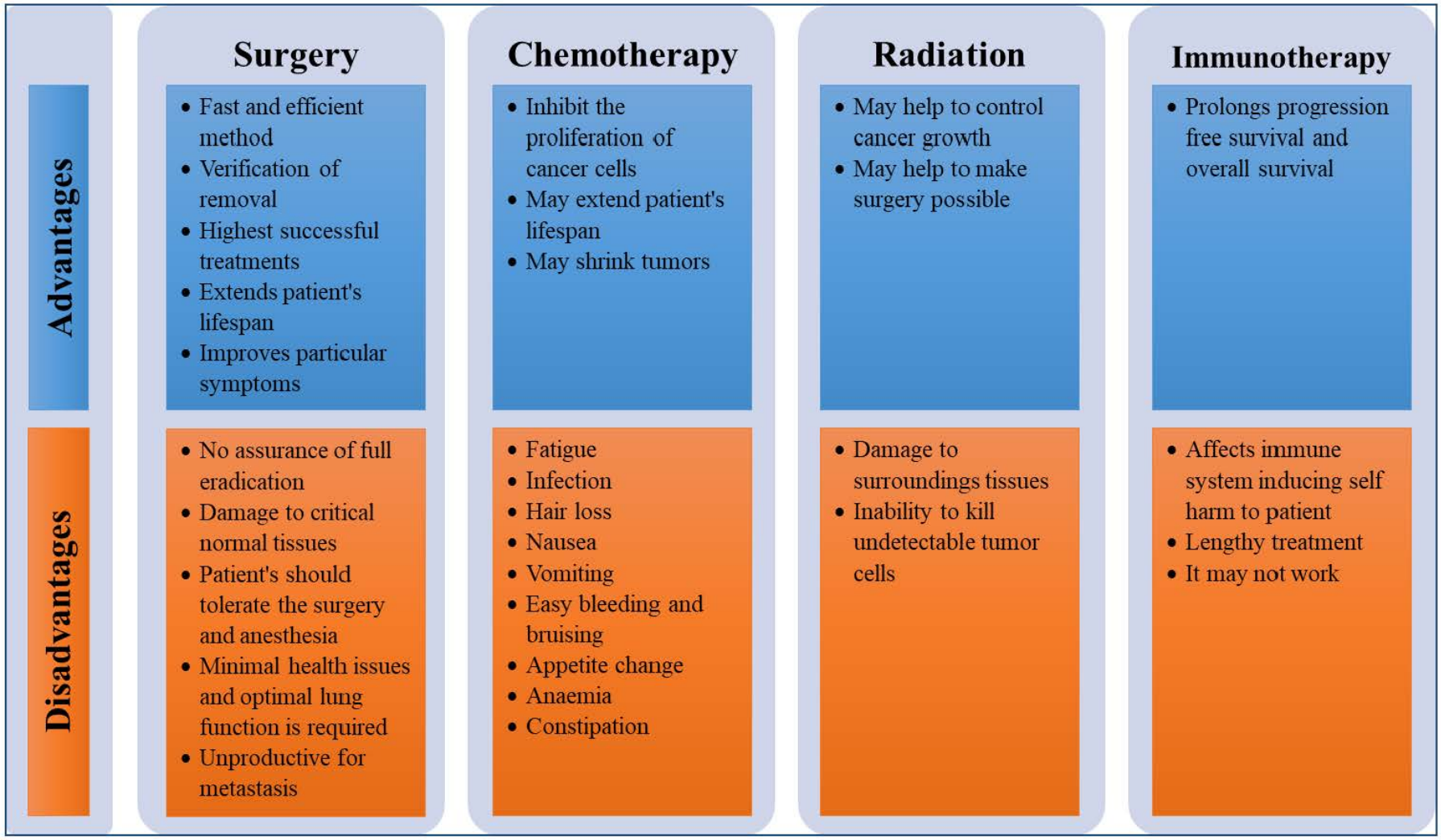

Figure 1.4 Advantages and disadvantages of traditional cancer treatment (Adapted from [34]).

1.2 Nanotechnology in cancer diagnosis and therapy:

Nanotechnology has emerged as a promising field in cancer research, offering innovative approaches to improve the accuracy and effectiveness of cancer diagnosis and treatment outcomes [35, 36]. Nanotechnology enables the delivery of chemotherapy drugs to tumor tissues by utilizing nanosized carriers, taking advantage of the enhanced permeability and retention effect. Additionally, nanomaterials can enhance the effectiveness of radiation therapy by delivering radiation to tumors while minimizing damage to surrounding healthy tissues [35, 37, 38]. This technology has also paved the way for advancements in photodynamic therapy (PDT) and photothermal therapy (PTT), two emerging and complementary treatment methods with great potential [37]. PDT is a medical treatment that uses a photosensitizer (light-absorbing agent), along with a light, generating heat killing targeted cells [38, 39]. The interaction between the light and the photosensitizer triggers a photochemical reaction that produces reactive oxygen species (ROS) [38]. These ROS cause damage to the targeted cells, leading to cell death or impairment. PTT is a medical treatment that uses photosensitizers to generate heat when exposed to specific wavelengths of light. The generated heat leads to localized hyperthermia i.e., targets and destroys cancer cells. In PDT, nanoparticles such as gold nanoparticles, quantum dots, and porphyrin nanoparticles are commonly used [38, 39]. In PTT, nanoparticles such as gold nanoparticles, carbon nanotubes, and magnetic nanoparticles are utilized [40]. The use of nanoparticles in these therapies offers several advantages, including improved therapeutic outcomes, enhanced targeting and accumulation in tumor tissue, and fewer side effects compared to traditional treatments [39]. Nanoparticles can also be used for the delivery of PDT and PTT agents, further enhancing their effectiveness [38]. Researchers are actively developing nanomaterial-based delivery platforms and studying the interactions between nanomaterials and biological systems to advance cancer diagnostics and therapeutics [35, 36]. One of the key advantages of nanotechnology in cancer treatment is its ability to specifically target cancer cells by engineering NPs to recognize and bind to cancer cells, delivering drugs or therapeutic agents directly to the tumor site [41]. This targeted approach increases the concentration of the treatment at the tumor, improving its effectiveness while reducing damage to healthy cells. Moreover, nanotechnology can improve drug delivery systems by encapsulating drugs into NPs, which protects drugs from degradation and improves their stability in the body [41]. This allows for controlled and sustained drug release, enhancing its therapeutic effect. Additionally, nanoparticles can overcome biological barriers, such as the blood-brain barrier, enabling the delivery of drugs to previously inaccessible areas.

Furthermore, nanotechnology enables the development of multifunctional platforms for cancer treatment. Nanoparticles can be designed to carry multiple therapeutic agents, including chemotherapy drugs, immune therapeutics, and gene therapies [36]. This combination therapy approach has the potential to overcome drug resistance and improve treatment outcomes. Despite the immense potential, there are still challenges to overcome in the field of nanotechnology for cancer treatment. The safety and biocompatibility of nanoparticles need to be thoroughly evaluated to ensure their long-term effects on the human body. Additionally, large-scale production and cost-effectiveness of nano-medicines need to be addressed for widespread application.

1.2.1 Metal nanoparticles for cancer treatment:

Metal nanoparticles, such as gold nanoparticles (Au NPs), zinc oxide nanoparticles (ZnO NPs), iron oxide nanoparticles (IO NPs), titanium dioxide nanoparticles (TiO_2 NPs), and silver nanoparticles (Ag NPs), have been extensively studied for their applications in cancer therapy [41]. These nanoparticles can be used for targeted drug delivery, PDT, PTT, cancer diagnosis, and enhancing the efficacy of radiation therapy. However, the clinical application of these NPs is limited due to their toxicity towards healthy cells. Ongoing research and development are focused on overcoming these challenges and optimizing metal NPs for safe and effective use in cancer treatment.

Au NPs are widely studied and are used as drug carriers, delivering therapeutic payloads directly to tumor cells [42-44]. In addition, they can serve as photothermal agents, selectively heating cancer cells and causing their destruction. Au NPs also act as contrast agents, aiding in the imaging and diagnosis of tumors. Furthermore, they can be modified by adding molecules, enhancing their ability to target and specifically bind to cancer cells. However, challenges remain in delivering Au NPs to target cells, and strategies like PEGylation [42] are being explored to overcome these obstacles.

However, ZnO NPs exhibit selective cytotoxicity towards cancer cells, making them an attractive agent for targeted cancer therapy [45-47]. ZnO NPs possess high selectivity, enhanced cytotoxicity, and biocompatibility, making them an ideal candidate for anticancer treatment. They can selectively localize to the cancer cells and induce the generation of reactive oxygen species (ROS), leading to DNA damage and cytotoxic effects on cancer cells. Furthermore, ZnO NPs have shown potential in cancer diagnosis, as they can specifically incorporate into tumor cells while accumulating less in normal cells, making them a potential diagnostic tool for early cancer imaging.

Additionally, IO NPs have been successfully used in various applications approved by the U. S. Food and Drug Administration (FDA), including cancer diagnosis, hyperthermia therapy, and iron deficiency anemia treatment [48]. In addition to these applications, recent studies have focused on utilizing IO NPs as radio-sensitizers in cancer radiation therapy [49]. IO NPs can enhance the therapeutic efficacy of radiation by increasing cell cycle arrest and inducing apoptosis in cancer cells [49].

Furthermore, TiO_2 NPs can be utilized in various therapies, such as photodynamic therapy (PDT), sonodynamic therapy, and drug delivery systems [50-52]. They can enhance the immune response against cancer cells and induce cell death through the generation of ROS similarly to ZnO nanoparticles. Additionally, TiO_2 NPs can be used for phototherapy, where they are associated with different light therapies to destroy cancer cells. Although TiO_2 NPs have limitations such as oxidative stress and limited light absorption.

Ag NPs can disrupt the interaction between cancer-associated fibroblasts and carcinoma cells, leading to cell death of cancer cells [53]. They can also be used as drug carriers to deliver cytotoxic drugs specifically to targeted cells, improving drug efficacy and reducing side effects [53] and offering potential solutions to the limitations of conventional chemotherapy [54]. The use of Ag NPs in cancer therapy faces challenges, such as ensuring targeted accumulation in cancerous tissues and minimizing toxicity to healthy tissues [53]. The advantages and disadvantages of commonly used nanoparticles for cancer treatment have been listed in Figure 1.5. This study focuses on the silver NPs, thus Ag NPs will be further discussed.

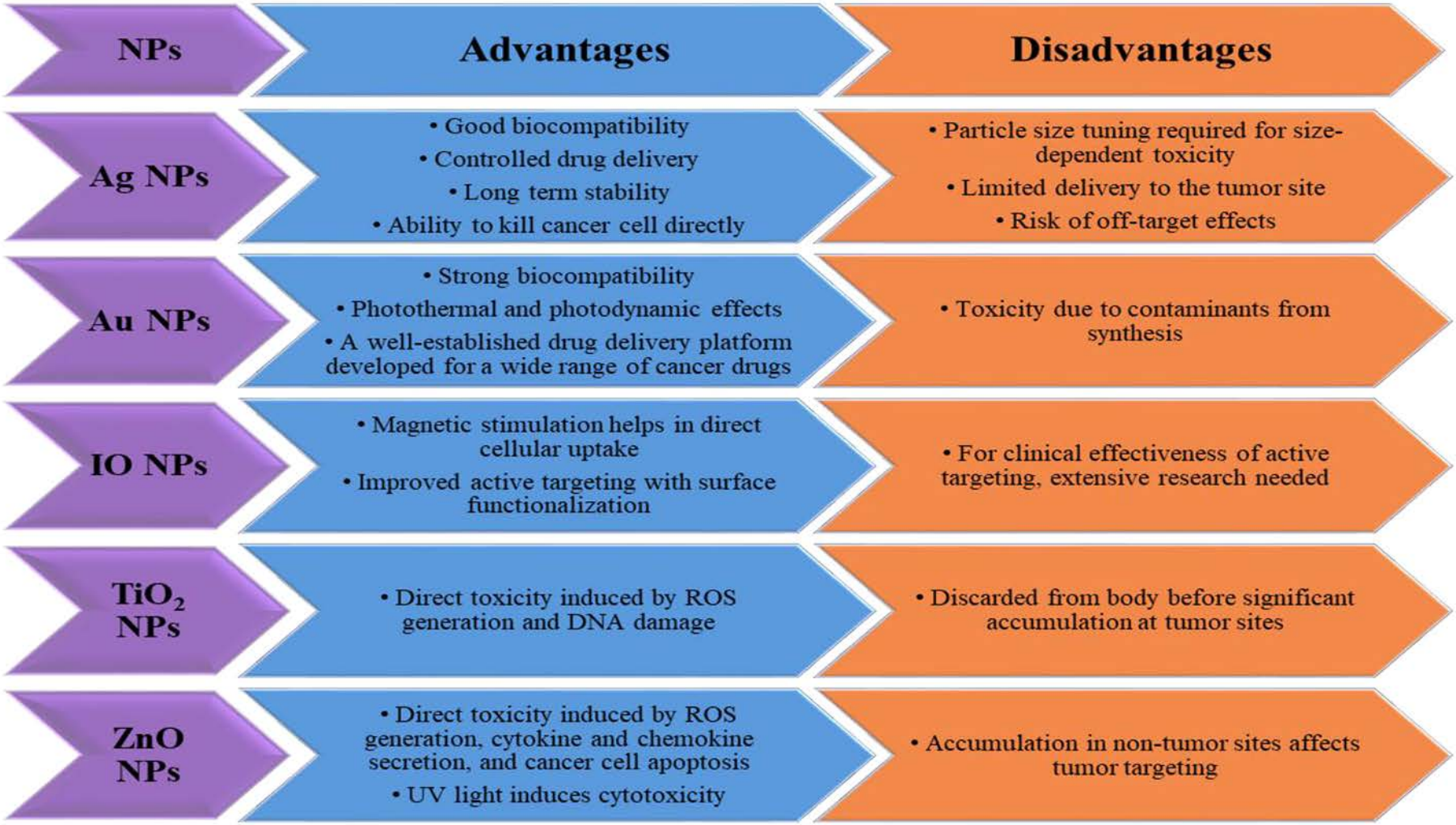

Figure 1.5 Advantages and disadvantages of commonly used metal nanoparticles (Adapted from [55]).

1.2.2 Mechanism of cytotoxicity of Ag NPs

Numerous intricate pathways for nanoparticle (NP) interaction with cells have been proposed [56-62], and distinguishing between the effects induced by NPs and metal ions can be challenging (Figure 1.6). One proposed pathway suggests the phenomenon of Ag NPs entering the cytoplasm and releasing Ag^+ ions is known as the Trojan-Horse mechanism [57, 63]. The plasma membrane is a vital component of a cell and plays a crucial role in maintaining cell integrity. It acts as a barrier, separating the cytoplasm (the internal environment of the cell) from the external environment [56]. The plasma membrane consists of a phospholipid bilayer, which is made up of two layers of phospholipid molecules. Individual cell organelles also have their own membranes with a phospholipid bilayer structure [56]. Ag NPs can enter the cytoplasm through two mechanisms: damaging the cell plasma membrane or utilizing membrane channel proteins [64]. The size of the Ag NPs plays a crucial role in this process, with smaller particles being more likely to enter the cytoplasm compared to larger ones [65, 66]. Once inside, cytoplasmic enzymes oxidize the Ag NPs, resulting in the release of Ag^+ ions [63]. Smaller Ag NPs release a larger content of Ag^+ ions in solution due to their higher surface area to volume ratio. This mechanism is not exclusive to Ag NPs and can occur with other nanoparticles as well. The release of Ag^+ ions within the cell can potentially disrupt cellular processes and induce the potential toxicity of Ag NPs [57, 58]. These ions interact with thiol groups of cell and mitochondrial membrane proteins, suppressing cell proliferation and causing mitochondrial dysfunction [56].

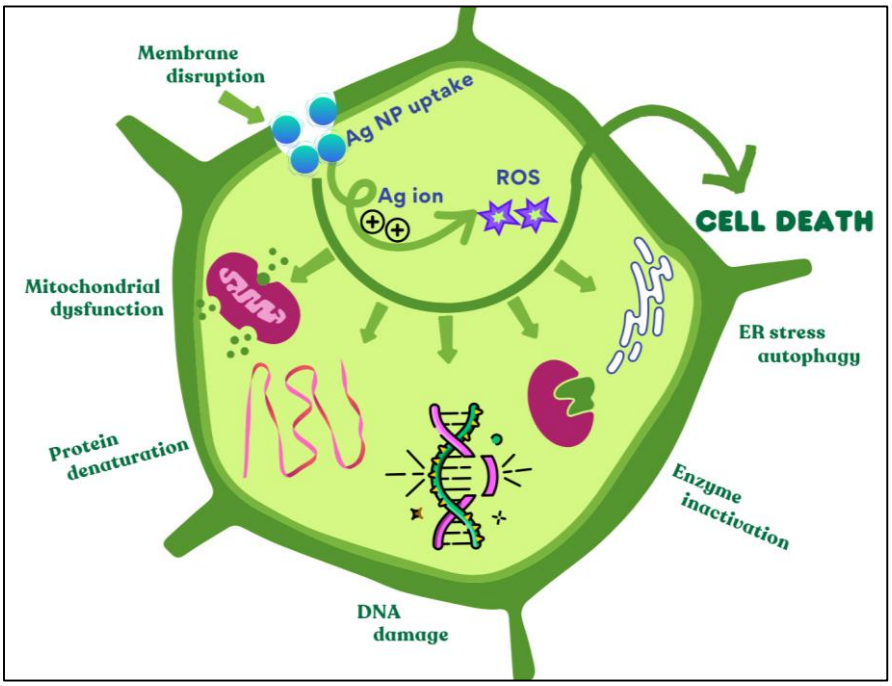

Figure 1.6 Cytotoxicity mechanism of Ag NPs.

Another pathway suggests that, noble metal NPs like Ag and Au NPs, have larger surface area to volume ratio, are effective electron acceptors [59]. When exposed to light, such as in photocatalytic reactions, noble metal NPs can efficiently capture electrons from photo-excited electron-hole pairs, preventing their quick recombination [67]. This electron-accepting behavior enhances the generation of reactive oxygen species (ROS), such as superoxide ions (O_2•–) and hydroxyl radicals (OH•) [67]. ROS are highly reactive molecules that can induce oxidative stress and damage cellular components, including DNA, proteins, and lipids [67]. The ability of noble metal NPs to inhibit electron recombination and promote ROS generation has significant implications in biomedical research. They can be utilized in targeted therapies, where the generation of ROS disrupts the membrane, causes lipid peroxidation, oxidizes proteins, damages mitochondria, and affects DNA [60, 61], hence selectively inducing cell death in cancer cells [67]. Additionally, noble metal NPs can be employed in imaging and sensing technologies for detecting biomolecules and ions, due to their unique electron transfer and catalytic abilities [68, 69].

Another pathway suggests the bond formation between positively charged Ag^+ ions and negatively charged biomolecules can lead to various consequences, including the loss of protein function, disruption in DNA synthesis, and impaired cell signaling. When Ag^+ ions interact with biomolecules such as proteins and DNA, they can disrupt the electrostatic interactions that are crucial for the proper functioning of these biomolecules [70, 71]. In the case of proteins, the positive charge of Ag^+ ions can interfere with the normal electrostatic interactions between proteins and other molecules, leading to a loss of protein function [71]. This disruption can affect various cellular processes and signaling pathways, ultimately impairing cell function. Additionally, the interaction of Ag^+ ions with DNA can interfere with DNA replication and synthesis, leading to DNA damage and impaired cell division [70, 72]. The disruption of these essential cellular processes can have detrimental effects on cell signaling and overall cellular function [61].

- ❖ The mechanism of cell death caused by silver nanoparticles differs from that of silver cations, and they also induce varying effects on different types of cells [58-62]. The physiochemical properties of NPs and conditions influence the interactions with biological systems. The physiochemical properties are NPs′ size, shape, functionalization and solution concentration, pH, temperature, time, which modify the NPs′ interactions with biological systems, playing a role in their cytotoxic effects [73-75]. Factors like size, shape, and concentration can influence the uptake, intracellular distribution, and overall toxicity of Ag

NPs [74]. The suggested pathways of the silver nanoparticle (Ag NP) cytotoxicity mechanism can be outlined as follows (Figure 1.6):

- Internalization of Ag NPs into macrophages via the scavenger receptor pathway: The scavenger receptor pathway involves the internalization of substances by scavenger receptors, which are a diverse family of cell-surface receptors [76]. Scavenger receptors recognize and bind to a variety of ligands and other harmful substances [77]. Once bound, these receptors facilitate the internalization and clearance of the ligands by cells such as macrophages and dendritic cells [76, 77]. Ag NPs can be taken up by macrophages through the scavenger receptor pathway [75]. This internalization process allows Ag NPs to enter the cells and interact with their intracellular components [73-75], and disrupting its functioning.
- Impairment of mitochondrial function: Ag NPs have been shown to impair mitochondrial function, leading to cellular toxicity [73-75]. They can accumulate in the mitochondrial membrane and disrupt its normal functioning.

Different cell lines have nearly similar size (10–15 μm) and are composed of nucleic acids, lipids (including membrane phospholipids), proteins, and carbohydrates in varying amounts and proportions [78-81]. However, differences in cellular response to NPs cannot be solely explained based on their physicochemical properties. The effects of NPs on cells vary depending on dominating molecular mechanisms, the ability of cell membranes to resist NPs, different types of repair proteins, and their amounts, among other factors [82]. Dose-dependent ROS generation, caspase-3 activation, mitochondrial membrane damage, and DNA fragmentation-induced cell death were observed for cancer cells treated with Ag NPs [83-85]. It is important to note that while all these pathways have been suggested, further research is needed to fully understand the mechanisms involved in silver nanoparticle cytotoxicity.

1.2.2.a Biphasic cytotoxicity: A Complex Cellular Response to Nanoparticles and Therapeutic Agents

In scientific research, it is crucial to understand the intricate nature of cellular responses to various stimuli, particularly in the context of nanoparticle interactions and drug treatments. Biphasic cytotoxicity represents a sophisticated and nuanced cellular response that challenges traditional dose-response paradigms and offers valuable insights into the complex dynamics of cell death and survival.

Biphasic cytotoxicity is a subset of multiphasic cytotoxicity, which encompasses cellular responses characterized by distinct phases of toxicity [86-90]. This phenomenon diverges from

the conventional linear dose-response relationship, revealing that cytotoxic effects can manifest in multiple, discrete stages [86-91]. In the case of biphasic cytotoxicity, two distinct phases are observed, each with its unique cellular response profile. The biphasic response typically consists of:

- Initial phase: Often characterized by a stimulatory effect, where cells may exhibit enhanced growth or metabolic activity at lower concentrations of the agent.
- Secondary phase: Generally marked by an inhibitory effect, where higher concentrations of the agent lead to cell death or growth inhibition.

The most common multiphase response is 'hormesis', where the initial stimulatory phase is followed by an inhibitory phase [87-89]. It is notable that while this pattern is common, variations can occur. In some cases, both phases may be inhibitory, with differing degrees of cellular inhibition observed at low and high concentrations. The underlying mechanisms of biphasic cytotoxicity are multifaceted and can be attributed to various factors:

- Dose-dependent cellular responses: Different concentrations of nanoparticles or therapeutic agents can trigger distinct cellular pathways and responses.
- Cellular adaptation and stress responses: Initial exposure may activate cellular defense mechanisms, leading to temporary resilience before succumbing to toxicity at higher doses.
- Receptor-mediated effects: Some agents may interact with multiple cellular receptors, each activated at different concentrations, resulting in varied cellular responses.
- Physicochemical properties of nanoparticles: The size, shape, and surface characteristics of nanoparticles can influence their interactions with cellular components, potentially leading to biphasic effects.

Researchers are actively exploring strategies to harness the benefits of biphasic responses while mitigating unwanted effects. These include [92]:

- Surface modifications of nanoparticles to alter their interaction with cellular components.
- Encapsulation techniques to control the release and cellular uptake of active agents.
- Red blood cell membrane-coating to improve biocompatibility and reduce off-target effects.
- Poly (ethylene glycol)-mediated approaches to modulate immunogenicity.
- Incorporation of antioxidant therapies to counteract oxidative stress-induced toxicity.

In conclusion, biphasic cytotoxicity represents a complex and fascinating aspect of cellular responses to nanoparticles and therapeutic agents. Understanding this phenomenon is crucial for advancing the knowledge in drug development, nanomedicine, and toxicology. It underscores the importance of comprehensive, multi-parametric studies in assessing the safety and efficacy of new therapeutic approaches. By embracing the complexity of biphasic responses, we can develop more sophisticated and effective strategies for harnessing the power of nanoparticles and other therapeutic agents in medical applications. The study on polyvinyl pyrrolidone coated Ag NPs showed dose- and exposure time-dependent cytotoxic effects on HeLa, MCF-7, and MDA-MB-231 inducing cell death processes like necrosis, early and late apoptosis stages [83], where apoptosis and necrosis processes were independent. This suggests the complex cell death mechanism induced by Ag NPs. Necrosis, which is a passive and accidental cell death process, was dominant at lower concentrations, and as concentration increases apoptosis, which is an active programmed cell death process, overcomes. Similar necrosis and apoptosis cell death modality was also observed for Ag NPs synthesized using *Guignardia mangiferae* [93].

Biphasic cytotoxicity has been observed in various studies investigating the cytotoxic effects of phytochemicals and nanoparticles on cells [86-89]. In most cases, the first phase is a stimulatory phase, which facilitates cell growth. The second phase generally is inhibitory, which represents cell inhibition. However, in the case of the cytotoxic effects of Ag NPs in this study, the observed phases were both inhibitory.

1.2.3 Mechanism of antibacterial activity of silver nanoparticles (Ag NPs)

Silver nanoparticles (Ag NPs) have garnered significant attention in the scientific community due to their potent antibacterial properties. The mechanism by which these nanoparticles induce bacterial cell death is multifaceted and involves several interconnected processes (Figure 1.7). This comprehensive analysis elucidates the complex interactions between Ag NPs and bacterial cells, highlighting the key factors contributing to their antimicrobial efficacy [94-97].

- Cell wall and membrane disruption: The primary antibacterial mechanism of silver nanoparticles (Ag NPs) involves their interaction with the bacterial cell wall and membrane. Due to their high affinity for negatively charged components of the bacterial envelope, particularly lipopolysaccharides in gram-negative bacteria, Ag NPs effectively adhere to the cell surface [94-96]. This interaction induces membrane permeabilization, leading to structural alterations that increase membrane permeability. As a result, vital intracellular components, such as potassium ions (K^+), DNA, and RNA, leak out of the cell.

Prolonged exposure to Ag NPs ultimately causes severe membrane damage and complete cellular disintegration, contributing to bacterial cell death.

- Oxidative stress induction: A critical aspect of the antibacterial mechanism of silver nanoparticles (Ag NPs) is the generation of reactive oxygen species (ROS), which induces oxidative stress within bacterial cells [95, 96]. Ag NPs catalyze the formation of ROS as by-product of reduction of molecular oxygen, including radicals with one or more unpaired electrons such as hydroxyl radicals (•OH), superoxide anions (O_2•–), singlet oxygen ($^1O_2$) and non-radicals hydrogen peroxide (H_2O_2). These reactive species cause oxidative damage to vital cellular components, such as proteins, lipids, and nucleic acids. Furthermore, Ag NPs interact with glutathione (GSH), a key antioxidant responsible for protecting cells from oxidative stress. By converting sulfhydryl groups (–SH) in GSH to disulfide bonds (–S–S), Ag NPs deplete intracellular glutathione levels, thereby exacerbating oxidative damage and further weakening the bacterial cell's defense system [98].
- Disruption of cellular energetics: Silver nanoparticles (Ag NPs) disrupt bacterial energy production and utilization by targeting key components of the cellular respiration process. Specifically, silver ions (Ag^+) interact with and oxidize critical electron carriers within the electron transport chain, thereby inhibiting its function. This disruption subsequently leads to a significant reduction in adenosine triphosphate (ATP) production, ultimately compromising the cell's energy homeostasis and impairing essential metabolic activities.
- Intracellular penetration and biomolecule damage: Silver nanoparticles (Ag NPs) have been shown to effectively penetrate bacterial cell membranes, leading to intracellular damage. Their entry into bacterial cells can occur through porins (water-filled channels), or via membrane disruptions caused by initial interactions with the cell surface. Once inside, silver ions (Ag^+) bind to phosphorus and sulfur groups in DNA, inducing DNA condensation and inhibiting replication. Moreover, Ag NPs can interact with intracellular proteins, leading to protein denaturation and the disruption of essential cellular processes. These mechanisms collectively contribute to the antimicrobial activity of Ag NPs [99].
- Modulation of signal transduction pathways: Recent studies suggest that Ag NPs may also interfere with bacterial signal transduction pathways, although this aspect requires further investigation [99].
- Synergistic effects of different silver compounds: The antibacterial activity of silver is not limited to metallic nanoparticles. Other silver compounds, such as silver chloride (AgCl) and silver phosphate (Ag_3PO_4) nanoparticles, also exhibit antimicrobial properties [100,

101]. These compounds may have unique mechanisms of action that complement those of Ag NPs, potentially offering synergistic antibacterial effects.

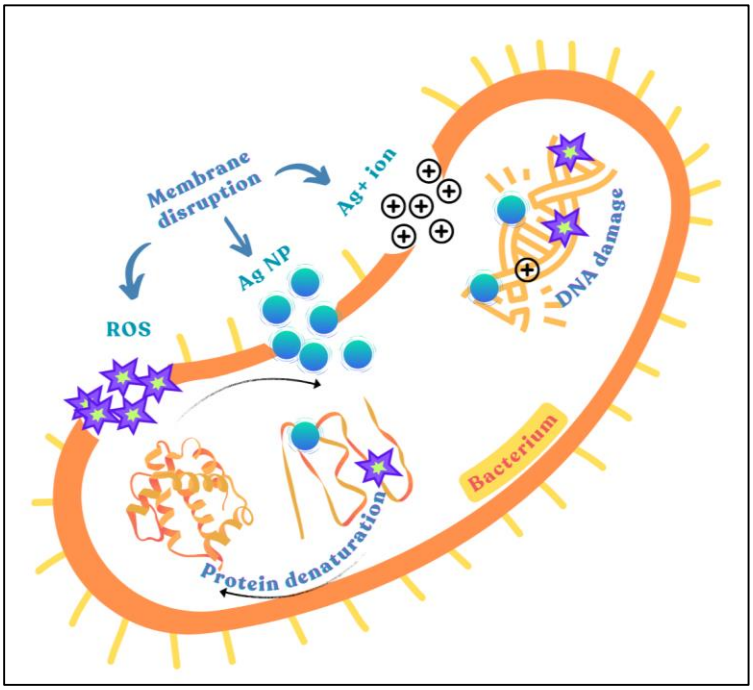

Figure 1.7 Antibacterial mechanism of Ag NPs.

1.3 Synthesis of silver nanoparticles (Ag NPs):

The synthesis of Ag NPs is an essential area of study in nanotechnology and can be classified into two main approaches as listed in Figure 1.8 [102]. The first approach is known as the top-down approach, which involves the production of particles from a bulk material. On the other hand, the second approach is called the bottom-up approach, where nucleation sites are created and subsequently grow into nanometer-sized particles. These two methods offer different strategies for the fabrication of Ag NPs with specific properties and applications.

The physical synthesis method, known as top-down synthesis, involves the production of particles ranging from 1–100 nm in size from bulk silver, usually in its solid phase. These methods include techniques like milling, pyrolysis, and spark discharging [103]. Physical synthesis allows for the rapid nucleation and growth of Ag NPs at the same rate, resulting in the formation of nanoparticles with desired characteristics [104]. These methods are commonly used to produce Ag NPs with uniform size and shape, as well as with the desired properties for their applications in cancer therapy and other fields. However, physical techniques can be combined with other methods to enhance the synthesis process. The physical synthesis method is commonly employed to achieve rapid and large-scale production within a short timeframe.

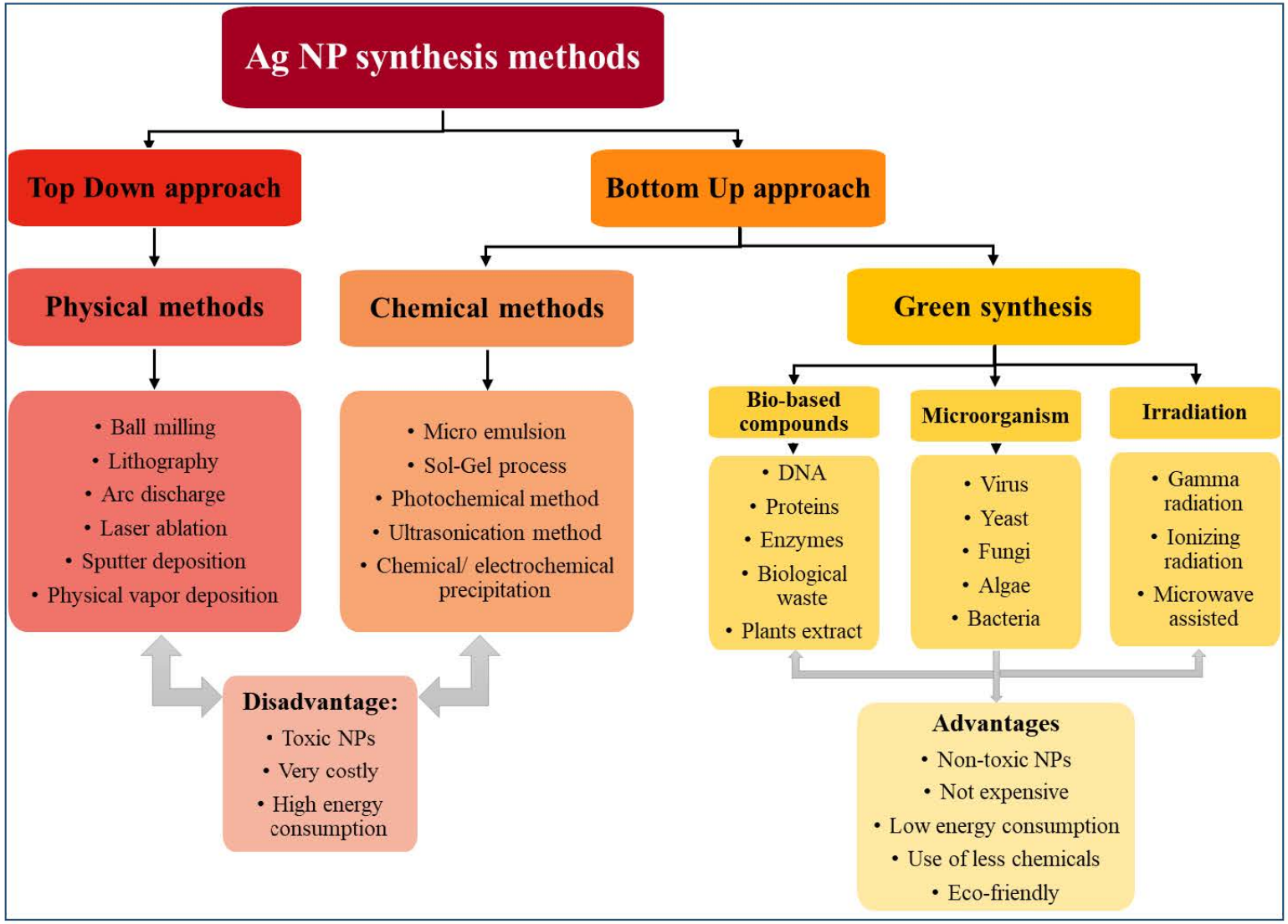

Figure 1.8 Different synthesis mechanism for Ag NPs (Adapted from [102]).

The bottom-up approach of silver nanoparticle synthesis primarily relies on the use of reducing agents. This approach can be divided into two distinct categories of methods. The first category involves the use of chemical reagents to reduce silver cations, resulting in zero-charged silver atoms that serve as templates for crystal growth into nanoscale particles. This method is commonly referred to as the "chemical" synthesis method [105, 106]. Stabilizers are often added in conjunction with these techniques to ensure stability, prevent aggregation, control morphology, and provide physiologically compatible properties [107-109]. Another category in the bottom-up synthesis methods involves the use of nonchemical reagents, such as biological agents or bio-extracted compounds, for the synthesis of nanostructures. These methods are often referred to as "biological" synthesis or a subcategory of green synthesis [102, 110].

1.3.1 Green synthesis of Ag NPs

In many studies, the focus has been on the synthesis of Ag NPs without considering factors like cost-effectiveness, time, eco-friendliness, energy consumption, and human well-being [111]. The utilization of organic reagents poses environmental and health risks, potentially leading to illnesses such as liver damage [112]. For instance, one common reducing agent used for Ag NP synthesis is hydrazine, which is highly toxic, cancerous, and lethal [113]. Furthermore, the wastewater produced during nanoparticle synthesis may contain detrimental chemicals [114]. Another drawback is the low yield, where only a small portion of the initial materials is transformed into nanoparticles, resulting in the wastage of raw materials. Additionally, the high costs associated with starting materials, equipment, labor, extended synthesis times, and the lack of control over size and shape can impose constraints on their practical applications [115, 116]. Green synthesis is adopted to address the shortcomings of traditional synthesis methods and to establish a more innovative, efficient, cost-effective, and environmentally friendly approach for the synthesis of nanoparticles. Although some studies have incorporated green synthesis techniques, they still rely on the use of chemicals and high energy consumption in physical synthesis methods, leading to increased costs [111]. Therefore, there is a need for alternative methods like biological synthesis using nonchemical reagents [113]. The limitations of traditional physical and chemical methods have led to a growing interest in exploring less harmful and economically feasible techniques. In this context, the emphasis has been on "green synthesis," which involves leveraging naturally occurring processes for the eco-friendly production of silver nanoparticles (Ag NPs). It's crucial to understand that green synthesis encompasses not only biological agent-assisted methods but

also environmentally friendly techniques that promote sustainable and responsible silver nanostructure production.

Green synthesis aims to advance innovative chemical technologies with the goal of reducing or entirely eliminating the utilization and generation of hazardous substances throughout the design, production, and utilization of chemical products. This entails minimizing or, where feasible, eradicating pollution arising from synthesis processes, steering clear of the consumption and waste of nonrenewable raw materials, refraining from the use of hazardous or polluting materials in product manufacturing, and shortening the synthesis time. Paul J. Anastas [117], often recognized as the pioneer of green chemistry, has defined it as "a work philosophy that involves the use of alternative tools and pathways to prevent pollution," encompassing both the design of the synthetic strategy and the treatment of potential secondary products arising from that pathway [117, 118].

Bacteria, fungi, algae, and plant species are some of the most commonly used biological resources for the green synthesis of Ag NPs [113, 115, 116, 118]. Leveraging different parts of a plant for nanoparticle synthesis is a widely adopted method, proving to be eco-friendly, rapid, and cost-effective, involving fewer steps in comparison to other methods [119, 120]. This efficiency makes plant-based synthesis more effective in nanoparticle production compared to methods utilizing microorganisms. Various plants and plant parts have been successfully employed in this process, each contributing unique phytochemicals, such as terpenoids, flavonoids, polyphenols, alkaloids, proteins, etc., which play a role in reducing metal ions and stabilizing the resultant nanoparticles [121]. Leaf extracts have been widely used, with studies reporting the synthesis of Ag NPs using extracts from papaya fruit [122]. Research has also explored the use of various other plant parts, including fruits, seeds, and roots, each offering distinct advantages in nanoparticle formation and stabilization [122]. For instance, leaf extracts of *Ocimum sanctum* (Tulsi), Aloe vera, *Azadirachta indica* (Neem), *Vernonia amygdalina* (Bitter leaf), etc., seed extracts of Cassia tora, flaxseed (*Linum usitatissimum*) have been found to yield stable Ag NPs with tailored properties suitable for biomedical applications [123]. The diversity of plant sources allows for the fine-tuning of nanoparticle characteristics, such as size and shape, which significantly influence their antimicrobial, antioxidant, and anticancer properties [123]. Recent studies have also highlighted the potential of using whole plant extracts in the green synthesis process, offering a holistic approach to nanoparticle production [124]. This growing body of research underscores the versatility and potential of plant-mediated green synthesis in producing Ag NPs with diverse applications in biomedicine and beyond.

1.3.1.a Principles of green synthesis:

Green synthesis is guided by a set of principles that aim to promote environmentally friendly and sustainable practices in chemical processes. While specific formulations may vary, the following 12 principles (Figure 1.9) are commonly recognized in the context of green synthesis [117]:

Figure 1.9 Principles of green synthesis.

1. Atom Economy: Maximize the incorporation of starting materials into the final product to reduce waste generation.

2. Prevention: Design processes to avoid or minimize the use of hazardous substances, reducing the need for additional waste management.

3. Less Hazardous Chemical Syntheses: Use and generate substances with minimal toxicity, reducing environmental and health risks.

4. Designing Safer Chemicals: Focus on developing chemicals that are safe for use, handling, and disposal, minimizing adverse effects on human health and the environment.

5. Safer Solvents and Auxiliaries: Choose environmentally benign solvents and auxiliary substances to reduce the environmental impact of chemical processes.

6. Energy Efficiency: Design processes to be energy-efficient, minimizing overall energy consumption and environmental impact.

7. Renewable Feedstocks: Utilize renewable raw materials or feedstocks to decrease dependence on non-renewable resources.

8. Reduce Derivatives: Minimize the use of unnecessary derivatization steps, reducing waste generation and improving overall efficiency.

9. Catalysis: Employ catalytic processes to increase reaction efficiency, reduce the need for stoichiometric reagents, and enhance selectivity.

10. Design for Degradation: Design products that break down into innocuous substances after use to minimize environmental persistence.

11. Real-time Analysis for Pollution Prevention: Implement real-time monitoring and control to minimize the formation of hazardous substances during chemical processes.

12. Inherently Safer Chemistry for Accident Prevention: Design inherently safer processes to prevent accidents, minimizing risks to human health and the environment.

These principles collectively guide the development of sustainable and environmentally friendly practices in the field of chemistry, contributing to the broader concept of green chemistry.

1.3.1.b Phases involved in the green synthesis of nanoparticles green nanoparticles for catalysis

In the green synthesis of nanoparticles, the process consists of several phases (Figure 1.10) [119].

1. Initial phase: Involves obtaining the reaction medium, which is the aqueous extract from one or more parts of the plant species or the culture media for microorganism growth. This phase also includes the precursor salt, serving as the source of metal ions.

2. Activation phase: Encompasses the chemical reduction of metal ions and the generation of nucleation centers, leading to the development and growth of nanoparticles.

3. Growth phase: Small adjacent nanoparticles spontaneously merge into larger particles, forming aggregates. This process is influenced by factors such as temperature, concentration, type of compounds, pH, and reaction time.

4. Termination phase: In this final phase, the shape of the nanoparticles is determined, and the participating compounds in the reaction play a role in stabilizing and enhancing their properties.

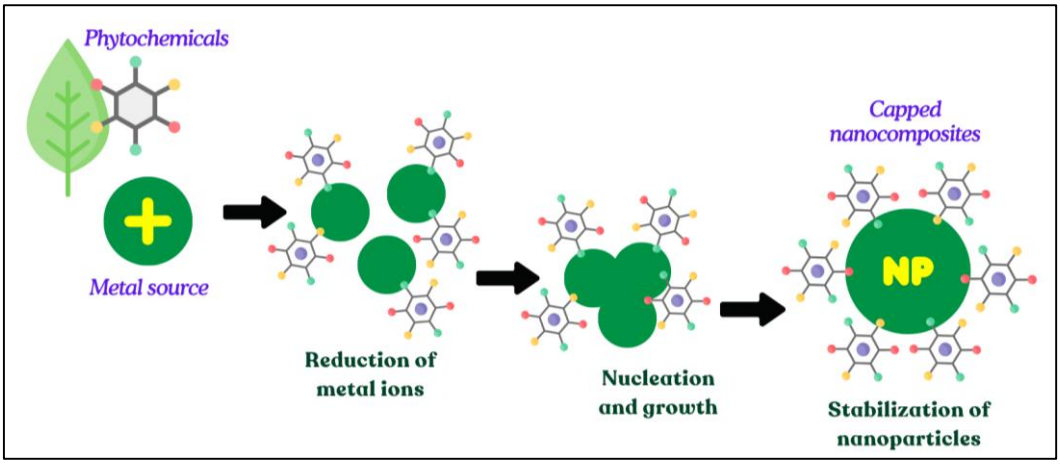

Figure 1.10 Phases involved in the green synthesis of nanoparticles.

1.3.1.c Factors affecting green synthesis

In any synthesis process, key reaction conditions, including temperature, pH, and reaction time, significantly impact the shape, size, and yield of the synthesized nanoparticles (Figure 1.11) [119, 120, 125].

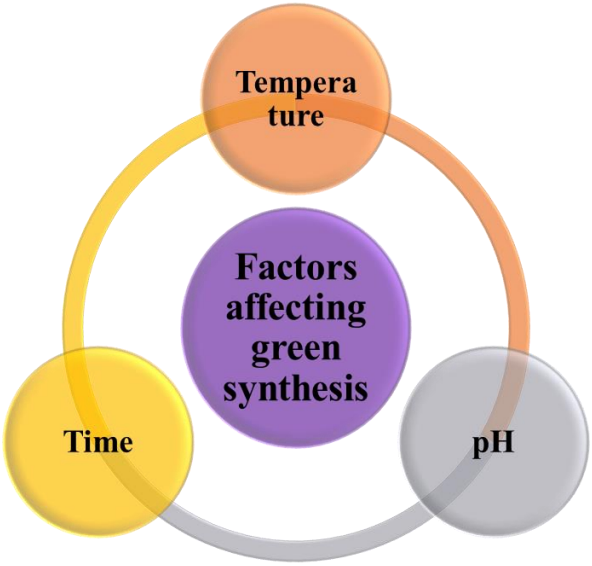

Figure 1.11 Factors affecting green synthesis.

A. Temperature: Among the most influential factors, temperature shapes the synthesized nanoparticles, determining their form (spherical, prismatic, flakes, triangular, octahedral, etc.) and size. As temperature rises, both the reaction rate and the formation of nucleation centers increase, leading to higher yields. Different temperatures foster distinct interactions between reactants, yielding various shapes; a greater temperature increase corresponds to larger nanoparticle sizes [105, 126].
B. pH: pH levels influence nucleation centers, generating more centers at higher pH values. Additionally, certain nanoparticles can only be synthesized in acidic or alkaline

conditions. For instance, magnetic nanoparticles typically form under alkaline pH, while metal oxide nanoparticles are generally synthesized under acidic or neutral pH conditions [127].

C. Time: The duration of the reaction is crucial in determining nanoparticle size. Prolonged reaction times have been observed to favor larger nanoparticle sizes and higher yields, attributed to the extended interaction time between reactants [128].

1.3.2 Brewery wastes for green synthesis of Ag NPs

Beer is an alcoholic beverage that has been enjoyed by millions of people worldwide for thousands of years and remains one of the most popular alcoholic beverages. An enormous amount of waste is produced by the brewing industry [129]. Beer comes in various styles and flavors, including lagers, ales, stouts, and India pale ale (IPAs), each with its unique characteristics. Different brewing techniques, ingredients, and yeast strains contribute to the wide range of beer varieties available. Beer is produced through a process called brewing. Barley, hops, yeast and water are used for brewing beer, where barley provides the fermentable sugars necessary for fermentation, while hops contribute bitterness, flavor, and aroma to the beer. Water is a crucial component that affects the beer's flavor profile, and yeast is responsible for fermenting the sugars and producing alcohol.

The brewing process typically involves 10 steps, including the malting, mashing, lautering, boiling, fermentation, conditioning, and packaging as shown in Figure 1.12 [130].

Step 1: Malting- involves soaking and germinating the barley grains to activate enzymes that convert starches into fermentable sugars.

Step 2: Mashing- combines malted barley with hot water to extract the sugars, creating a liquid known as wort.

Step 3: Lautering- involves separating the liquid wort from the solid grains constituting to the first type of waste (**BW3**) called Brewer's spent grains (BSG).

Step 4: Boiling- the wort is the boiled and hops are added at different times to achieve desired bitterness and flavor.

Step 5: Wort clarification- involves the clarification of the wort from undissolved hop particles and proteins using a whirlpool, resulting to the second type of waste (**BW5**) called wort precipitate.

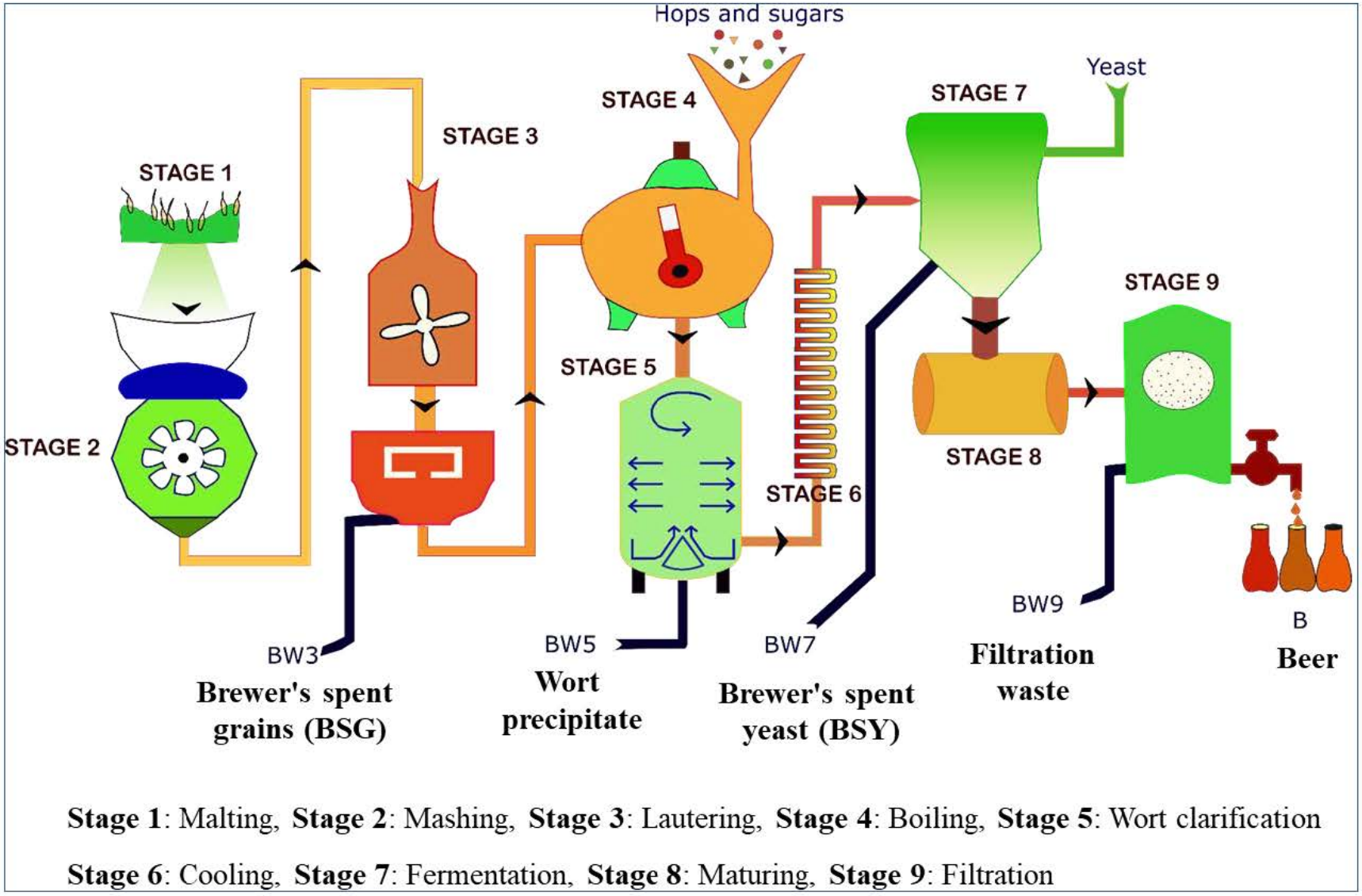

Figure 1.12 Brewing process [131].

Step 6: Cooling- cooling the obtained wort.

Step 7: Fermentation- involves yeast addition to the cooled wort. The yeast consumes the sugars present in the grains, converting them into alcohol and carbon dioxide, resulting in the characteristic effervescence of beer. After the completion of fermentation, the slurry obtained from the precipitation of this wort constitutes to the third type of waste (**BW7**) which has the yeast added for fermentation.

Step 8: Maturing- involves secondary fermentation of wort at low temperature (~1-2 °C). This allows the wort to mature and develop its flavors.

Step 9: Filtration of liquid wort- the clear liquid wort i.e., the beer (**B**) is filtered out from remaining yeast and protein-tannin that sank to the bottom. This constitutes the filtration waste (**BW9**).

Step 10: Packaging- packing of the beer in bottles, cans, or kegs for distribution and consumption.

The constituents and applications of different brewery wastes and beer are listed in Figure 1.13. The organic content of brewery waste makes it a valuable resource for various applications, offering potential benefits in terms of sustainability, resource recovery, and environmental impact reduction [132]. Furthermore, advancements in biotechnology and biochemistry have led to the exploration of brewery waste for the production of biofuels and biochemicals. The carbohydrates present in the waste can be converted into bioethanol through fermentation processes, offering a renewable and sustainable alternative to fossil fuel-based transportation fuels. Additionally, the waste streams from breweries can serve as a feedstock for the production of various biochemicals, including enzymes, organic acids, and biopolymers, which have applications in various industries. Overall, brewery waste, with its high organic content, presents opportunities for waste valorization and resource recovery. By implementing appropriate waste management strategies and exploring innovative technologies, the organic content of brewery waste can be effectively harnessed, contributing to a more sustainable and circular economy [132].

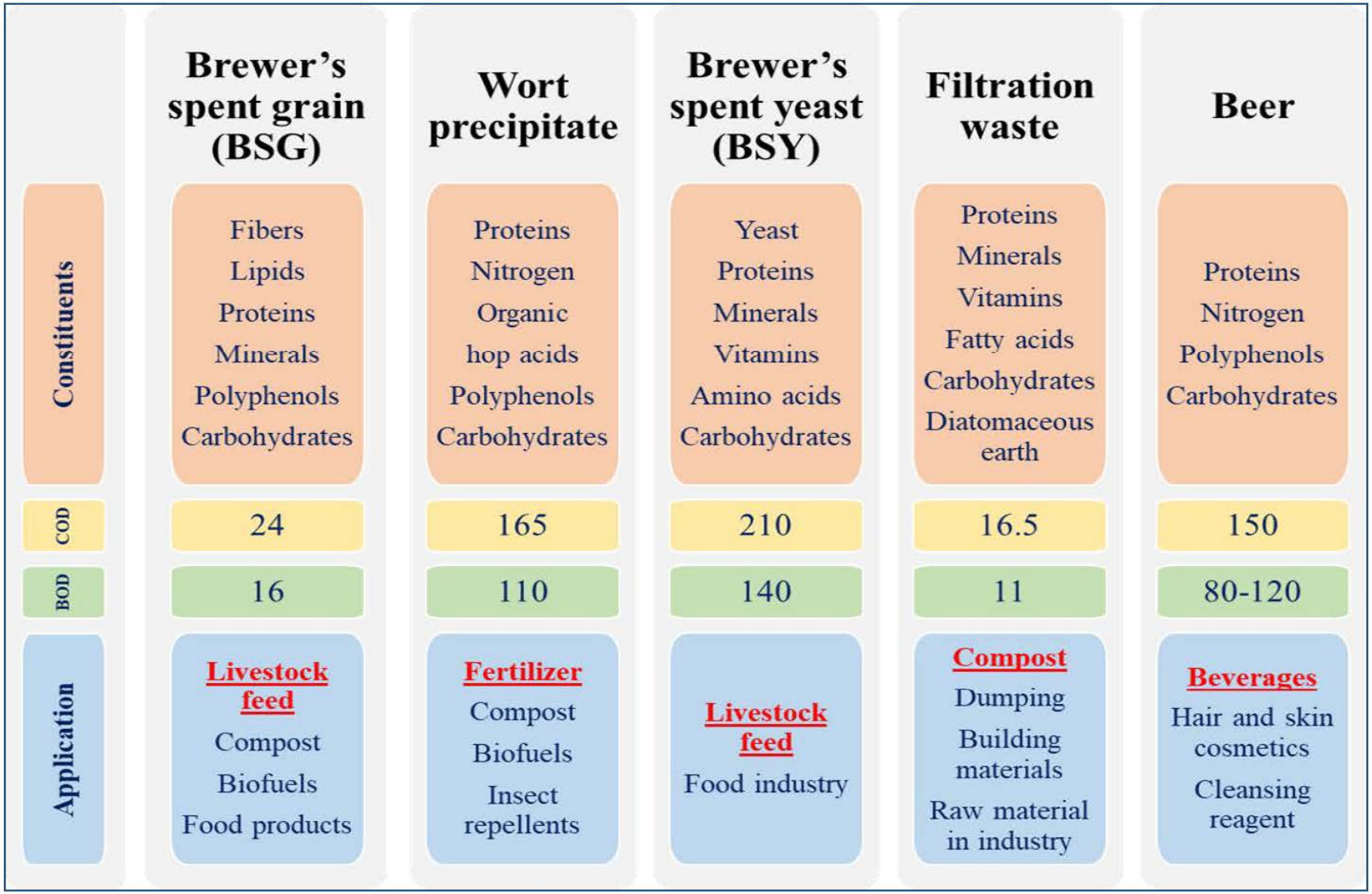

Figure 1.13 Constituents and applications of different brewery wastes and beer [131].

1.3.2.a Brewer's spent grains (BSG)

Spent grains, a significant byproduct of brewing primarily composed of malted barley, offer valuable carbohydrates, proteins, and fibers suitable for bioconversion [130]. Biotechnological processes can utilize them to produce enzymes, organic acids, and other chemicals. With high protein and fiber content, spent grains are nutritious livestock feed, often donated or sold by breweries to farmers. They can also contribute to biofuel and biogas production through anaerobic digestion or fermentation, promoting renewable energy. In food production, spent grains enhance bakery products and can be transformed into dietary supplements or used as a partial flour substitute. By exploring innovative uses for spent grains, the brewing industry can reduce waste, optimize resources, and enhance overall sustainability.

1.3.2.b Wort precipitate

Brewery waste, known as "wort precipitate," consists of solid materials that settle during the brewing process, originating from the coagulation of proteins and particles in the boiled wort [130, 132]. This sediment comprises various organic and inorganic compounds, including proteins, polyphenols, carbohydrates, hop residues, and yeast remnants. Breweries are addressing the disposal challenge by exploring alternative uses for wort precipitate, such as converting it into high-protein animal feed, using it in composting for nutrient-rich agricultural applications, and utilizing it as a feedstock for bioenergy production through anaerobic digestion. These sustainable approaches contribute to the circular economy and environmentally friendly practices in the brewing industry.

1.3.2.c Brewer's spent yeast (BSY)

Brewer's spent yeast (BSY) is a byproduct of the brewing process, resulting from the completion of yeast cells' primary fermentation duty, which involves converting sugars into alcohol [133]. After fermentation, the spent yeast settles at the bottom of the fermentation vessel. BSY is a valuable byproduct rich in proteins, B-complex vitamins, and minerals. It finds common application as a supplement in animal feed, providing essential nutrients to livestock. The pharmaceutical and nutraceutical industries are also interested in extracting bioactive compounds from BSY. Some breweries reuse BSY for subsequent beer batches, contributing to sustainability and waste reduction. The versatile nutritional composition of BSY enables its potential application in various sectors [133].

1.3.2.d Filtration waste

Filtration waste from breweries refers to the solid residue produced during the beer filtration process, which eliminates yeast, hop particles, and sediment, ensuring a clear final product

[134]. The waste includes retained solids from the beer and the filter aid material. Proper disposal is essential due to environmental concerns, given the waste's organic and inorganic components. Sustainable approaches involve composting, utilizing filtration waste as a feedstock for bioenergy production through anaerobic digestion, and exploring recycling options for spent filter media [132]. These practices align with the circular economy, supporting the brewing industry's overall sustainability goals (Figure 1.12).

1.3.3 Leaf extract for green synthesis of Ag NPs

The field of research and development of Ag NPs using plant extracts is emerging. Plant structures, both intracellular and extracellular, can be utilized to produce different types of metal nanoparticles [122-124]. Intracellular processes involve using seed plants in high-metal media and hydroponic solutions, such as metal-rich soils. On the other hand, extracellular processing methods involve preparing extract leaves by boiling or macerating leaves in water or ethanol. Medicago sativa is a plant that has been able to synthesize silver and gold nanoparticles by utilizing its biomolecules and is the first plant recorded to be used for the extracellular synthesis of nanoparticles [135]. Since then, plants have garnered significant attention as a medium for nanoparticle synthesis.

1.4 Characterization of Ag NPs

The characterization of Ag NPs involves assessing their physical, chemical, and structural properties. Here are some common characterization techniques used for Ag NPs [136]:

1. Transmission Electron Microscopy (TEM) provides high-resolution images of Ag NPs, allowing researchers to determine their size, shape, and distribution [137]. It helps in confirming the presence of nanoparticles and estimating their average diameter.

2. Scanning Electron Microscopy (SEM) provides information about the surface morphology and topography of Ag NPs [137]. It offers a three-dimensional view of the nanoparticles and is useful for understanding their agglomeration behavior.

3. X-ray Diffraction (XRD) is used to investigate the crystalline structure and phase purity of Ag NPs [138]. It can identify the crystallographic planes and lattice parameters, providing information about the size and composition of the nanoparticles.

4. UV-Visible Spectroscopy is employed to study the optical properties of Ag NPs [139]. It measures the absorption and scattering of light by the nanoparticles, providing information about their size, shape, and concentration.

5. Fourier Transform Infrared Spectroscopy (FTIR) helps in analyzing the surface functional groups and chemical bonding of Ag NPs [140]. It can identify the presence of stabilizing agents or surface coatings on the nanoparticles.

6. Dynamic Light Scattering (DLS) measures the hydrodynamic diameter and size distribution of Ag NPs in a liquid medium [141]. It provides information about particle stability, aggregation, and the influence of environmental factors.

7. Zeta Potential Analysis determines the surface charge of Ag NPs. It helps in understanding their stability and interaction with other particles or biological systems.

8. Energy-Dispersive X-ray Spectroscopy (EDXS) is utilized to analyze the elemental composition of Ag NPs [142]. It provides information about the presence of impurities or other elements incorporated into the nanoparticles.

9. Thermogravimetric Analysis (TGA) measures the thermal stability and decomposition behavior of Ag NPs [143]. It helps in determining the weight loss and thermal properties of the nanoparticles.

10. X-ray Photoelectron Spectroscopy (XPS) is a technique used to investigate the chemical and oxidation states of Ag NPs [144, 145]. XPS analysis allows researchers to determine the electron binding energy of specific elements, such as silver (Ag), which provides information about its chemical environment and oxidation state [146]. By analyzing the XPS spectra of Ag NPs, researchers can gain insights into their physical and chemical properties, aiding the characterization and understanding of these nanoparticles.

By employing these characterization techniques, researchers can gain a comprehensive understanding of the physical, chemical, and structural properties of Ag nanoparticles, which is crucial for optimizing their synthesis methods and exploring their potential applications.

The bioactivity of Ag NPs is dependent on several characteristic properties, including their size, shape, morphology, and coating. Research has shown that the biocidal and cytotoxic properties of Ag NPs vary depending on their linear size and shape, as well as the cell line used and the nanoparticle coating [147]. For example, smaller Ag NPs have been found to exhibit higher antibacterial activity, while larger Ag NPs more effectively interfere with copper metabolism [147]. The morphology and structure of Ag NPs also play a crucial role in determining their biological activity [136]. It is important to note that the bioactivity of Ag NPs can have both positive applications, such as broad-spectrum bactericidal and virucidal properties, as well as potential toxic effects that need to be considered [148].

1.5 Aim of the project NPs

The project goal was to understand the mechanism of the cytotoxicity effect towards cancer cells exhibited by biocompatible silver nanocomposites prepared by green synthesis method from different reducing agent precursors, investigated in a wide concentration range for various cell lines (normal and cancer cells) and bacteria strain. The brewery product, different staged brewery wastes, and leaf extracts were used as reducing agent precursors for a green synthesis of silver nanocomposites to enhance the biocompatibility of the nanocomposites. Various structural and surface compositions were evaluated and studied in relation to the biocompatible and cytotoxic effects of nanocomposites.

The experimental section part discussed in Chapter 2 describes the experimental methods and procedures applied in the project. This includes the materials, chemicals, and biological samples used in the project. It also reports the preparation of precursors using brewery wastes and leaves, elemental and chemical analysis of precursors, synthesis method for Ag nanocomposites using the precursors, characterization techniques applied for understanding the chemistry of Ag nanocomposites and the assays used for testing their anticancer and bactericidal activity. Further, two chapters discuss in detail the results obtained for silver nanocomposites synthesized using different precursors. Chapter 3 and Chapter 4 report the synthesis of silver nanocomposites using brewery wastes and leaf extracts respectively. These chapters extensively discuss the results of silver nanocomposites′ structural and chemical properties characterization and study their biocompatible and cytotoxic effects on selected five different human cells and antibacterial effect on *Escherichia coli* bacteria. These chapters also unravel the biphasic cytotoxicity effect exhibited by nanocomposites on the investigated human cells. Chapter 5 describes the major differences observed between the nanocomposites synthesized using brewery wastes and leaf extracts. Finally, concluding remarks on the overall project and some future perspectives are presented.

2. Experimental methods

2.1 Materials and chemicals

The materials and chemicals used are as follows:

1. Silver nitrate ($AgNO_3$), purity 99.9% (Avantor Performance Materials Poland S. A. former POCH S.A., Gliwice, Poland).
2. Brewery wastes from stages 5 (**BW5**), 7 (**BW7**), 9 (**BW9**) and beer (**B**) from Jabłonowo brewery (Wólka Kosowska, Poland).
3. Leaves of *Malus sylvestris L., Pinus sylvestris L., Sorbus aucuparia L.*
4. Doubly distilled deionized water (resistivity 15 MΩ cm).
5. Trypan blue solution (Sigma-Aldrich, Merck, Poland).
6. Trypsin-EDTA (ethylenediamine tetraacetic acid) with phenol red (Sigma-Aldrich, Merck, Poland).
7. Dulbecco's modified Eagle's medium (DMEM with 1g l^{-1} glucose) without phenol red (Sigma-Aldrich, Merck, Poland).
8. Roswell Park Memorial Institute (RPMI) 1640 cell media without phenol red (Sigma-Aldrich, Merck, Poland).
9. Fetal bovine serum (FBS) (Sigma-Aldrich, Merck, Poland).
10. Penicillin-streptomycin (PS) (Sigma-Aldrich, Merck, Poland).
11. L-Glutamine (LG) (Sigma-Aldrich, Merck, Poland).
12. Dimethyl sulfoxide (DMSO) (Sigma-Aldrich, Merck, Poland).
13. Calcein acetoxymethyl (Calcein AM) (Invitrogen Thermo Fisher Scientific, Massachusetts, USA).
14. Propidium Iodide (Invitrogen Thermo Fisher Scientific, Massachusetts, USA).
15. CyQUANT™ MTT reagent [3–(4,5–Dimethylthiazol–2–yl)–2,5–Diphenyl tetrazolium Bromide].
16. CyQUANT™ lactate dehydrogenase (LDH) cytotoxicity assay (Invitrogen Thermo Fisher Scientific, Massachusetts, USA). LDH assay kit included 10× lysis buffer, reaction mixture and stop solution for performing the experiment.
17. 96-well advanced Tissue culture TC™ clear bottom black-welled microplates (Corning Co-star, USA).
18. Tissue culture treated 8 well clear bottom plates (Cellvis, USA).
19. Lysogeny broth (LB) agar media (Carl Roth GmbH + Co. KG, Karlsruhe, Germany).

20. Mueller Hinton (MH) broth (Becton, Dickinson and Company, Franklin Lakes, USA).
21. AlamarBlue reagent (Life Technologies Europe BV, Bleiswijk, Netherlands).

All the chemicals purchased except $AgNO_3$, were of molecular biology grade, i.e. specifically purified and assayed for Molecular Genetics applications.

2.2 Biological samples

The five human cell lines and the bacterial strain used for this project are as follows:

1. Human embryonic kidney normal cell line (HEK293).
2. Human cervical cancer cell line (HeLa).
3. Human adenocarcinomic alveolar basal epithelial cell line (A549).
4. Human breast cancer cell line (MCF-7).
5. Human epithelial breast cancer cell line (MDA-MB-231).
6. Gram-negative strain *Escherichia coli* ATCC 25922 (*E. coli*).

The cell lines were purchased from ATCC (Manassas, Virginia, USA).

2.3 Preparation and analysis of precursors/extracts

2.3.1 Brewery wastes and product filtrates

The brewery wastes from stages 5 (**BW5**), 7 (**BW7**), 9 (**BW9**) were filtered using 150 mm Whatman filter paper. Brewery product, beer (**B**) was used without any chemical or physical processing. All solutions and bulk brewery wastes were refrigerated at 4(±1) ºC during the course of experiments.

2.3.2 Leaf extract

The leaves were gathered and removed from the stems. These leaves were washed with distilled water, air dried overnight and stored in open boxes till experimentation. Leaf extracts were prepared by stirring a water suspension (500 ml) of leaves (25 g) at 100(±1) °C for 2 h. Then, the extract was filtrated using 150 mm Whatman filter paper. The leaf extracts obtained from *Malus sylvestris L.*, *Pinus sylvestris L.*, *Sorbus aucuparia L.* were denoted as **LE1**, **LE2** and **LE3** extracts, respectively. Throughout the project, the leaf extracts were stored at 4(±1) ºC.

2.3.3 Analysis of precursors/extracts

The brewery wastes and leaf extracts were investigated for the presence of elements like nitrogen (N), potassium (K), calcium (Ca), magnesium (Mg), phosphorous (P), aluminium (Al), iron (Fe), boron (B) and manganese (Mn) and contain also traces of elements such as zinc (Zn), copper (Cu), nickel (Ni), etc., total carbohydrates, polyphenols, total nitrogen, nitrate (NO_3^-), total fermenting sugars (fructose, glucose, maltose + sucrose, maltotriose), sulfate

(SO_4^{2-}), total phosphate (PO_4^-), and other chemical compounds. Elemental composition in the extracts was determined after microwave mineralization by inductively coupled plasma mass spectrometry (ICP-MS). Composition of anions such as PO_4^-, Cl^-, SO_4^{2-} and NO_3^- was determined by ion exchange chromatography with conductivity detection and suppressor. The Kjeldahl titration (PN-A-04018:1975) was performed to determine total nitrogen content [149]. The spectrophotometric method (PN-A-79093-13:2000) was employed to evaluate the total polyphenol content [150]. The spectrophotometric method according to 9.26, 8.14 Analytica EBC, 2.7.3 MEBAK (2013) was employed to assess the total carbohydrates content [151]. The total carbohydrates content was quantified using high-performance liquid chromatography with refractometric detection (HPLC/RID) according to 9.27, 8.7 Analytica EBC, 2.7.2 MEBAK (2013) [152]. The sulfate content was determined using high-performance liquid chromatography with conductometric detection (HPLC/CD) according to 2.22.1 MEBAK (2013) [153]. The total organic carbon was determined using the spectrophotometric method according to CLA/SR/26/2012 [154]. The chemical compounds present were determined using high-performance liquid chromatography and mass spectrometry (HPLC-MS).

2.4 Preparation of silver nanocomposites

Brewery byproducts (**BW5**, **BW7**, and **BW9**), product-beer (**B**), and leaf extracts (**LE1**, **LE2**, and **LE3**) mediated nanocomposite synthesis was a simple "one-pot" synthesis procedure (Scheme 2.1). A measured amount (50 ml) of the filtered brewery wastes (**BW5** or **BW7** or **BW9**) or brewery product **B** or leaf extract (**LE1** or **LE2** or **LE3**) was heated using magnetic stirrer at a constant stirring rate of 100 rpm until the desired temperature [25(±1), 50(±1), or 80(±1) °C] was attained (Table. 2.1). Subsequently, silver nitrate salt was added to the above solution to achieve a final concentration of 100 mM. The synthesis reaction was carried out for 120 min. Following the reaction, the solution was cooled for up to 5 to 10 min to ~ 35 °C after synthesis. The solution was then centrifuged at 10,000 rpm in a centrifuge model MPW 351R (MPW MED. INSTRUMENTS, Warsaw, Poland). The temperature of the centrifuge was maintained at 20 °C. The supernatant was discarded, following which distilled water was used to wash the nanoparticles twice, which was sufficient to obtain pure nanocomposites. Each washing was followed by centrifugation at 10,000 rpm. Finally, the nanoparticles were kept for drying for 24h at ~ 35 - 37 °C in an oven under natural airflow conditions, after which the ground powder form of nanoparticles was used directly or dispersed in solvent for further analyses. The nanoparticles were characterized for their surface morphology and composition along with bulk phase and elemental composition.

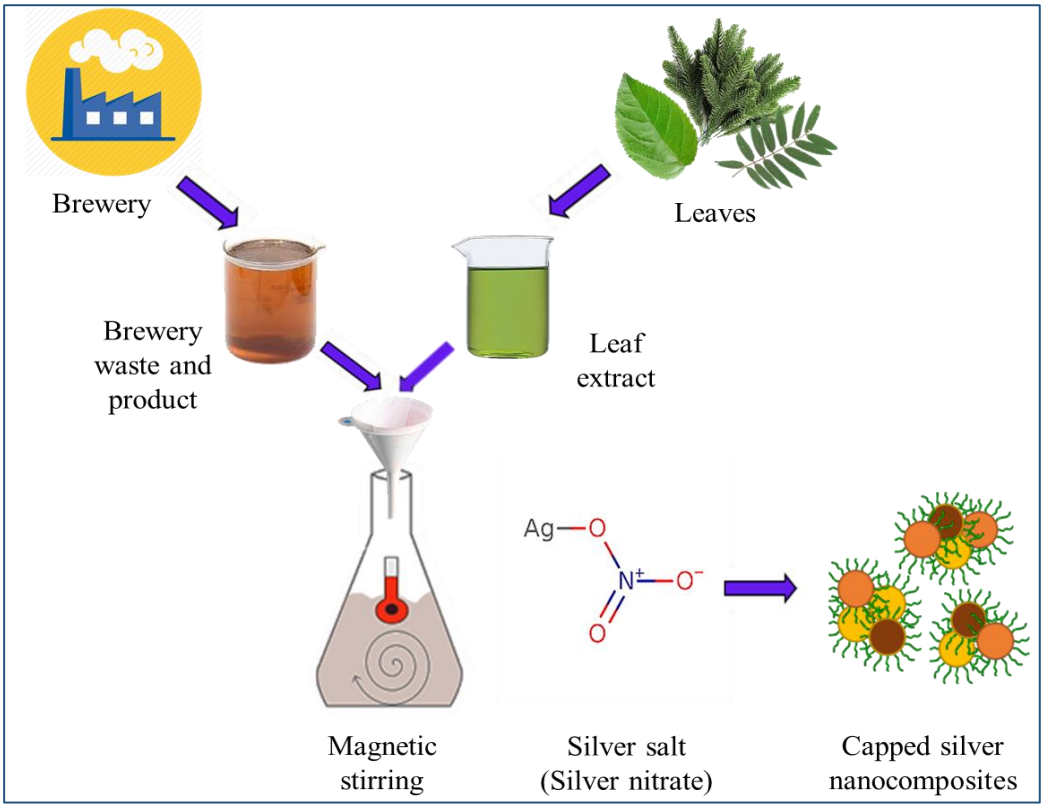

Scheme 2.1 Synthesis of nanocomposites using brewery wastes (**BW5** or **BW7** or **BW9**) or brewery product **B** or leaf extract (**LE1** or **LE2** or **LE3**).

Table. 2.1 The nomenclature of nanocomposites synthesized using brewery byproducts and product, and leaf extracts at different temperatures.

BW nanocomposites	Precursor	Synthesis temp. (±1) °C
BW5Ag1	BW5	25
BW5Ag2		50
BW5Ag3		80
BW7Ag1	BW7	25
BW7Ag2		50
BW7Ag3		80
BW9Ag1	BW9	25
BW9Ag2		50
BW9Ag3		80
BAg1	B	25
BAg2		50
BAg3		80

LE nanocomposites	Precursor	Synthesis temp. (±1) °C
LE1Ag1	LE1	25
LE1Ag2		50
LE1Ag3		80
LE2Ag1	LE2	25
LE2Ag2		50
LE2Ag3		80
LE3Ag1	LE3	25
LE3Ag2		50
LE3Ag3		80

2.5 Characterization of **BW** and **LE** nanocomposites

2.5.1 X-ray diffraction (XRD)

X-ray diffraction is a powerful and widely used analytical technique in the field of materials science, chemistry, and structural biology [138]. It is based on the fundamental principle that when a crystalline material is exposed to X-rays, these high-energy electromagnetic waves are scattered by the regularly spaced atoms within the crystal lattice. This scattering results in a diffraction pattern, which contains information about the atomic arrangement, crystal structure, and spacing between the crystal planes. X-ray diffraction has revolutionized our understanding of the molecular and atomic structure of a wide range of materials, including minerals, metals, polymers, and biological macromolecules. Its ability to provide precise, non-destructive insights into the three-dimensional arrangement of atoms has made it an indispensable tool for researchers seeking to uncover the mysteries of matter at the atomic and molecular level.

The Empyrean D8 X-ray diffractometer (Bruker Inc., Billerica, MA, USA) was used to record the powder XRD (PXRD) patterns of polycrystalline nanomaterials. This apparatus was equipped with Bragg–Brentano geometry, an X-ray tube (Cu K_α radiation) with K_β filters, and a goniometer in a θ–θ vertical system. The slits used were ¼ ° fixed divergence slit with anti-scatter slit and ⅛ ° anti-scatter slit. The measurements were performed at 40 kV potential and 40 mA current settings. The identification of chemical compounds and their phases in the nanoparticles was achieved using X'Pert Highscore Plus software.

2.5.2 Energy-dispersive X-ray fluorescence spectroscopy (EDXRF)

Energy-dispersive X-ray fluorescence spectroscopy (EDXRF) is a sophisticated analytical technique that has found extensive utility across various scientific disciplines [155]. EDXRF is a non-destructive method for elemental analysis that relies on the interaction between high-energy X-rays and a sample's atoms. When a sample is irradiated with X-rays, it responds by emitting fluorescent X-rays, whose energies are characteristic to the respective elemental composition of the material. EDXRF is particularly esteemed for its ability to determine the concentration of a wide range of elements, from trace elements to major components, in a diverse array of sample types. This method provides researchers with a rapid, precise, and non-invasive means of elemental analysis, making it invaluable in fields such as geology, environmental science, metallurgy, and material characterization, among others. Its versatility and capacity for quantitative analysis have established EDXRF as an indispensable tool for scientists and researchers seeking to gain insight into the elemental composition of various substances.

A MiniPal 4 PW4025/00 EDXRF spectrometer (PANanalytical Inc., Malvern, UK) was used to analyze the elemental composition of nanomaterials. The samples were placed in a sample holder with a transparent bottom prepared using Prolene 4 film. The irradiation was carried out for 120 seconds.

2.5.3 Scanning electron microscopy (SEM)/ Energy Dispersive X-ray Spectroscopy (EDXS)

Scanning Electron Microscopy combined with Energy Dispersive X-ray Spectroscopy (SEM-EDXS) represents a powerful and versatile analytical tool that has revolutionized our ability to investigate the microstructure and elemental composition of a wide range of materials [137, 142]. SEM-EDXS is a cutting-edge microscopy technique that integrates the high-resolution imaging capabilities of a scanning electron microscope with the elemental analysis capabilities of energy dispersive X-ray spectroscopy. In this sophisticated method, a focused electron beam is scanned across the sample's surface, generating high-resolution images by detecting the emitted secondary electrons. Simultaneously, EDXS captures the characteristic X-rays emitted when the electrons interact with the atoms in the sample [142]. This allows for the identification and quantification of elements within the specimen, enabling researchers to explore the fine structural details and elemental composition of materials with exceptional precision. SEM-EDXS has become an indispensable tool in fields as diverse as materials science, geology, biology, and forensics, providing researchers with invaluable insights into the topographical and compositional features of specimens at the micro- and nanoscale.

The Nova NanoSEM 450 (FEI, Hillsboro, OR, USA) recorded images of the nanocomposites at 10 kV high voltage in immersion imaging mode, including charge neutralization (CN) for nanocomposites with low electrical conductivity. EDXS attachment added to SEM instrument was used for surface elemental mapping of the silver nanocomposites at 10 kV. The powdered nanocomposites were deposited on double-sided carbon tape and attached to the sample holder.

2.5.4 X-ray photoelectron spectroscopy (XPS)

X-ray Photoelectron Spectroscopy (XPS), also known as Electron Spectroscopy for Chemical Analysis (ESCA), is a highly advanced and versatile surface analysis technique that has revolutionized the way we understand the composition and chemical state of materials [144]. Based on the interaction between X-rays and the electrons of atoms at the surface of a sample, XPS provides detailed information about the elemental composition and chemical bonding of materials in a non-destructive and quantitative manner. By measuring the kinetic energies of photoelectrons emitted from different atomic levels, XPS allows researchers to determine the

elemental composition, oxidation states, and chemical environments of the elements present on the sample's surface. This invaluable tool finds applications in a wide range of fields, including surface chemistry, materials science, and catalysis, making it an indispensable instrument for scientists seeking to unlock the secrets of surface properties and chemical reactivity in various materials and compounds.

The X-ray photoelectron spectroscopy (XPS) spectra were obtained by employing the ESA-31 electron spectrometer [156] in an ultra-high vacuum system having a homemade X-ray excitation source [156] that utilized Al X-rays with a wavelength of 8.3 Å (K_α line: 1486.67 eV), a homemade hemispherical electron energy analyzer [156] with a 0.5% relative energy resolution without retardation. But for the increasing of the XPS energy resolution, the survey XPS spectra were recorded with retardation ratio (k) of 4 and the narrow scan spectra with the retardation ratio of 8. The XPS measurement system equipped with an electron gun (LEG62-VG Microtech, Vacuum Generators, East Grinstead, UK), and an argon (Ar^+) ion source of AG21 (VG Scientific, Vacuum Generators, East Grinstead, UK). During the XPS measurements, a fixed retarding ratios (FRR) mode of k=4 and k=8 was employed, with photon incidence and electron emission angles set to 70° and 0°, respectively, with respect to the specimen's surface normal. Background (due to the inelastic electron scattering in the sample) subtraction from the XPS spectra was carried out using XPS/AES QUASES simple backgrounds, version 4.2, 1999-2001, developed by Tougaard Inc., Odense SO, Denmark [157]. To analyze the obtained photoelectron spectra, Gaussian-Lorentzian asymmetric components were fitted to each spectrum following Tougaard's method for inelastic background subtraction [157]. This fitting procedure was performed using the XPS peak fitting program for WIN95/98 XPSPEAK, version 4.1 (XPSPEAK4.1, R W M Kwok, Shatin, Hong Kong). Finally, quantification of the results was carried out using the XPS MultiQuant program, version 7, 1999-2001, a multimodel XPS quantification software designed for 32-bit Windows, developed by M. Mohai in Budapest, Hungary [158, 159].

2.5.5 Transmission electron microscopy (TEM)

Transmission Electron Microscopy (TEM) stands as one of the most powerful and versatile tools in the realm of microscopy and nanoscale analysis [137]. TEM harnesses the remarkable wave-like properties of electrons to investigate the world at an unprecedented level of detail. By transmitting a focused beam of high-energy electrons through a specimen, TEM generates images that provide unparalleled insights into the structure, composition, and properties of materials. With the capability to visualize features at the atomic and molecular scales, TEM

has become instrumental in countless scientific disciplines, including materials science, biology, and nanotechnology. Its ability to reveal the fine structure of specimens, from individual atoms to nanoscale architectures, makes it an essential instrument for researchers aiming to explore and understand the complexities of matter at the nanoscale, pushing the boundaries of scientific knowledge and technological innovation.

A high-resolution transmission electron microscope (HR-TEM), Tecnai 20F X-Twin, equipped with an electron source, a cathode with field emission gun (FEG), EHT = 200 keV, a camera Orius and a high angle annular dark-field (HAADF) detector, was used. This TEM was equipped with an energy-dispersive X-ray spectrometer (EDX) with the energy resolution of 134 eV (EDAX RTEM SN9577+) and parallel electron energy loss spectrometer (PEELS) with the energy resolution of 0.8 eV. The quantification was performed according to the modified standardless/ thin foil method. The preparation of samples proceeded in the following steps: sonication for 5s of a few milligrams of sample in ethanol (99.8% anhydrous) using ultrasounds, applying a drop of the solution of 5 µl on a carbon coated copper mesh with holes (Lacey type Cu 400 mesh, Plano), evaporating the solvent at room temperature and then investigating the remaining dried powder stuck on the copper mesh.

2.6 Anticancer activity testing of **BW** and **LE** nanocomposites

The constituents of the media for culturing the cells used in this project are:

- The HEK293, HeLa and A549 cells were cultured in DMEM media supplemented with 10% v/v FBS, 100 U/ml PS, and 2mM of LG.
- MCF-7 cells were cultured in DMEM media supplemented with 10% v/v FBS, 100 U/ml PS, 2mM of LG and insulin (0.1% v/v).
- MDA-MB-231 cells were cultured in RPMI media with 10% v/v FBS, 100 U/ml PS, and 2 mM of LG.

The cells were grown at 37 °C in a humidified incubator with 5% CO_2. PBS was used to wash the cells. 0.25% solution of Trypsin- Ethylene diamine tetraacetic acid (Trypsin-EDTA) was used to detach the adherent cells for passaging. The cells were passaged after reaching 80% confluence. All the cell lines were cultured in tissue culture (TC) treated T75 flasks (Cell Star, Greiner Bio-One, Austria) and maintained at 37 °C in a 5% CO_2 humidified incubator during the experiment.

2.6.1 Live/dead assay:

The Live/Dead Assay is a crucial technique in cell biology and microbiology, aimed at determining the viability and vitality of cells or microorganisms within a given population.

This assay utilizes a combination of fluorescent dyes to distinguish between living and dead cells based on their membrane integrity. Typically, living cells with intact cell membranes will take up one fluorescent dye, while dead cells with compromised membranes take up another. The resulting fluorescence patterns can be visualized and quantified using fluorescence microscopy or flow cytometry, providing valuable information about cell viability and population health. The Live/Dead Assay is a fundamental tool in various fields, including microbiology, tissue engineering, and pharmaceutical research, offering researchers a means to assess the impact of experimental conditions, treatments, or environmental factors on cell or microbial populations. This technique plays a pivotal role in advancing our understanding of cellular responses and is crucial in optimizing processes involving cell cultures or microbial communities.

Calcein AM, or Calcein Acetoxymethyl ester, is a widely utilized fluorescent dye that has significantly contributed to cellular and molecular biology research [160]. This cell-permeant compound is converted by intracellular esterases into calcein, a highly fluorescent compound that emits a green fluorescence signal upon excitation with ultraviolet or blue light. Calcein AM is particularly valuable for live cell imaging and viability assays, as it is retained by live cells with intact membranes, allowing researchers to visualize and quantify viable cells. The versatility of Calcein AM extends to various applications, including the assessment of cell viability, measurement of cell proliferation, and monitoring cellular transport processes. Its non-toxic nature and ability to penetrate cell membranes make it an essential tool for scientists exploring a wide range of cellular processes and experimental conditions, offering insights into cell health and behavior.

Propidium Iodide (PI) is a vital and widely used fluorescent dye in cell biology and cytometry [161]. This molecule is known for its ability to stain and label dead or damaged cells by binding to nucleic acids, such as DNA, with high affinity. When excited by an appropriate wavelength of light, PI fluoresces with a distinctive red color, allowing researchers to distinguish between live and dead cells. PI is an essential tool for cell viability and cell cycle analysis, as well as for assessing the integrity of cell membranes. Its robust and straightforward staining procedure, along with its compatibility with various microscopy and flow cytometry platforms, has made it a staple in a multitude of biological and biomedical applications. Researchers rely on PI to gain insights into cell health, to identify and quantify dead or apoptotic cells, and to monitor changes in DNA content, contributing to our understanding of cellular behavior and the outcomes of experimental treatments or conditions.

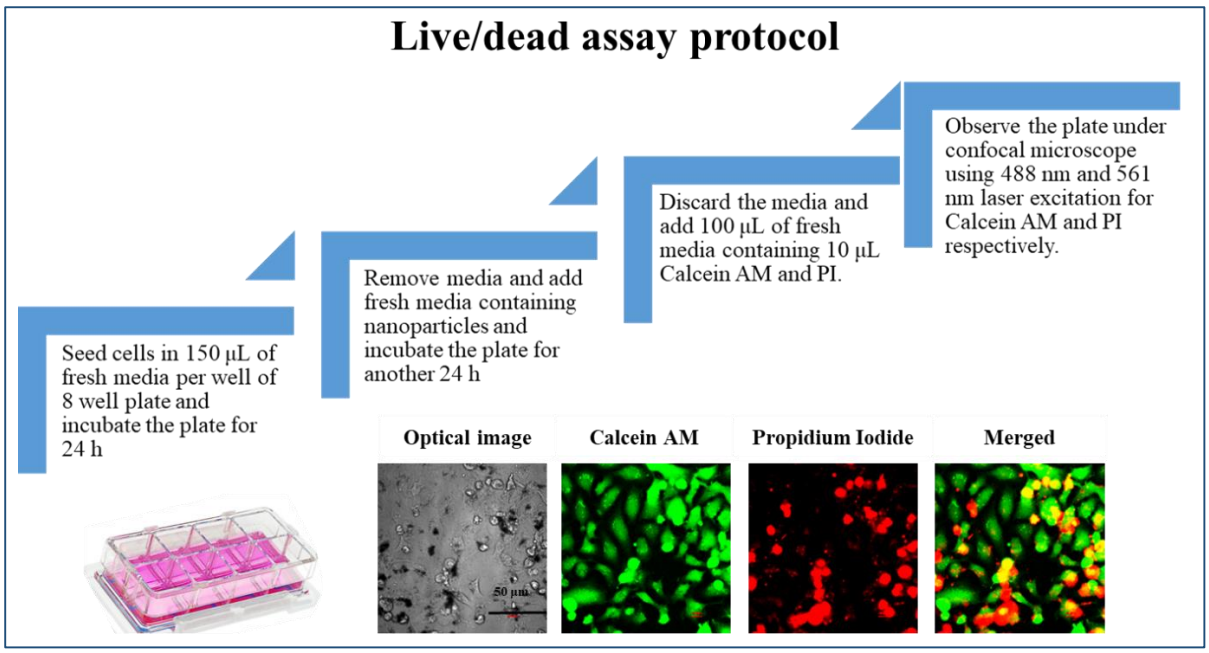

Figure 2.1 Live/dead assay protocol for cytotoxicity assessment of silver nanocomposites.

The assay was performed on HEK293 and HeLa cells taken as exemplary cancer cell lines for visual comparison of the effect of nanocomposites on healthy and cancerous cells. The experimental procedure outlined in the product data sheet provided by Thermo Fisher Scientific, Massachusetts, USA (Figure 2.1) [160, 161], was followed for the conducted experiments. For the HeLa cell line, 10^4 cells were seeded per well, while for the HEK293 cell line, 5×10^4 cells were seeded per well in 150 µl of media using an 8-well plate. The cells were then incubated for 24 h. Since HeLa cells exhibit faster growth than HEK293 cells, a five times higher cell concentration was used to achieve a similar cell count on the day of nanocomposite addition. After the initial 24-h incubation period, **BW** and **LE** nanocomposites were introduced into each well at two different concentrations (1 and 25 µg ml^{-1}). One well containing untreated cells was used as a control. Following an additional 24 h incubation, the cells were washed with PBS solution to eliminate any residual nanoparticles. Subsequently, 100 µl of fresh media, along with 10 µl of solutions containing Calcein AM and PI, were added to each well. The 8-well plates were then observed under a Nikon A1 inverted confocal microscope (Nikon Instruments) with the assistance of NIS Elements software (Nikon Instruments). The fluorescence signals from viable and dead cells were captured using fluorescein isothiocyanate (FITC) and tetramethylrhodamine isothiocyanate (TRITC) settings, respectively, utilizing excitation of 488 nm laser for Calcein AM and 561 nm laser for PI. Fluorescence was collected in the range of 500-550 nm (Calcein AM) and 570-620 nm (PI). All the images were captured using a scale of 50 µm.

2.6.2 LDH assay:

The Lactate Dehydrogenase (LDH) assay is a fundamental biochemical technique that plays a critical role in various fields of life sciences and medicine. LDH is a ubiquitous enzyme present in most living cells and is involved in anaerobic metabolism, converting pyruvate to lactate while regenerating nicotinamide adenine dinucleotide (NAD^+) [162]. The LDH assay measures the activity of this enzyme and is used to assess cell membrane integrity and cellular damage. By quantifying the release of LDH into the surrounding medium, researchers can evaluate the cytotoxicity of substances, monitor cell viability, and diagnose various medical conditions, including myocardial infarction and tissue damage. The LDH assay is a versatile and well-established tool, indispensable for a wide range of applications in cell biology, clinical diagnostics, and drug development, offering valuable insights into cellular health and pathological processes. LDH assay is mainly used to check for cell damage. However, LDH assay by itself cannot indicate the type of cell damage or presence of cell death. Therefore, it is typically performed in conjunction with other tests that aid in diagnosing the type of cell damage and cell death.

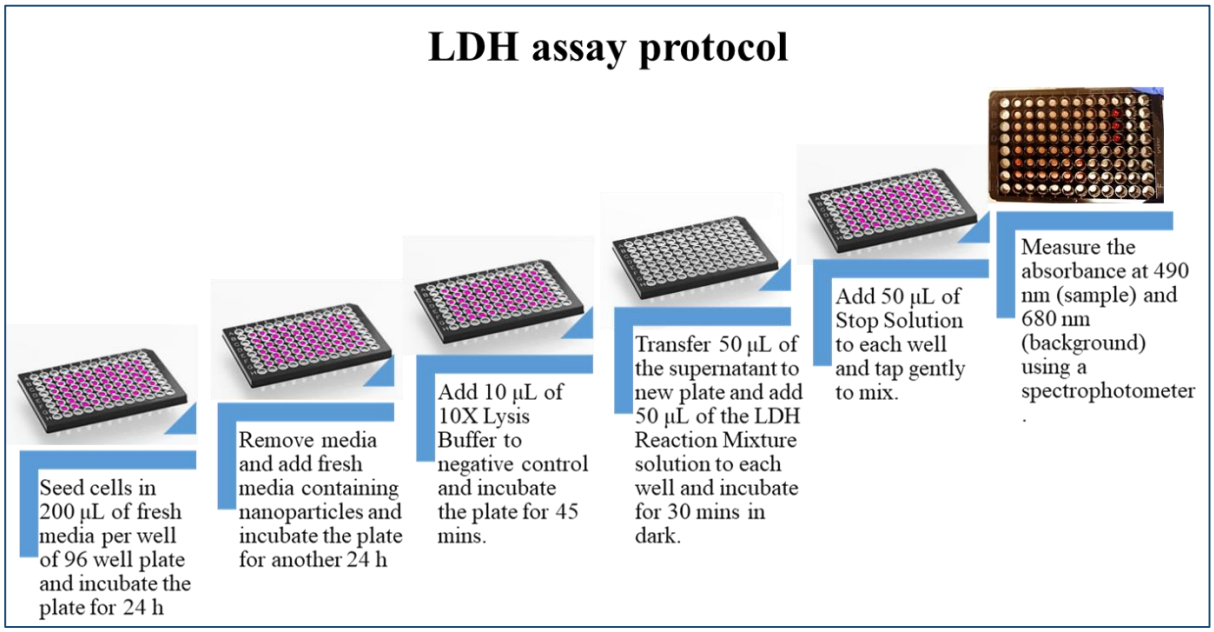

Figure 2.2 LDH assay protocol for cytotoxicity assessment of silver nanocomposites.

The protocol described in the product data sheet of Invitrogen CyQUANT™ LDH cytotoxicity assay kit [162] was used for the experiments (Figure 2.2). The cells were seeded in a 96-well plate, with 10^4 cells per well for HeLa and A549 cell lines, and 5×10^4 cells per well for HEK293, MCF-7, and MDA-MB-231 cell lines. A total of 200 µl of media was added to each well, and the plate was incubated for 24 h. Within the plate, two sets of triplicate wells

containing untreated cells were designated as negative and positive controls. After the initial 24-h incubation period, **BW** and **LE** nanocomposites were added to the wells at various concentrations (0.05, 0.1, 0.2, 0.4, 0.5, 0.6, 0.8, 1, 2.5, 5, 10, 12.5, 15, 20, 25, and 50 μg ml^{-1}), with triplicate wells for each concentration except the control wells. Following a total incubation period of 48 h, 10 μl of water was added to one set of triplicate wells containing untreated cells (positive control) to measure the spontaneous LDH activity ($A_{control}$). In another set of triplicate wells containing untreated cells (negative control), 10 μl of 10× Lysis Buffer from the LDH assay kit was added to measure the maximum LDH activity ($A_{maximum}$). The plate was further incubated for 45 min. Next, 50 μL of the supernatant from all wells was transferred to a new 96-well plate for the LDH assay. To each well in the new plate containing the supernatant, 50 μl of the Reaction Mixture prepared from the LDH assay kit was added. The new plate was then incubated in the dark at room temperature for 30 minutes. Subsequently, 50 μl of Stop Solution was added to each well to halt the coupled enzymatic reaction responsible for formazan formation. The solution in each well was mixed by gently tapping the plate. The absorbance of red formazan product was measured at 490 nm (overall sample) and 680 nm (background) on a spectrophotometer equipped for plate reading (Agilent BioTex Synergy HTX, Santa Clara, CA, USA).

Calculation of cell viability was performed according to the following equations [162]:

$LDH_{cell\ death}$ (%) = ($A_{sample} - A_{control}$)/ ($A_{maximum} - A_{control}$) * 100,
where absorbance $A = A_{490\ nm} - A_{680\ nm}$.

2.6.3 MTT assay:

The MTT (3-(4,5-dimethylthiazol-2-yl)-2,5-diphenyltetrazolium bromide) assay is a widely employed and essential technique in cell biology and drug discovery. This colorimetric assay measures cell viability and metabolic activity by assessing the reduction of MTT, a yellow tetrazolium salt, to formazan crystals within metabolically active cells [163]. As a reliable indicator of viable cell populations, the MTT assay enables researchers to quantify the effects of experimental treatments, toxins, or drugs on cell health and proliferation. It is a versatile tool used in diverse applications, including drug screening, cytotoxicity testing, and the evaluation of cell proliferation, making it an indispensable asset for studying cellular responses and developing new therapeutic strategies. The MTT assay's simplicity and sensitivity have contributed significantly to our understanding of cell physiology and its role in drug development and disease research. However, the MTT assay has limitations as well. It is an

endpoint assay, offering a snapshot of cell viability at a specific time. It does not provide mechanistic insights into the mode of cell death or specific cellular pathways involved. Hence, it is combined with other assays for deeper understanding of different cytotoxicity pathways.

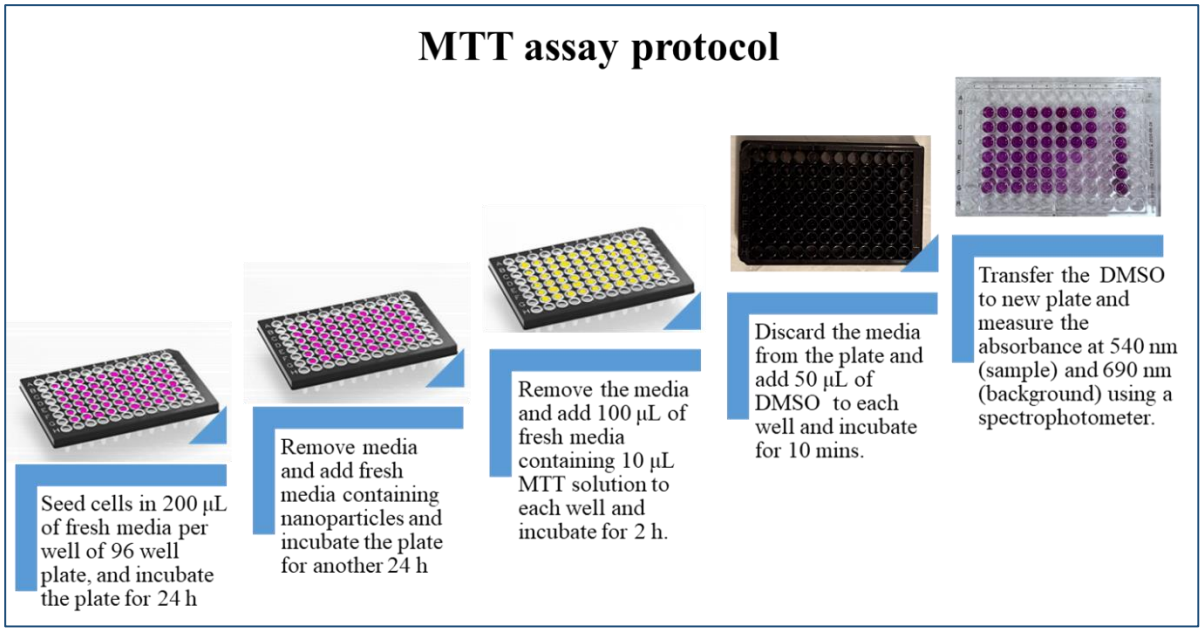

Figure 2.3 MTT assay protocol for cytotoxicity assessment of silver nanocomposites.

The protocol described in the product data sheet of Thermo Fisher Scientific, Massachusetts, USA [163] was used for the experiments (Figure 2.3). The cells were seeded in a 96-well plate, with 10^4 cells per well for HeLa and A549 cell lines, and 5×10^4 cells per well for HEK293, MCF-7, and MDA-MB-231 cell lines. A total of 200 µl of media was added to each well, and the plate was incubated for 24 h. To ensure similar cell counts on the day of nanocomposite addition, a five times higher concentration of HeLa and A549 cells were used compared to HEK293, MCF-7, and MDA-MB-231 cells. Following the initial 24-h incubation, **BW** and **LE** nanocomposites were added to each well in triplicate at various concentrations (0.05, 0.1, 0.2, 0.4, 0.5, 0.6, 0.8, 1, 2.5, 5, 10, 12.5, 15, 20, 25, and 50 µg ml^{-1}). Two sets of triplicate wells containing untreated cells were used as controls ($A_{control}$). After an additional 24-h incubation period, the cells were washed with a PBS solution to remove any residue from the nanocomposites. Then, 100 µl of fresh media containing 10 µl of MTT stock solution (5 mg ml^{-1} in PBS) was added to each well, and the plate was further incubated for 2 h. The media with MTT was subsequently discarded, and 50 µl of DMSO was added to all wells, followed by a 10-min incubation. To measure the absorbance of the dissolved purple formazan crystals, the supernatant from each well was transferred to a new 96-well plate. The absorbance was

measured at 540 nm (overall sample) and 690 nm (background) using a spectrophotometer equipped for plate reading (Agilent BioTex Synergy HTX, Santa Clara, CA, USA).

Calculation of cell viability was performed according to the following equations [163]:

$MTT_{cell\ death}$ (%) = ($A_{control} - A_{sample}$)/$A_{control}$ * 100

where absorbance $A = A_{540\ nm} - A_{690\ nm}$.

2.6.4 MTT assay biphasic response curve analysis using Origin software:

Origin provides extensive support for analyzing pharmacologic data through a range of built-in features. Whether assessing dose-response parameters, fitting a standard curve, or conducting a global fit across multiple datasets, Origin significantly enhances the efficiency and effectiveness of the analysis. The dose-response (or concentration-response) analysis often involves fitting the observed response of a system to different concentrations of a drug sample to generate a curve and obtain various parameters such as Reduced Chi-Square, Adj. R-Square, effective concentration to cause half of the maximum possible effect (EC_{50}), etc. The sigmoidal fitting for biphasic response has been calculated using the following function [164]:

A1 = Bottom, A2 = Top,

LOGx01 = 1st EC_{50},

LOGx02 = 2nd EC_{50},

h1 = slope1, h2 = slope2, p = proportion

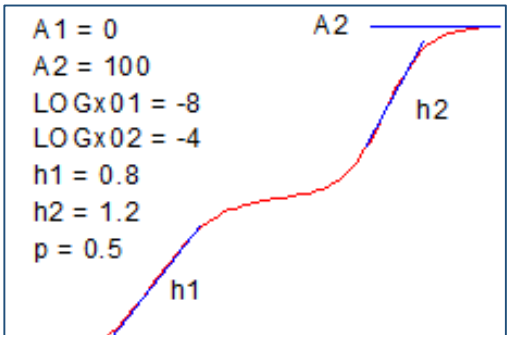

Figure 2.4 curve fitting parameters

Sigmoidal fitting function (Figure 2.5):

$$y = A1 + (A2 - A1)\left[\frac{p}{1 + 10^{(LOGx01 - x)h1}} + \frac{1 - p}{1 + 10^{(LOGx02 - x)h2}}\right]$$

double span = A2 - A1;

Phase1 = span*p/(1+ $10^{(LOGx01-x)*h1)}$);

Phase2 = span* (1-p)/(1+$10^{(LOGx02-x)*h2)}$);

y=A1 + Phase1 + Phase2;

2.7 Bactericidal activity testing of **BW** nanocomposites

Nanocomposites synthesized at 25(±1) and 80 (±1) °C were tested for their activity against the Gram-negative strain *Escherichia coli* ATCC 25922. The bacterial strain was grown overnight

on LB agar media. An inoculum of the strain was prepared in the MH broth by adding the colonies from the agar plates to achieve an optical density of 0.1, corresponding to ~10^8 CFU ml^{-1}. The nanoparticles were ultrasonicated using the VCX 130 ultrasonic processor at 30% amplitude for 10 min in the pulse mode to enable uniform dispersion. The pulse mode was used to prevent over-heating of the solution. The nutrient broth and agar media were sterilized in a Varioklav steam sterilizer (HP Medizintechnik GmbH, Oberschleissheim, Germany).

2.7.1 MIC/MBC determination

The minimum inhibitory concentration (MIC) of nanoparticles was determined as the primary parameter that would enable further advanced studies. Stock solutions of 1 mg ml^{-1} nanocomposites were prepared in MH nutrient broth containing 10% PBS. PBS enabled better dispersion of nanocomposites. Serial dilution was performed on a 96-well plate to obtain nanocomposite concentrations between 0.5 and 50 µg ml^{-1}. The bacterial strain was then added to the 96-well plates to achieve a final concentration of 5×10^5 CFU ml^{-1}. After 24 h, AlamarBlue reagent was added. The plates were further incubated for 2 h, after which the absorbance value was measured using the plate reader. After MIC determination, the minimum bactericidal concentration (MBC) was determined by plating the dilutions on agar plates. Concentrations of nanocomposites higher than MIC up to 4 times were contacted with 15 ml bacteria inoculum (10^5–10^6 CFU ml^{-1}) of *E. coli* for 24 h in an orbital shaker incubator at 220 rpm and 37 °C temperature. A 50 µl solution was taken from the tubes and plated after serial dilutions on agar plates. The lowest nanocomposite concentration that resulted in the absence of colonies on agar plates after 24 h incubation was considered the bactericidal concentration.

2.7.2 Time-kill kinetics experiment

The time-kill kinetics were observed at sub-MIC, MIC, and MBC concentrations of nanocomposites obtained from MIC/MBC determination experiment, between 0 and 24 h of nanoparticles contact with bacterial inoculum. The time-kill studies were performed by exposing a 5 ml inoculum (10^5–10^6 CFU ml^{-1}) of *E. coli* to a defined concentration of nanocomposites in 15 ml centrifuge tubes for up to 24 h. The tubes were covered with aluminum foil to prevent the interaction of nanocomposites with light radiation. A 50 µl solution was taken from the tubes and plated after serial dilutions on agar plates. The number of colonies was counted, and the final concentration of *E. coli* was determined in a 1 ml solution. A positive control without nanoparticles was used as a reference for bacteria growth.

3. Brewery waste synthesized silver nanocomposites

This work deals with the recycling of the large amounts of wastes produced from stages 5 (**BW5**), 7 (**BW7**), and 9 (**BW9**) of the brewing industry, and beer (**B**) for preparing nanomaterials [100, 101]. The project was initiated with the analysis of brewery wastes (Section 3.1) to understand their composition and determine the value-added compounds in the wastes. Following this, the nanocomposites were synthesized and then characterized for their structure, composition, morphology, and surface composition (Section 3.2) [100, 101]. Furthermore, the anticancer activity (Section 3.3), and bactericidal activity (Section 3.4) of these materials were studied.

3.1 Brewery wastes and product analyses[§]

The brewery wastes from three production stages: **BW5**, which is the wort precipitate obtained in the fifth stage, and **BW7** which is the Brewer's spent yeast obtained in the seventh stage, **BW9**, which is filtration waste obtained in the ninth (last) stage and product **B**, beer were characterized in detail to understand their composition (Table 3.1). These brewery wastes and product **B** are packed with numerous organic compounds like carbohydrates, polyphenols, nitrogen, fermenting sugars (fructose, glucose, maltose + sucrose, maltotriose), sulfate (SO_4^2), phosphate (PO_4^-), and other carbon-based compounds. As the sucrose content in **BW5**, **BW7**, **BW9**, and **B** was negligible, the total fermentable sugars can be equated to reducing sugars present in brewery wastes. The influence of these composition changes on the nanocomposite formation, is discussed in detail in section 3.5. They also contained elements like nitrogen (N), potassium (K), chlorine (Cl), calcium (Ca), magnesium (Mg), and phosphorous (P), and also traces of elements such as aluminium (Al), iron (Fe), manganese (Mn), zinc (Zn), copper (Cu), nickel (Ni), etc.

[§]The brewery wastes analyses reported in Table 3.1 were performed by Dr. Dorota Michałowska and Prof. Marek Ł. Roszko at the Institute of Agriculture and Food Biotechnology - State Research Institute, Warsaw, Poland, and the TOC analysis was performed at the Central Research Laboratory of the University of Life Sciences, Lublin, Poland, and included for description purposes jointly with the thesis, entitled "Synthesis, characterization, and testing of catalytic nanomaterials – greener route to synthetic methods" by Dr. Alcina Johnson Sudagar under the supervision of Prof. Dr. hab. Włodzimierz Kutner from the Molecular Films Research group at the Institute of Physical Chemistry, Polish Academy of Sciences, Warsaw, Poland.

Table 3.1 Composition analysis of brewery wastes **BW5**, **BW7**, **BW9**, and **B** in solution form.

Analysis	**Subtype**	**Units**	**Brewery wastes**			**Brewery product**
			BW5	**BW7**	**BW9**	**B**
Total nitrogen		mg l^{-1}	975.8	7454.5	443.8	782.6
Total polyphenols			92.65	181.2	87.75	213.65
Total sulfates			119.65	193.03	103.4	121.1
Total carbohydrates			1,56,700	4500	1200	38,500
Fermentable sugars	Total		1,15,800	1600	600	22,800
	Fructose		2100	700	100	300
	Glucose		12,500	300	100	16,700
	Maltose + sucrose		76,500	500	200	1500
	Maltotriose		24,700	100	200	4300
Elemental content	K	mg l^{-1}	657 ± 111	2710 ± 460	284 ± 48.3	558 ± 94.9
	P		525 ± 20	97 ± 3.9	149 ± 6	266 ± 10.6
	Cl		365 ± 1.0	<4	165 ± 1.0	286 ± 2.0
	Mg		125.9 ± 21.4	228.3 ± 38.8	56.1 ± 9.5	103.9 ± 17.7
	Ca		69.3 ± 10.4	55.0 ± 8.3	68.0 ± 10.2	27.8 ± 4.2
	Na		58.0 ± 5.8	64.0 ± 6.4	42.9 ± 4.3	55.8 ± 5.6
	Mn		0.73 ± 0.06	1.64 ± 0.13	0.22 ± 0.02	0.14 ± 0.01
	Fe		0.3 ± 0.04	0.8 ± 0.11	6.0 ± 0.84	0.2 ± 0.03
	Al		0.01 ± 0.01	0.01 ± 0.01	0.01 ± 0.01	0.09 ± 0.01
	Zn		0.43 ± 0.06	2.6 ± 0.36	<0.05	<0.05
	Cu		0.08 ± 0.01	0.32 ± 0.03	<0.05	<0.05
	Ni		<0.05	<0.05	<0.05	<0.05
Total organic carbon		%	7.78	7.24	2.84	6.43

BW5 was abundant in carbohydrates, fermentable sugars, phosphorous, chlorine and calcium but had smaller amount of polyphenols. These constituents were several folds (2–200 times) higher than **BW7**, **BW9** and **B**. **BW7** has almost 10× higher nitrogen and potassium content as compared to **BW5**, **BW9** and **B**. Furthermore, **BW7** was also rich in sulfates, polyphenols, and magnesium. **BW9** is the last stage of waste produced in the brewery production line before packaging the final product **B**; thus, it contains only tiny amounts of filtrate material diluted in large quantities of water. **BW9**, therefore, is noticeably deficient in polyphenols, carbohydrates, sugars, nitrogen, sulfates, potassium and magnesium as compared to **BW5**, **BW7** and **B**. Contrastingly, **BW9** was rich in calcium. Subsequently, the total organic carbon (TOC) content in **BW9** is also significantly lower than in others. Brewery product **B** has a large quantity of glucose and polyphenols in the composition.

3.2 Characterization of **BW** nanocomposites

Nanocomposites were synthesized by varying the temperature of synthesis using each brewery waste **BW5**, **BW7**, **BW9,** and product **B** and $AgNO_3$ as precursors.

3.2.1 Crystallography and phase analysis by X-ray diffraction (XRD)§

The X-ray diffraction patterns provided valuable insights into the differences between nanocomposites precipitated at various temperatures using different brewery wastes (**BW5**, **BW7**, **BW9**) and product **B**. The PXRD patterns of the nanocomposites presented in Figure 3.1, showed characteristic reflexes corresponding to the phases of silver chloride (AgCl), metallic silver (Ag_{met}), and silver orthophosphate (Ag_3PO_4). For AgCl, the reflexes appeared at specific 2θ values, such as 27.8° (111), 32.3° (002), 46.3° (022), and 54.9° (113), 57.5° (222), 67.5° (004), 74.5° (133), 76.8° (024), and 85.8° (224), indicating a face-centered cubic NaCl-like structure with space group Fm-3m from ICDD 98-005-6538 reference patter. Ag reflexes were observed at 2θ values of 38.1° (111), 64.5° (022), and 77.4° (113) representing cubic structure with space group Fm-3m from ICDD 98-060-4629 reference pattern, and their presence strongly depended on the synthesis temperature, reflecting cubic structured silver nanoparticles. The reflexes characteristic of Ag_3PO_4 were found at 2θ values of 20.9° (011), 29.7° (002), 33.3° (012), 36.6° (112), 47.9° (013), 52.8° (222), 55.1° (023), 57.4° (123), 61.7° (004), 72.0° (124), and 87.4° (234), corresponding to a cubic structure with space group P4-3n. At a synthesis temperature of 80(±1) °C, an additional reflex at 69.98° (024) 2θ was observed.

§ The XRD diffraction patterns and analyses are produced in common with the thesis, entitled: "Synthesis, characterization, and testing of catalytic nanomaterials – greener route to synthetic methods" by Dr. Alcina Johnson Sudagar under the supervision of Prof. Dr. hab. Włodzimierz Kutner from the Molecular Films Research group at the Institute of Physical Chemistry, Polish Academy of Sciences, Warsaw, Poland.

The appearance of new reflexes and the narrowing of existing reflexes with increasing synthesis temperature indicated an enhancement in phase crystallinity. The crystal structure of Ag_3PO_4 consisted of a body-centered cubic lattice with isolated tetrahedral PO_4 and coordination of Ag and O atoms as described by Ma et al. (2016) [165]. Similar crystallographic structures were observed for the nanoparticles in all **BW** nanocomposites.

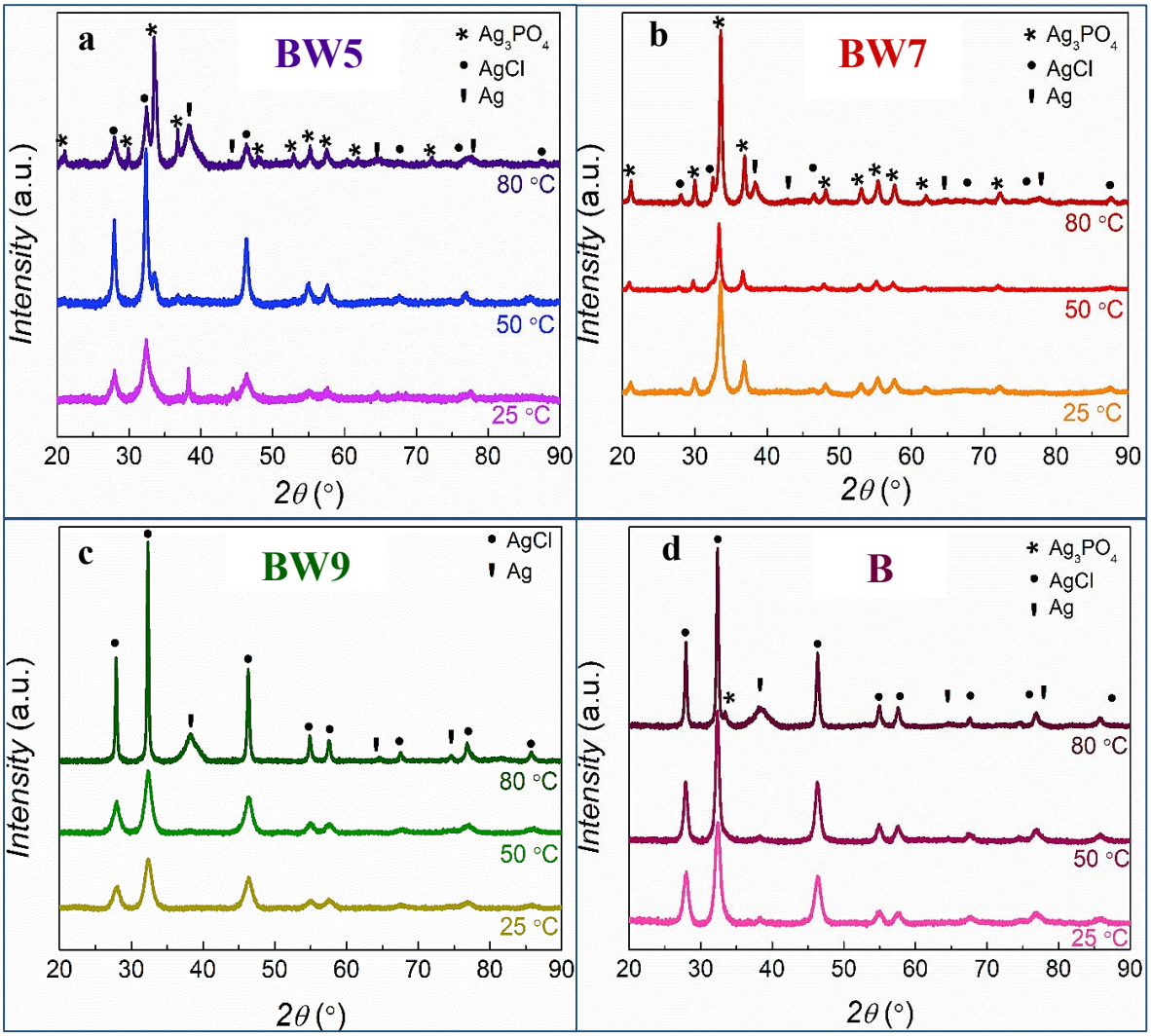

Figure 3.1 X-ray diffractograms of nanocomposites synthesized at different temperatures using brewery wastes (a) **BW5**, (b) **BW7** (c) **BW9**, and (d) **B**. (Syntheses conditions: 25(±1) °C → Ag1, 50(±1) °C→ Ag2, and 80(±1) °C→ Ag3).

The phase composition was determined by analyzing the most intense reflexes for each phase: (002) at 2θ = 32.3° for AgCl, (111) at 2θ = 38.1° for metallic Ag (Ag_{met}), and (012) at 2θ = 33.3° for Ag_3PO_4. The Reference Intensity Ratio (RIR) method, using corundum as a reference, was employed [166]. The Scherrer's equation, accounting for the same reflexes in the 2θ range of 20°–60° and employing a constant of 0.94, was used to calculate the average crystallite size and standard deviations, when multiple reflexes were considered. The results, including

crystallite size and its dependence on synthesis temperature, are presented in Table 3..2. Overall, increasing synthesis temperature led to improved crystallinity for all three phases (Ag_3PO_4, AgCl, and Ag), as indicated by narrower peaks and the formation of larger particles.

Table 3.2 Phase content and nanocrystallites size of **BW5**, **BW7**, **BW9**, and **B** nanocomposites.

Samples	Synthesis temp., (±1) °C	PXRD analysis					
		Ag phase content (wt.%)			Nanocrystallites size (nm)		
		Ag_3PO_4	AgCl	Ag_{met}	Ag_3PO_4	AgCl	Ag_{met}
BW5Ag1	25	5.9	91.5	2.6	4.8	4.0	18.1
BW5Ag2	50	13.8	85.7	0.5	5.6	8.1	14.0
BW5Ag3	80	30.0	41.5	28.5	12.1	6.7	3.2
BW7Ag1	25	90.0	10.0	-	9.9	5.5	-
BW7Ag2	50	88.7	11.3		15.5	7.5	
BW7Ag3	80	77.1	11.8	11.1	16.2	16.5	7.3
BW9Ag1	25	-	100	-	-	5.6	-
BW9Ag2	50		97.0	3.0		5.6	2.9
BW9Ag3	80		73.2	26.8		19.4	3.6
BAg1	25	4.2	94.2	1.6	4.9	6.1	10.9
BAg2	50	2.0	96.7	1.3	9.2	7.9	7.6
BAg3	80	19.1	51.8	29.1	10.8	10.7	3.0

The brewery waste from stage 5, **BW5**, predominantly yielded AgCl composite, with AgCl phase content reaching up to 91.5 wt.% at room temperature synthesis. Minor amounts of Ag and Ag_3PO_4 nanoparticles were also present. Increasing the synthesis temperature led to the introduction of more Ag_3PO_4 nanoparticles (up to 30 wt.%) and Ag_{met} (up to 28.5 wt.%), resulting in changes in crystallite sizes. The growth of Ag_3PO_4 crystallites and nucleation of Ag_{met} crystallites were favored with increasing temperature. The smaller crystallite size of AgCl at 80(±1) °C could be attributed to Ag nanoparticle growth at the expense of AgCl. Silver oxides were not detected in the PXRD diffractograms, likely due to their low content. In the case of stage 7 brewery waste, **BW7**, the major phase obtained was silver orthophosphate nanoparticles (Ag_3PO_4), and its content decreased from 90 to 77.1% with increasing synthesis temperature. AgCl nanoparticles were present in minor quantities (10 wt.%) at room temperature synthesis. The size of Ag_3PO_4 nanoparticles increased with increasing synthesis temperature, while the AgCl phase slightly grew in content and crystallite size, as **BW7** had a relatively low chlorine content. At 80(±1) °C, Ag_{met} nanoparticles were also formed due to the reduction of Ag^+ ions. The growth of AgCl and Ag_3PO_4 crystallites was favored with increasing synthesis temperature.

For stage 9 brewery waste, **BW9**, the synthesis resulted in pure AgCl nanoparticles (73.2–100 wt.%), and Ag_{met} nanoparticles (3–26.8 wt.%) were incorporated at temperatures above 50(±1) °C. The Ag_{met} phase increased at the expense of the AgCl phase with a higher synthesis temperature. AgCl nanoparticles' crystallite size increased with temperature, while Ag nanoparticles remained relatively constant. This indicated that AgCl nanoparticle growth was favored over nucleation with increasing synthesis temperature.

In the case of the finished beer product, **B**, a mixed composite of AgCl, Ag_3PO_4, and Ag_{met} nanoparticles was obtained. AgCl was the major phase, but its content decreased with higher synthesis temperature. At 80(±1) °C, Ag_3PO_4 and metallic Ag phases increased at the expense of AgCl. This suggests that the PO_4^{3-} could be a part of the organic composition of precursors released at elevated temperatures, which combines with Ag^+ ions to form Ag_3PO_4. The crystallite size of AgCl increased with synthesis temperature, while Ag_{met} nanoparticles showed a strong temperature dependence, with decreasing crystallite size. Ag nanoparticles in **B** nanocomposites had a constant crystallite size. The highest size and phase content of Ag_3PO_4 was observed at 80(±1) °C. Increasing synthesis temperature favored the growth of AgCl and Ag_3PO_4 nanoparticles, while nucleation was favored for Ag_{met} nanoparticles.

3.2.2 Elemental analysis by energy dispersive X-ray fluorescence (EDXRF) spectroscopy§

The elemental composition of the **BW** nanocomposites was analyzed using the EDXRF method (Energy Dispersive X-ray Fluorescence), providing information on the presence of silver (Ag), chlorine (Cl), phosphorus (P), and sulfur (S) in all the **BW** nanocomposites. The weight percentages of these elements were calculated and presented in Table 3..3. The peak area corresponding to Ag was the highest, confirming the formation of Ag metal-based nanoparticles.

In the case of **BW5** nanocomposites, the Ag content increased from 86.5 to 92.2 wt.% with increasing synthesis temperature. This increase is consistent with the growth of a larger amount of Ag_{met} nanoparticles (28.5 wt.%) in the composite, as observed in PXRD (Table 3..2). The Cl content in **BW5** nanocomposites decreased with increasing temperature, indicating a preference for Ag_{met} nanoparticle formation. This observation aligns with the decrease in the AgCl phase observed in the PXRD analysis (Table 3..2).

§ The EDXRF analyses is produced in common with the thesis, entitled: "Synthesis, characterization, and testing of catalytic nanomaterials – greener route to synthetic methods" by Dr. Alcina Johnson Sudagar under the supervision of Prof. Dr. hab. Włodzimierz Kutner from the Molecular Films Research group at the Institute of Physical Chemistry, Polish Academy of Sciences, Warsaw, Poland.

Table 3.3 Elemental composition of **BW5**, **BW7**, **BW9** and **B** nanocomposites.

Sample	Synthesis temp., (±1) °C	EDXRF analysis			
		Elemental composition, wt.%			
		Ag	P	Cl	S
BW5Ag1	25	86.5	5.3	7.7	0.5
BW5Ag2	50	88.4	2.9	8.1	0.6
BW5Ag3	80	92.2	3.0	4.4	0.5
BW7Ag1	25	93.5	4.8	1.0	0.8
BW7Ag2	50	93.7	4.3	1.1	0.8
BW7Ag3	80	94.4	3.9	1.0	0.8
BW9Ag1	25	83.1	0.1	15.1	1.6
BW9Ag2	50	83.8	0.2	14.6	1.5
BW9Ag3	80	89.3	0.6	9.3	0.8
BAg1	25	86.4	0.5	12.0	1.1
BAg2	50	85.3	0.7	13.0	1.1
BAg3	80	91.9	1.4	6.1	0.6

The Ag content in **BW7** nanocomposites remained relatively constant, with slight variations attributed to the growth of minor amounts of Ag phases with increasing temperature. The P content decreased with increasing temperature, which is in line with the decreasing Ag_3PO_4 phase and growth of Ag_{met} nanoparticles observed in PXRD (Table 3..2). The Cl content remained almost constant in all **BW7** nanocomposites, reflecting the low AgCl (up to 12 wt.%) phase content as observed in PXRD (Table 3..2). For **BW9** nanocomposites, the weight percentage of Ag increased, while that of Cl decreased with increasing synthesis temperature. This decrease in Cl content is consistent with the increase in the Ag phase observed in the XRD analysis (Table 3..2). P and S were present only in trace amounts in **BW9** nanocomposites, suggesting their association with the carbonaceous shell.

In the case of **B** nanocomposites, the weight percentage of Ag initially decreased from 25(±1) to 50(±1) °C and then increased at 80(±1) °C. This trend can be attributed to the growth of the Ag_3PO_4 phase observed in XRD analysis (Table 3..2). Conversely, the Cl content showed an inverse behavior, increasing from 25(±1) to 50(±1) °C and then decreasing at 80(±1) °C. The P content increased with synthesis temperature, concurrent with the increase in the Ag_3PO_4 phase observed in XRD (Table 3..2). S was present in trace amounts, potentially indicating its role in the organic coating stabilizing the nanoparticles, as supported by XPS analysis. However, the Ag_3PO_4 phase content (Table 3..2) cannot be directly compared to the P content

(Table 3..3) in **BW5**, **BW7**, **BW9**, and **B** nanocomposites, suggesting the presence of different chemical forms of P, possibly in the organic overlayer.

3.2.3 Morphological analysis by scanning electron microscopy (SEM) and energy dispersive X-ray analysis (EDAX)

The SEM images of nanocomposites are presented in Figure 3.2 At 25(±1) °C, the **BW5** nanocomposite (**BW5Ag1**) exhibits aggregated layers' characteristic of AgCl, along with small balls and globules, as depicted in Figure 3.2a. As the synthesis temperature increases, the Ag_3PO_4 and Ag_{met} content increases in the structure of **BW5Ag3**, and a fused globular morphology is observed, as shown in Figure 3.2b. Thus, indicating Ag_3PO_4 and Ag_{met} provides globular structure to the nanocomposites.

The morphology of the Ag_3PO_4-rich sample **BW7Ag1**, obtained using **BW7** at 25(±1) °C, displays globular structures that appear to be composed of several smaller balls (Figure 3.2c). As the AgCl content increases in the structures with increasing synthesis temperature (**BW7Ag3**), the flakey aggregated layers, similar to those in **BW5** nanocomposites, fuse with the balls, as observed in the red-marked areas in Figure 3.2d. The size of these globular structures in **BW7** nanocomposites ranges from ~ 10 – 350 nm.

In the **BW9** nanocomposites synthesized at 25(±1) °C (**BW9Ag1**), the AgCl nanoparticles exhibit an aggregated flakey layered morphology, as indicated by the red square in Figure 3.2e. Nanoparticle aggregates within the organic shell have diameters ranging from 20 – 150 nm, as indicated by the black arrows in Figure 3.2e. As the synthesis temperature increases to 80(±1) °C (**BW9Ag3**), and Ag_{met} nanoparticles are introduced, the morphology slightly changes to a mixture of layers and globular structures, as highlighted in red squares in Figure 3.2f.

Similarly, the **B** nanocomposites synthesized at 25(±1) °C (**BAg1**) show a combination of layered structures of AgCl and smaller balls representing Ag_3PO_4, which fuse to form a uniform composite structure, as shown in the Figure 3.2g (red square). These balls resemble the structures observed in **BW7** nanocomposites predominantly containing Ag_3PO_4. As the synthesis temperature is increased to 80(±1) °C (**BAg3**), the growth of Ag_3PO_4 and Ag_{met} nanoparticles alters the morphology to aggregated platelet structures composed of tiny balls and globules, as depicted in Figure 3.2h (red square).

SEM Images

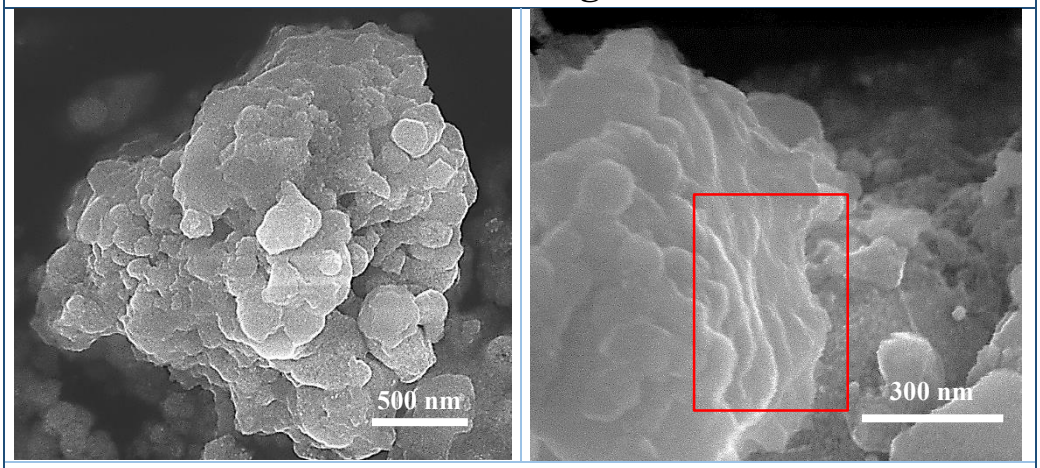

a. BW5Ag1

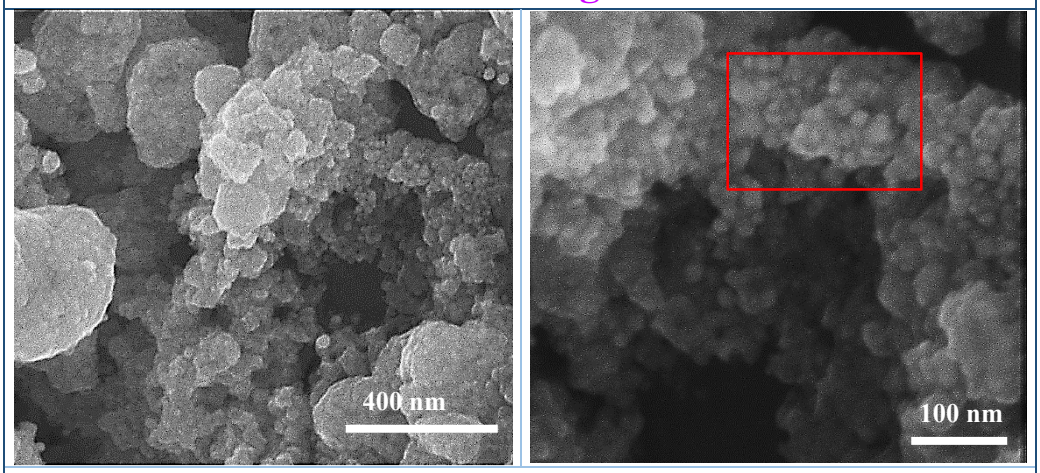

b. BW5Ag3

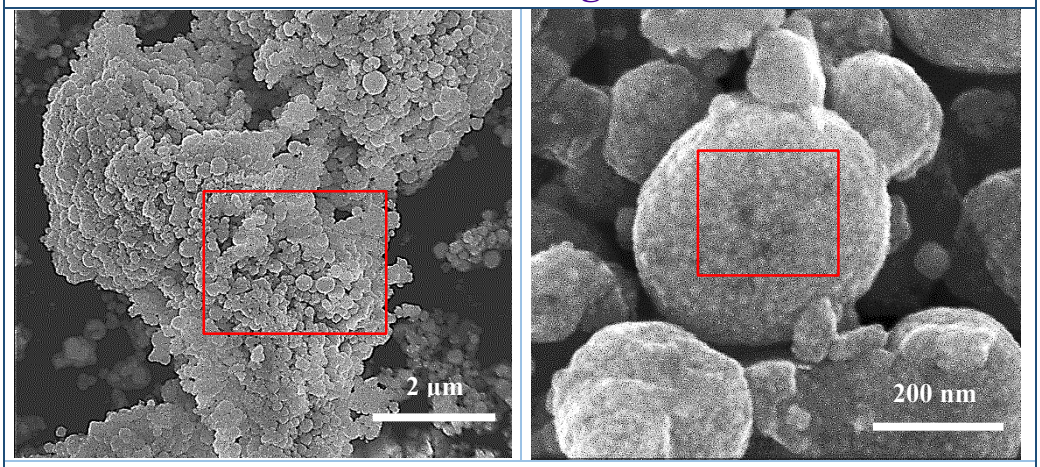

c. BW7Ag1

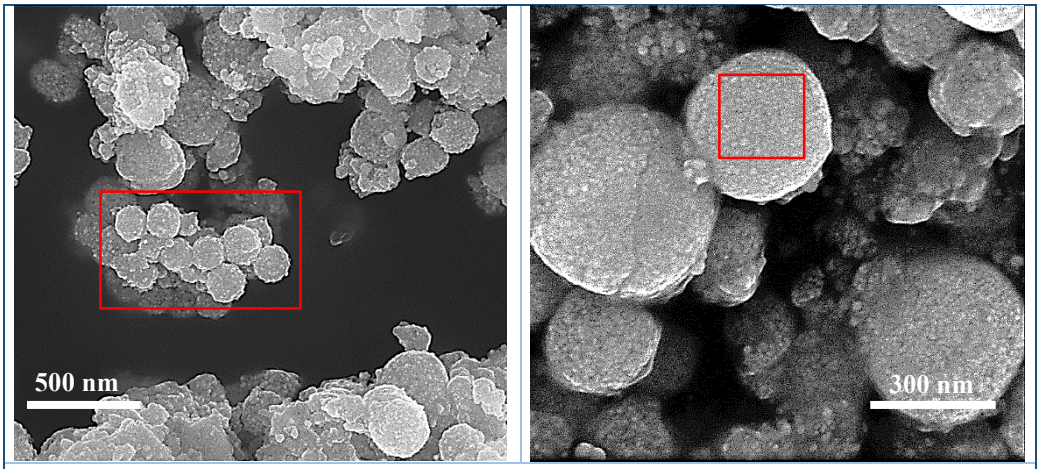

d. BW7Ag3

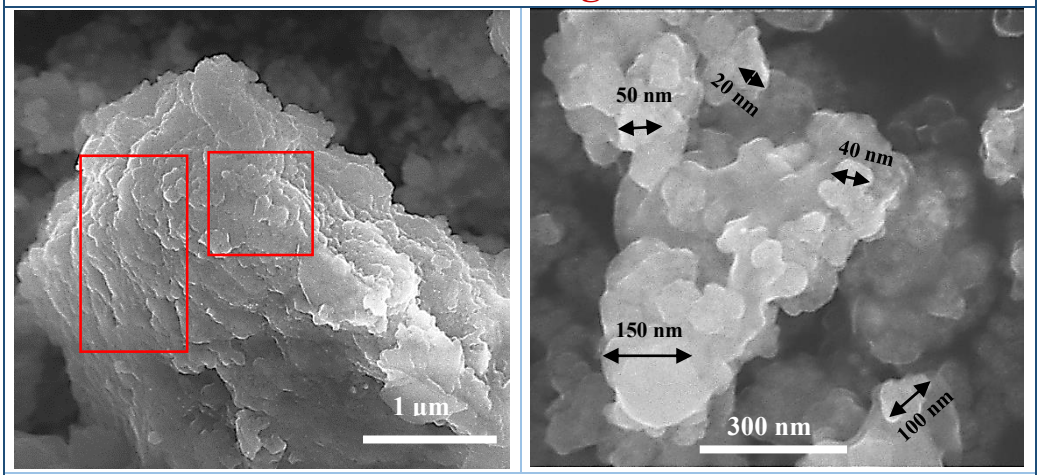

e. BW9Ag1

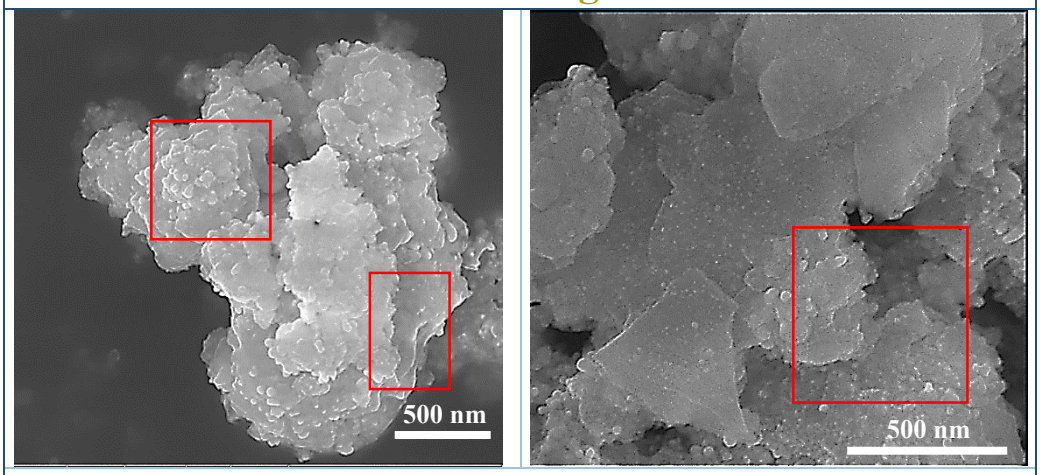

f. BW9Ag3

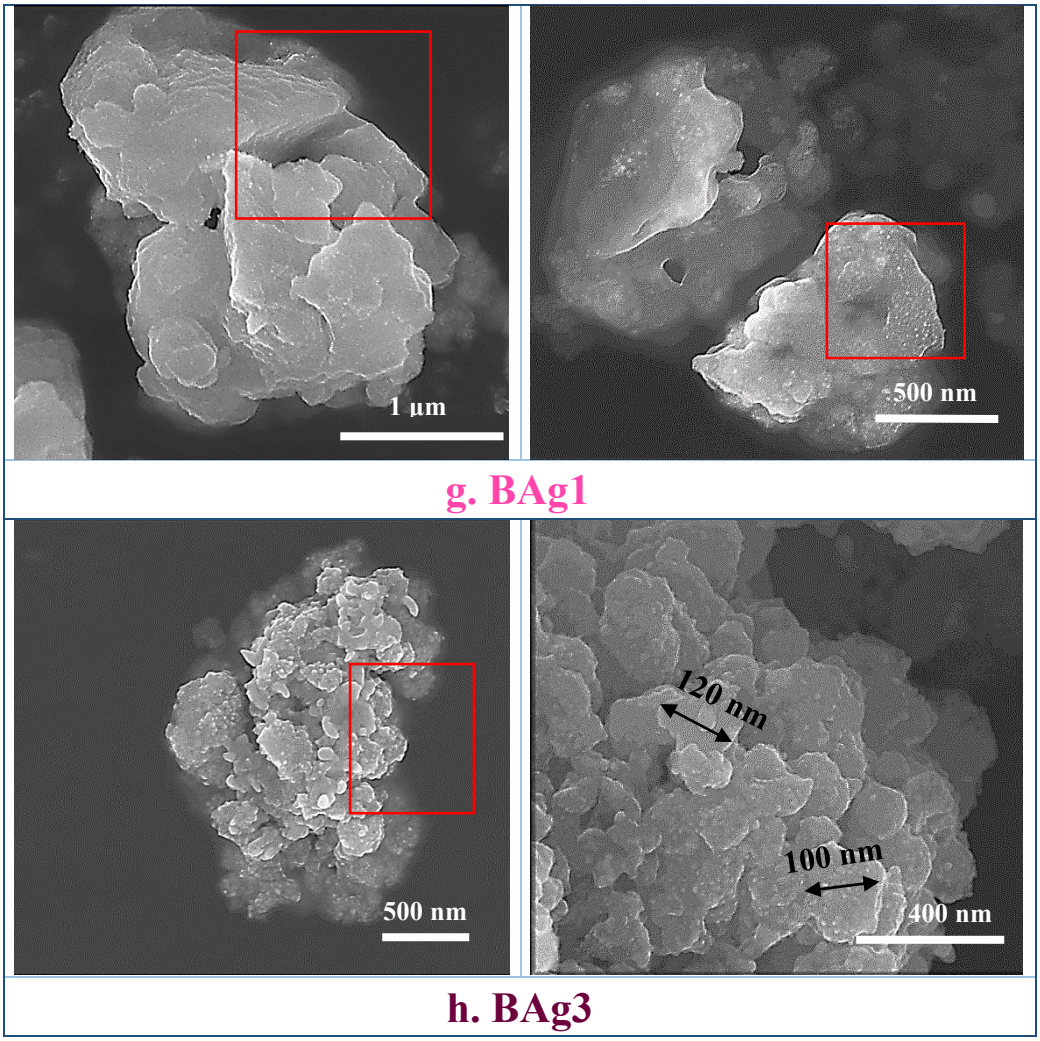

Figure 3.2 SEM images of nanocomposites synthesized using brewery waste **BW5**, **BW7**, **BW9**, and product **B** at 25(±1) °C and 80(±1) °C (Syntheses conditions: 25(±1) °C → Ag1, and 80(±1) °C→ Ag3).

Elemental mapping of the **BW5**, **BW7**, **BW9**, and **B** nanocomposites synthesized at 25(±1) °C and 80(±1) °C (Figure 3.3 a–h), reveals that the distribution of Ag, Cl, and P elements is uniform. This implies that the morphological changes in the nanoparticles' shapes and sizes are attributed to the incorporation of specific phases in the structure. However, these phases are not present independently but rather exist as a composite of mixed phases.

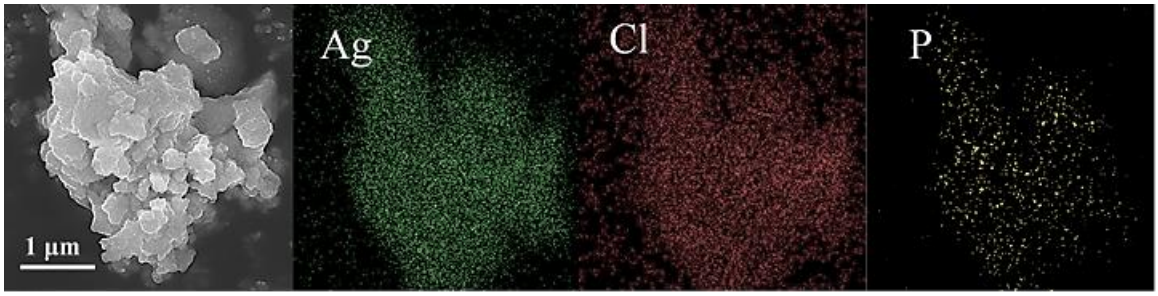

Figure 3.3a Elemental mapping of **BW5Ag1** nanocomposite.

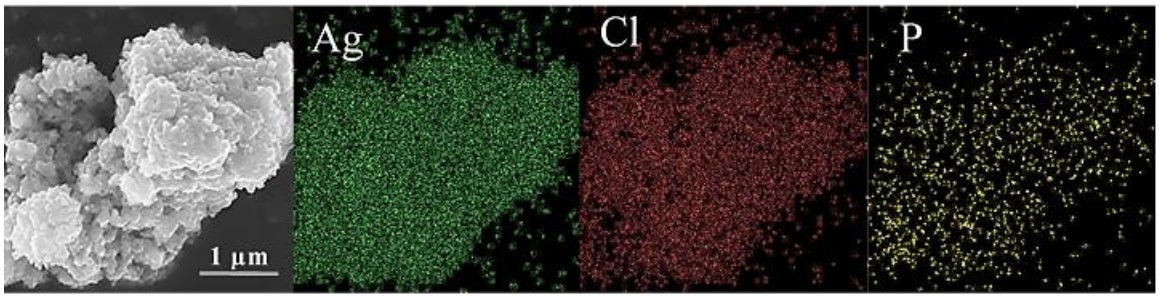

Figure 3.3b Elemental mapping of **BW5Ag3** nanocomposite.

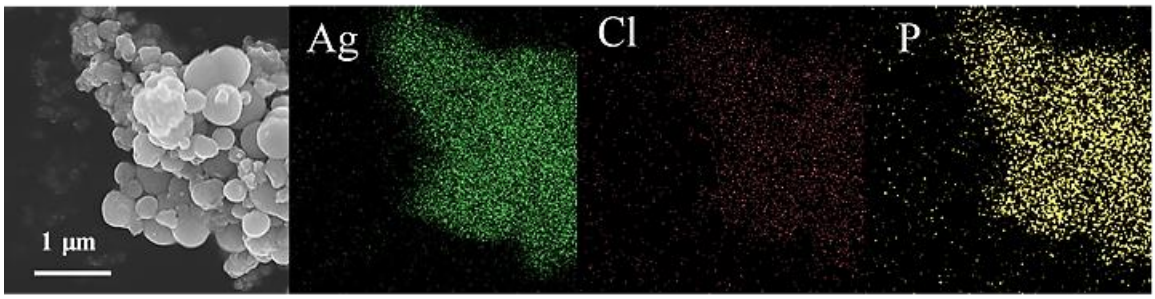

Figure 3.3c Elemental mapping of **BW7Ag1** nanocomposite.

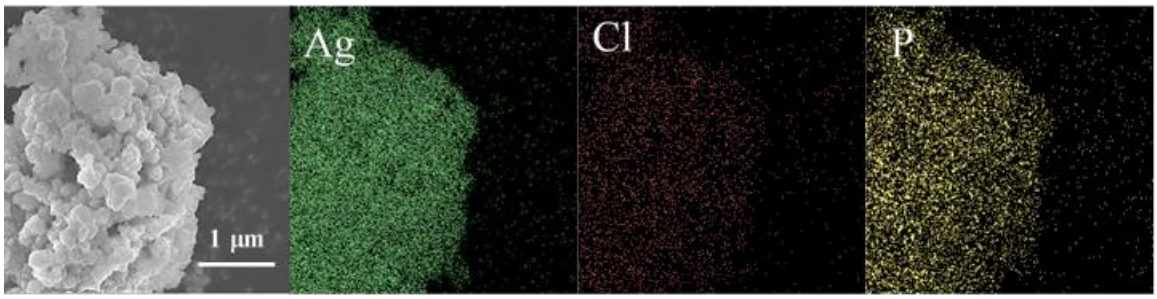

Figure 3.3d Elemental mapping of **BW7Ag3** nanocomposite.

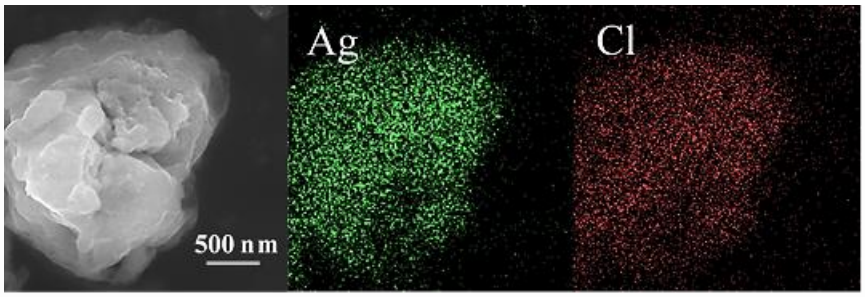

Figure 3.3e Elemental mapping of **BW9Ag1** nanocomposite.

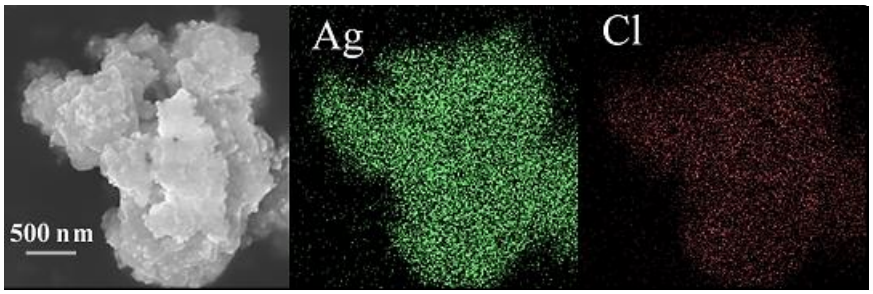

Figure 3.3f Elemental mapping of **BW9Ag3** nanocomposite.

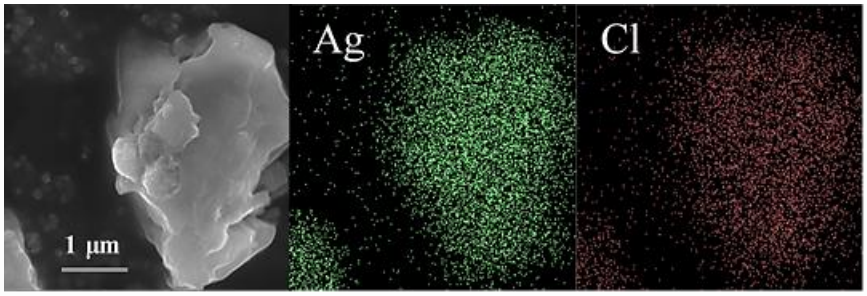

Figure 3.3g Elemental mapping of **BAg1** nanocomposite.

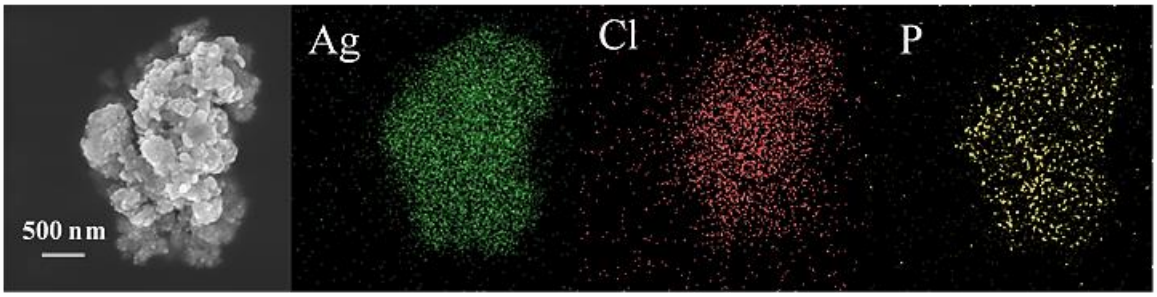

Figure 3.3h Elemental mapping of **BAg3** nanocomposite.

3.2.4 Surface chemical analysis by X-ray spectroscopy (XPS) of **BW** nanocomposites

The Figure 3.4 displays the XPS spectra for the **BW5**, **BW7**, **BW9** and **B** nanocomposites. To determine the surface content of elements in the **BW** nanocomposites, the quantification was performed using the peak areas of the Ag $3d_{5/2–3/2}$, C 1s, N 1s, O 1s, P 2p, S 2p, B 1s, and Cl 2p photoelectron lines after Tougaard background subtraction [157]. The XPS MultiQuant software [158, 159] used Scofield photoionization cross-sections [167], inelastic electron scattering (IMFP) [168], and analyzer transmission function. The surface elemental composition is presented in Table 3.4.

The surface analysis of **BW5**, **BW7**, **BW9**, and **B** nanocomposites revealed the presence of several elements, including Ag (Ag $3d_{5/2–3/2}$), C (C 1s), O (O 1s), N (N 1s), Cl (Cl 2p), and S (S 2p). Additionally, P (P 2p) was detected in **BW5** and **BW7** nanocomposites, while **B** nanocomposites contained trace amounts of P. The elemental composition on the surface depended on both the synthesis temperature of the nanocomposites and the brewery waste used as a precursor.

Nitrogen (N 1s BE = 399.4 ± 0.1 eV [169]) indicated the presence of an amino group ($C–NH_2$) in protein structures. Chlorine (Cl 2p BE = 198.6 ± 0.1 eV) was identified as AgCl. In **BW7** nanocomposites, with Ag_3PO_4 as the predominant phase, the phosphorous peak (P 2p BE = 132.9 ± 0.1 eV) indicated phosphate (PO_4), phosphite (PO_2), or phosphine (P=N=P) groups. In **BW5** and **B** nanocomposites, with AgCl as the predominant phase, the phosphorous peak (P

2p BE = 133.3 ± 0.1 eV) indicated hydrogen phosphate (HPO_4), diphosphate (P_2O_7), triphosphate (P_3O_{10}), dioxide diphosphorus ($H_4P_2O_2$), or phosphate in the organic matrix, such as methyl phosphate (PO_3CH_3). The chemical state of sulfur indicated two forms, depending on the nanoparticle synthesis temperature. The chemical form at BE = 162.9 ± 0.1 eV indicated sulfur linked in an organic environment, while the chemical form at BE = 168.0 ± 0.1 eV indicated sulfonyl (SO_2), sulfonate (SO_3), or sulfate (SO_4) groups. This latter form of sulfur started occurring between 50(±1) and 80(±1) °C.

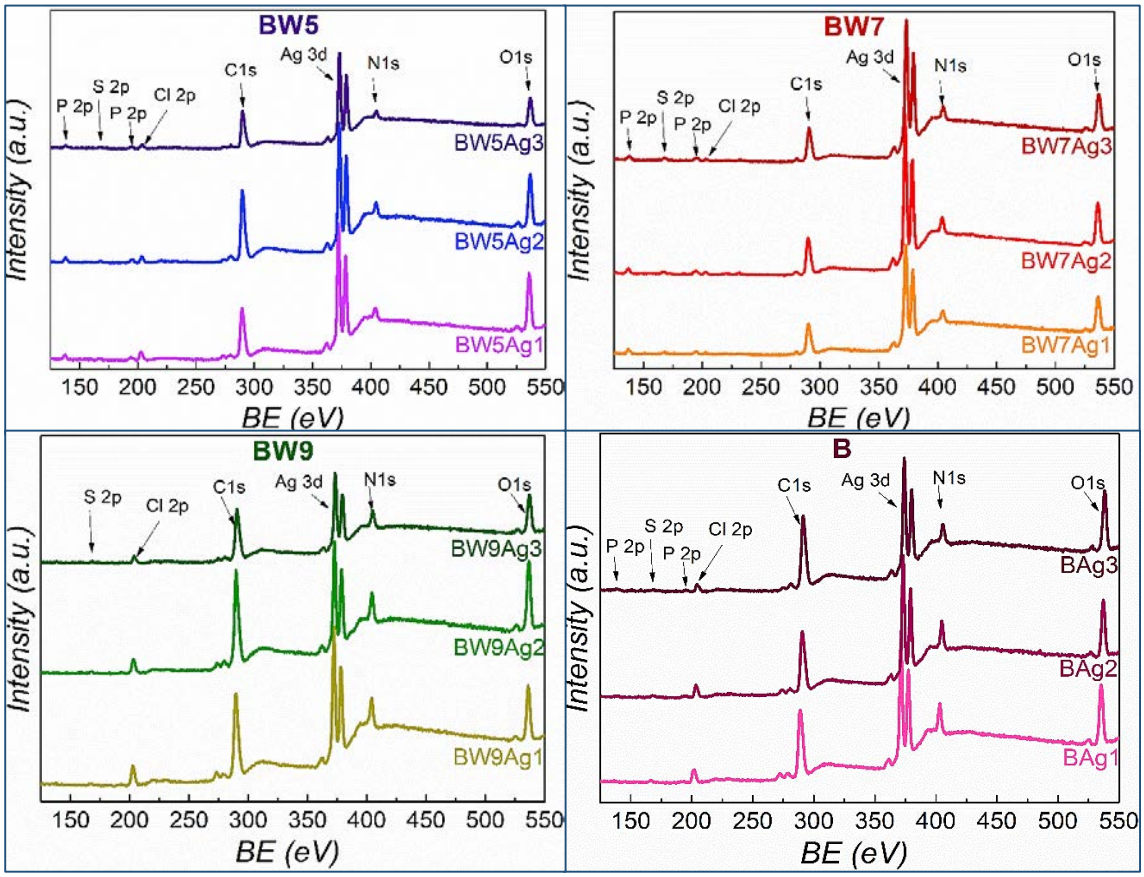

Figure 3.4 XPS spectra of **BW5**, **BW7**, **BW9** and **B** nanocomposites obtained at 25(±1), 50(±1), and 80(±1) °C. (Syntheses conditions: 25(±1) °C → Ag1, 50(±1) °C→ Ag2, and 80(±1) °C→ Ag3).

The ratio of C to Ag was found to be higher in **BW9** nanocomposites, indicating a thicker carbon overlayer consisting of carbon and C–O groups on the silver nanoparticles composite. Conversely, the C to Ag ratio was smaller in **BW7** nanocomposites, indicating a thinner carbon overlayer. A similar trend was observed for the C to O ratio, with **BW9** nanocomposites showing a larger ratio, indicating oxygen deficiency in their carbon overlayer compared to **BW7** nanocomposites. The decreasing trend of the C to O ratio with synthesis temperature suggested an enrichment of the overlayer with oxygen, possibly involving Ag oxide forms and

surrounding organic material. The Ag to O ratio was the highest in **BW7** nanocomposites and relatively lower in **B** nanocomposites, indicating the formation of a higher amount of silver oxides and the incorporation of a greater amounts of carbon-oxygen groups when **B** was used. With increasing temperature, the Ag to O ratio increased in **BW5**, **BW7**, and **B** nanocomposites, but not in **BW9** nanocomposites. A comparison of the elemental weight content in the bulk and at the surface, as determined by EDXRF and XPS analyses, respectively, was conducted for Ag, P, Cl, and S. The XPS results from Table 3.4 were normalized to 100 percent. An increasing trend in Ag content with increasing temperature was observed, while P, Cl, and S content decreased.

Table 3.4 Surface elemental composition of **BW5**, **BW7**, **BW9**, and **B** nanocomposites.

Sample	Synthesis temp., (±1) °C	XPS Analysis						
		Surface Elemental Composition (wt.%)						
		C	O	Ag	N	P	S	Cl
BW5Ag1	25	25.7	15.6	46.8	2.6	4.1	1.3	3.9
BW5Ag2	50	33.3	12.9	43.2	2.8	3.6	1.0	3.2
BW5Ag3	80	26.9	11.2	48.8	2.3	3.5	4.2	3.1
BW7Ag1	25	24.0	14.0	50.7	5.0	3.0	1.3	2.0
BW7Ag2	50	24.6	14.7	50.5	4.4	2.5	1.4	1.9
BW7Ag3	80	19.5	12.5	59.3	3.3	3.4	1.4	0.6
BW9Ag1	25	35.2	10.5	38.3	5.1	-	1.0	8.7
BW9Ag2	50	41.4	13.8	31.4	5.4		1.1	6.2
BW9Ag3	80	36.8	13.3	38.3	5.8		1.3	4.5
BAg1	25	33.8	14.1	39.4	5.4	0.4	0.9	5.3
BAg2	50	29.8	13.0	39.3	5.8	0.6	1.2	5.0
BAg3	80	26.5	13.7	51.1	5.0	0.6	0.8	2.3

3.2.4.a Surface chemical forms of Ag, C, and O

The XPS spectra of Ag $3d_{5/2–3/2}$, C 1s, and O 1s were fitted using Gaussian-Lorentzian asymmetric components after Tougaard inelastic background subtraction [157] with the XPSPEAK 4.1 software. To evaluate the chemical compounds present, the binding energy (BE) values for all elements were determined after calibration on C 1s photoelectron peak at 284.4 eV and averaging of respective values for all **BW** nanocomposites prepared at different temperatures.

The Ag $3d_{5/2–3/2}$ BE values used for different Ag chemical states were 367.8 eV for Ag_3PO_4, 368.1 eV for AgCl, and 368.3 eV for Ag_{met}. Oxidized Ag structures, such as Ag oxides (AgO, Ag_2O), and AgOH, were reported to exhibit a shift towards smaller BE values compared to

Ag_{met} [100, 101, 169]. Similarly, a shift towards smaller BE values from Ag_{met} was observed for Ag-glucose structures. To optimize the fitting conditions, an additional peak was considered at a smaller BE value than that characteristic for Ag oxidized forms. The fitting procedure involved maintaining constant ratios of full width at half maximum (FWHM) for peaks representing each chemical form and no constraint on the BE value of the additionally assumed peak. The results of the fitting procedure of Ag $3d_{5/2–3/2}$ spectra, representing the content of different chemical forms, are presented in the figures (Figures 3.5).

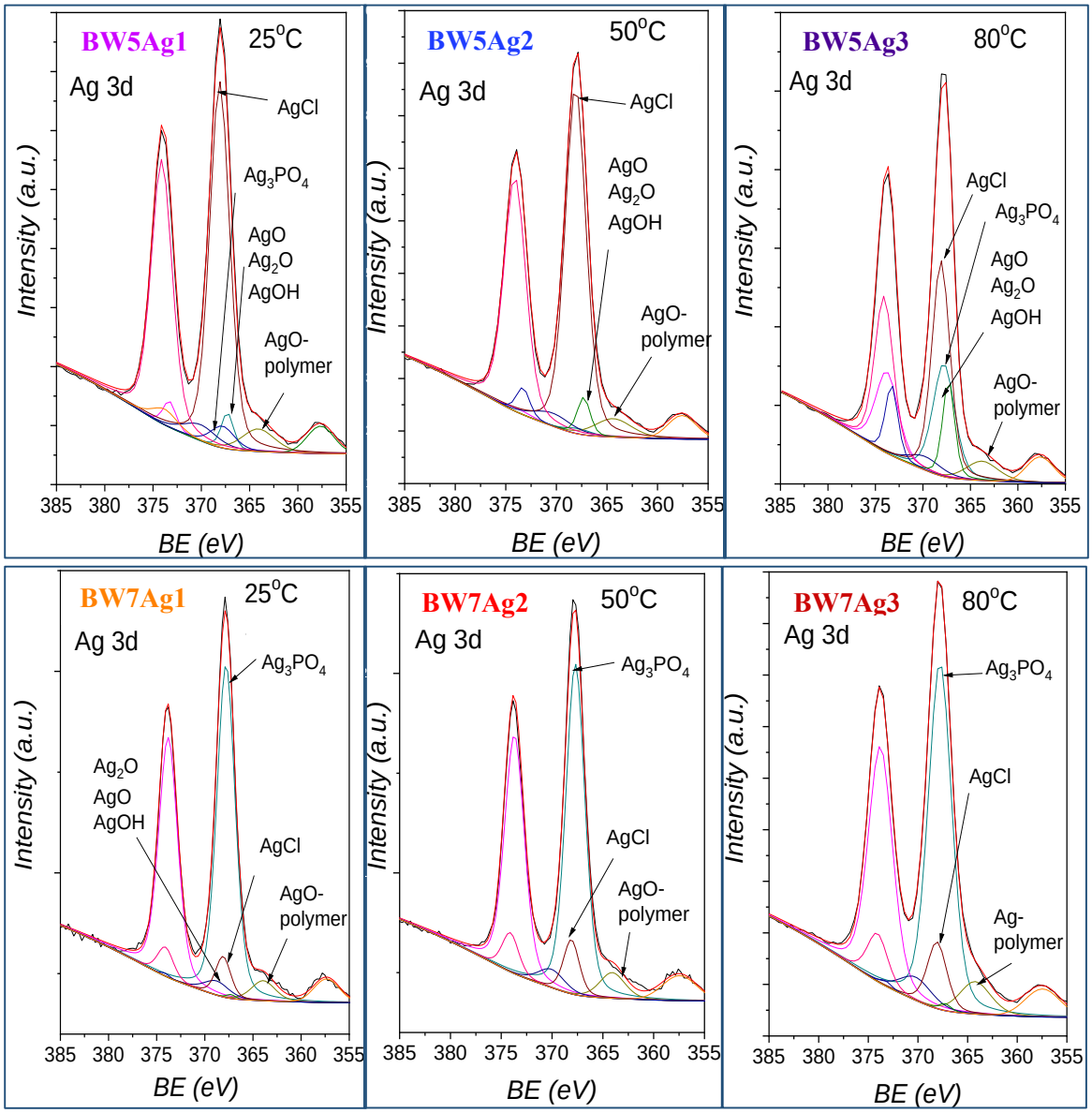

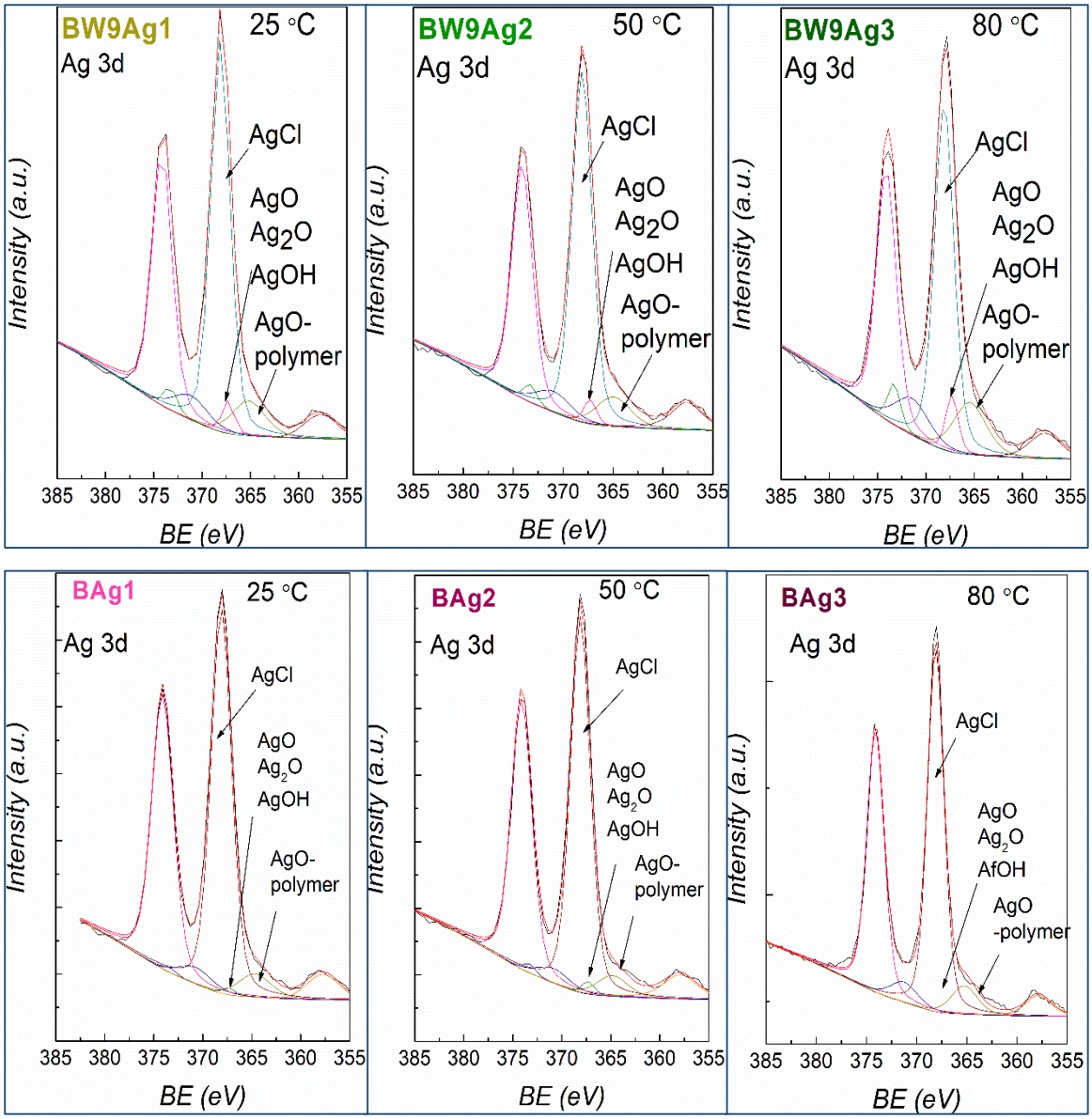

Figure 3.5 The Gaussian–Lorentzian asymmetric functions to different atomic chemical states fitted Ag $3d_{5/2–3/2}$ XPS spectra recorded from **BW5**, **BW7**, **BW9**, and **B** nanocomposites. (Syntheses conditions: 25(±1) °C → Ag1, 50(±1) °C→ Ag2, and 80(±1) °C→ Ag3).

The fitting of C 1s spectra (Figure 3.6) for the **BW** nanocomposites revealed distinct binding energy (BE) values corresponding to different carbon chemical forms. Specifically, BE of 284.4 eV were assigned to C sp^2 hybridizations, 285.3 eV to C sp^3 hybridizations, 286.3 eV to a hydroxyl group (C–OH), 287.4 eV to a carbonyl group (C=O) [100, 101, 169, 170], while no carboxyl groups (COOH) were detected on the surface of **BW** nanocomposites.

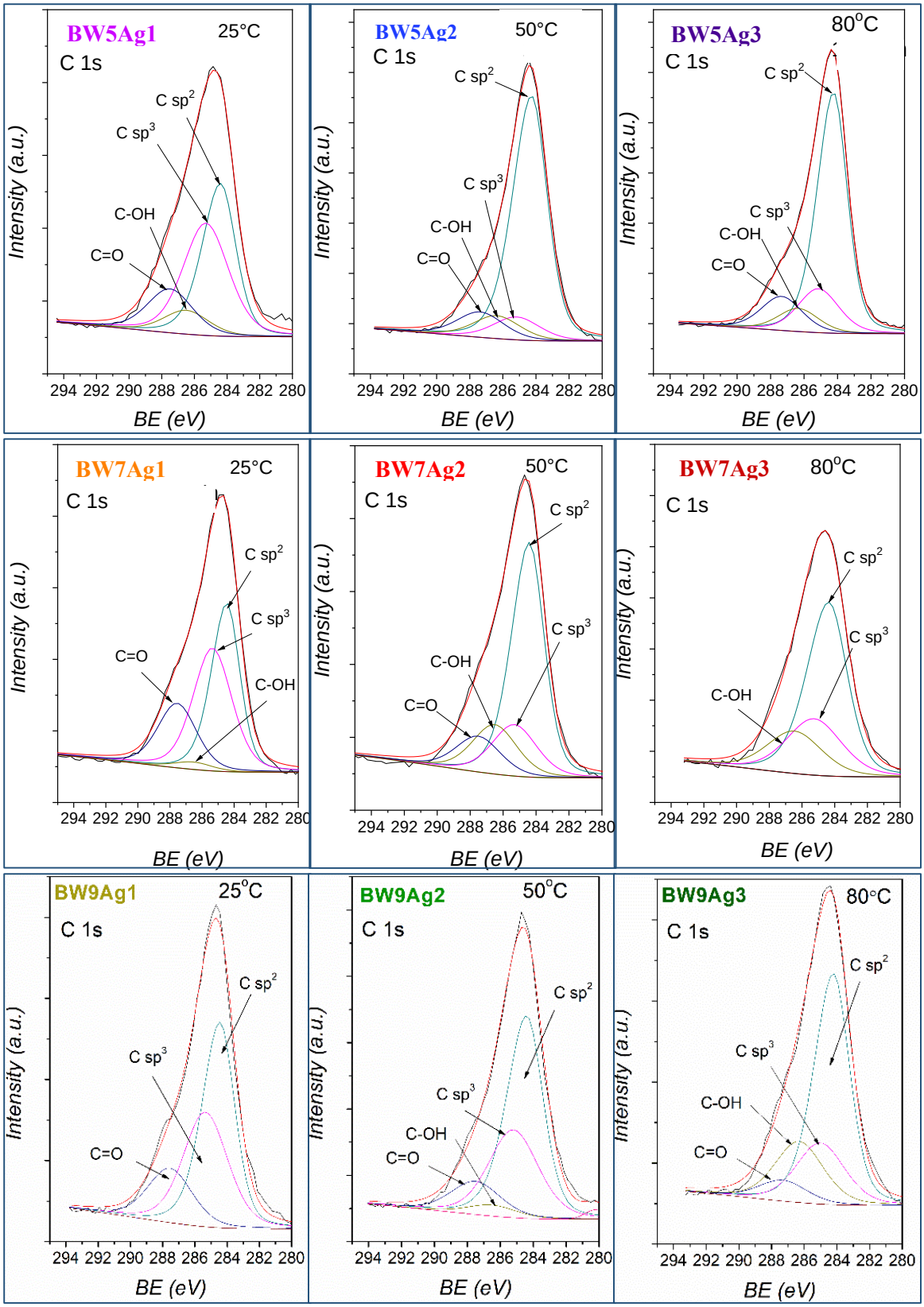

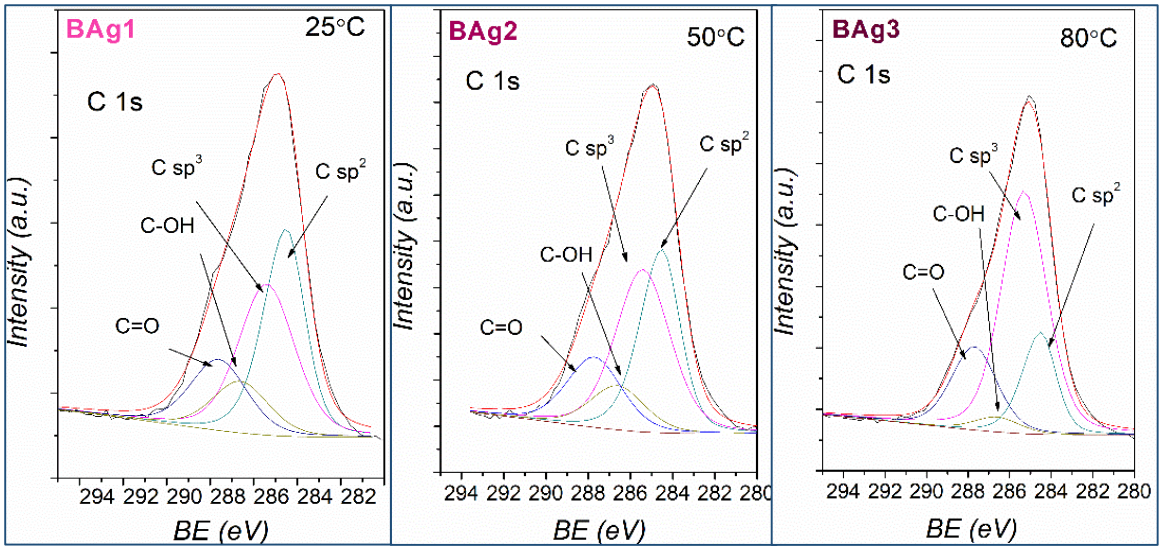

Figure 3.6 The Gaussian–Lorentzian asymmetric functions to different atomic chemical states fitted C 1s XPS spectra recorded from **BW5**, **BW7**, **BW9**, and **B** nanocomposites. (Syntheses conditions: 25(±1) °C → Ag1, 50(±1) °C→ Ag2, and 80(±1) °C→ Ag3).

The O 1s spectrum fitting provided the BE values of 529.9 ± 0.2 for oxidized silver (Ag–O) states, 531.2 ± 0.2 eV for carbonyl groups (C=O), and 532.5 ± 0.1 eV for hydroxyl groups (C–O) [170, 171]. The atomic contents of oxygen groups (C–OH, C=O) and Ag–O chemical state derived from the O 1s spectra fitting aligned well with the results from C 1s fitting (C–OH, C=O) and Ag $3d_{5/3–3/2}$ (Ag–O) spectra, confirming consistency across these measurements. The resulting fitted O 1s spectra are shown in Figure 3.7.

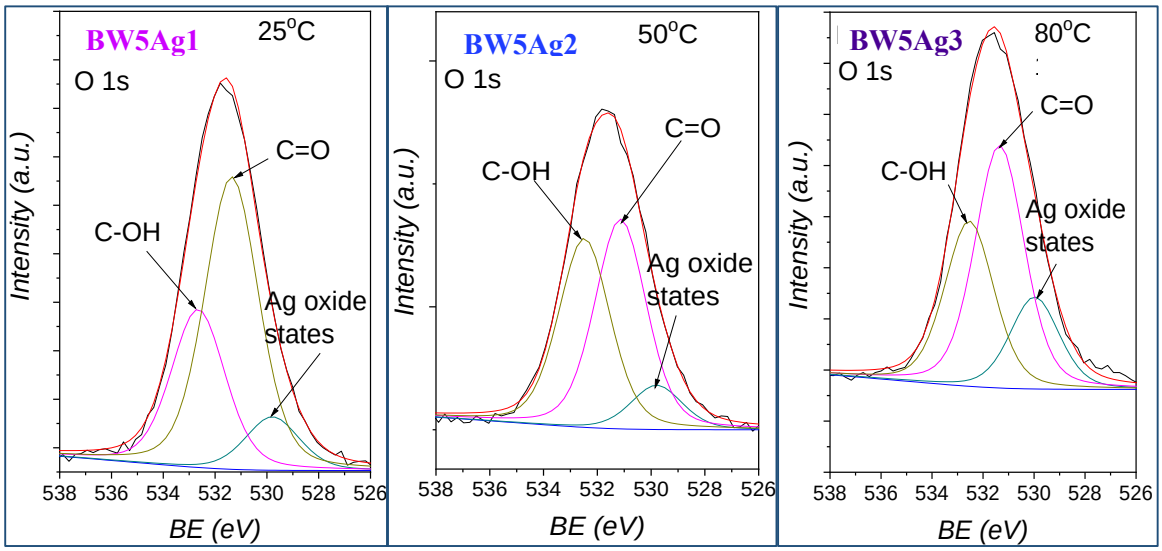

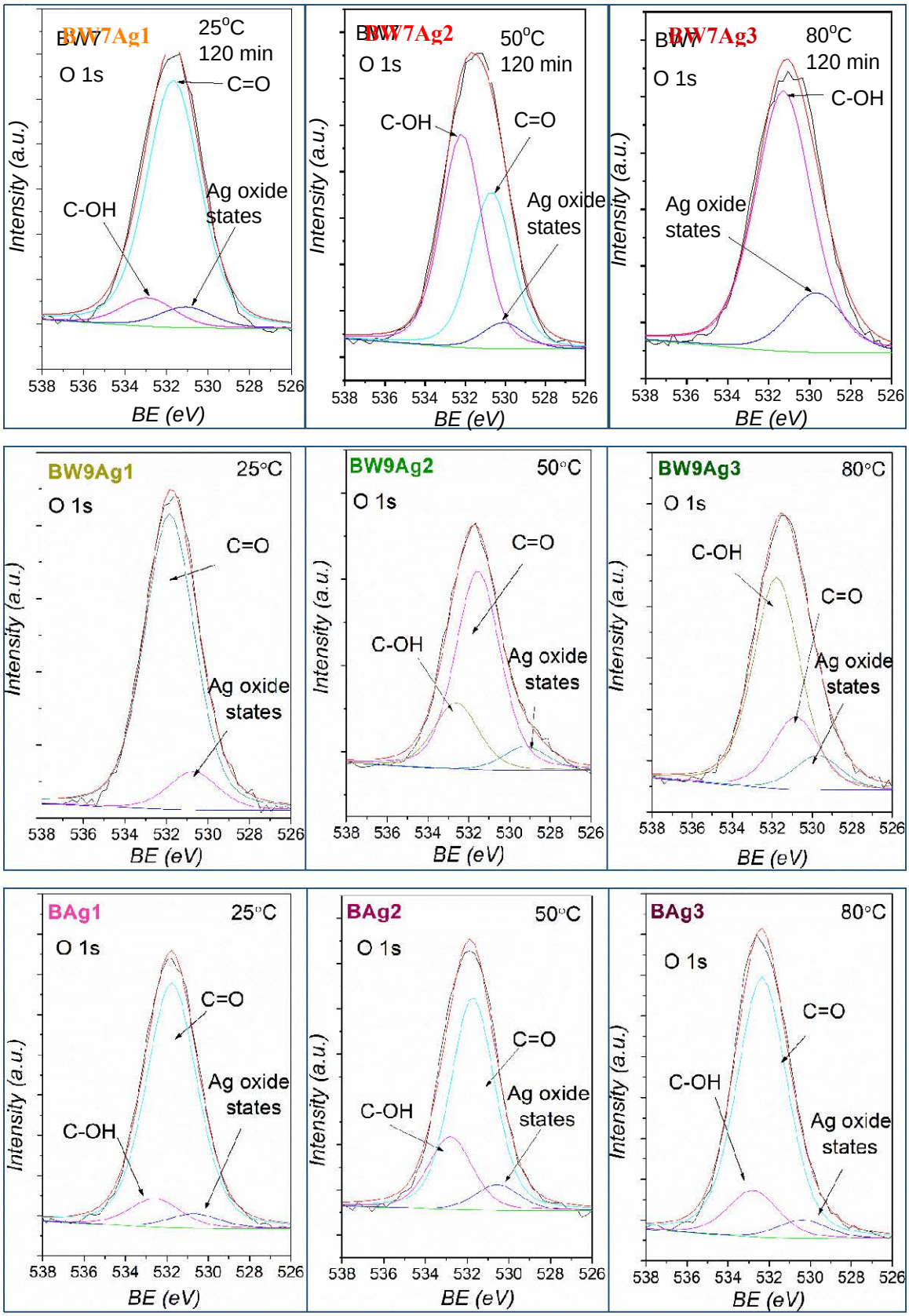

Figure 3.7 The Gaussian–Lorentzian asymmetric functions to different atomic chemical states fitted O 1s XPS spectra recorded from **BW5**, **BW7**, **BW9**, and **B** nanocomposites. (Syntheses conditions: 25(±1) °C → Ag1, 50(±1) °C→ Ag2, and 80(±1) °C→ Ag3).

The carbon overlayer thickness on the **BW** nanocomposites was evaluated using Tougaard Quases-Analyze software [172]. This method utilized the Ag $3d_{5/2–3/2}$ spectra to determine the surface morphology parameters by analyzing the inelastic background around the photoelectron transitions. Based on a Buried Layer (BL) model of uniform over-layer and the inelastic mean free path (IMFP) of Ag $3d_{5/2–3/2}$ photoelectrons attenuated in the carbon overlayer which is 3.1 nm [168], by subtracting the inelastic background, the carbon overlayer thickness was determined (Figure 3.8).

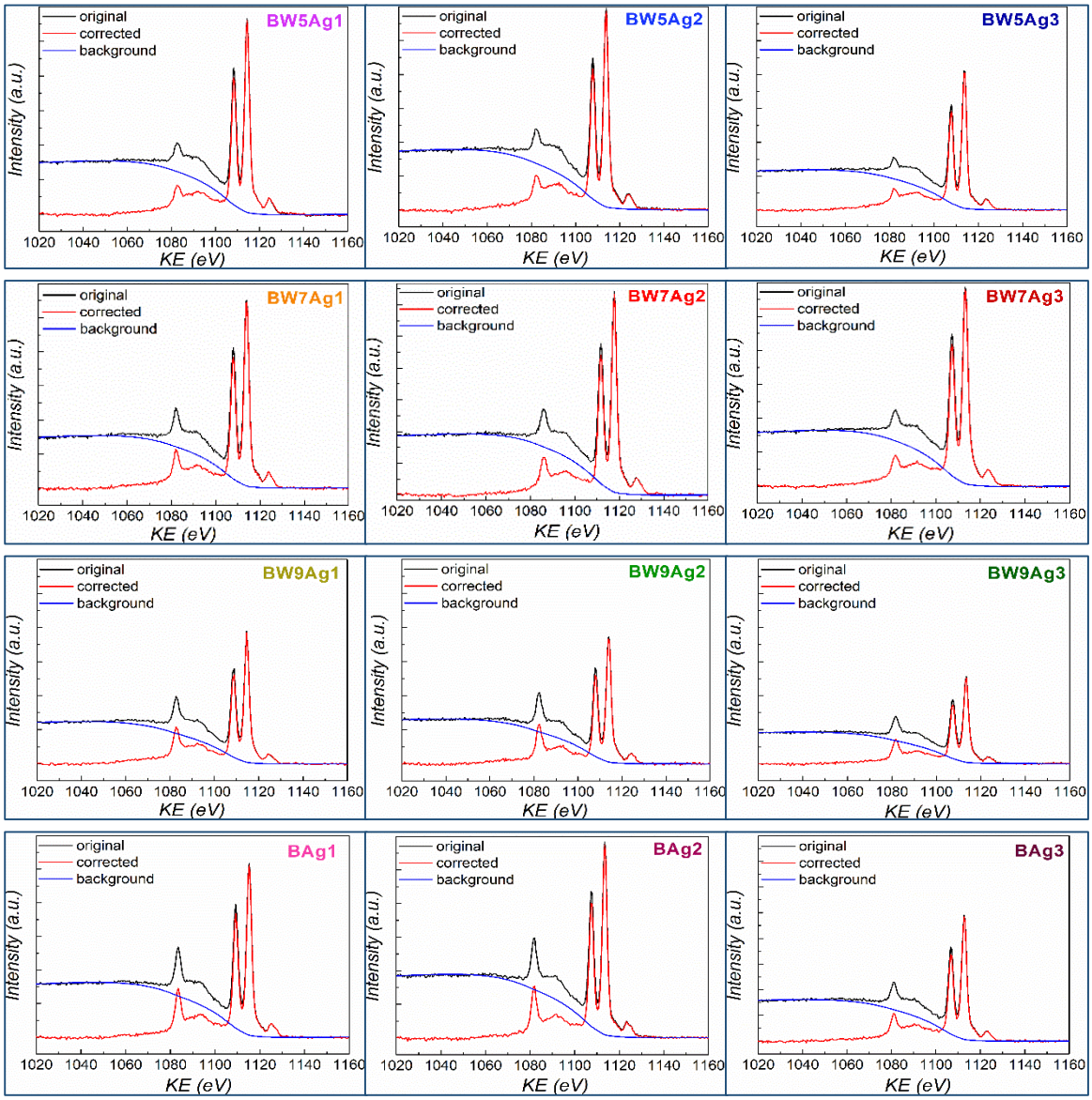

Figure 3.8 QUASES-Analyze software and Buried Layer (BL) model analysis of Ag $3d_{5/2/–3/2}$ spectra for **B** nanocomposites. (Syntheses conditions: 25(±1) °C → Ag1, 50(±1) °C→ Ag2, and 80(±1) °C→ Ag3 [168]) .

3.2.4.b Surface Ag chemical state content in **BW** nanocomposites

The analysis results from the fitting of the Ag chemical states on the surface of nanocomposites, as listed in Table 3.5, revealed some key findings. Notably, no Ag_{met} was detected on the surface of any nanocomposites. Instead, the surface is composed of Ag_3O_4, AgCl, and various Ag oxidized states (Ag_2O, AgO, AgOH). Additionally, a peak at BE= 363.8 ± 0.3 (**BW5**), 364.09 ± 0.11 (**BW7**), 365.4 ± 0.3 eV (**BW9**), and 364.9 ± 0.4 eV (**B**), is observed. This peak is attributed to oxidized Ag form linked with organic material through hydrogen bonding forming a type of organometallic complex referred to as the "AgO-polymer" form. This AgO-polymer chemical state, resulting from the interaction between AgO and carbohydrate, polyphenol, or amino groups, leads to a shift in BE towards smaller BE values compared to typical Ag oxides and AgOH. This BE shift depends on the content of carbohydrates, polyphenols, and nitrogen-containing amino groups derived from the brewery wastes used for the synthesis.

Table 3.5 Surface Ag chemical state content of **BW5**, **BW7**, **BW9**, and **B** nanocomposites.

Sample	**Synthesis temp., (±1) °C**	**Ag chemical state (wt.%)—Ag $3d_{5/2-3/2}$**			
		AgCl BE=368.1 eV	**Ag_3PO_4** BE=367.8 eV	**Ag_2O, AgO, AgOH** BE=367.3 eV	**AgO–polymer** †BE
BW5Ag1	25	37.92	2.74	2.32	3.82
BW5Ag2	50	36.47	0.71	2.51	3.52
BW5Ag3	80	23.34	14.73	7.01	3.72
BW7Ag1	25	4.35	42.75	0.25	3.35
BW7Ag2	50	5.57	40.72	-	4.21
BW7Ag3	80	7.48	45.52	0.49	5.81
BW9Ag1	25	31.54	-	1.75	5.01
BW9Ag2	50	26.30		1.20	3.90
BW9Ag3	80	28.15		2.96	7.19
BAg1	25	35.74	-	0.38	3.38
BAg2	50	36.96		0.75	3.19
BAg3	80	35.64		-	4.36

† BE= 363.8±0.3 (**BW5**), 364.09±0.11 (**BW7**), 365.4±0.3 eV (**BW9**), and 364.9±0.4 eV (**B**)

The surface of **BW5**, **BW9**, and **B** nanocomposites show a predominance of AgCl chemical form, while **BW7** nanocomposites primarily display Ag_3PO_4 as the dominant Ag chemical form. Interestingly, both **BW9** and **B** nanocomposites lack Ag_3PO_4 on their surfaces. The content of the Ag oxides (Ag_2O, AgO, AgOH) is highest in **BW5** nanocomposites and lowest in **BW7** nanocomposites, while **BW9** nanocomposites have the highest amount of AgO-

polymer. As the synthesis temperature increases, the content of Ag oxides and AgO-polymer also increases, indicating a more facile formation of AgO-polymer state over Ag oxides and AgOH at higher temperatures. This implies that the different organometallic structures formed by the interaction between silver oxides and organic materials differ depending on organic matter content originating from amino groups, polyphenols, carbohydrates, and sugars present in the precursor (**BW5**, **BW7**, **BW9**, and **B**) (Table 3.1) and the temperature of synthesis.

Comparing the surface silver content evaluated by XPS (Table 3.4 and 3.5) and in bulk calculated by XRD (Table 3.2), similar trends are observed under synthesis temperature across all nanocomposites. However, no Ag_{met} is detected on the surface of any of the nanocomposites, and no Ag_3PO_4 is present on the surface of **BW9** and **B** nanocomposites. As synthesis temperature increases the surface AgCl phase content in **BW5**, **BW9**, and **B** nanocomposites shows a slight decrease, whereas the total AgCl content in the bulk significantly decreases (Table 3.2), indicating a shift in silver phase distribution as a result of temperature changes.

3.2.4.c Surface C chemical state content and overlayer thickness in **BW** nanocomposites

The nanocomposites synthesized at varying temperatures exhibit differences in the content of hydroxyl (C–OH) and carbonyl (C=O) groups on their surface and organic overlayer thickness, depending on synthesis conditions (Table 3.6). Specifically, the **BW9** nanocomposites shows the highest C sp^2 content, while the **B** nanocomposites have the highest content of C sp^3 groups compared to other nanocomposites. At a synthesis temperature of 50(±1) °C, the **BW5** and **BW7** nanocomposites demonstrate an increase in C sp^2 at the expense of C sp^3. Whereas C sp^2 and C sp^3 content is highest for **BW9** nanocomposite synthesized at 50(±1) °C, contradicting with the lowest levels in **B** nanocomposites.

Regarding carbon-oxygen functional groups, the surface of **BW7** nanocomposites predominantly contains C–OH groups, whereas **BW5**, **BW9**, and **B** nanocomposites are richer in C=O groups. Interestingly, in **BW9** nanocomposites, the increasing synthesis temperature favors the increase of C–OH groups at the expense of C=O groups.

Amorphization of carbon in the nanocomposites correlates with an increase in the thickness of the carbon overlayer, whereas carbonization is associated with a decrease in its thickness. Nanocomposites synthesized using **BW9** and **B**, which are rich in polyphenols, carbohydrates, and fermentable sugars, display a thicker overlayer corresponding to the higher content of carbon-oxygen functional groups. This suggests a more complex and rich surface composition for these nanocomposites compared to those synthesized using **BW5** and **BW7**.

Table 3.6 Surface C chemical state content of **BW5**, **BW7**, **BW9**, and **B** nanocomposites.

Sample	Synthesis temp., (±1) °C	C chemical state (wt.%)- C 1s				C overlayer thickness (nm)
		C sp^2 BE=284.4 eV	C sp^3 BE=285.3 eV	C–OH BE=286.3 eV	C=O BE=287.4 eV	
BW5Ag1	25	10.36	9.57	2.03	3.74	2.30
BW5Ag2	50	24.38	2.87	2.87	3.18	2.45
BW5Ag3	80	17.60	4.04	2.13	3.13	2.39
BW7Ag1	25	9.78	8.96	0.55	4.71	2.07
BW7Ag2	50	14.2	3.92	3.76	2.72	2.42
BW7Ag3	80	11.37	4.64	3.49	-	1.80
BW9Ag1	25	17.31	12.13	-	5.76	2.35
BW9Ag2	50	22.75	12.40	1.56	4.69	2.89
BW9Ag3	80	20.68	6.88	6.88	2.36	2.77
BAg1	25	9.06	16.31	0.88	7.55	2.59
BAg2	50	8.74	13.34	1.97	5.75	2.45
BAg3	80	11.81	35.16	2.17	12.06	2.65

Moreover, at a synthesis temperature of 50(±1) °C, the overall carbon-oxygen content on the surface of **BW5**, **BW7**, and **BW9** nanocomposites is enhanced, resulting in a thicker overlayer. This behavior contrasts with that observed in **B** nanocomposites, where lower thickness was noted. This emphasizes the influence of synthesis temperature on the surface chemistry and composition of the nanocomposites.

3.2.5 Particle size distribution by transmission electron microscopy (TEM)

The particle size distribution of nanocomposites observed under TEM showed variation based on the different synthesis temperatures and precursors used.

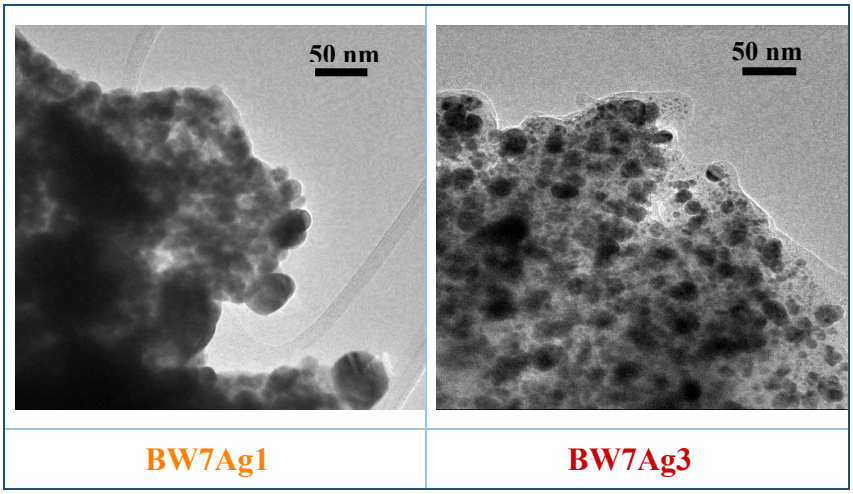

Figure 3.9 TEM image of **BW7Ag1** and **BW7Ag3** nanocomposites. (Syntheses conditions: 25(±1) °C → Ag1, and 80(±1) °C→ Ag3).

The effect of synthesis temperature on the particle size was studied by comparing the TEM images of **BW7Ag1** synthesized at 25(±1) °C and **BW7Ag3** synthesized at 80(±1) °C (Figure 3.9). The **BW7Ag1** nanocomposite is composed of large sized nanoparticles, while the **BW7Ag3** nanocomposite consists of small-sized nanoparticles. This implies that increasing temperature favors nucleation overgrowth. This behavior suggests that smaller-size nanoparticles are present at higher Ag_{met} content in the nanocomposites (Table 3.2). The effect of different precursors (**BW5**, **BW7**, **BW9**, and **B**) on the particle size of nanocomposites is shown in Figure 3.10. The **BW5** and **BW7** nanocomposites have smaller nanoparticles compared to **BW9** and **B** nanocomposites.

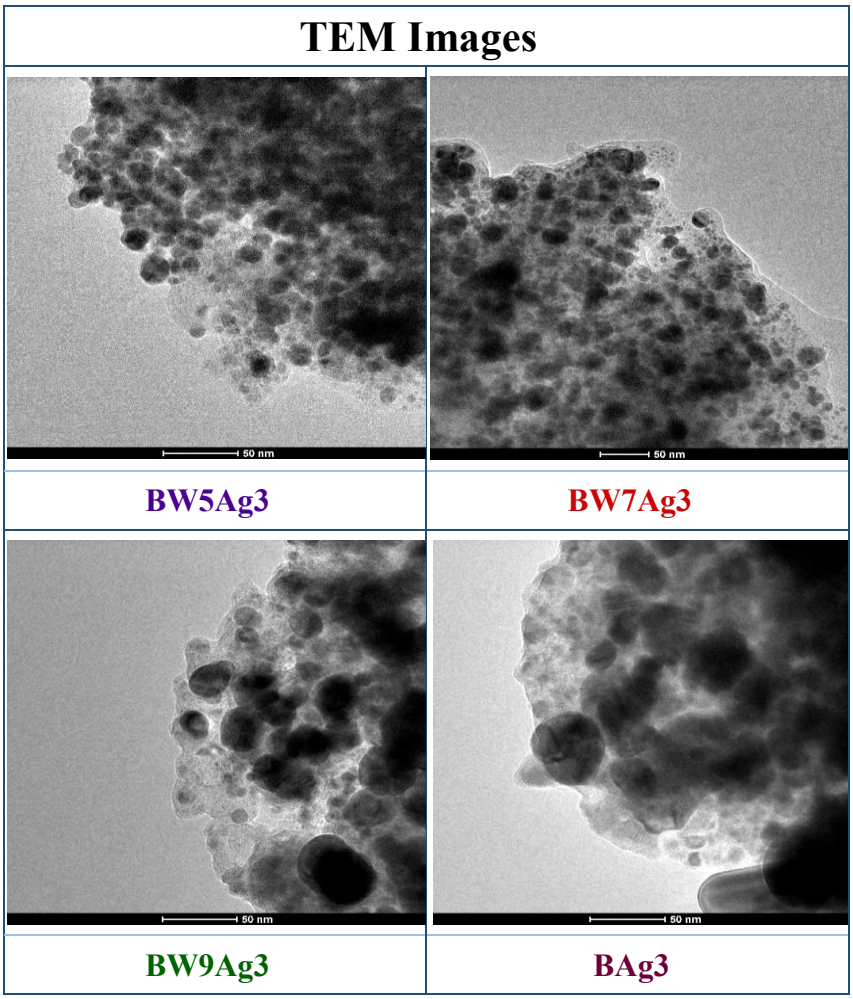

Figure 3.10 TEM image of **BW5Ag3**, **BW7Ag3**, **BW9Ag3**, and **BAg3** nanocomposites. (Syntheses conditions: 80(±1) °C→ Ag3).

3.3 Anticancer activity testing of **BW** nanocomposites

The activity of silver nanocomposites synthesized utilizing brewery wastes **BW5**, **BW7**, **BW9** and product **B** at temperatures of 25(±1) °C denoted as **Ag1**, and 80(±1) °C denoted as **Ag3**, was evaluated in terms of their impact on biological cells. Fluorescent microscopic studies were

conducted on both normal (HEK293) and cancerous (HeLa) cells to investigate the impact of varying concentrations of nanocomposites on cell growth. In addition to the microscopic studies, LDH and MTT assays were employed to evaluate the biocompatibility of the nanocomposites towards the normal (HEK293) cell line, as well as their cytotoxic effects on four different cancer cell lines (HeLa, A549, MCF-7, MDA-MB-231). These complementary assays provided valuable insights into the effect of the nanocomposites on normal and cancer cell lines. The fluorescent microscopic studies allowed for direct visualization and analysis of the effects on cell growth, while the LDH assay and MTT assay provided quantitative assessments of the biocompatibility and cytotoxicity across different cell lines. By employing multiple evaluation methods, a comprehensive understanding of the interactions between nanocomposites and cells was obtained, shedding light on their potential as biocompatible and cytotoxic agents in normal and cancerous cells context, respectively. The HeLa cell line, commonly employed in biological research, along with the A549 cell line representing lung cancer cells, and the MCF-7 and MDA-MB-231 cell lines representing breast cancer cells, were utilized to investigate the nanoparticle effects on diverse cancer cell types. Notably, the impact of silver nanoparticles synthesized with different brewery by-products and product at varying temperatures exhibited distinct influences on cell cytotoxicity.

3.3.1 Live/dead assay

Confocal images of HEK293 and HeLa cells treated with low (1 μg ml^{-1}) and high (25 μg ml^{-1}) concentrations of $AgNO_3$ as well as **BW** nanocomposites synthesized at 25(±1) °C and 80(±1) °C are presented in Figure 3.11. The confocal images reveal distinct observations based on the concentration of the nanocomposites. At lower concentrations, a decrease in cell growth was evident in the nanocomposite-treated cells compared to the control (Figure 3.11). Furthermore, at higher nanocomposites' concentration, a drop in cell number was accompanied by an increase in cell death (Figure 3.11).

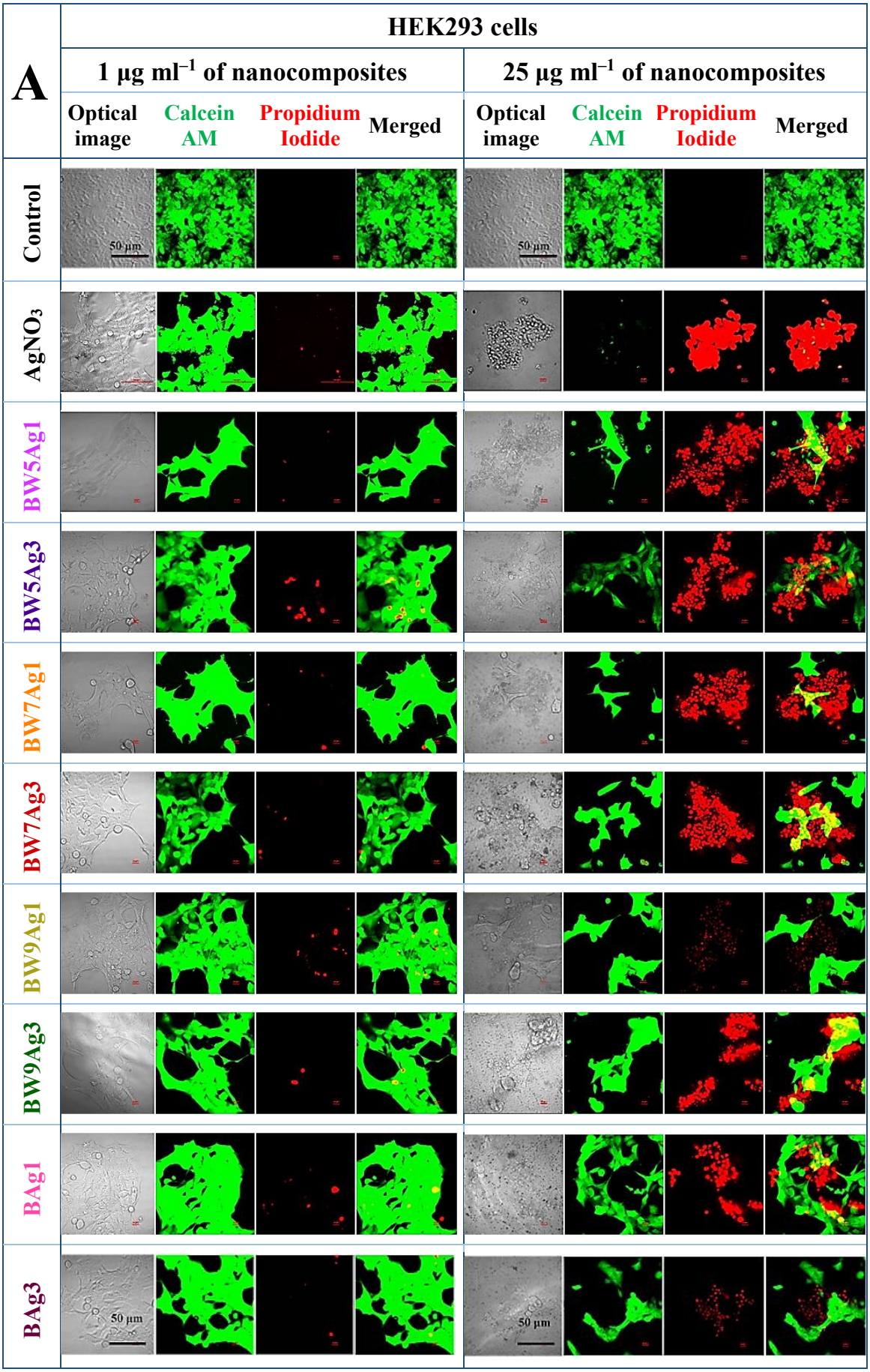

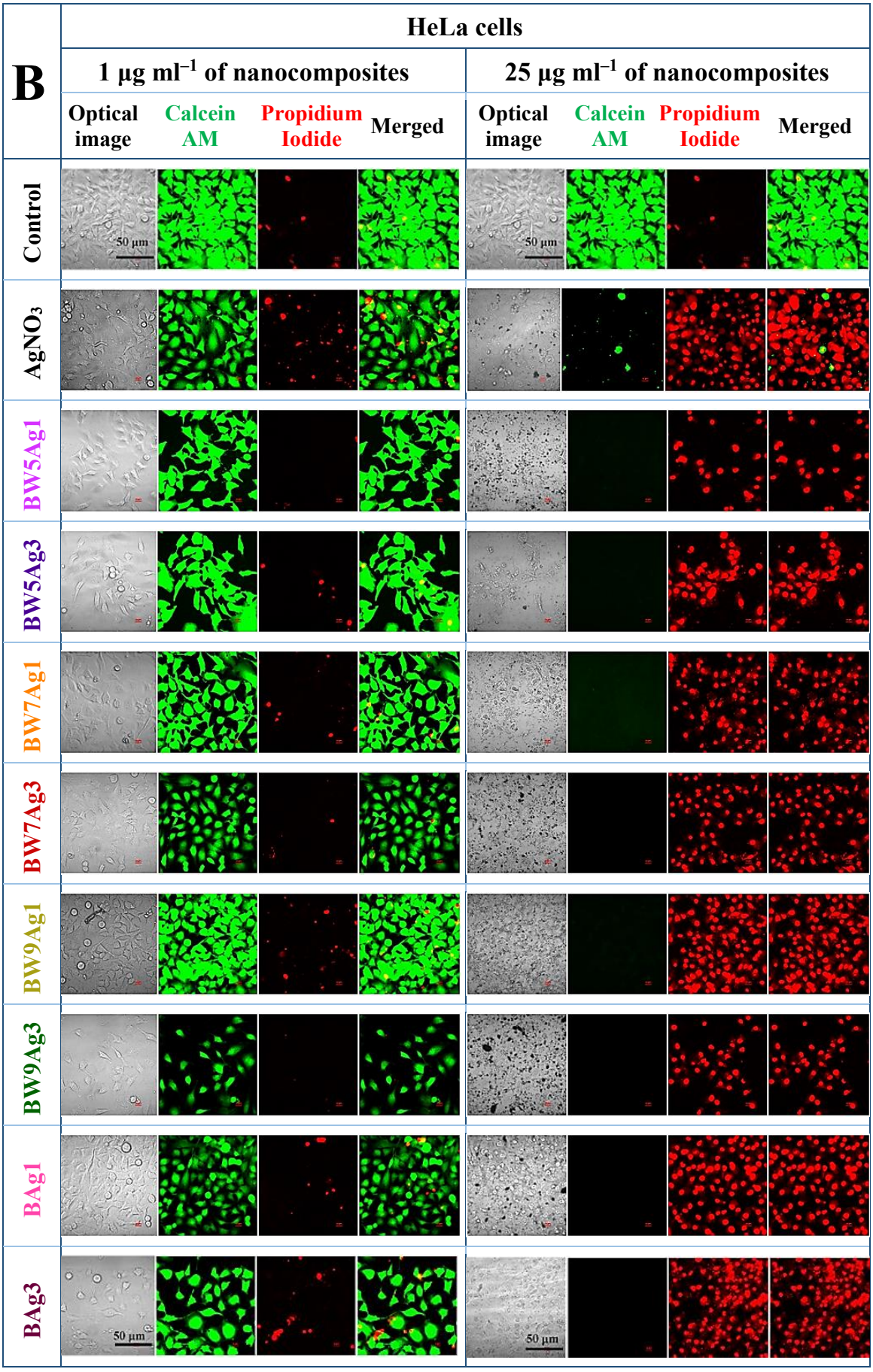

Figure 3.11 Confocal images of A) normal HEK293 and B) HeLa cancer cells with and without treatment to $AgNO_3$ and **BW** nanocomposites at 1 μg ml^{-1} and 25 μg ml^{-1} concentration. (Syntheses conditions: 25(±1) °C → Ag1, and 80(±1) °C→ Ag3). (Scale bars: 50 μm.)

The impact of 1 μg ml^{-1} of $AgNO_3$ on HEK293 cells results in a more significant decrease in cell growth compared to nanocomposites. This indicates that nanocomposites exhibit higher biocompatibility at lower concentrations. Furthermore, at 25 μg ml^{-1} concentration, $AgNO_3$ is highly toxic, causing complete cell death, while nanocomposites display 70–90 % (observations based on images in Figure 3.11A) cytotoxicity in normal HEK293 cells. The cytotoxic response of 1 μg ml^{-1} of nanocomposites on cancerous HeLa cells showed a decrease in cell growth than control, suggesting a dominating cell growth inhibition over cell death (Figure 3.11B). Contrastingly at 25 μg ml^{-1} of nanocomposites, prominent 95–100 % cell death of HeLa cells was observed. This clearly indicates that two different phenomena occur when nanocomposites interact with HEK293 and HeLa cells at different concentrations.

3.3.2 LDH assay

The relationship between the percentage of disrupted cells, compared to control (determined by LDH assay), and the concentration of **BW** nanocomposites synthesized at 25(±1) °C and 80(±1) °C is shown in Figure 3.12. LDH is an enzyme present in living cells, and its release signifies cell membrane damage or destruction. The measurement of LDH activity is proportional to the number of damaged cells.

A similar LDH activity trend was exhibited by all the nanocomposites on all tested cell lines. The observed LDH activity in cells increased with increasing Ag NP concentration from 0.1 μg ml^{-1} and reached the highest activity around 4-8 μg ml^{-1} wherein a cell death of 30-60 % was observed. Interestingly, further increase in Ag NP concentration up to 50 μg ml^{-1} caused a gradual drop to 0 % in the LDH activity signifying a decreasing number of damaged cells. Contrastingly, the images obtained in confocal microscopy as seen in Figure 3.11 exhibited 50-100 % cell death at higher concentrations (25 μg ml^{-1}) of NP. The reason for these uncorrelated results at higher NP concentration is growth inhibition eventually leading to cell death. Due to extensive growth inhibition, fewer cells were present in higher-concentration Ag NP-treated samples. Therefore, the total number of cells was in the order of control>lower concentration treated cells> higher concentration treated cells. Consequently, the LDH signal obtained for samples treated with the higher NP concentrations was lower than the control even in cases where NPs caused complete cell disruption.

LDH DATA

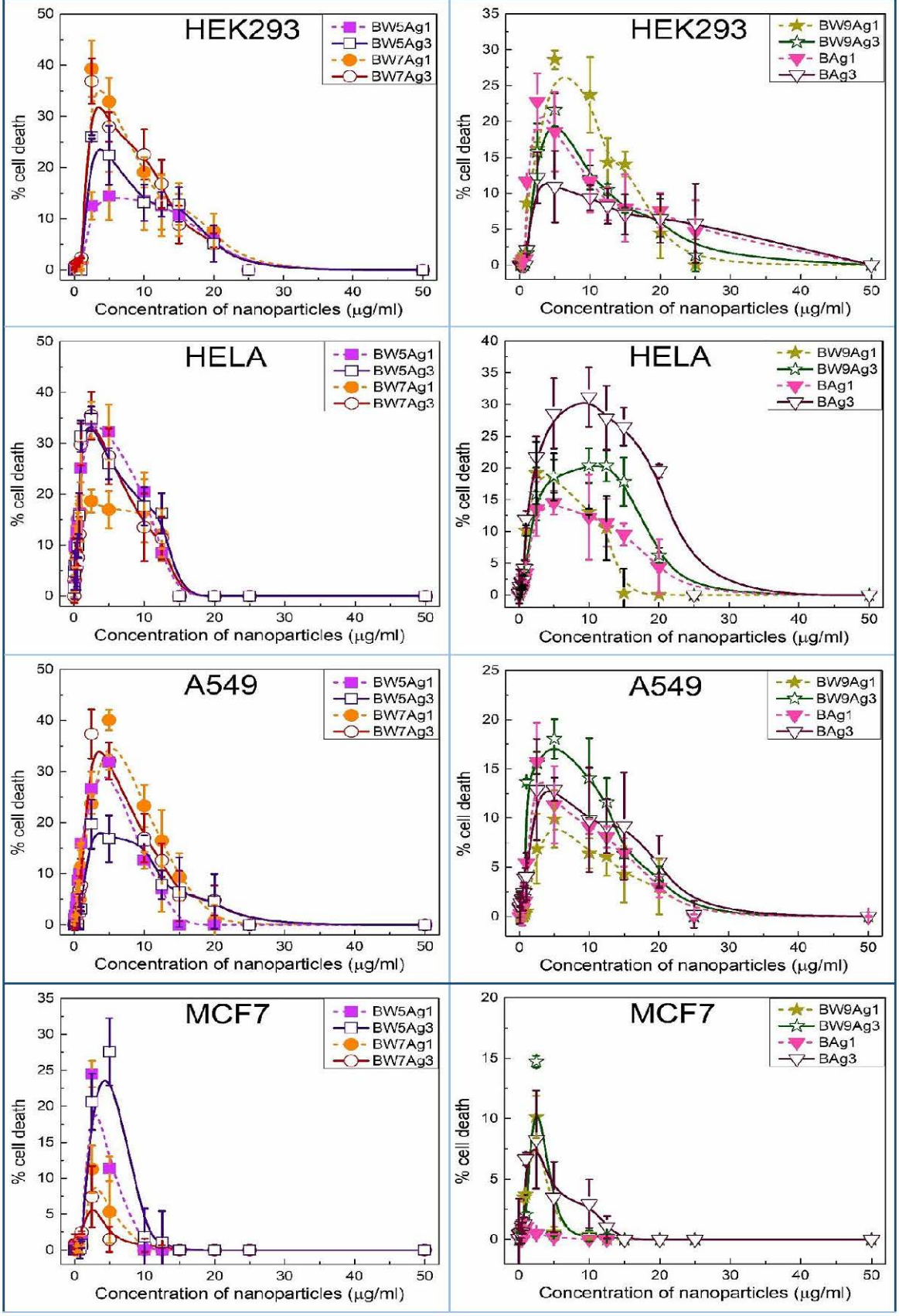

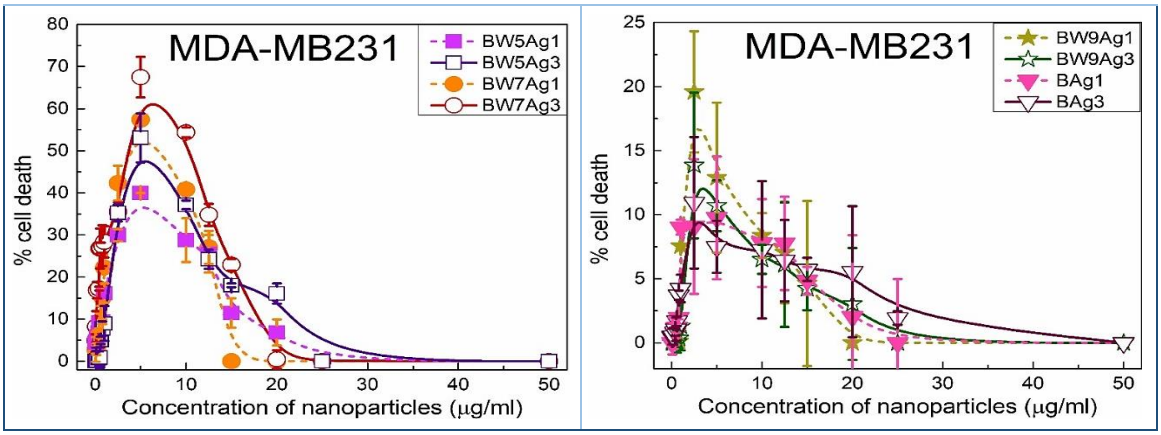

Figure 3.12 Dependence of percent of cell death of normal (HEK293) and different cancer cells by LDH assay on the concentration of **BW** nanocomposites synthesized at 25(±1) °C and 80(±1) °C. (Syntheses conditions: 25(±1) °C → Ag1, and 80(±1) °C→ Ag3).

At lower NP concentrations the treated cells exhibited inhibition of cell proliferation which is in accordance with confocal microscopy observation (Figure 3.11). Such behavior confirms the complex cytotoxicity caused by nanocomposites. Furthermore, **BW7** and **BW5** nanocomposites exhibited relatively higher LDH activity indicating that the cell growth decreases more slowly with increasing concentration compared to **BW9** and **B** nanocomposites. Similar concentrations of all nanocomposites (3–5 μg ml^{-1}) were required to achieve maximum LDH activity (30–70 % cell death). Nanocomposites synthesized at 25(±1) °C (**BW5Ag1**, **BW7Ag1**, **BW9Ag1** and **BAg1**) affected the growth rate more rapidly, resulting in maximum growth inhibition (0 % LDH activity) at lower concentrations (15–25 μg ml^{-1}).

3.3.3 MTT assay

The MTT assay was performed to observe the cytotoxic response of cells to nanocomposites, and the calculated cell death induced by nanocomposites at different concentration ranges was plotted (Figures 3.13) and fitted using the Origin software's the BiDoseResponse function (Figures 3.14). This analysis was performed because the silver nanocomposites displayed a complex bi-phase cytotoxicity mechanism. The half-maximal effective concentration (EC_{50}) was evaluated for each nanocomposite's dose-response relationship (Figure 3.14 and Table 3.7). In a pharmacological context, EC_{50} refers to the concentration of a drug required for 50% cell viability or cell death in a specific cell line under investigation. Since a complex two-phase mechanism of cell toxicity was observed, separate EC_{50} values were determined for each phase and subsequently compared for all studied cell lines (Figure 3.15, and Table 3.7). The biphasic responses observed were both inhibitory phases. This type of response is rarely observed contrary to the commonly observed hormetic dose response.

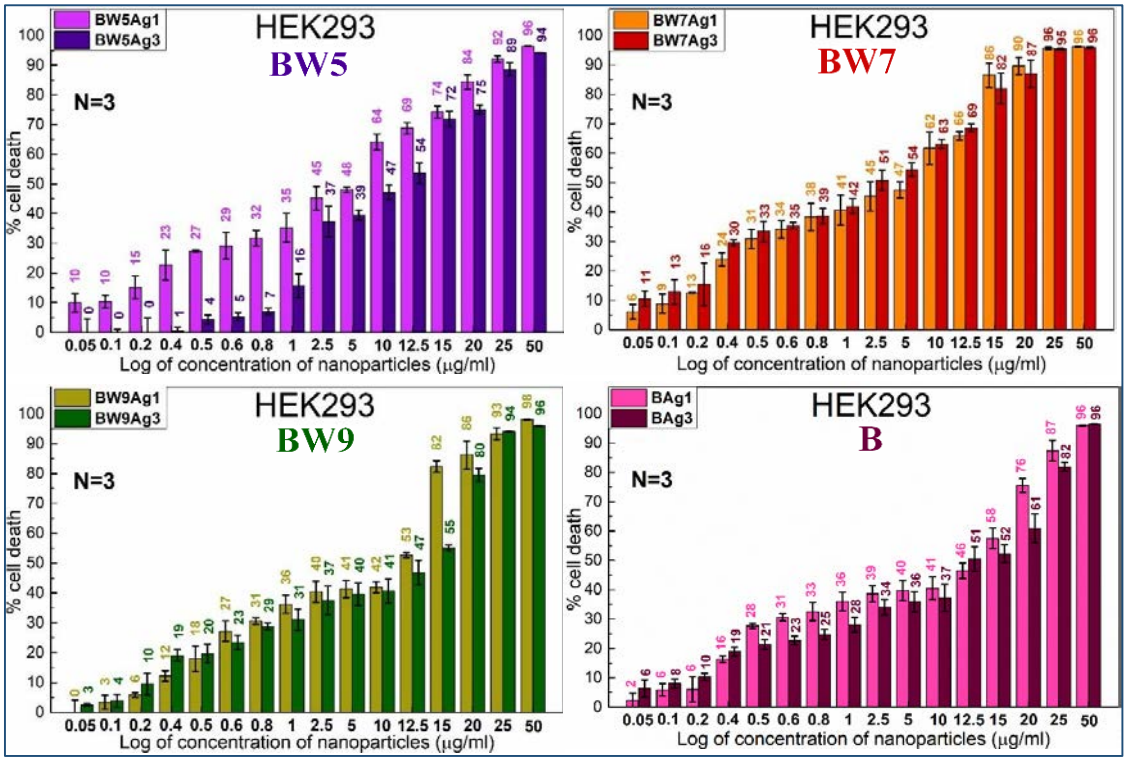

Figure 3.13a Cytotoxic dose-response curves analyzed using MTT assay for **BW5**, **BW7**, **BW9**, and **B** nanocomposites synthesized at 25(±1) °C and 80(±1) °C on HEK293 cells. (Syntheses conditions: 25(±1) °C → Ag1, and 80(±1) °C→ Ag3).

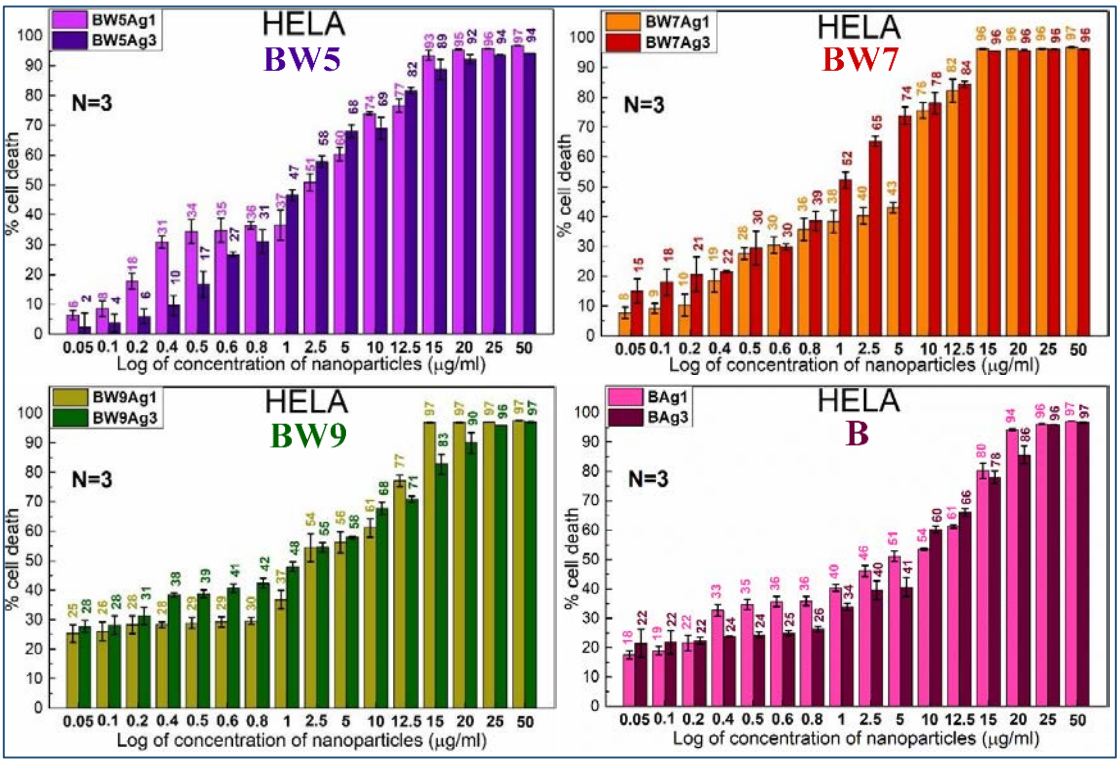

Figure 3.13b Cytotoxic dose-response curves analyzed using MTT assay for **BW5**, **BW7**, **BW9**, and **B** nanocomposites synthesized at 25(±1) °C and 80(±1) °C on HeLa cells. (Syntheses conditions: 25(±1) °C → Ag1, and 80(±1) °C→ Ag3).

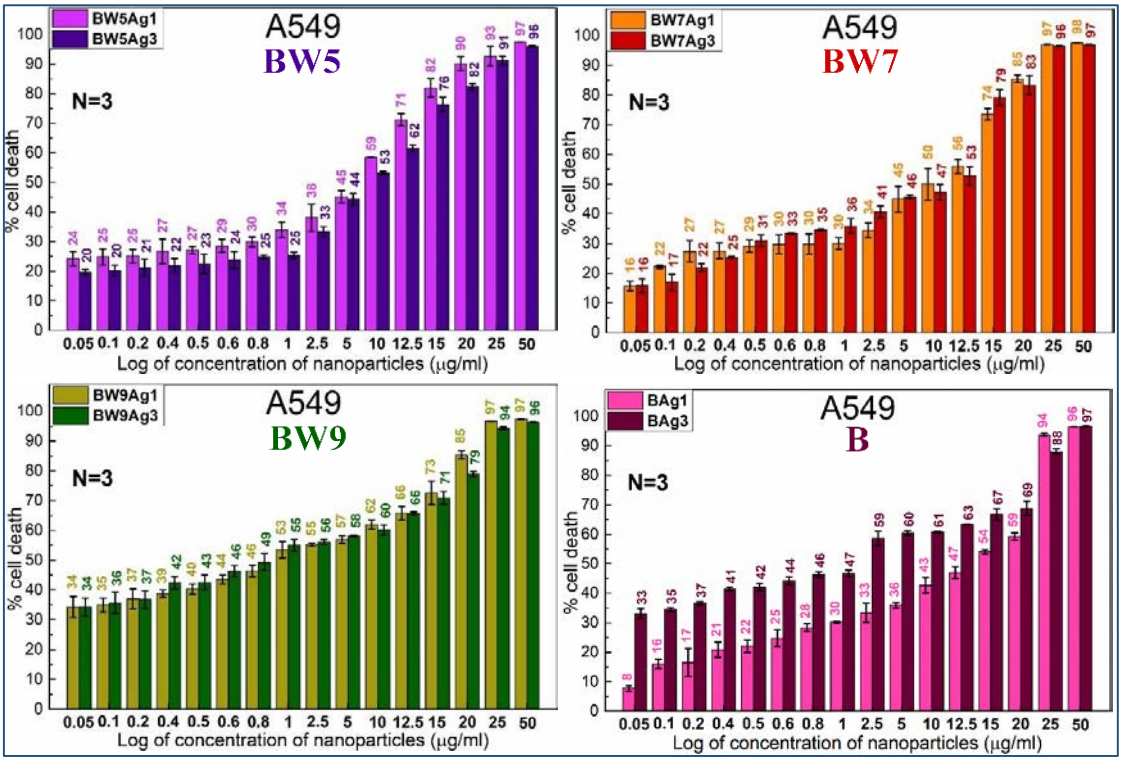

Figure 3.13c Cytotoxic dose-response curves analysed using MTT assay for **BW5**, **BW7**, **BW9** and **B** nanocomposites synthesized at 25(±1) °C and 80(±1) °C on A549 cells. (Syntheses conditions: 25(±1) °C → Ag1, and 80(±1) °C→ Ag3).

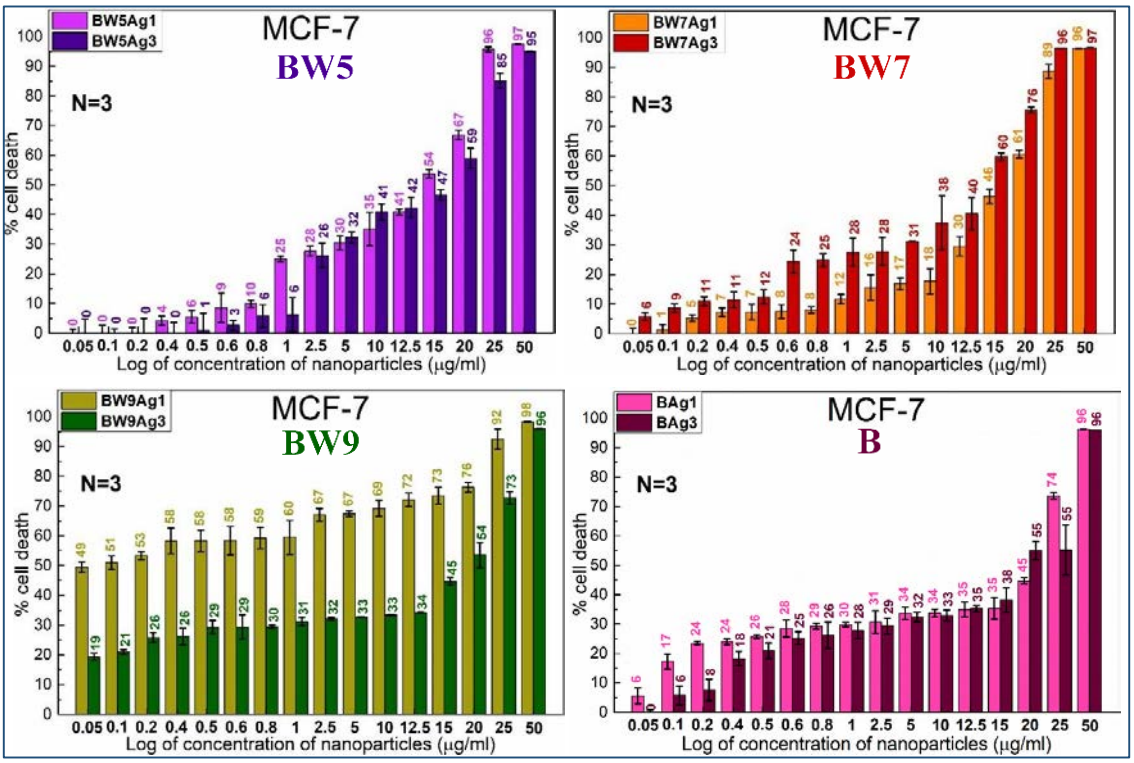

Figure 3.13d Cytotoxic dose-response curves analysed using MTT assay for **BW5**, **BW7**, **BW9** and **B** nanocomposites synthesized at 25(±1) °C and 80(±1) °C on MCF-7 cells. (Syntheses conditions: 25(±1) °C → Ag1, and 80(±1) °C→ Ag3).

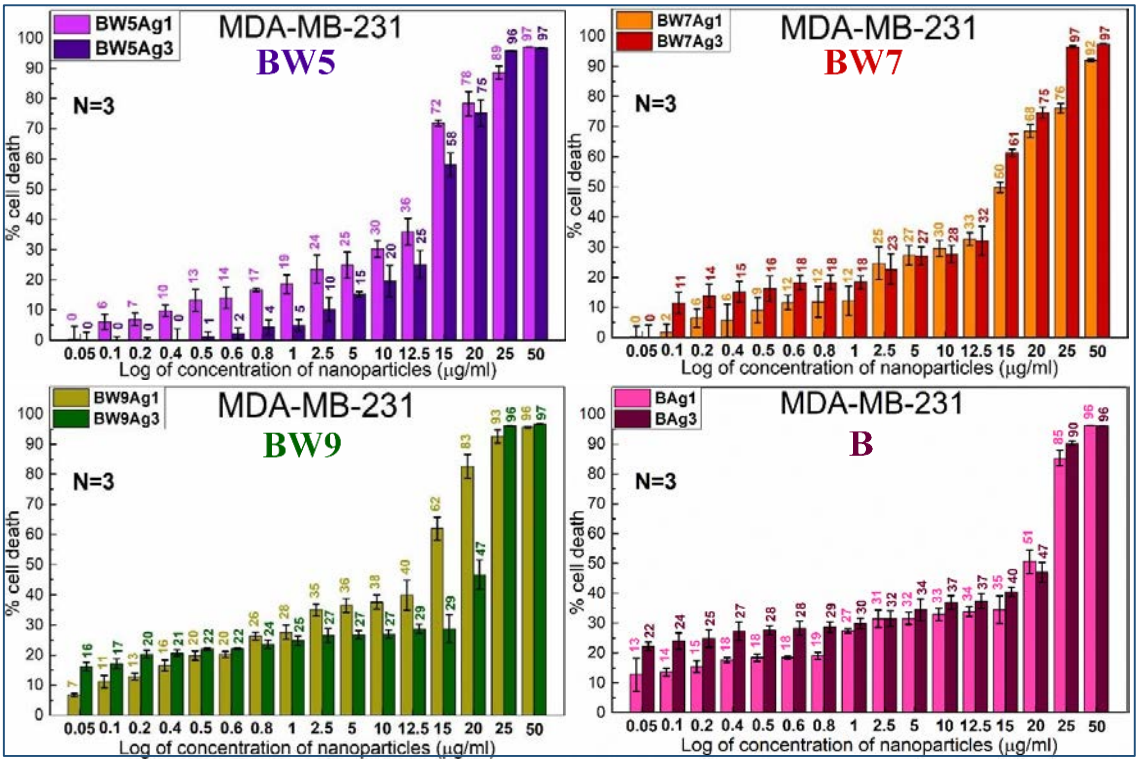

Figure 3.13e Cytotoxic dose-response curves analyzed using MTT assay for **BW5**, **BW7**, **BW9** and **B** nanocomposites synthesized at 25(±1) °C and 80(±1) °C. on MDA-MB-231 cells (Syntheses conditions: 25(±1) °C → Ag1, and 80(±1) °C→ Ag3).

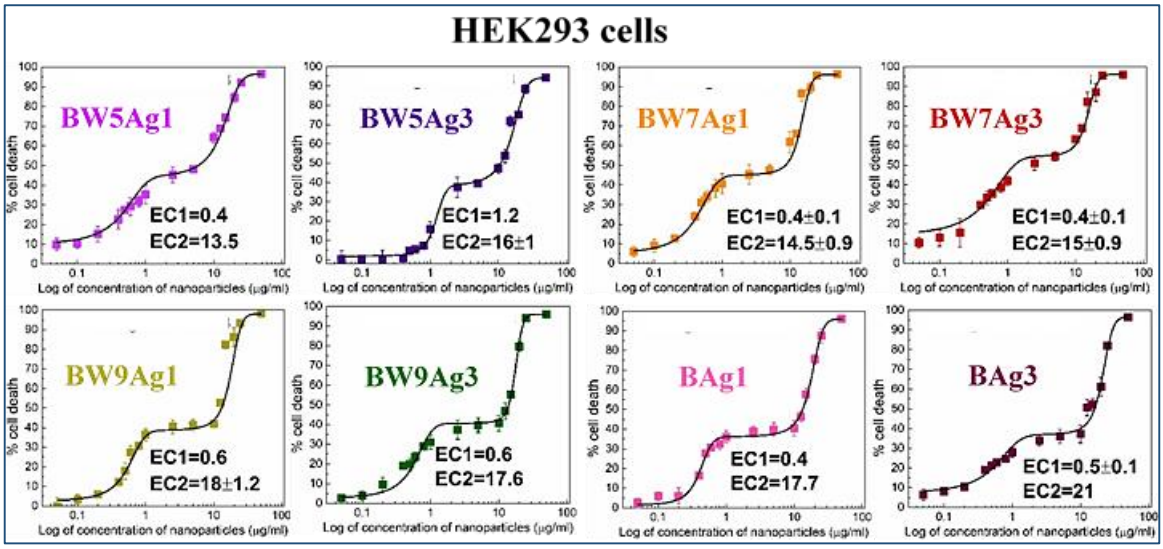

Figure 3.14a Fitted cytotoxic dose-response curves of MTT assay data and EC_{50} values obtained for **BW5**, **BW7**, **BW9**, and **B** nanocomposites synthesized at 25(±1) °C and 80(±1) °C on HEK293 cells. (Syntheses conditions: 25(±1) °C → Ag1, and 80(±1) °C→ Ag3).

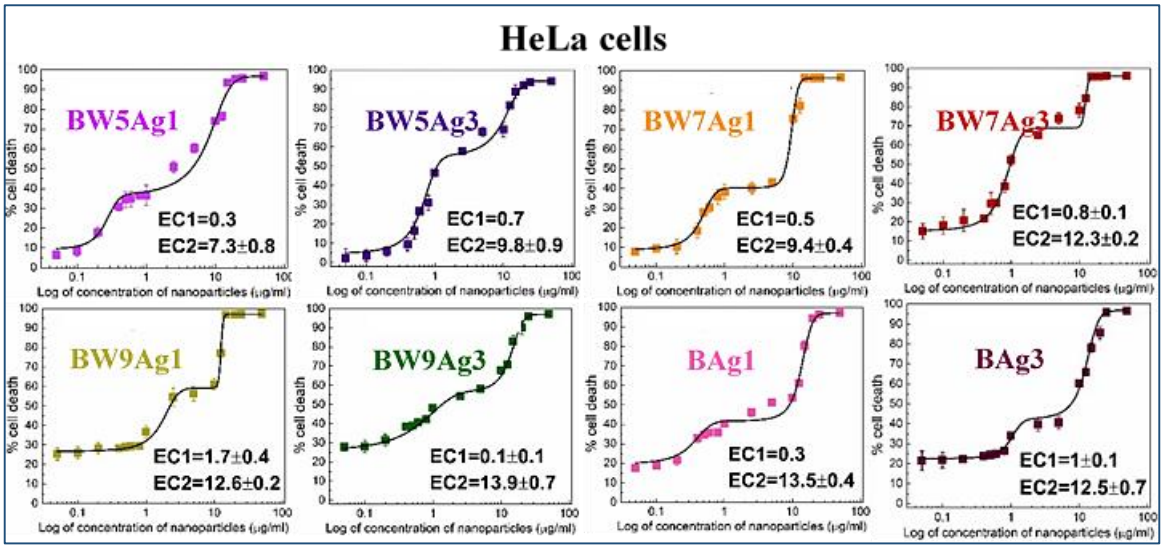

Figure 3.14b Fitted cytotoxic dose-response curves of MTT assay data and EC_{50} values obtained for **BW5**, **BW7**, **BW9**, and **B** nanocomposites synthesized at 25(±1) °C and 80(±1) °C HeLa cells. (Syntheses conditions: 25(±1) °C → Ag1, and 80(±1) °C→ Ag3).

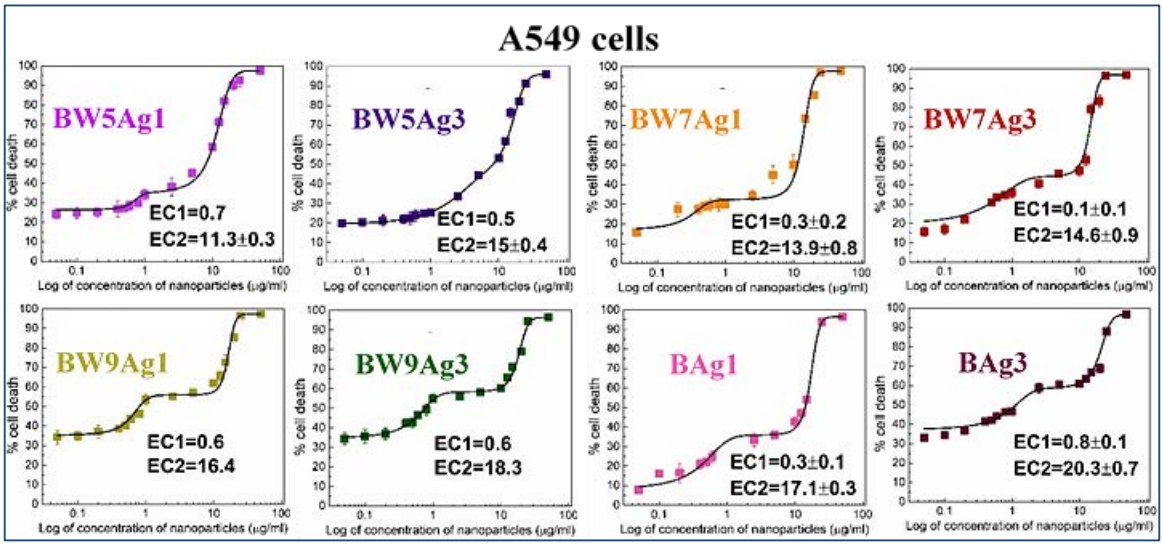

Figure 3.14c Fitted cytotoxic dose-response curves of MTT assay data and EC_{50} values obtained for **BW5**, **BW7**, **BW9**, and **B** nanocomposites synthesized at 25(±1) °C and 80(±1) °C on A549 cells. (Syntheses conditions: 25(±1) °C → Ag1, and 80(±1) °C→ Ag3).

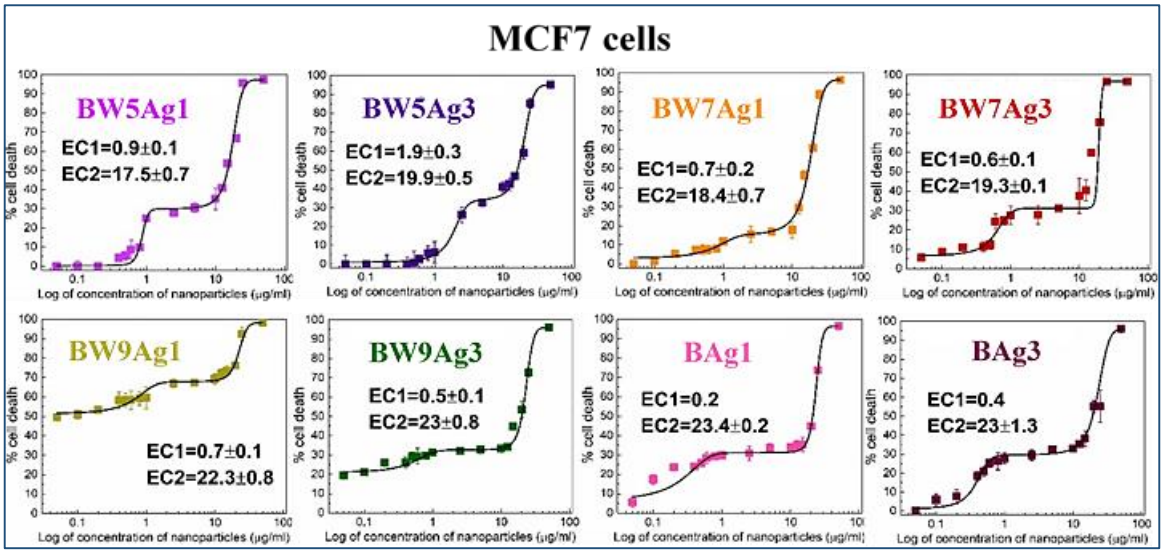

Figure 3.14d Fitted cytotoxic dose-response curves of MTT assay data and EC_{50} values obtained for **BW5**, **BW7**, **BW9**, and **B** nanocomposites synthesized at 25(±1) °C and 80(±1) °C on MCF-7 cells. (Syntheses conditions: 25(±1) °C → Ag1, and 80(±1) °C→ Ag3).

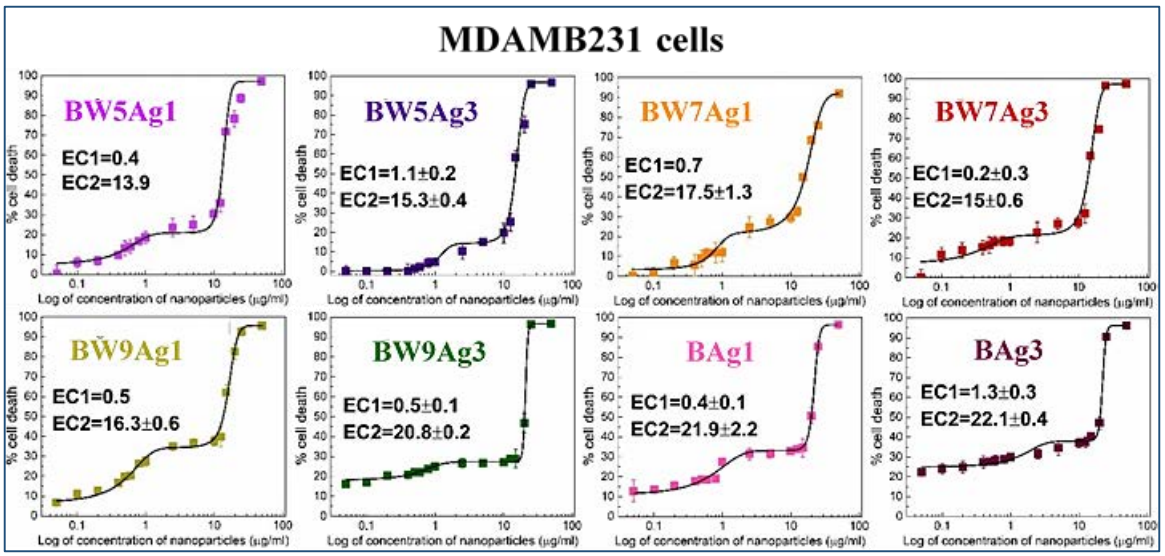

Figure 3.14e Fitted cytotoxic dose-response curves of MTT assay data and EC_{50} values obtained for **BW5**, **BW7**, **BW9**, and **B** nanocomposites synthesized at 25(±1) °C and 80(±1) °C on MDA-MB-231 cells. (Syntheses conditions: 25(±1) °C → Ag1, and 80(±1) °C→ Ag3).

Table 3.7 EC_{50} values of **BW** nanocomposites synthesized at 25(±1) °C → Ag1, and 80(±1) °C→ Ag3 on different cell lines.

Cell line/ Sample	EC_{50} (µg ml^{-1})									
	HEK293		HeLa		A549		MCF-7		MDA-MB-231	
	1st phase	2nd phase	1st phase	2nd phase	1st phase	2nd phase	1st phase	2nd phase	1st phase	2nd phase
BW5Ag1	0.4	13.5	0.3	7.3±0.8	0.7	11.3±0.3	0.9±0.1	17.5±0.7	0.3	13.9
BW5Ag3	1.2	16±1	0.7	9.8±0.9	0.5	15±0.4	1.9±0.1	19.9±0.5	1.1±0.2	15.30.4
BW7Ag1	0.4±0.1	14.5±0.9	0.5	9.4±0.4	0.3±0.2	13.9±0.8	0.7±0.2	18.4±0.7	0.7	17.5±1.3
BW7Ag3	0.4±0.1	15±0.9	0.8±0.1	12.3±0.2	0.1±0.1	14.6±0.9	0.6±0.1	19.3±0.1	0.2±0.3	15±0.6
BW9Ag1	0.6	18±1.2	1.7±0.4	12.6±0.2	0.6	16.4	0.7±0.1	22.3±0.8	0.5	16.3±0.6
BW9Ag3	0.6	17.6	0.1±0.1	13.9±0.7	0.6	18.3	0.5±0.1	23±0.8	0.5±0.1	20.8±0.2
BAg1	0.4	17.7	0.3	13.5±0.4	0.3±0.1	17.1±0.3	0.2	23.4±0.2	0.4±0.1	21.9±2.2
BAg3	0.5±0.1	21	1±0.1	12.5±0.7	0.8±0.1	20.3±0.7	0.4	23±1.3	1.3±0.3	22.1±0.4

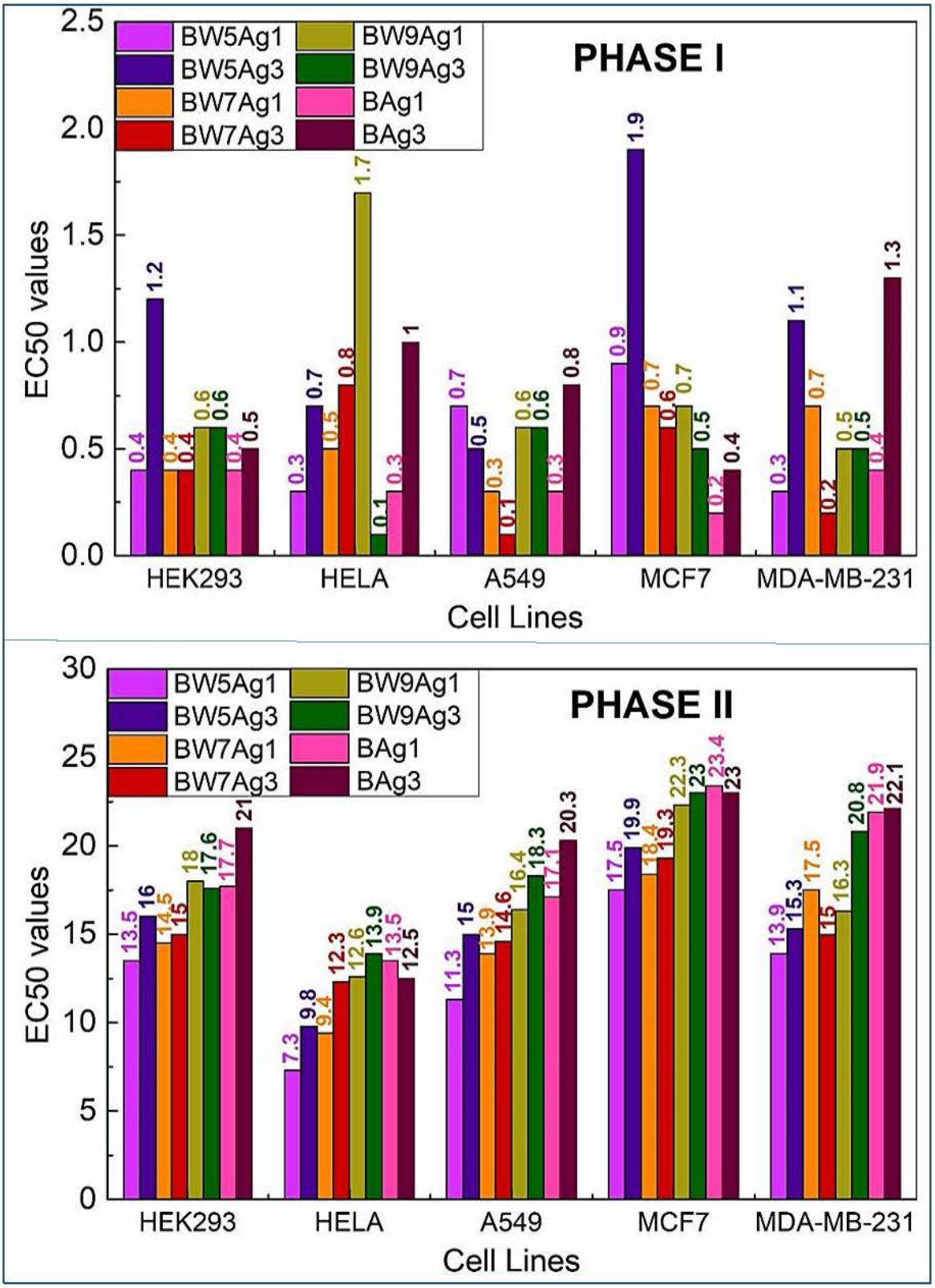

Figure 3.15 Comparison of EC_{50} values (μg ml^{-1}) for phase I and phase II of **BW5**, **BW7**, **BW9**, and **B** nanocomposites synthesized at 25(±1) °C and 80(±1) °C on different cell lines. (Syntheses conditions: 25(±1) °C → Ag1, and 80(±1) °C→ Ag3).

The biocompatibility of the nanocomposites was assessed using the MTT assay on the HEK293 cell line (Figure 3.13–3.15). A higher cell viability indicates greater biocompatibility of the substance towards the cell line. EC_{50} values for phase I of HEK293 (Figure 3.15) were compared and found that the **BW5Ag3** nanocomposites exhibited higher biocompatibility compared to other nanocomposites. For phase II, the **BAg3** nanocomposite demonstrated the highest biocompatibility towards HEK293 compared to other nanocomposites. **BW5Ag3**, **BW7Ag3**, and **BAg3** nanocomposites demonstrated higher cell viability compared to **BW5Ag1**, **BW7Ag1**, and **BAg1** respectively, while **BW9Ag1** and **BW9Ag3** showed almost similar biocompatibility. This suggests that for phase II response, nanocomposites synthesized at 80(±1) °C (**BW5Ag3**, **BW7Ag3**, **BW9Ag3**, and **BAg3**) are more biocompatible than those synthesized at 25(±1) °C (**BW5Ag1**, **BW7Ag1**, **BW9Ag1**, and **BAg1**) (Figure 3.15). Overall, **BAg3** nanocomposite was the most biocompatible while **BW5Ag1** was the least biocompatible towards HEK293 cells.

To evaluate the biocompatibility of a material for medical applications, the cytotoxicity induced by the material should be tested, and its EC_{50} value should be lower for cancerous cells (HeLa, A549, MCF-7, and MDA-MB-231 cell lines) compared to normal cells (HEK293 cells) (Figure3.15). Analyzing the phase I EC_{50} values, it was found that **BW5Ag1**, **BW9Ag3**, and **BAg1** induced cell growth inhibition at very low concentrations in HeLa cells, **BW7Ag3** in A549 cells, **BAg1** in MCF-7 cells, and **BW7Ag3** in MDA-MB-231 cells, making them more toxic compared to other nanocomposites. Considering the phase II of cell toxicity, in general, the nanocomposites synthesized at 25(±1) °C (**BW5Ag1**, **BW7Ag1**, **BW9Ag1**, and **BAg1**) exhibited higher cytotoxicity, with increased cell death at lower concentrations compared to the nanocomposites synthesized at 80(±1) °C (**BW5Ag3**, **BW7Ag3**, **BW9Ag3**, and **BAg3**). All nanocomposites induced toxicity in HeLa and A549 cells at lower concentrations than MCF-7 and MDA-MB-231 cell lines. Moreover, **BW5Ag1** exhibited higher toxicity to all cell lines compared to other nanocomposites.

Therefore, the nanocomposites exhibited a biphasic cytotoxicity towards normal HEK293, and cancerous (HeLa, A549, MCF-7, and MDA-MB293) cell lines, with both phases being inhibitory. In conclusion from all three assays namely live/dead, LDH, and MTT it was found that during the initial phase (at lower concentrations), cell inhibition is the dominant mechanism, while during the subsequent phase (at higher concentrations), cell destruction became the prevailing mechanism after a certain level of cell inhibition (~ 40–50 %) was achieved.

3.4 Bacterial susceptibility testing

The bacterial susceptibility test was performed against *E. coli* for nanocomposites synthesized at 25(±1) °C (**BW5Ag1**, **BW7Ag1**, **BW9Ag1**, and **BAg1**) and 80(±1) °C (**BW5Ag3**, **BW7Ag3**, **BW9Ag3**, and **BAg3**) [100, 101].

3.4.1 MIC/ MBC determination

The nanocomposites synthesized at different temperatures exhibited varying effects on bacterial growth inhibition. Specifically, the nanocomposites synthesized at 25(±1) °C demonstrated stronger antibacterial activity against the *E. coli* bacterial strain compared to those synthesized at 80(±1) °C, as shown in Table 3.8. These nanocomposites were selected for testing due to their diverse compositions.

For instance, **BW5Ag1** and **BW9Ag1**, synthesized at 25(±1) °C, were slightly more effective in inhibiting bacterial growth than their counterparts **BW5Ag3** and **BW9Ag3**, synthesized at 80(±1) °C respectively. Additionally, **BAg1** nanocomposite was significantly more lethal to *E. coli* as compared to **BAg3**. Interestingly, despite the difference in synthesis temperature, the minimum inhibitory concentration (MIC) of **BW7Ag1** and **BW7Ag3** nanocomposites was determined to be 9.375 µg ml^{-1} (Table 3.8), indicating a similar threshold for these specific nanocomposites regardless of synthesis temperature.

Table 3.8 Minimum inhibitory concentration (MIC) of **BW5**, **BW7**, **BW9**, and **B** nanocomposites synthesized at 25(±1) °C, and 80(±1) °C. (Syntheses conditions: 25(±1) °C → Ag1, and 80(±1) °C→ Ag3).

Sample	MIC (µg ml^{-1})†
BW5Ag1	12.5
BW5Ag3	15.625
BW7Ag1	9.375
BW7Ag3	9.375
BW9Ag1	15.625
BW9Ag3	18.75
BAg1	15.625
BAg3	25

† MIC values against *Escherichia coli*

BW5 nanocomposite at 25(±1) °C (**BW5Ag1**) completely killed the tested bacteria at MIC (Figure 3.16a). Therefore, at 12.5 µg ml^{-1}, no colonies were observed on agar plates even after 24 hours of contact between nanoparticles and the bacterial inoculum. However, at concentrations lower than 12.5 µg ml^{-1}, the nanocomposite inhibition capacity is unable to out-pace the bacteria growth beyond 8 hours. Contrastingly, the **BW5** nanocomposite at 80(±1) °C (**BW5Ag3**) only marginally inhibited the bacterial growth at MIC concentration (12.5 µg ml^{-1}) (Figure 3.16b). The **BW5Ag3** nanocomposite killed the inoculum only at a much higher concentration of 15.635 µg ml^{-1}, indicating that this nanocomposite synthesized at a higher temperature using **BW5** has the least antimicrobial activity. The sub-MIC concentration time-kill curves for all nanocomposites indicate that they are able to inhibit bacterial growth for up to 8 hours; however, they are out-paced by the bacterial cell reproduction speed.

BW7 nanocomposites (**BW7Ag1** and **BW7Ag3**) at MIC concentration (9.375 µg ml^{-1}) inhibited bacterial growth entirely up to 12 hours, and then slight growth was observed between 12 and 24 hours (Figure 3.16 c–d). It could indicate a tolerance developed in the bacterial strain to the nano-particles or the inability of the nanoparticles to continue the inhibition mechanism.

At MIC, nanocomposites inhibit bacterial growth until 12 hours, then slight growth is seen between 12 and 24 hours except for **BW9Ag1** (Figure 3.16e). However, at sub-MIC, the inhibition capacity of **BW9Ag1** and **BAg1** is adequate for 8 hours, completely inhibiting the bacterial growth, while **BW9Ag3** and **BAg3** partially inhibit the growth till 12 hours (Figure 3.16 e–h). After 12 hours, the inhibition potency of nanocomposites stops, and bacteria regrows. The MIC of nanocomposites synthesized at 80(±1) °C (**BW9Ag3** and **BAg3**) is higher than nanocomposites synthesized at 25(±1) °C (**BW9Ag1** and **BAg1**), suggesting antimicrobial activity is inversely related to the synthesis temperature (Figure 3.16 e–h). Subsequently, it can be concluded that antimicrobial activity is strongly affected by the presence of Ag_3PO_4 and AgCl phases in the nanocomposites. The nanocomposites synthesized at 25(±1) °C contain higher amounts of these phases than those synthesized at 80(±1) °C and, therefore, exhibit better antibacterial activity. This observation ultimately suggests that Ag^+ ions release is the primary factor responsible for the antibacterial activity of the nanocomposites.

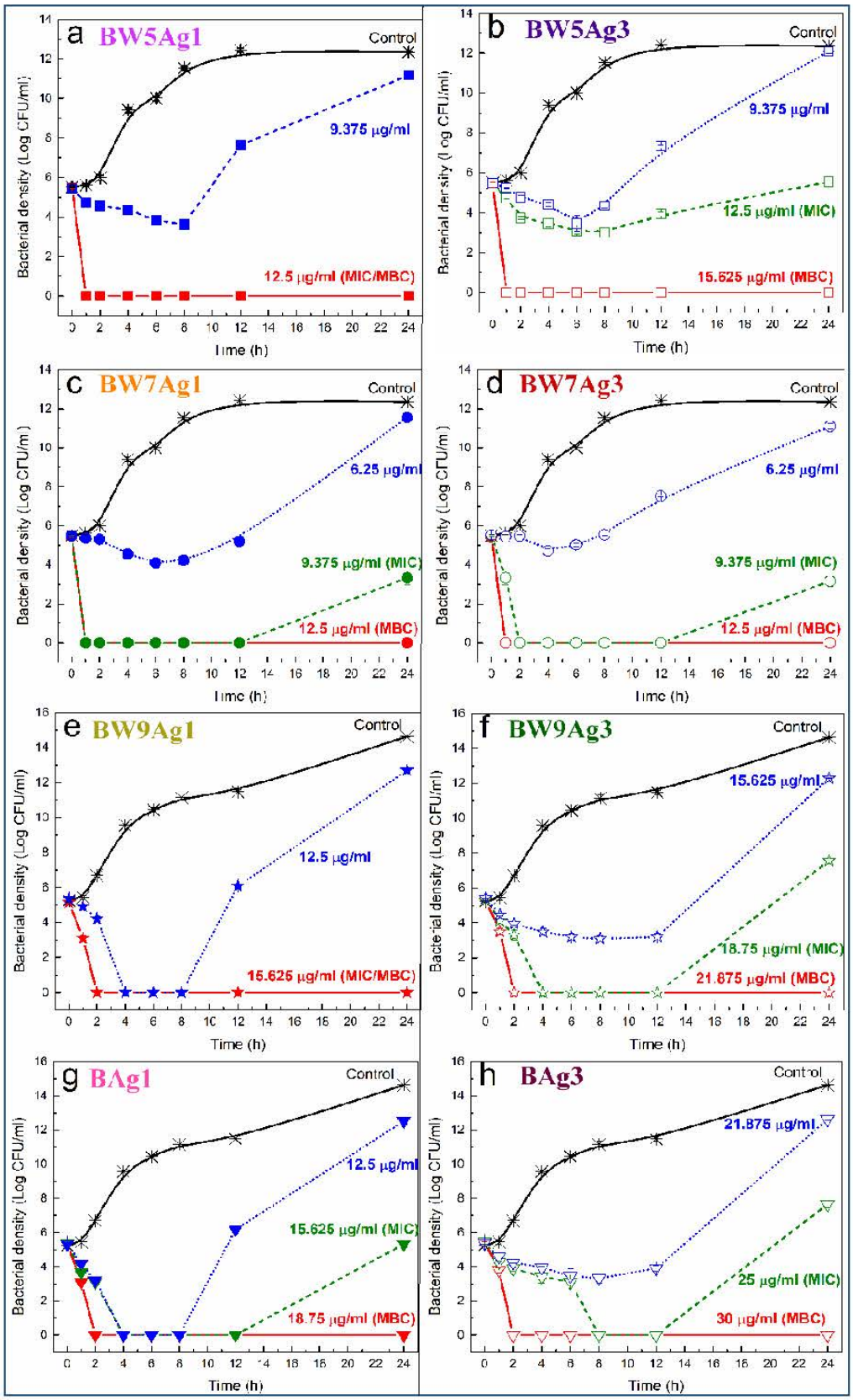

Figure 3.16 Time-kill curves obtained for *E. coli* exposed to different concentrations of **BW5**, **BW7**, **BW9**, and **B** nanocomposites synthesized at 25(±1) °C and 80(±1) °C. (Syntheses conditions: 25(±1) °C → Ag1, and 80(±1) °C→ Ag3).

3.4.2 Time-kill kinetics

Time-kill kinetics indicated the rate at which the nanocomposites affect the bacterial strain *E. coli* (Figure 3.17). Low-temperature synthesis has led to more potent nanocomposites for antibacterial activity. The nanocomposites **BW7Ag1** and **BW5Ag1** take up to 1 hour to kill the inoculum at MIC concentrations (Figure 3.17a). The **BW7Ag3** nanocomposite takes 2 hours to kill, and the **BW5Ag3** nanocomposite does not exhibit complete killing even after 2 hours of contact time (Figure 3.17a). This indicates that **BW7Ag1** affects the bacteria at the fastest rate. At MIC, the **BW9Ag1** and **BAg1** nanocomposites affect the *E. coli* bacterial strain faster than **BW9Ag3** and **BAg3** nanocomposites (Figure 3.17c). At minimum bactericidal concentration (MBC), **BW7** nanocomposites kill the bacteria after 30 minutes, **BW5Ag1** kills after 1 hour and **BW5Ag3**, **BW9**, and **B** nanocomposites kill after a 2-hour incubation (Figure 3.17 b and d). Thus, **BW7Ag1** and **BW7Ag3** nanocomposites affect at a faster rate as compared to all other **BW** nanocomposites (Figure 3.17 b and d).

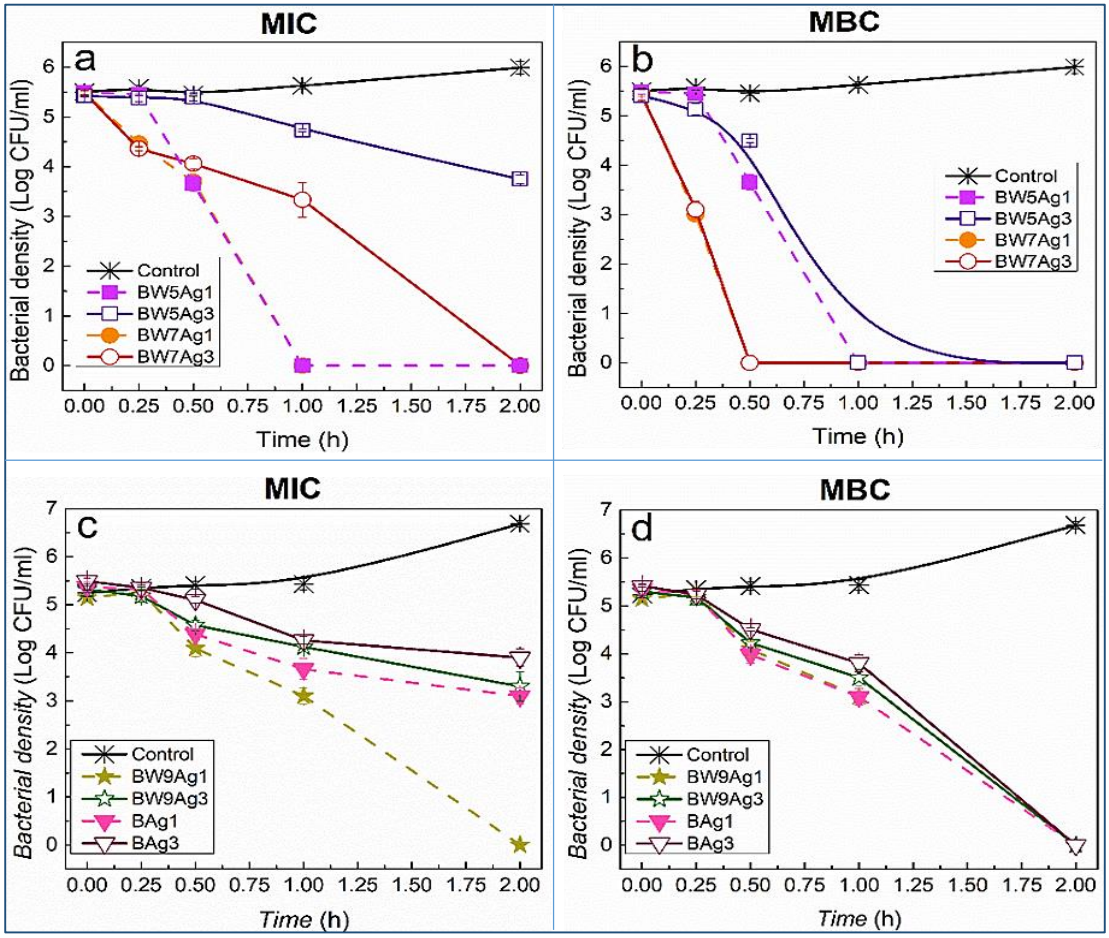

Figure 3.17 Time-kill kinetics obtained for *E. coli* exposed to (a,c) MIC and (b,d) MBC concentrations of **BW5**, **BW7**, **BW9** and **B** nanocomposites synthesized at 25(±1) °C and 80(±1) °C. (Syntheses conditions: 25(±1) °C → Ag1, and 80(±1) °C→ Ag3).

3.5 Discussion

❖ Brewery wastes and beer

Brewery waste from stages 5, 7 and 9 (**BW5**, **BW7**, and **BW9**), and beer (**B**), contains a variety of organic groups, including sulfates, nitrates, polyphenols, carbohydrates, and sugars (Table 3.1). These organic constituents in the brewery waste and beer, play a crucial role in the synthesis of nanocomposites, influencing their properties and functionality. Notably, they act as capping agents, stabilizing the nanoparticles by preventing agglomeration and enhancing their biocompatibility. Thus, brewery waste and beer serve a dual purpose as both synthesis precursor and capping agents for the **BW**-derived nanocomposites. Among these, the **BW9** displayed unique functional groups and had a lower overall organic content compared to **BW5**, **BW7**, and **B** extracts. These variations in organic content and functional groups among the precursors (brewery waste and beer) significantly impact the properties and performance of the synthesized nanocomposites, particularly in applications such as biomedicine or environmental remediation.

❖ Characterization of **BW** nanocomposites

Several nanocomposites were prepared using **BW5**, **BW7**, **BW9**, and **B**, by changing the temperature between (25(±1), 50(±1), and 80(±1) °C), to understand the growth mechanism. The temperature of synthesis affected the relative compositions of the three phases of silver, namely Ag_3PO_4, AgCl, and Ag_{met}, in the **BW5**, **BW7**, and **B** nanocomposites and the relative compositions of AgCl, and Ag_{met} in **BW9** nanocomposites (Table 3.2). The lack of chlorine in the **BW7** and the abundance of phosphorus-based compounds caused silver phosphate formation in majority (Table 3.1). The presence of yeast and a nitrogen-rich environment that is highly deficient in sugars can also be instrumental in the growth of silver phosphate. Contrastingly, **BW5**, **BW9** and **B** are rich in phosphorous and chlorine; therefore, competing reactions favored the growth of majorly AgCl. The spontaneous formation of AgCl results from the exchange reaction between silver nitrate and a source of halide present in the brewery wastes. Therefore, in the presence of high amounts of Cl in the **BW5**, **BW9** and **B**, AgCl is obtained in major quantities. After the formation of AgCl, the excess silver nitrate follows another exchange reaction with the phosphate source leading to Ag_3PO_4 in **BW5** and **B** nanocomposites. As the Cl content in **BW7** is very low, the major phase in **BW7** nanocomposites is predominantly Ag_3PO_4 [100, 101]. The conversion of silver salt by beer and all brewery wastes led to incorporating higher amounts of the minor contents in the nanocomposite structure with increasing synthesis temperature.

Increasing synthesis temperature led to decreasing content and increasing nanocrystallite size of major phase i.e. AgCl or Ag_3PO_4 in **BW** nanocomposites (Table 3.2). Overall silver content increases with increasing synthesis temperature (Table 3.3). Increasing synthesis temperature led to a decrease in total phosphorus content in **BW5** and **BW7** nanocomposites. Contrastingly, increasing synthesis temperature increased total phosphorus content in **BW9** and **B** nanocomposites, where it is present in trace amounts. The surface of **BW** nanocomposites consists majority of silver (40–60 wt.%), carbon content ~20–40 wt.%, and oxygen content ~10–15 wt.% (Table 3.4). These synthesized nanocomposites also exhibited a uniform distribution of elements on their surface (Figure 3.3). The overlayer has the largest thickness when the synthesis temperature is 50(±1) °C (Table 3.6). The high temperature appears to be facilitating the attachment of organic groups to the nanoparticle surface.

❖ Cytotoxicity analysis of **BW** nanocomposites

The presence of a biphasic cytotoxicity mechanism, characterized by a two-step cell cytotoxicity process dependent on the concentration of nanocomposites, was validated through the Live/Dead, LDH, and MTT assays (Figure 3.11–3.15 and Table 3.7). By examining the confocal images obtained from the live/dead assay, it was observed that lower concentrations of nanocomposites resulted in the inhibition of cell growth, while higher concentrations induced ~ 40–80 % cell death in HEK293 and nearly 100 % cell death in HeLa cells (Figure 3.11). HEK293, HeLa, A549, MCF-7 and MDA-MB-231 cell lines were used to assess the dose dependent response of nanocomposites through LDH and MTT assays. LDH activity decreased with increasing nanocomposites' concentration for all cell lines indicating the increasing cell inhibition with nanocomposites concentration (Figure 3.12). Nanocomposites synthesized at 25(±1) °C (**BW5Ag1**, **BW7Ag1**, **BW9Ag1** and **BAg1**) showed faster cell inhibition rate compared to nanocomposite synthesized at 80(±1) °C (**BW5Ag3**, **BW7Ag3**, **BW9Ag3** and **BAg3**). Importantly, the nanocomposites induced damage to cell membrane causing release of LDH from the cells. MTT results showed increase in cell death with increasing concentration of **BW** nanocomposites. MTT absorbance intensity is lower when both number of cells and their viability (metabolic activity) is lower. And these two effects are undistinguishable. Whereas LDH can sense only disrupted cells and is sensitive to the cell number. Exactly the same process can give different outcome in different assays. The similar increase in cell death at lower concentrations in both LDH and MTT supports the accuracy of data. However, with increasing concentrations of **BW** nanocomposite at higher range, increasing MTT suggests the cell death whereas decreasing LDH activity could suggest lower cell number at higher **BW** nanocomposite concentrations.

The biocompatibility of the nanocomposites was observed in the normal embryonic kidney (HEK293) cell line within a specific range, where they demonstrated toxicity towards cancer cell lines i.e., 7–23 μg ml^{-1} for HeLa, A549, MCF-7, and MDA-MB-231 cells. This conclusion was derived from the EC_{50} values obtained through the MTT assay (Figure 3.13–3.15 and Table 3.7). The nanocomposites synthesized at 80(±1) °C (**BW5Ag3**, **BW7Ag3** and **BAg3)** were found to be more biocompatible to HEK293 cells than those synthesized at 25(±1) °C (**BW5Ag1**, **BW7Ag1** and **BAg1**).

The nanocomposites were found to be more toxic toward HeLa and A549 cell lines than MCF-7 and MDA-MB-231 cell lines (Figure 3.15, and Table 3.7). All cells being similar in size, approximately 10–15 μm, and consisting of nucleic acids, lipids (including membrane phospholipids), proteins, and carbohydrates, however, the specific composition and amounts of these components may vary [78-81]. The nanocomposites synthesized at 25(±1) °C (**BW5Ag1**, **BW7Ag1**, **BW9Ag1** and **BAg1**) demonstrated enhanced cytotoxicity at lower concentration compared to the nanocomposites synthesized at 80(±1) °C (**BW5Ag3**, **BW7Ag3**, **BW9Ag3** and **BAg3**). All nanocomposites induced higher toxicity towards HeLa and A549 cells compared to MCF-7 and MDA-MB-231 cell line as MCF-7 and MDA-MB-231 cells are more resistant to cell death as compared to HeLa and A549 cells. More potent **BW5Ag1** nanocomposite exhibited a higher level of cell death at lower concentrations compared to other nanocomposites, indicating its amplified toxicity across all cell lines. This cytotoxic effect can be attributed to the presence of a significant amount of small-sized AgCl and Ag_3PO_4 in the nanocomposite. These forms of silver act as sources for Ag^+ ions, and their small size permits them to pass through size specific channels in the cell membranes. Moreover, larger sized Ag forms may potentially damage the cell membrane, resulting in toxicity. Furthermore, the surface of the **BW5Ag1** nanocomposite contains phosphorous and oxygen-rich organic groups, which weaken the electrostatic repulsion between the nanocomposite and negatively charged hydrolyzed cell constituents, thereby promoting bonding and enhanced penetration through membrane. Moreover, the larger surface area of the smaller NPs carrying a positive charge, enhances the adsorption of biomolecules and catalytic processes. This may lead to the damage or disruption of cell membranes and organelles. Also, the impact of the ORR occurring on nanocomposites on the biological activity of nanomaterials has been analyzed (paper not published), highlighting the reactive oxygen species (ROS) - H_2O_2 production by nanocomposites. The cytotoxic effects of H_2O_2 are context-dependent. While low concentrations function as signaling molecules in cell proliferation and differentiation, higher concentrations induce oxidative stress, mitochondrial dysfunction, and cell death.

In contrast to **BW5Ag1** nanocomposites, other nanocomposites showed higher EC_{50} values in phase II toxicity, indicating lower cytotoxic effects on cancer cells compared to **BW5Ag1** nanocomposites. Based on the results obtained from the live/dead, LDH, and MTT assays, the effective concentrations (EC_{50}) deduced using the MTT assay in phase I correspond to the inhibition concentration (IC_{50}), while phase II corresponds to the lethal concentrations (LC_{50}) responsible for cell death.

In summary, the average cytotoxicity of **BW** nanocomposites on the cancer cells decreases with decreasing content of AgCl, and Ag_3PO_4 forms in the nanocomposites due to lower Ag^+ ions availability, and increased oxygen-rich surface carbon groups and crystallite size. This could indicate variation in nanocomposites' surface chemical environment depending on extracts as observed previously in XPS and FTIR analyses [100, 101] and could play a significant role in biological response, therefore, it is important to study the surface of nanocomposites in depth to understand and synthesize optimized green nanocomposites for high biocompatibility and cytotoxic effects. H_2O_2 ROS generated from **BW** nanocomposites also impact the overall cytotoxicity.

❖ Bacterial susceptibility analysis of **BW** nanocomposites

The antimicrobial properties of nanocomposites synthesized at 25 °C (**BW5Ag1**, **BW7Ag1**, **BW9Ag1**and **BAg1**) and 80 °C (**BW5Ag3**, **BW7Ag3**, **BW9Ag3**and **BAg3**) were studied [100, 101]. Nanocomposites synthesized at 25 °C demonstrated superior antibacterial activity, particularly in BW9, B, and BW5, due to the higher surface content and smaller size of AgCl nanoparticles, which is the dominant phase. In contrast, nanocomposites synthesized at 80 °C contained more silver oxides and Ag–O polymer groups, leading to stronger silver binding and a thicker carbon overlayer, which slowed the release of Ag^+ ions. In B nanocomposites, Ag_3PO_4 particles were absent on the surface, limiting their antimicrobial effectiveness.

XPS analysis revealed that carbon groups (C sp^3, C=O, C sp^2, and C–OH) are essential for interacting with the negatively charged *E. coli* cell wall. Surfaces rich in oxygen but not C-bonded exhibited higher antimicrobial activity, explaining the superior performance of **BW7** and **BW5** nanocomposites compared to **BW9** and **B**. The higher antibacterial activity of **BW7** and **BW5** nanocomposites is attributed to greater surface Ag_3PO_4 content and oxygen, which enhance the release of Ag^+ ions and damage biomolecules. The **BW9** and **B** nanocomposites synthesized at 25 °C showed better activity due to fewer C sp^2 and C–OH groups on the surface.

The impact of the oxygen reduction reaction (ORR) on nanocomposites and their biological activity was also examined, emphasizing the role of H_2O_2 production in enhancing antibacterial activity (paper not published). H_2O_2 generation is the primary mechanism for antibacterial activity, as observed in H_2O_2-containing honey [173, 174]. The one-electron reduction produces radicals that damage proteins and DNA, while the two-electron reduction affects cysteine, selenium, and methionine. The catalytic reaction predominantly follows a two-electron ORR pathway via H_2O_2 intermediate formation in a neutral solution. **BW7Ag1** and **BW7Ag3** exhibited the highest antibacterial activity, despite lower Ag_3PO_4 content in **BW7Ag3**, due to a larger surface area. Lower activity in **BW5Ag1**≈ **BW5Ag3**> **BW9Ag1**≈ **BW9Ag3** nanocomposites is linked to reduced Ag_3PO_4 content and lower H_2O_2 production.

3.6 Conclusion

Brewery wastes from stages 5 (**BW5**), 7 (**BW7**), and 9 (**BW9**) of the brewing process, and beer (**B**) sourced from Jabłonowo brewery in Wólka Kosowska, Poland, were successfully valorized for the synthesis of green silver nanocomposites. The **BW5**, **BW9**, and **B** nanocomposites predominantly consist of the AgCl phase, with smaller quantities of metallic silver and Ag_3PO_4 phase. Notably, **BW9** nanocomposites completely lack the presence of the Ag_3PO_4 phase. In contrast, **BW7** nanocomposites have a dominant Ag_3PO_4 phase, a minor AgCl phase, and additionally, a minor metallic silver phase in nanocomposites synthesized at 80(±1) °C. Increasing synthesis temperature aided the growth of minor phases in the composite. The nanocomposites' surface was composed of organic groups present in the brewery wastes and beer. The resulting overlayer thickness was ~ 1.5–3 nm. Nanocomposites were biocompatible to normal HEK293 cell lines in the concentration range where they were cytotoxic to cancerous cells i.e., 7–23 μg ml^{-1} for HeLa, A549, MCF-7, and MDA-MB-231 cells. The nanocomposites showed biphasic anticancer activity based on the concentration of nanocomposites towards HeLa, A549, MCF-7, and MDA-MB-231 cell lines. The nanocomposites′ concentration-dependent biphasic phase responses observed were both inhibitory phases. The cytotoxic response of **BW5Ag1** nanocomposite synthesized using stage 5 brewery waste at 25 (±1) ℃ after 2 hours, determined using MTT assay in terms of lethal concentration (LC_{50}) for HEK293, was found to be 2× higher than for HeLa cells, and almost similar for A549 and MCF-7, and lower for MDA-MB-231 cell lines. The **BW5Ag1** nanocomposite demonstrated the highest anticancer activity, which can be attributed to several key factors. Firstly, its elevated silver content, combined with the small particle size of various silver forms, including metallic silver (Ag_{met}), silver chloride (AgCl), and silver phosphate (Ag_3PO_4), facilitated enhanced Ag^+ ion

release. These Ag^+ ions readily interact with cellular components, disrupting key biological processes within cancer cells. The presence of phosphorus further contributes to cytotoxicity. A critical factor in the cytotoxic response was the generation of reactive oxygen species (ROS), particularly hydrogen peroxide (H_2O_2). The **BW7Ag1** and **BW7Ag3** nanocomposites exhibited the highest antibacterial activity, primarily due to their elevated content of Ag_3PO_4 in a finely dispersed small-particle form. Ag_3PO_4 acts as an effective reservoir for Ag^+ ions, which interact with bacterial membranes, disrupt ion homeostasis, and induce structural damage. The nanocomposites also generated substantial amounts of ROS, which further amplified their bactericidal effects.

4. Leaf extract synthesized silver nanocomposites

This work deals with the using leaf extracts of *Malus sylvestris L.* (**LE1**), *Pinus sylvestris L.* (**LE2**), and *Sorbus aucuparia L.* (**LE3**) for preparing nanomaterials [175]. The project was initiated with the analysis of leaf extracts (Section 4.1) to understand their composition and determine the value-added compounds. Following this, the nanocomposites were synthesized and then characterized for their structure, composition, morphology and surface composition (Section 4.2). Furthermore, the anticancer activity (Section 4.3) of these materials was studied.

4.1 Leaf extract analysis

The leaf extracts of *Malus sylvestris L.* (**LE1**), *Pinus sylvestris L.* (**LE2**), *Sorbus aucuparia L* (**LE3**) were rich in nitrogen (N), potassium (K), calcium (Ca), magnesium (Mg), phosphorus (P), aluminum (Al), iron (Fe), boron (B), and manganese (Mn), and also contained trace amounts of elements such as zinc (Zn), copper (Cu), nickel (Ni), etc. (Table 4.1). Additionally, they contained significant amounts of phosphates, sulfates, nitrates, polyphenols, carbohydrates, and fermentable sugars (Table 4.1). Extracts of **LE1**, **LE2**, and **LE3** were analyzed to quantify various elements and compounds. The **LE1** extract had the highest levels of nitrogen, sulfate, nitrate, polyphenols, carbohydrates, and fermentable sugars. Conversely, the **LE2** extract had the lowest levels of nitrogen, chlorine, sulfate, nitrate, polyphenols, carbohydrates, and fermentable sugars. The **LE3** extract was rich in elements such as chlorine (Cl), calcium (Ca), potassium (K), magnesium (Mg), iron (Fe), copper (Cu), phosphorus (P), and phosphate compounds, although its content of nitrogen, sulfate, nitrate, polyphenols, carbohydrates, and fermentable sugars was lower than in **LE1** but higher than in **LE2**. The trend for carbohydrate, polyphenol, total fermentable sugar, and sulfate content in the leaf extracts was **LE1** > **LE3** > **LE2**. Notably, the chlorine content in the **LE3** extract was five times higher than in the **LE1** extract and ten times higher than in the **LE2** extract. The leaves were found to be rich in organic matter, which could aid in the reduction of metal precursors and stabilization of nanoparticles. The organic matter and elements were more abundant in the **LE1** and **LE3** extracts compared to the **LE2** extract.

Table 4.1 Content of elements and compounds in leaf extracts.

Analysis	Subtype	Units	LE1	LE2	LE3
Phosphate		mg l^{-1}	76.10±1.41	104.52±0.12	250.92±0.32
Sulfate			55.41±0.57	16.88±0.12	36.66±0.09
Nitrate			3.20±0.29	1.12±0.03	1.03±0.02
Polyphenols			8600±113.14	59.9	4440±56.57
Carbohydrates			10200±142	650±70	4050±212
Fermentable sugars	Total		3700	800	1000
	Fructose		800	<100	600
	Glucose		1400	800	300
	Maltose + sucrose		1450±71	<100	<100
	Maltotriose		<100	<100	<100
Elemental content	N	mg l^{-1}	510±12.45	126.7±2.97	182±1.98
	K		405	223	745
	Ca		178	8	936
	Cl		51	23	225
	Mg		85	19	196
	P		25	34	82
	Na		7.84	2.97	4.28
	Al		1.09	4.2	1.55
	Fe		1.54	0.8	1.97
	B		1.2	0.91	0.84
	Mn		0.36	5.83	3.18
	Zn	µg l^{-1}	568	546	404
	Cu		137	44	143
	Ni		75.5	97.7	89.6
	Cr		32.5	17	28.5
	As		5.6	0.77	11.4
	Be		≤5	≤5	≤5
	Se		≤5	≤5	≤5
	V		1.99	1.19	2.39
	Co		1.7	2.96	3.29
	Cd		0.77	0.59	1.18
	Tl		0.84	0.11	5.08

4.2 Characterization of **LE** nanocomposites

Nanocomposites were synthesized by varying the temperature of synthesis using each leaf extract **LE1**, **LE2**, and **LE3** and $AgNO_3$ as precursor.

4.2.1 Crystallography and phase analysis by X-ray diffraction (XRD)

The X-ray diffractograms revealed essential information about nanocomposites synthesized using different leaf extracts (**LE1**, **LE2**, and **LE3** extracts) at temperatures 25(±1) °C, 50(±1) °C and 80(±1) °C. The PXRD patterns showed reflexes similar to the peaks observed in **BW** nanocomposites, which are characteristic for metallic silver Ag_{met} (ICDD 98-060-4629), silver chloride AgCl (ICDD 98-005-6538) and only in **LE2** nanocomposite synthesized at 25(±1) °C and 50(±1) °C presence of silver phosphate Ag_3PO_4 (ICDD 98-002-7843) is also observed in minor amounts (Figure 4.1). These minor peaks have been disregarded in other research since they could not be positively identified. However, the presence of the Ag_3PO_4 phase was confirmed as the observed peaks can be related to the peaks obtained for Ag_3PO_4 phases in **BW** nanocomposites [100, 101].

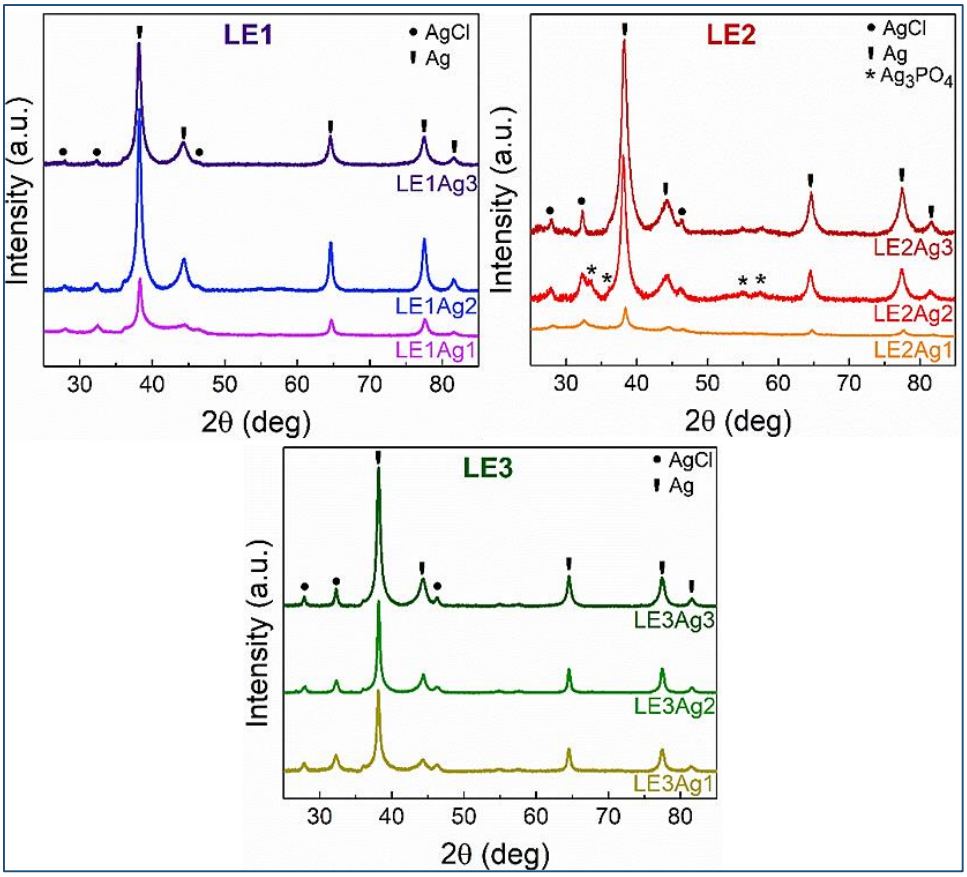

Figure 4.1 X-ray diffractograms of nanocomposites synthesized at different temperatures using **LE1**, **LE2**, and **LE3** extracts. (Syntheses conditions: 25(±1) °C → Ag1, 50(±1) °C→ Ag2, and 80(±1) °C→ Ag3).

Major Ag_{met} phase (60–90 wt.%) and minor AgCl phase (5–30 wt.%) were detected in **LE1**, **LE2** and **LE3** nanocomposites, whereas additionally minor Ag_3PO_4 phase (2–8 wt.%) was also detected in **LE2** nanocomposite synthesized at lower temperatures as 25(±1) °C and 50(±1) °C (Table 4.2). The Ag_{met} and AgCl proportions in the composite and their crystallite size change with temperature depending on the extract composition and its reducing ability to convert Ag^+ ions into Ag. Synthesis temperature affected the growth of different phases in the nanocomposite. For **LE1** nanocomposites, the Ag phase increases at the expense of the AgCl phase at 50(±1) °C and then the Ag phase slightly decreases while AgCl increases at 80(±1) °C. In **LE2** nanocomposites, the Ag phase increases at the expense of AgCl and Ag_3PO_4 with increasing synthesis temperature, while Ag_3PO_4 was present only at lower temperatures like 25(±1) and 50(±1) °C. In the case of **LE3** nanocomposites, the Ag phase increases at the expense of the AgCl phase with increasing synthesis temperature. The highest amount of AgCl and least amount of Ag_{met} was present in **LE2Ag1** and **LE2Ag2** along with some Ag_3PO_4. Formation of Ag_3PO_4 phase instead of Ag in nanocomposites synthesized using **LE2** extract at 25(±1) °C and 50(±1) °C, might be due to the least amount of polyphenols and carbohydrates and the highest ratio of phosphate to chlorine in the extract, thus decreasing the reducing efficiency of extract or lower temperatures did not aid the reduction of Ag_3PO_4 using **LE2** extract [100, 101, 175].

The Ag_{met} crystallite size in **LE1** and **LE2** nanocomposites decreased as the synthesis temperature increased (Table 4.2), signifying that the nucleation of Ag_{met} was more favorable. In contrast, for **LE3** nanocomposites, the Ag_{met} crystallite size initially increased and then decreased with rising temperature. On the contrary, the AgCl crystallite size in **LE2** and **LE3** nanocomposites increased with increasing temperature, signifying the growth of AgCl was more favorable over nucleation. For **LE1** nanocomposites, the AgCl crystallite size initially increases and then decreases with increasing temperature. **LE3** nanocomposite exhibited the largest Ag_{met} and AgCl nanocrystallite sizes, while **LE2** nanocomposite had the smallest Ag_{met} nanocrystallites of nearly similar size. The AgCl crystallite size in **LE2** nanocomposites increases with the synthesis temperature. The composition of the extracts influences the nucleation and growth rates for different phases.

Table 4.2 Phase content and crystallite size evaluated from PXRD for **LE** nanocomposites.

Sample	Synthesis temp., °C	PXRD Analysis					
		Ag Phase Content (wt.%)			Nanocrystallites Size (nm)		
		Ag_{met}	AgCl	Ag_3PO_4	Ag_{met}	AgCl	Ag_3PO_4
LE1Ag1	25	78.4	21.6	-	8.36	8	-
LE1Ag2	50	94.3	5.7	-	8	10.4	-
LE1Ag3	80	89.9	10.1	-	7.8	6.8	-
LE2Ag1	25	60.99	31.1	8	6.9	8	5.9
LE2Ag2	50	85.6	11.95	2.5	6.5	8.8	10.8
LE2Ag3	80	90.6	9.4	-	5.9	11.7	-
LE3Ag1	25	74.8	25.2	-	9.6	9.0	-
LE3Ag2	50	81.5	18.5	-	11.4	10.9	-
LE3Ag3	80	86	14	-	8.9	13.8	-

4.2.2 Elemental analysis by energy dispersive X-ray fluorescence (EDXRF) spectroscopy

The elemental analysis using EDXRF, within its detection sensitivity, revealed the presence of Ag, Cl, S, P, and Si elements in the nanocomposites (Table 4.3).

Table 4.3 Elemental composition of **LE** nanocomposites by EDXRF.

Sample	Synthesis temp., °C	EDXRF Analysis				
		Elemental Composition (wt.%)				
		Ag	Cl	P	S	Si
LE1Ag1	25	97.3	2	0.3	0.3	0.2
LE1Ag2	50	98	1	0.6	0.4	-
LE1Ag3	80	97.1	2.3	0.3	0.3	-
LE2Ag1	25	93.4	3.3	2.6	0.6	0.1
LE2Ag2	50	96.5	2	1.3	0.1	0.1
LE2Ag3	80	96.9	2.6	0.4	0.1	-
LE3Ag1	25	91.6	7.5	0.3	0.3	0.3
LE3Ag2	50	93.7	5.4	0.2	0.2	0.5
LE3Ag3	80	97.8	2	0.1	0.1	-

Synthesis temperature influenced the elemental composition of nanocomposites. As the synthesis temperature increased, Ag content increased, while Cl, S, and P generally decreased, though some deviations from this trend can be observed at 50(±1) °C. In particular, the phosphorus content in **LE2** nanocomposites decreases with increasing synthesis temperature.

This pattern of increasing Ag and decreasing P content aligns with the decreasing Ag_3PO_4 content observed in the PXRD analysis (Table 4.2).

4.2.3 Morphological analysis by scanning electron microscopy (SEM) and energy dispersive X-ray analysis (EDAX)

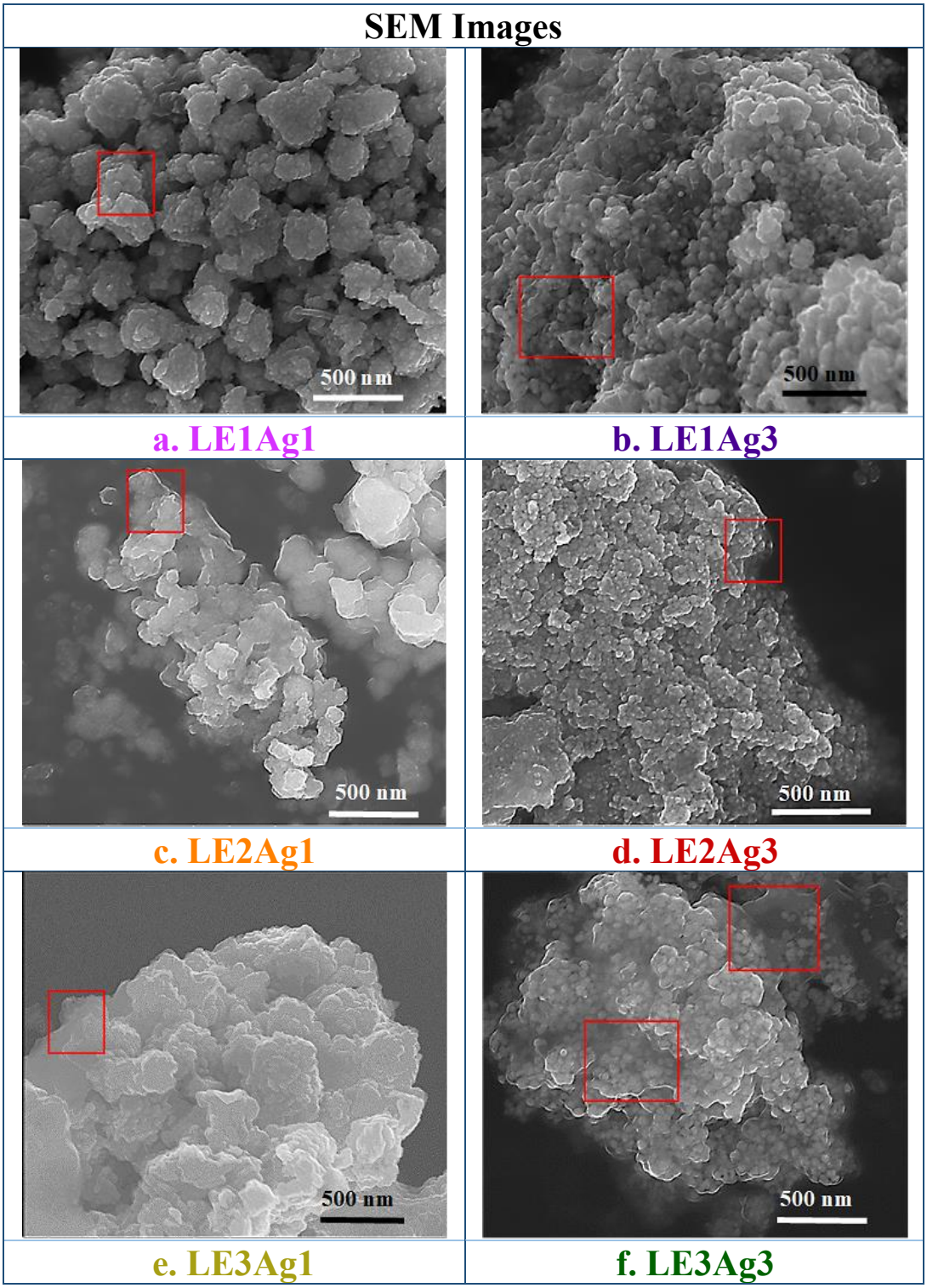

Figure 4.2 SEM micrographs of nanocomposites synthesized at different temperatures using **LE1**, **LE2** and **LE3** extracts. (Syntheses conditions: 25(±1) °C → Ag1, and 80(±1) °C→ Ag3).

SEM micrographs revealed distinct surface morphologies for all the nanocomposites synthesized using leaf extracts of **LE1**, **LE2**, and **LE3** at 25(±1) and 80(±1) °C (Figure 4.2). Fused nanoparticles (NP) structures with organic capping were observed, with **LE2** nanocomposites exhibiting the smallest sizes (Figure 4.2 c–d), while **LE3** (Figure 4.2 e–f) and **LE1**(Figure 4.2 a–b) nanocomposites exhibited progressively larger NPs. The organic capping of NPs is highlighted in the red boxed areas in Figure 4.2. At 25(±1) °C, the nanocomposites displayed an aggregated structure of fused globular or platelet-like morphology, formed by the dissolution of smaller NPs (Figure 4.2 a, c, and e). However, when the synthesis temperature increased to 80(±1) °C, the aggregates consisted of small-sized, more distinct NPs (Figure 4.2 b, d, and f).

EDAX elemental mapping confirmed that Ag and Cl were homogenously distributed within the nanocomposites (Figure 4.3). Furthermore, an increase in AgCl content– ordered as **LE1Ag1**< **LE3Ag1**< **LE2Ag1** in nanocomposites synthesized at 25(±1) °C led to a transition from the globular structure to a platelet-like structure (Figure 4.2 a, c, and e). This structural transformation is consistent with the observations from nanocomposites synthesized using brewery wastes, where increasing AgCl content in the nanocomposites produced more layered structures [100, 101].

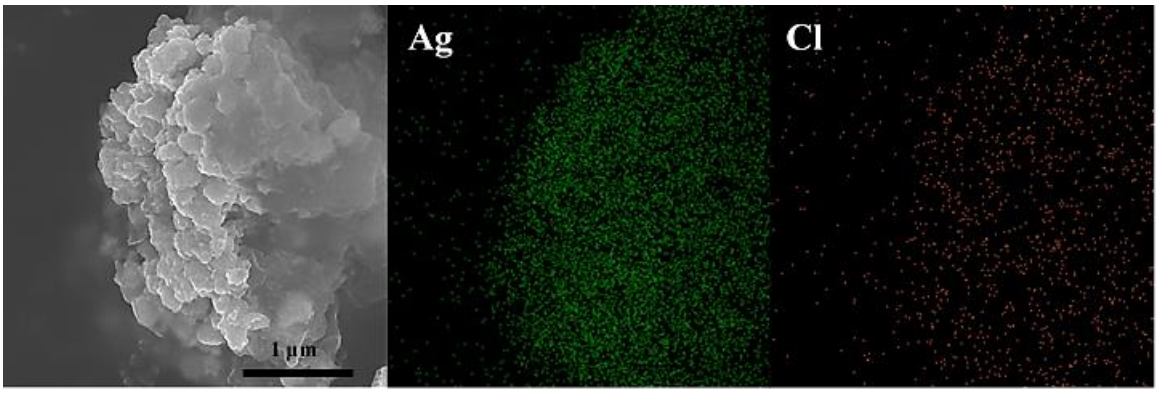

Figure 4.3a Elemental mapping of **LE1Ag1** nanocomposite.

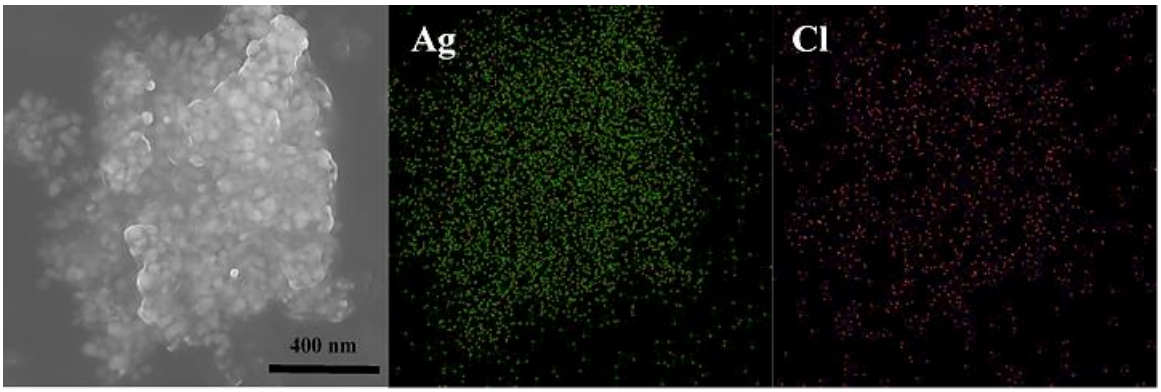

Figure 4.3b Elemental mapping of **LE1Ag3** nanocomposite.

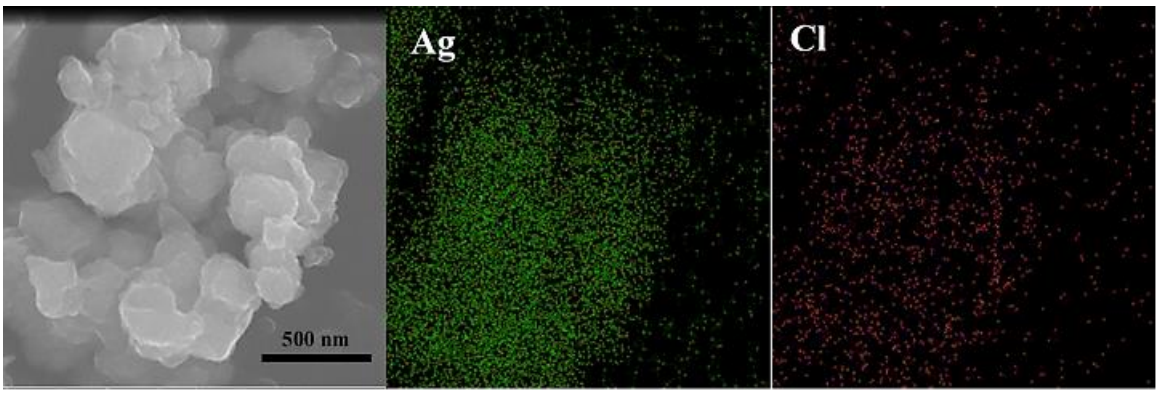

Figure 4.3c Elemental mapping of **LE2Ag1** nanocomposite.

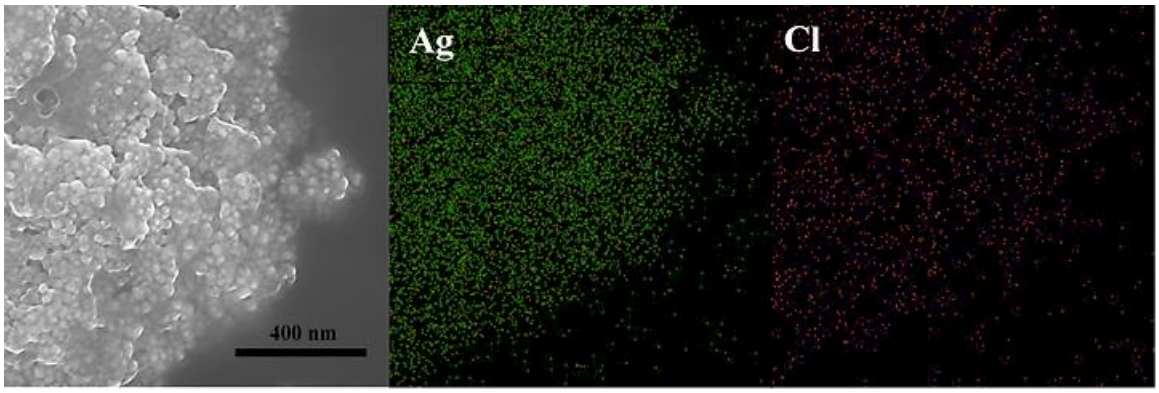

Figure 4.3d Elemental mapping of **LE2Ag3** nanocomposite.

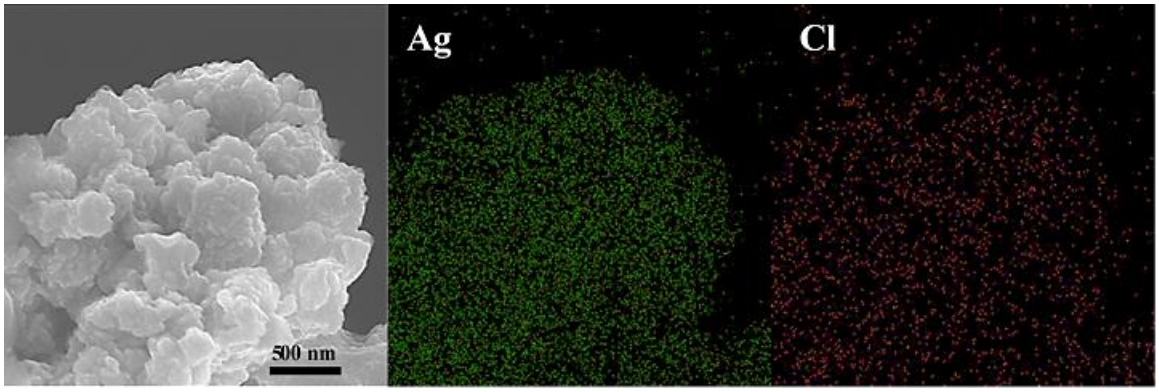

Figure 4.3e Elemental mapping of **LE3Ag1** nanocomposite.

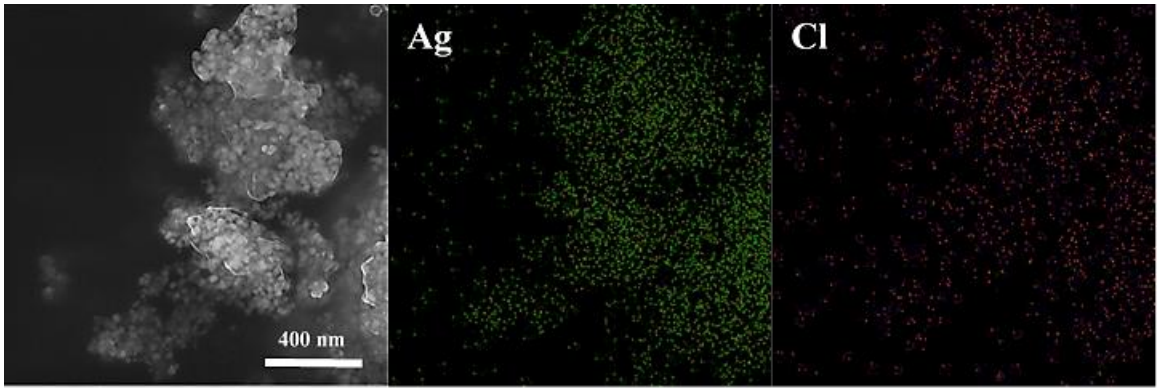

Figure 4.3f Elemental mapping of **LE3Ag3** nanocomposite.

4.2.4 Surface chemical analysis by X-ray photoelectron spectroscopy (XPS) of **LE** nanocomposites

The presence of organic groups on the surface of nanocomposites suggests effective capping of nanocomposites with the organic matter derived from the leaf extracts [175]. Interestingly, **LE2** nanocomposites exhibit unique bands representing saturated carbon groups which are distinct from these nanocomposites.

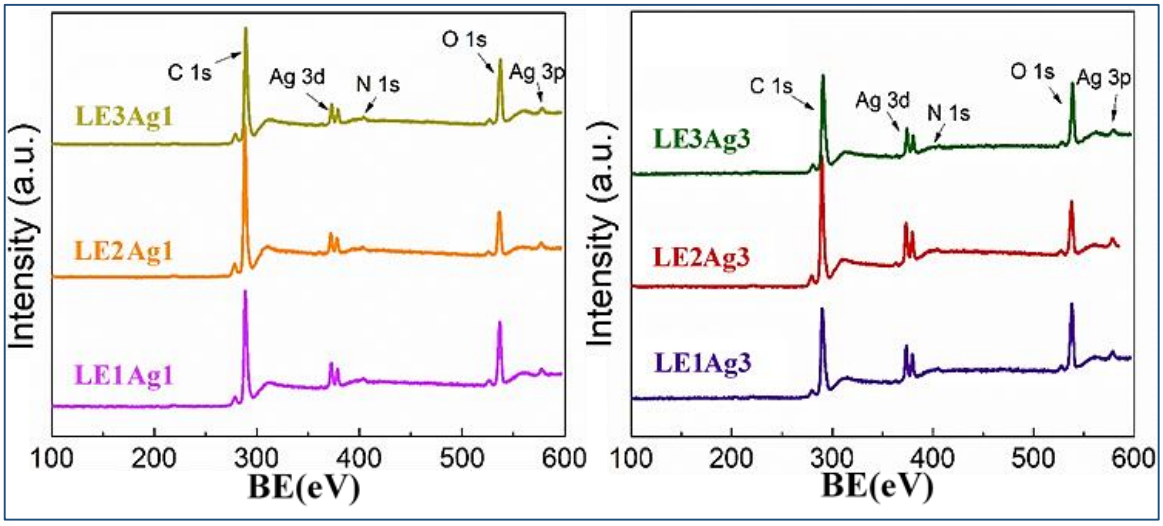

Figure 4.4 The XPS survey spectra of using **LE1**, **LE2** and **LE3** nanocomposites. (Syntheses conditions: 25(±1) °C → Ag1, and 80(±1) °C→ Ag3).

The survey XPS spectra of **LE** nanocomposites confirm the presence of C, O, Ag, N, Cl, S, and P (Figure 4.4, Table 4.4). The surface elemental quantification was performed by accounting for the areas under Ag 3d, C 1s, O 1s, N 1s, P 2p, S 2p, and Cl 2p photoelectron peaks using the procedure described in Chapter 3.

The weight percentages of surface Ag, Cl, S, and O derived from XPS analysis are presented in Table 4.4. The surface composition analysis confirms that the C and O weight percent dominate the nanocomposites′ surfaces, with a relatively smaller amount of Ag, N, Cl, S, and P (Table 4.4). The spectra fitting results of various chemical forms of Ag 3d, C 1s, and N 1s present in **LE1**, **LE2**, and **LE3** nanocomposites synthesized at 25(±1) °C and 80(±1) °C are shown in Figures 4.5, 4.6, and 4.7, respectively. The corresponding weight percent quantification of Ag, C, and N chemical forms resulting from the fitting were listed in Table 4.5, 4.6, and 4.7, respectively.

Table 4.4 Surface weight composition of **LE** nanocomposites by XPS.

Sample	Synthesis temp., (±1) °C	XPS Analysis						
		Surface Elemental Composition (wt.%)						
		C	O	Ag	N	Cl	S	P
LE1Ag1	25	65.3	21.6	11.4	1.3	0.4	-	-
LE1Ag2	50	65.9	22.4	10.5	1.2	-	-	-
LE1Ag3	80	57.1	24.6	17.0	0.4	0.9	-	-
LE2Ag1	25	74.5	14.7	8.9	1.1	-	-	0.9
LE2Ag2	50	74.5	15.7	9.1	0.8	-	-	-
LE2Ag3	80	64.3	17.0	18.1	0.6	-	-	-
LE3Ag1	25	65.6	22.8	9.7	0.7	0.7	0.3	0.2
LE3Ag2	50	65.6	18.2	13.8	0.7	1.1	-	0.5
LE3Ag3	80	61.9	23.6	12.9	0.6	1.0	-	-

The surface composition of nanocomposites varies with synthesis temperature. Surface oxygen and silver increase at the expense of surface carbon and nitrogen content in nanocomposites with increasing temperature. Notably, the surface of **LE2** nanocomposites was lacking Cl content. Furthermore, the surface of **LE2** nanocomposites has the highest carbon content and is oxygen deficient, whereas the surfaces of **LE1** and **LE3** nanocomposites contains less carbon content and are oxygen-rich.

Phosphorous was detected at BE of 133.8 eV in **LE2Ag1** nanocomposite, which can correspond to phosphine, phosphate, phosphorene, phosphite, phosphorous groups, or bonding of $AgPO_3$–S [169]. Chlorine was observed at BE of 198.6 eV and identified as AgCl [169].

4.2.4.1 Surface Ag chemical state content in **LE** nanocomposites

Prior to evaluating the chemical state of elements, the binding energy (BE) of the XPS spectra was calibrated to the maximum of the Ag $3d_{5/2\text{-}3/2}$ spectra, corresponding to the predominant state observed in the PXRD patterns (Table 4.2) and C 1s BE at 284.4 eV. Similar fitting procedure was applied as in Chapter 3 with the results presented in the following figures: Ag $3d_{5/2\text{-}3/2}$ (Figure 4.5), C 1s (Figure 4.6) and N 1s (Figure 4.7). The content of respective chemical forms of Ag, C and N resulting from this fitting procedure is presented in Table 4.5, Table 4.6 and Table 4.7, respectively. The carbon overlayer thickness on Ag NPs was determined using an overlayer equation [176] and TPP-2M IMFP [168] based on the Ag 3p and Ag 3d photoelectron lines in the **LE** nanocomposites (Table 4.5).

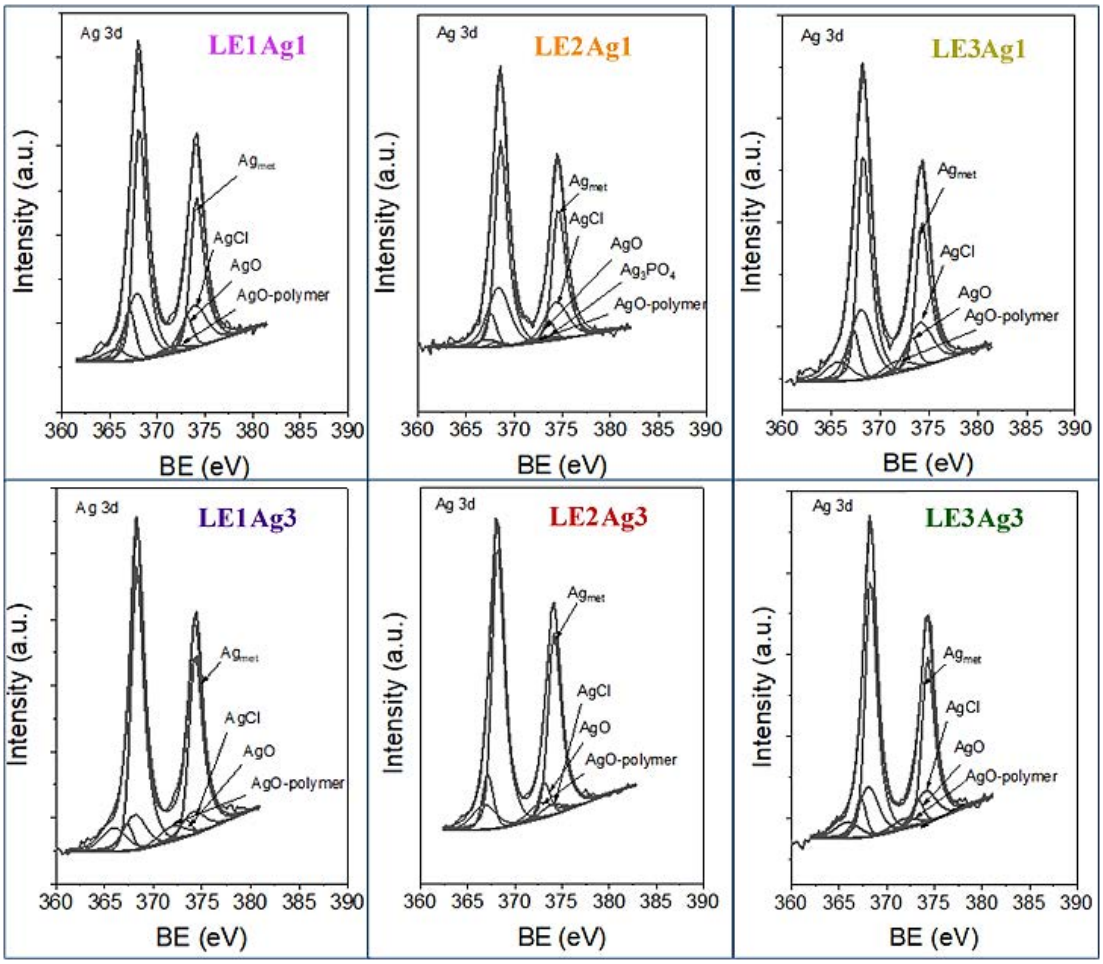

Figure 4.5 XPS spectra of Ag 3d in **LE1**, **LE2**, and **LE3** nanocomposites. (Syntheses conditions: 25(±1) °C → Ag1, and 80(±1) °C→ Ag3).

For **LE1** nanocomposites, the surface content of Ag and AgO-polymer increases with synthesis temperature, while that of AgCl and AgO decreases, and no Ag_2O is detected (Table 4.5). In **LE2** nanocomposites, the surface content of AgCl, Ag, Ag–O, and AgO-polymer increases with the synthesis temperature. While Ag_3PO_4 is present on the surface of **LE2Ag2** and only Ag_2O is observed in **LE2Ag3**. For **LE3** nanocomposites, the surface Ag content increases with synthesis temperature, while AgCl, AgO, and AgO-polymer show slight variations.

The higher ratio of AgO-polymer to Ag oxidized forms suggests that AgO-polymer state formation is more favorable compared to Ag oxides. This AgO-polymer ratio increases with temperature for **LE1** nanocomposites, indicating that AgO groups formed are increasingly complex with the organic materials from extracts, such as polyphenols, carbohydrates, and sugars, forming organometallic structures as the synthesis temperature is increased. In contrast, in **LE2** nanocomposites, higher temperature promotes the dissolution, causing the breakdown of complex organometallic structures into AgO groups. This could be possibly due to the lower content of complex organic matter like polyphenols, carbohydrates, and sugars in **LE2** extract.

Table 4.5 Comparison of surface Ag chemical states content in **LE1**, **LE2**, and **LE3** nanocomposites.

Sample	Synthesis temp., (±1) °C	Ag chemical states (wt.%)- Ag $3d_{5/2-3/2}$					
		AgCl BE=368.1 ±0.2 eV	**Ag_{met}** BE=368.3 ±0.2 eV	**Ag_3PO_4** BE=367.8 ±0.2 eV	**Ag_2O** BE=367.7 ±0.2 eV	**AgO** BE=367.3 ±0.2 eV	**AgO–polymer** BE=365.5 ±0.4 eV
LE1Ag1	25	2.89	6.84	-	-	1.14	0.53
LE1Ag2	50	0.3	7.72	-	-	1.58	0.9
LE1Ag3	80	2.27	12.18	-	-	0.92	1.63
LE2Ag1	25	1.21	6.23	1.9	-	0.81	0.65
LE2Ag2	50	1.32	4.96	-	-	0.51	0.41
LE2Ag3	80	2.32	10.63	-	1.81	1.67	1.67
LE3Ag1	25	2.54	5.52	-	-	0.89	0.75
LE3Ag2	50	2.98	7.99	-	-	1.6	1.23
LE3Ag3	80	2.5	8.5	-	-	0.99	0.91

4.2.4.2 Surface C chemical state content and overlayer thickness in **LE** nanocomposites

The chemical states of carbon forms identified were C sp^2, C sp^3 hybridizations, along with hydroxyl (C–OH), carbonyl (C=O) and carboxyl (C–OOH) groups (Figure 4.6) with BE values consistent with the literature reports [100, 101, 170, 175]. Additionally, vacancy defects may be present within carbon structures of the nanocomposite [177]. The calculated carbon overlayer thickness evaluated using overlayer equation for C 1s [176] are presented in (Table 4.6).

On the surface of **LE1** nanocomposites, all carbon states show slight variations, except for vacancy defects, which decrease as the synthesis temperature increases. In **LE2** nanocomposites, the C sp^2, C sp^3 content, along with carbon overlayer thickness decreases with increasing synthesis temperature, while C–OH, C=O, COOH, and vacancy defects fluctuate randomly. In **LE2Ag2**, the absence of C=O could be attributed to the presence of Ag_3PO_4 on the surface, suggesting that surface Ag_3PO_4 may be causing the oxidation of aldehyde and ketone groups into carboxylic acid.

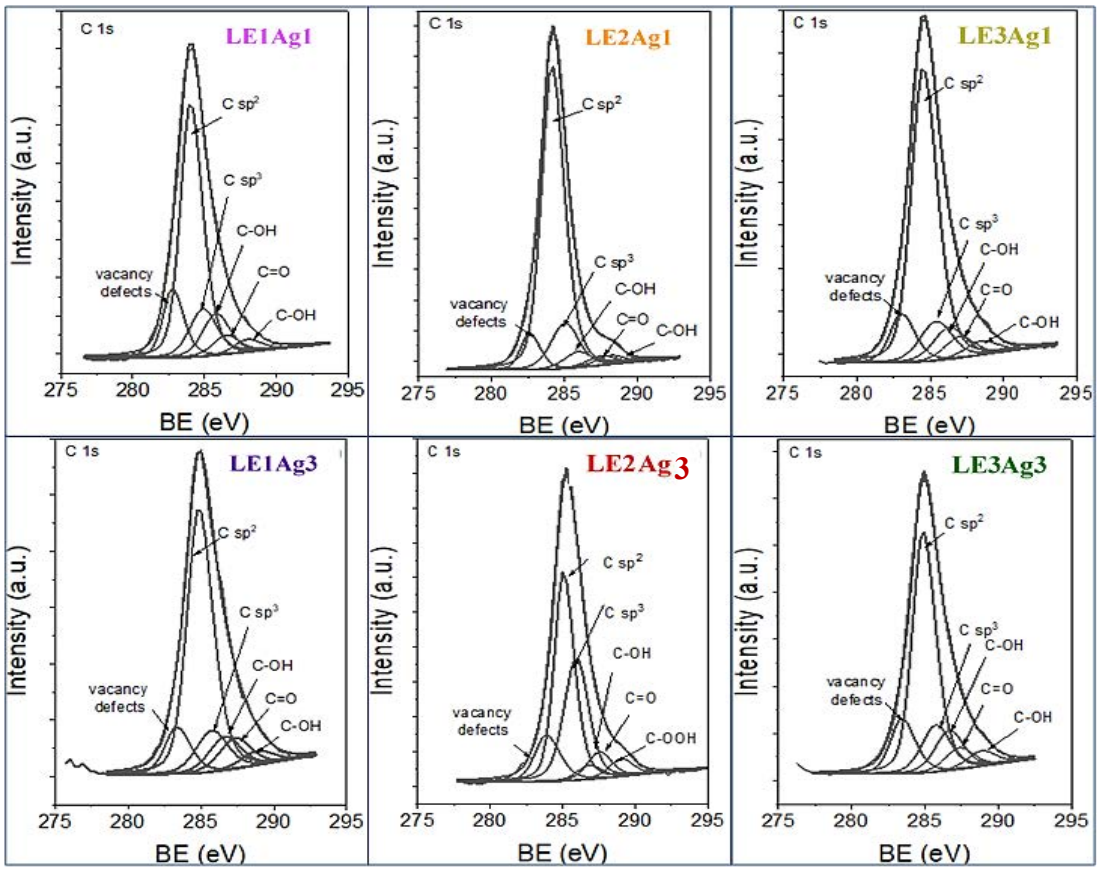

Figure 4.6 XPS spectra of C 1s in **LE1**, **LE2**, and **LE3** nanocomposites. (Syntheses conditions: 25(±1) °C → Ag1, and 80(±1) °C→ Ag3).

For **LE3** nanocomposites, C sp^3, C–OH, and vacancy defects increase with increasing temperature, while C=O, COOH, and carbon overlayer thickness vary inconsistently, and C sp^2 decreases. This indicates the decomposition of C sp^2 bonds into C sp^3, likely forming C–OH bonds. The carbon overlayer thickness was found to be between ~ 6–8 nm. **LE2Ag1** nanocomposite had the thickest carbon overlayer, measuring ~ 8.2 nm, and **LE2Ag3** nanocomposite had the thinnest carbon overlayer, measuring ~6.4 nm, in comparison to other nanocomposites. Nanocomposites synthesized at 25(±1) °C (**LE1Ag1**, **LE2Ag1**, and **LE3Ag1**) have a thicker carbon overlayer compared to their respective counterparts synthesized at 80(±1) °C (**LE1Ag3**, **LE2Ag3**, and **LE3Ag3**). This indicates that higher synthesis temperature leads to a thinner overlayer. The nanocomposites were characterized by organic and inorganic groups on their surfaces. Notably, it can be observed that **LE2** nanocomposites exhibited distinct surface environments compared to **LE1** and **LE3** nanocomposites. Among them **LE2Ag1** nanocomposite had the thickest carbon overlayer, measuring ~ 8.2 nm, in comparison to other nanocomposites. The calculated carbon overlayer thickness evaluated using overlayer equation for C 1s and for Ag (Ag 3p and 3d) photoelectron lines were comparable.

Table 4.6 Comparison of surface C chemical state content and overlayer thickness in **LE1**, **LE2**, and **LE3** nanocomposites.

Sample	Synthesis temp., (±1) °C	C chemical state (wt.%)- C 1s						C overlayer thickness (nm)
		Vac. def. BE=283 ±0.1 eV	C sp^2 BE=284.4 eV	C sp^3 BE=285.3 eV	C–OH BE=286.2 eV	C=O BE=287.8 eV	C–OOH BE=288.4 eV	
LE1Ag1	25	9.18	36.5	7.76	6.74	3.08	2.04	7.45±0.28
LE1Ag2	50	8.75	32.49	10.92	9.87	1.99	1.88	8.05±0.78
LE1Ag3	80	5.94	33.79	5.97	4.86	4.45	2.09	6.55±1.07
LE2Ag1	25	5.41	53.25	9.01	3.13	1.9	1.8	8.2±0.14
LE2Ag2	50	10.94	49.17	6.38	4.73	-	3.28	8.03±0.25
LE2Ag3	80	7	40.54	7.53	4.5	2.41	2.32	6.38±0.60
LE3Ag1	25	6.64	41.89	6.34	5.2	3.26	2.27	7.8±0.14
LE3Ag2	50	6.37	40.06	7.46	5.92	2.62	3.17	6.98±0.67
LE3Ag3	80	8.25	33.92	7.49	6.34	3.43	2.47	7.1±0.42

4.2.4.3 Surface N chemical state content in **LE** nanocomposites

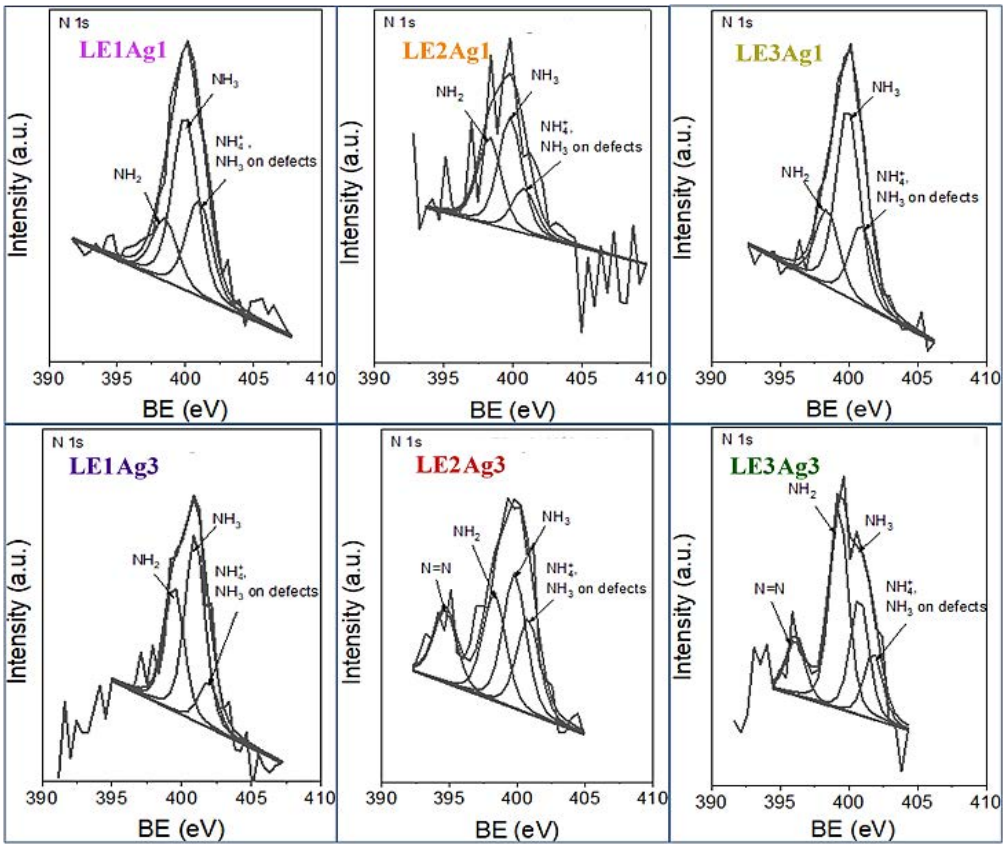

Figure 4.7 XPS spectra of N 1s in **LE1**, **LE2**, and **LE3** nanocomposites.
(Syntheses conditions: 25(±1) °C → Ag1, and 80(±1) °C→ Ag3).

The nitrogen peak (Figure 4.7) was fitted to four chemical forms, attributed to N=N groups, C–NH_2, C–NH_3 and C–NH_4^+ or C–NH_3 associated with vacancy defects (Table 4.7) [169, 178].

Table 4.7 Chemical states of N and their weight percent at the surface of **LE** nanocomposites.

Sample	Synthesis temp., ((±1) °C)	N chemical state (wt.%) – N 1s			
		N=N BE=395.5±0.2 eV	NH_2 BE=398.4±0.2 eV	NH_3 BE=399.9±0.2 eV	NH_4^+ NH3 on vac. BE=401.4±0.3 eV
LE1Ag1	25	-	0.2	0.82	0.28
LE1Ag2	50	-	0.26	0.55	0.39
LE1Ag3	80	-	0.14	0.21	0.05
LE2Ag1	25	-	0.35	0.54	0.21
LE2Ag2	50	-	-	0.8	-
LE2Ag3	80	0.12	0.08	0.2	0.2
LE3Ag1	25	-	0.14	0.41	0.15
LE3Ag2	50	-	0.11	0.47	0.12
LE3Ag3	80	0.08	0.27	0.16	0.09

4.3 Anticancer activity testing of **LE** nanocomposites

The biological activity of **LE** nanocomposites synthesized at 25(±1) °C and 80(±1) °C were evaluated. Therefore, different **LE** nanocomposites' concentrations were added to normal (HEK293) and cancerous (HeLa) cells and observed under a fluorescent microscope to understand their impact on cell growth. Determination of the biocompatibility with normal (HEK293) cell line and cytotoxicity towards four different cancerous (HeLa, A549, MCF-7, MDA-MB-231) cell lines, LDH and MTT assays were performed (Figure 4.9–4.10). The HeLa cell line, commonly used in biological research, represents cervical cancer, while the A549 line is frequently studied for lung cancer, and MCF-7 and MDA-MB-231 are well-known breast cancer cell lines. These were selected to assess the nanocomposites' effects on different cancer types. **LE** nanocomposites synthesized from various leaf extracts at different temperatures exhibited differential effects on cell cytotoxicity.

4.3.1 Live/dead assay

Confocal images of HEK293 and HeLa cells treated with low (1 μg ml^{-1}) and high (25 μg ml^{-1}) concentrations of $AgNO_3$ and **LE** nanocomposites synthesized at 25(±1) °C and 80(±1) °C are presented in Figure 4.8. A comparison of confocal images of control cells and nanocomposite-treated cells reveals that, at both concentrations tested, **LE** nanocomposites have negatively affected the cell growth. Particularly, at higher concentration of

nanocomposites, increased cell death was observed, as indicated by a considerable rise in PI (propidium iodide) staining (red colour in fluorescent micrographs).

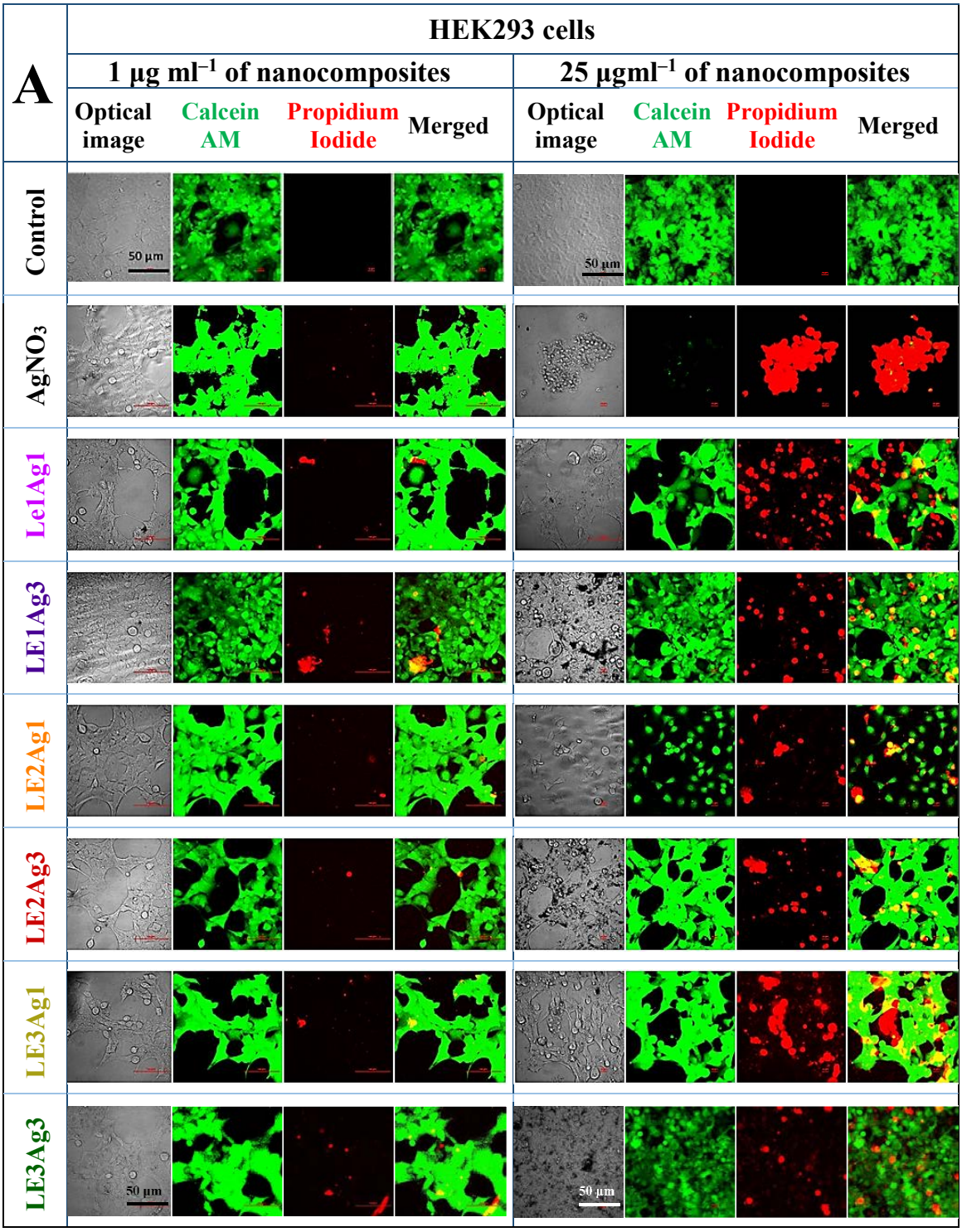

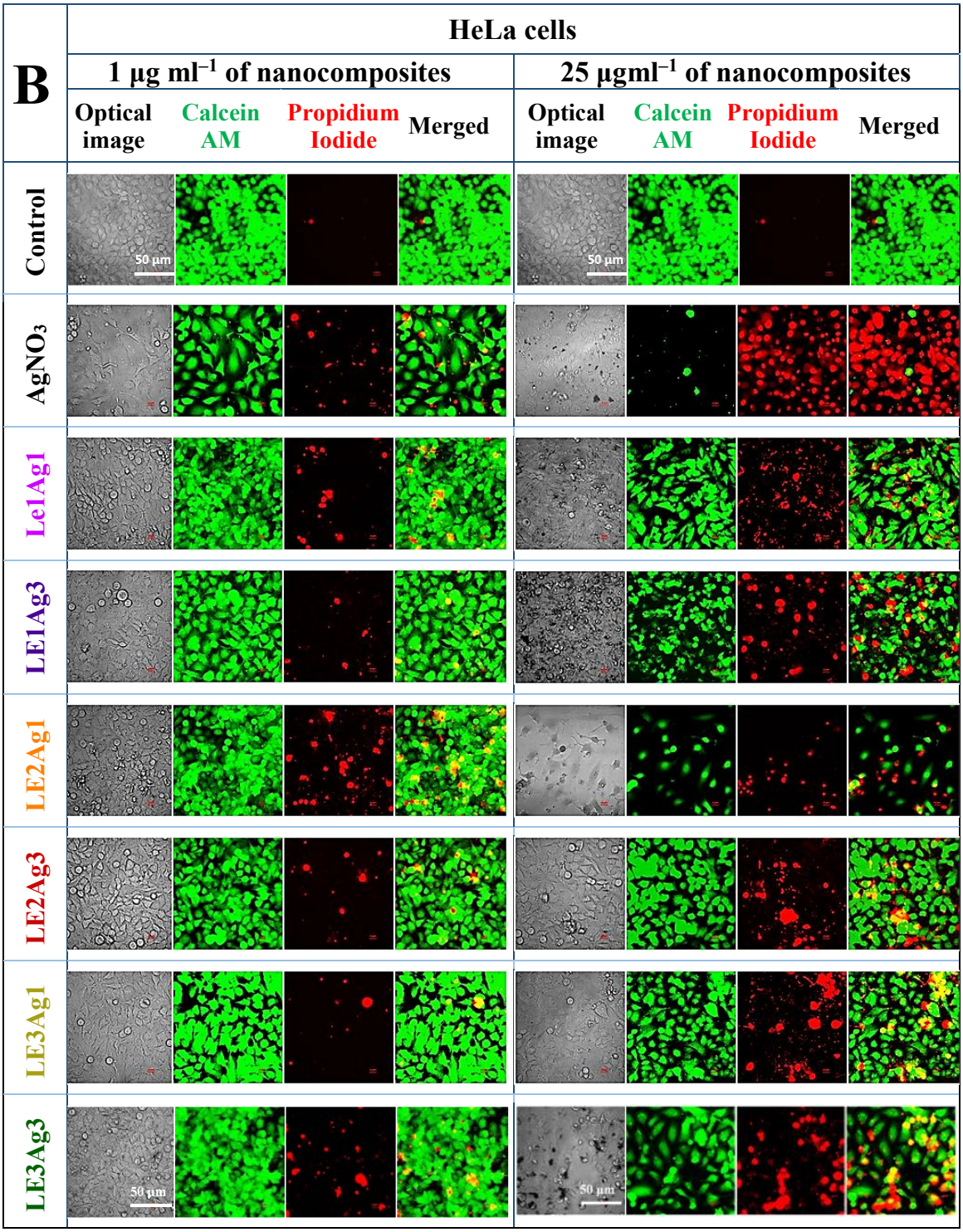

Figure 4.8 Confocal images of A) normal HEK293 and B) HeLa cancer cells with and without treatment to $AgNO_3$ and **LE1**, **LE2** and **LE3** nanocomposites synthesized at 25(±1) °C and 80(±1) °C at 1 µg ml^{-1} and 25 µg ml^{-1} concentration. (Syntheses conditions: 25(±1) °C → Ag1, and 80(±1) °C→ Ag3). (Scale bars: 50 µm)

A low concentration of $AgNO_3$ significantly reduced the growth of HEK293 cells, with a stronger inhibitory effect compared to the nanocomposites (Figure 4.8A). This suggests that the nanocomposites were more biocompatible at lower concentrations. At higher concentrations, $AgNO_3$ induced 100% cell death, whereas the nanocomposites remained biocompatible with HEK293 cells (Figure 4.8A). Among the nanocomposites, **LE2Ag1** exhibited the highest cytotoxicity response against HeLa cells. (Figure 4.8B). Although $AgNO_3$ showed the greatest cytotoxic effect at high concentrations (Figure 4.8B), it was not biocompatible with HEK293 cells (Figure 4.8A).

4.3.2 LDH assay

The LDH assay was employed to determine the percentage of damaged cells in comparison to the control. HEK293 normal cell line and different cancer cell lines (HeLa, A549, MCF-7, and MDA-MB-231) were treated with increasing concentrations of **LE** nanocomposites synthesized at 25(±1) °C and 80(±1) °C. The results, presented in Figure 4.9, indicate a consistent trend across all cell lines, where LDH activity decreased as nanocomposite concentrations increased. LDH, an enzyme present in most living cells, is released upon cell membrane damage. The LDH release levels correlate with damaged cells [179].

The observed LDH activity of cells was highest at a lower nanocomposite concentration of 0.1 $\mu g\ ml^{-1}$ and the activity decreased with increasing concentration. This suggests that as the concentration of nanocomposites increases, cell proliferation is reduced (cells grow and divide less), resulting in a decreasing number of cells present as compared to the control, which was further damaged by nanocomposites. This lowering of cell number led to a decrease in the released LDH levels (released LDH $\propto$ damaged cell number), even for complete cell disruption at higher concentrations [180]. Furthermore, a similar reduction of LDH levels at higher concentrations is often observed with certain NPs. When Ag NPs interact with the released LDH from cells, they tend to adsorb LDH enzyme [180]. Washing these cells prior to measuring absorbance to remove Ag NPs also eliminates the LDH adsorbed onto the Ag NPs from the assay reactants, which can result in an underestimation of overall released LDH levels from damaged cells [180]. Additionally, Ag NPs can generate ROS, contributing to LDH inactivation and a further decrease in the measured LDH signal [180]. These phenomena were more pronounced at higher Ag NP concentrations.

This pattern indicates that **LE** nanocomposites inhibit cell growth at lower concentrations, while at higher concentrations, they induce both cell growth inhibition and cell death. Nanocomposite synthesized at 80(±1) °C (**LE1Ag3**, **LE2Ag3**, and **LE3Ag3**) had a slower cell

growth, requiring higher concentrations of nanocomposites (30–50 μg ml^{-1}) to achieve maximum growth inhibition. In contrast, nanocomposites synthesized at 25(±1) °C (**LE1Ag1**, **LE2Ag1**, and **LE3Ag1**) inhibited cell growth rapidly, achieving maximum cell growth inhibition at lower concentrations (10–20 μg ml^{-1}). This confirms the complex mechanism of cell death and growth inhibition driven by nanocomposites.

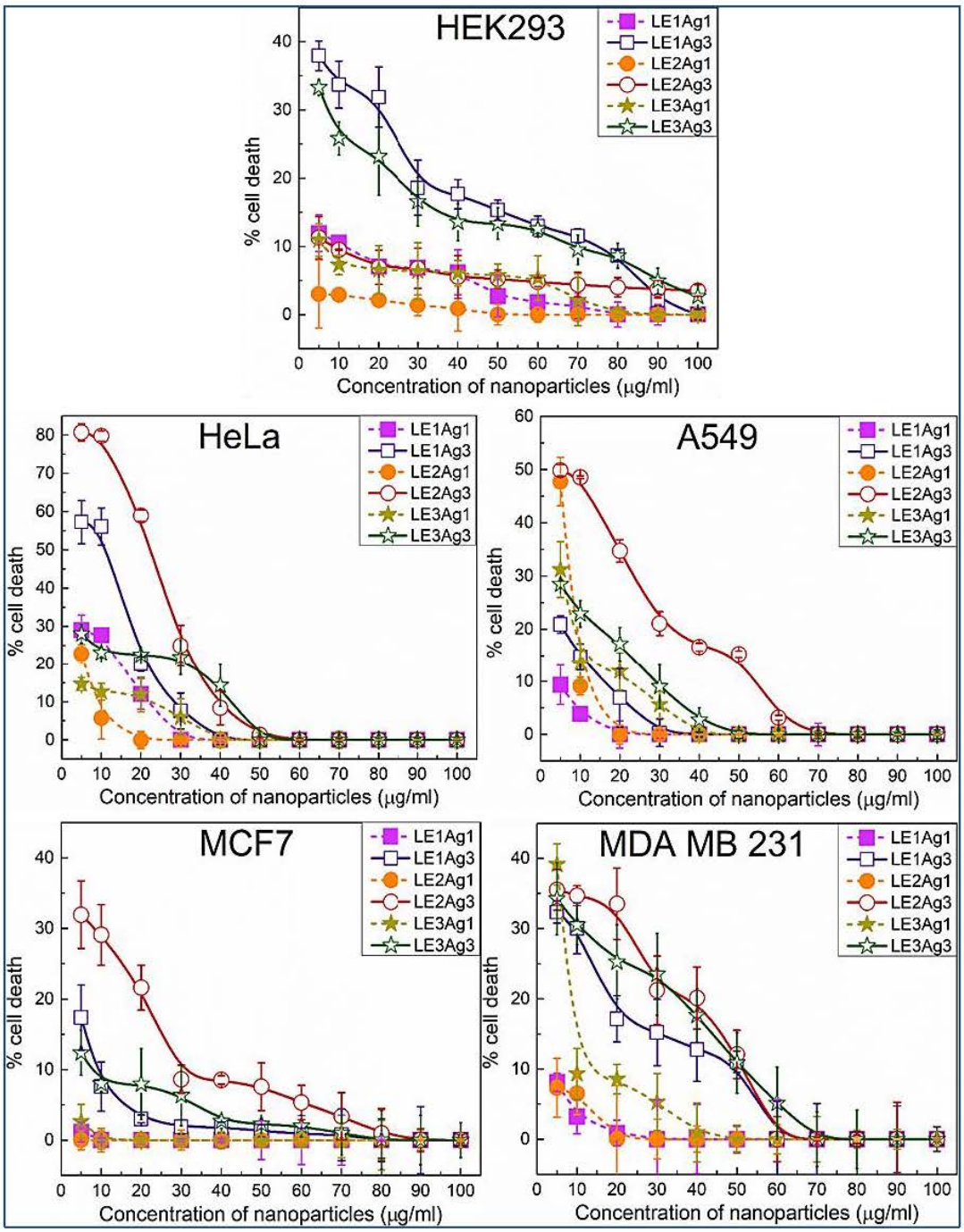

Figure 4.9 Dependence of percent of cell death of normal (HEK293) and different cancer cells by LDH assay on the concentration of **LE1**, **LE2**, and **LE3** nanocomposites synthesized at 25(±1) °C and 80(±1) °C. (Syntheses conditions: 25(±1) °C → Ag1, and 80(±1) °C→ Ag3).

4.3.3 MTT assay

The cytotoxic response of nanocomposites on the cells, assessed through the MTT assay, was analyzed and plotted using the Origin sigmoidal fitting procedure via the BiDoseResponse function. This analysis was necessary because the **LE** nanocomposites displayed a complex biphasic cytotoxicity mechanism (Figure 4.10–4.11) [181]. The EC_{50} value, representing the half maximal effective concentration, –in a pharmacological context the concentration of a drug required to achieve half of the maximum possible effect (i.e. 50% cell viability or cell death) for a particular cell line under study) –was evaluated for each nanocomposite (Figure 4.11and Table 4.8). Given that all **LE** nanocomposites exhibited a complex two-phase mechanism of cytotoxicity, the separate EC_{50} values for each phase were calculated and compared (Figure 4.12).

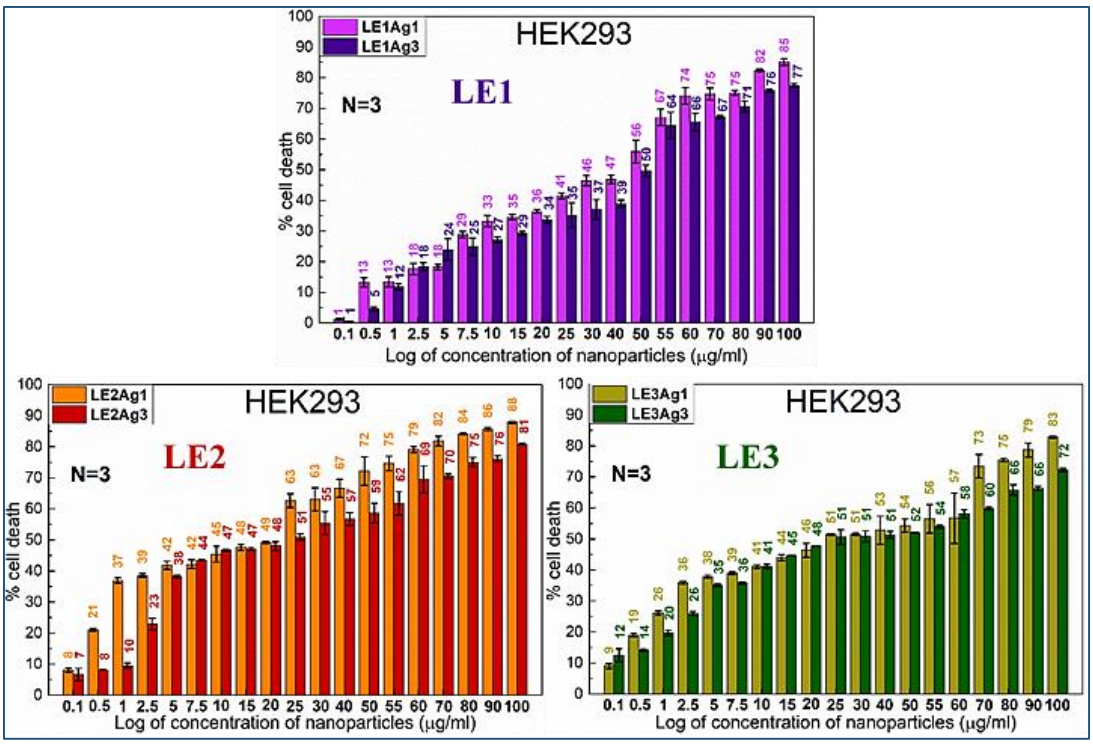

Figure 4.10a Cytotoxic dose-response curves analyzed using MTT assay for **LE1**, **LE2**, and **LE3** nanocomposites synthesized at 25(±1) °C and 80(±1) °C on HEK293 cells. (Syntheses conditions: 25(±1) °C → Ag1, and 80(±1) °C→ Ag3).

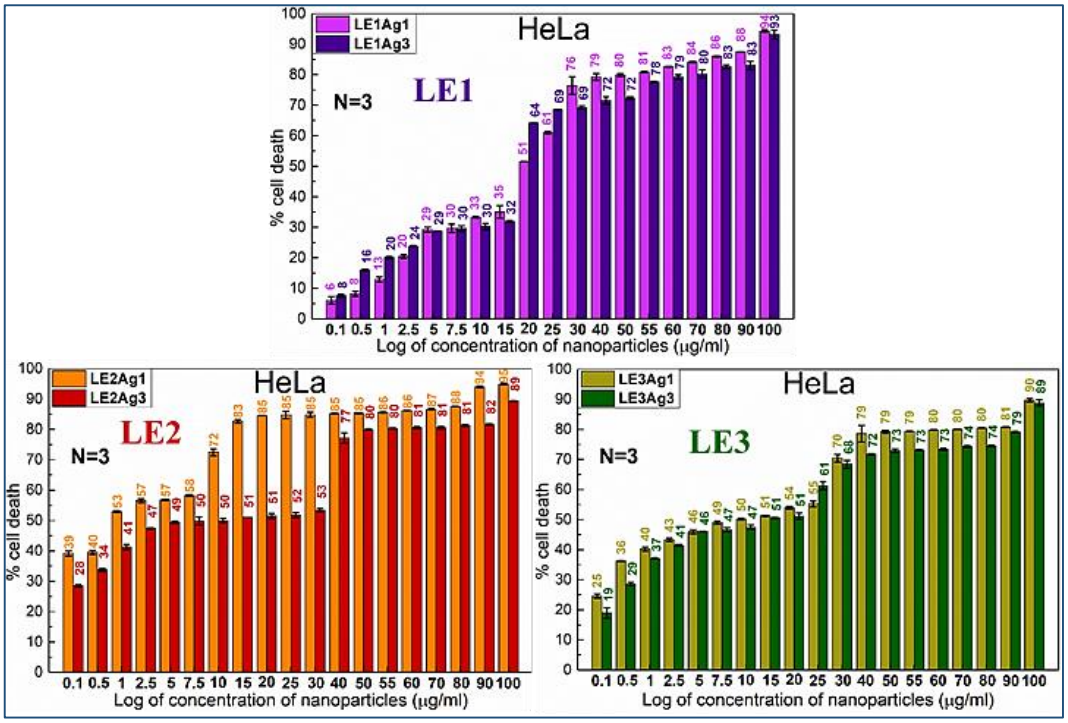

Figure 4.10b Cytotoxic dose-response curves analyzed using MTT assay for **LE1**, **LE2**, and **LE3** nanocomposites synthesized at 25(±1) °C and 80(±1) °C on HeLa cells. (Syntheses conditions: 25(±1) °C → Ag1, and 80(±1) °C→ Ag3).

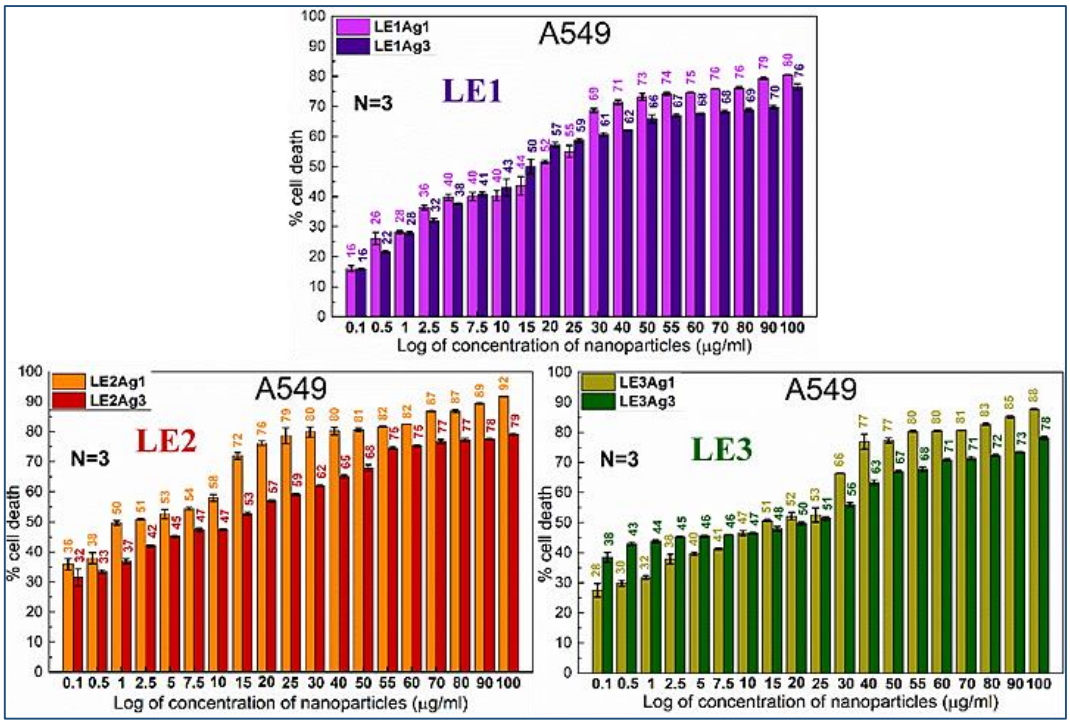

Figure 4.10c Cytotoxic dose-response curves analyzed using MTT assay for **LE1**, **LE2** and **LE3** nanocomposites synthesized at 25(±1) °C and 80(±1) °C on A549 cells. (Syntheses conditions: 25(±1) °C → Ag1, and 80(±1) °C→ Ag3).

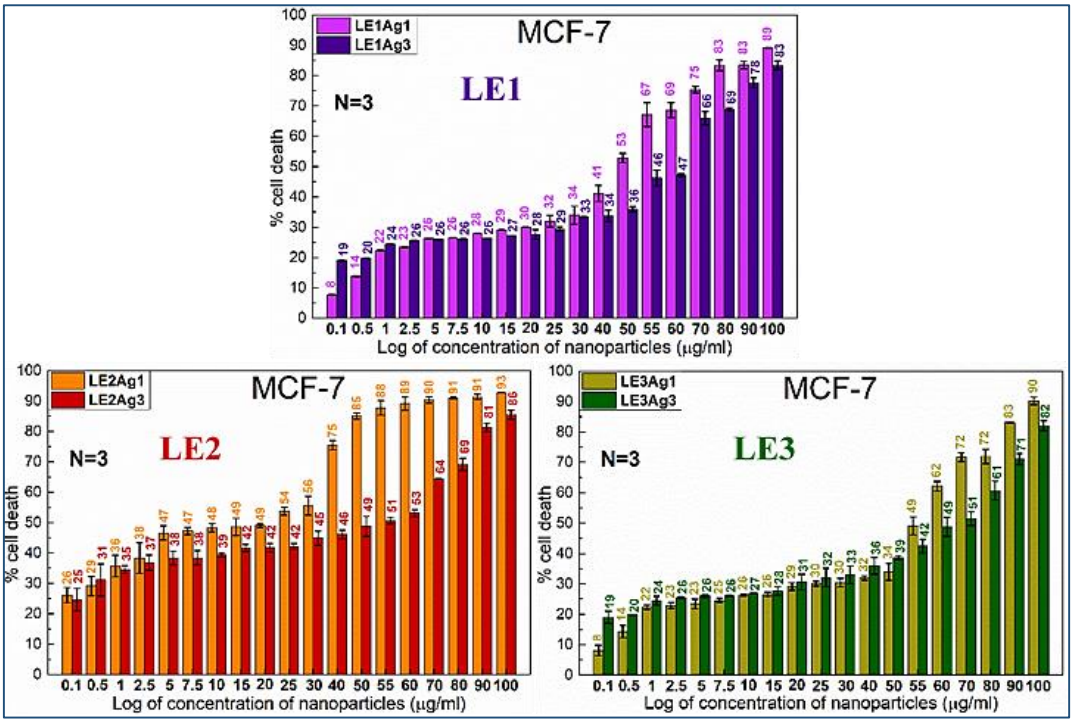

Figure 4.10d Cytotoxic dose-response curves analyzed using MTT assay for **LE1**, **LE2** and **LE3** nanocomposites synthesized at 25(±1) °C and 80(±1) °C on MCF-7 cells. (Syntheses conditions: 25(±1) °C → Ag1, and 80(±1) °C→ Ag3).

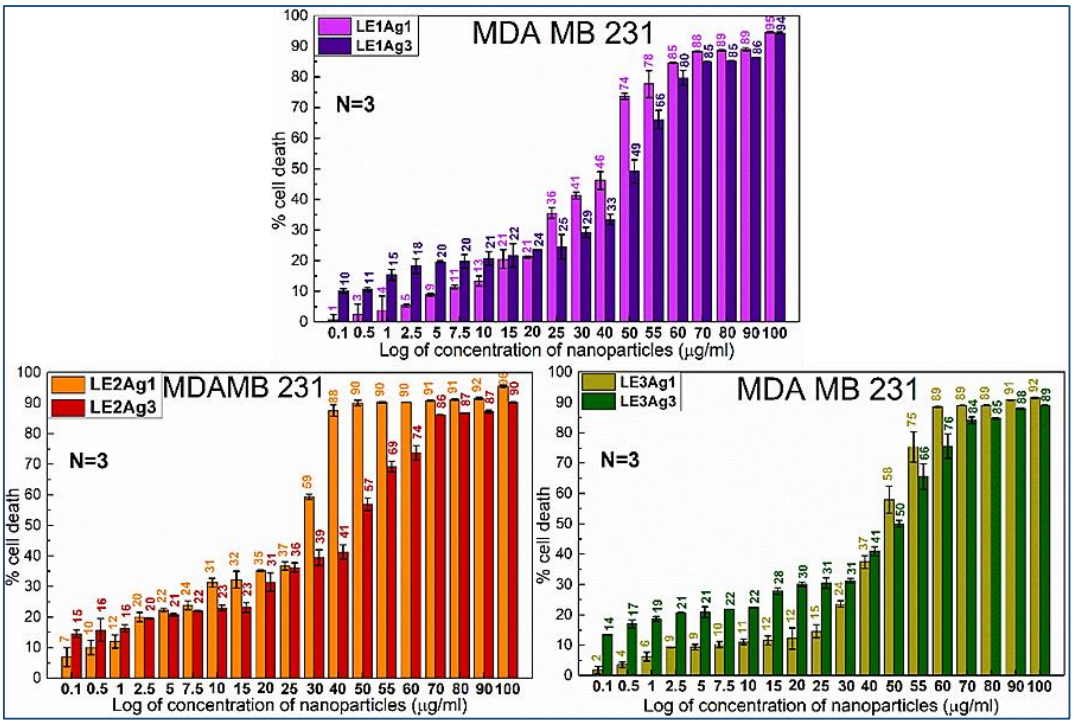

Figure 4.10e Cytotoxic dose-response curves analyzed using MTT assay for **LE1**, **LE2** and **LE3** nanocomposites synthesized at 25(±1) °C and 80(±1) °C on MDA-MB-231 cells. (Syntheses conditions: 25(±1) °C → Ag1, and 80(±1) °C→ Ag3).

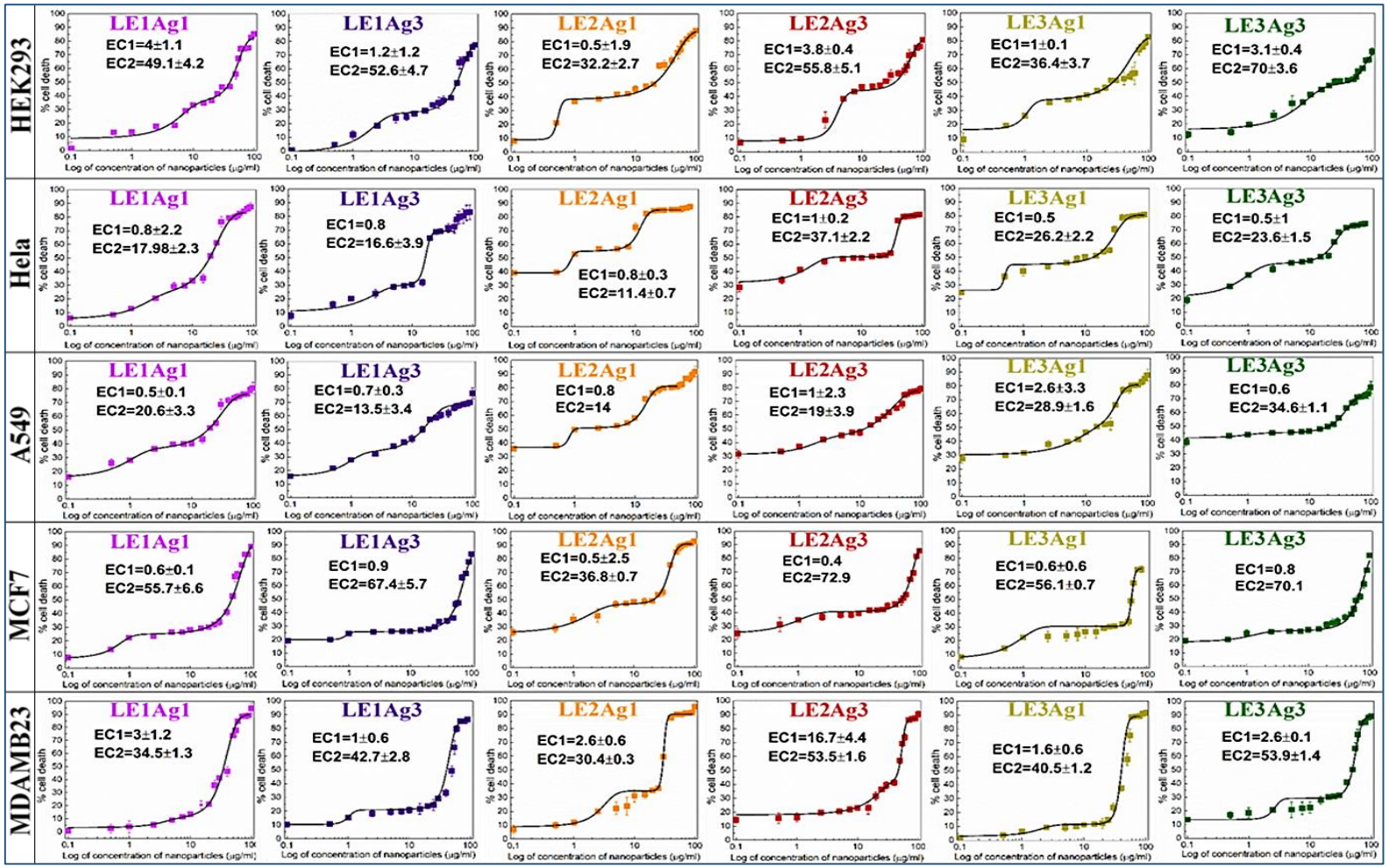

Figure 4.11 Fitted cytotoxic dose-response curves of MTT assay data and EC_{50} values obtained for **LE** nanocomposites on different cancer cells. (Syntheses conditions: 25(±1) °C → Ag1, and 80(±1) °C→ Ag3).

Table 4.8 EC_{50} values of **LE** nanocomposites synthesized at 25(±1) °C and 80(±1) °C on different cell lines.

Cell line/ Sample	EC_{50} (μg ml^{-1})									
	HEK293		HeLa		A549		MCF-7		MDA-MB-231	
	1st phase	2nd phase	1st phase	2nd phase	1st phase	2nd phase	1st phase	2nd phase	1st phase	2nd phase
LE1Ag1	4±1.1	49.1±4.2	0.8±2.2	18±2.3	0.5±0.1	20.6±3.3	0.6±0.1	55.7±6.6	3±1.2	34.5±1.3
LE1Ag3	1.2±1.2	52.6±4.7	0.8	16.6±3.9	0.7±0.3	13.5±3.4	0.9	67.4±5.7	1±0.6	42.7±2.8
LE2Ag1	0.5±1.9	32.2±2.7	0.8±0.3	11.4±0.7	0.8	14	0.5±2.5	36.8±0.7	2.6±0.6	30.4±0.3
LE2Ag3	3.8±0.4	55.8±5.1	1±0.2	37.1±2.2	1±2.3	19±3.9	0.4	72.9	16.7±4.4	53.5±1.6
LE3Ag1	1±0.1	36.4±3.7	0.5	26.2±2.2	2.6±3.3	28.9±1.6	0.6±0.6	56.1±0.7	1.6±0.6	40.5±1.2
LE3Ag3	3.1±0.4	70±3.6	0.5±1	23.6±1.5	0.6	34.6±1.1	0.8	70.1	2.6±0.1	53.9±1.4

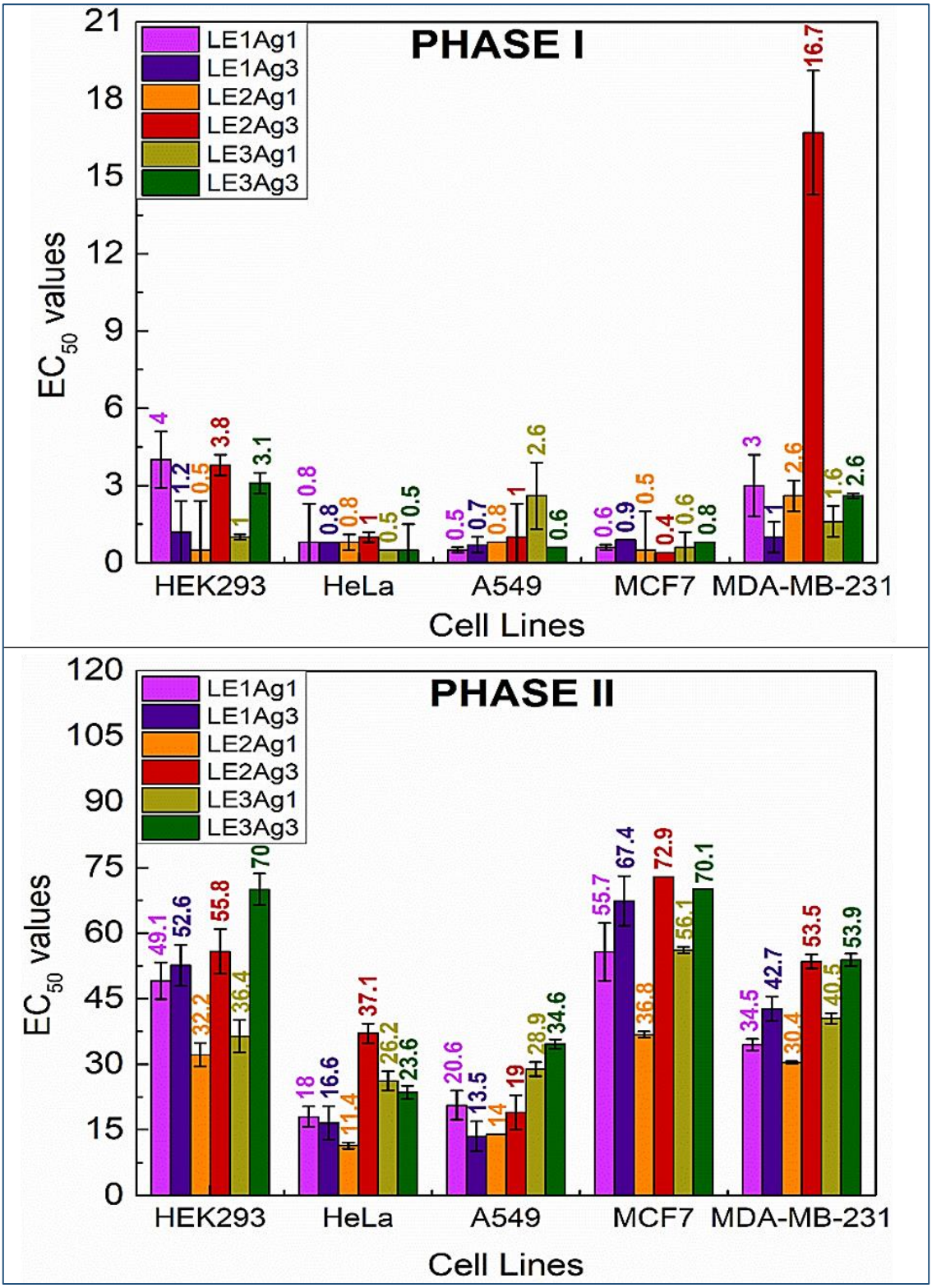

Figure 4.12 Comparison of EC_{50} values (μg ml^{-1}) for phase I and phase II of **LE1**, **LE2**, and **LE3** nanocomposites synthesized at 25(±1) °C and 80(±1) °C in different cell lines. (Syntheses conditions: 25(±1) °C → Ag1, and 80(±1) °C→ Ag3).

❖ MTT assay on HEK293 cells: The biocompatibility of the materials was assessed using MTT assay on normal cells –HEK293 (Figure 4.10–4.12). A higher cell viability indicates greater biocompatibility of the substance towards the cell line. By comparing the EC_{50} values obtained for phase I –based on cell viability or cell death induced by nanocomposites at various concentration ranges for HEK293 (Figure 4.10–4.12, and Table 4.8), the **LE1Ag1**, **LE2Ag3**, and **LE3Ag3** nanocomposites demonstrated superior biocompatibility relative to others.

In phase II, the highest cell viability was detected for **LE3Ag3, LE2Ag3**, and **LE1Ag3** nanocomposites. This indicates that, in consideration to the phase II cell death mechanism, nanocomposites synthesized at 80(±1) °C exhibited better biocompatibility as compared to the nanocomposites synthesized at 25(±1) °C (Figure 4.10–4.12, and Table 4.8).

❖ MTT assay on cancer cells: To evaluate the biocompatibility of a material for medical applications, it is crucial to examine the cytotoxicity induced by the material. Specifically, the EC_{50} value of the material exhibited against cancerous cells should be lower (in this study- HeLa, A549, MCF-7, and MDA-MB-231 cell lines) as compared to normal cells i.e., HEK293 for this study (Figure 4.10–4.12 and Table 4.8).

In phase I, all nanocomposites exhibited lower EC_{50} values ranging from 0.5 to 1 μg ml^{-1} for the HeLa, A549, and MCF-7 cell lines, and contrastingly higher EC_{50} values were observed for the MDA-MB-231 cell line. Thus, all nanocomposites were more toxic against HeLa, A549, and MCF-7 cell lines compared to MDA-MB-231 cell lines. Additionally, **LE3Ag1** against A549 and **LE2Ag3** against MDA-MB-231 cell line induced growth inhibition only at very high concentrations, suggesting that they were less toxic compared to other nanocomposites. Notably, **LE2Ag3** demonstrated a very broad phase I response against the MDA-MB-231 cell line, indicating its ability to inhibit cell growth over a wider concentration range.

Considering the phase II of cell toxicity, **LE1Ag3**, **and LE2Ag1** nanocomposites exhibited higher toxic effects on HeLa and A549 cell lines. In contrast, for MCF-7 and MDA-MB-231 cell lines, the nanocomposites synthesized at 25(±1) °C (**LE1Ag1**, **LE2Ag1** and **LE3Ag1**) exhibited higher cytotoxicity i.e., higher cell death along with cell growth inhibition, than the nanocomposites synthesized at 80(±1) °C (**LE1Ag3**, **LE2Ag3**, and **LE3Ag3**). Moreover, the **LE2Ag1** nanocomposite was found to be more toxic as compared to other nanocomposites.

Overall, the results from all three biological experiments indicate that in the 1st phase (at lower concentrations of nanocomposites) cell growth inhibition was the predominant phenomena. In the 2nd phase (at higher nanocomposite concentrations), the mechanism shifted to cell destruction after achieving a certain level of cell inhibition (~ 30–50%).

4.4 Discussion

❖ Leaf Extracts

Extracts from the leaves of *Malus sylvestris L.*(**LE1**), *Pinus sylvestris L.* (**LE2**), and *Sorbus aucuparia L.* (**LE3**) were found to contain various organic groups, including phosphates, sulfates, nitrates, polyphenols, carbohydrates, and sugars (Table 4.1). The presence of these diverse organic compounds in the leaf extracts is significant for the synthesis of nanocomposites, as they can influence the properties and functionality of the resulting materials. Moreover, these groups also act as capping agents which help stabilize the nanoparticles, preventing agglomeration and enhancing biocompatibility. Thus, these extracts served as both the synthesis and capping agents for the **LE** nanocomposites. Notably, the **LE2** extract exhibited distinct functional groups and had a lower overall organic content compared to **LE1** and **LE3** extracts. These differences in organic content and functional groups among the extracts affects the effectiveness of the synthesized nanocomposites in various applications, particularly in biomedicine or environmental remediation.

❖ Characterization of **LE** nanocomposites

Nanocomposites were synthesized using leaf extracts at different temperatures ranging between 25(±1) and 80(±1) °C. The synthesized nanocomposites were composed of different phases (Ag_{met}, AgCl, and Ag_3PO_4), with Ag_{met} being the predominant phase. Increasing synthesis temperature leads to increasing content and decreasing crystallite size of the major phase i.e. metallic silver in **LE** nanocomposites. The sizes of the nanocrystallites varied, measuring between 5.9 nm to 11.4 nm for Ag_{met}, 6.8 nm to 13.8 nm for AgCl, and 5.9 nm to 10.8 nm for Ag_3PO_4. At a lower synthesis temperature of 25(±1) °C, the nanocomposites formed spherical nanoparticle clusters, while at a higher synthesis temperature of 80(±1) °C, smaller NPs aggregated to form larger nanostructures (Table 4.2 and Figure 4.1).

Increasing the synthesis temperature led to a rise in silver content, accompanied by a decrease in the AgCl phase in all nanocomposites, and a decrease in the Ag_3PO_4 phase which is present only in **LE2** nanocomposites. This trend indicates a higher reduction of silver ions into silver at elevated temperatures (Table 4.2). The **LE1** extract contains a greater number of alcohol groups compared to the **LE3** extract, while the **LE2** extract lacked alcohol groups altogether. Alcohols can be oxidized to carbonyl groups, facilitating the reduction of metal ions. Hence, the nanocomposites synthesized using **LE1** extract contain higher metallic silver content compared to those synthesized using **LE2** and **LE3** extracts.

These synthesized nanocomposites also exhibited a uniform distribution of elements on their surface (Figure 4.3). The surface of **LE** nanocomposites consists majorly of carbon (55–75 wt.%), oxygen ~15–25 wt.%, and silver ~8–20 wt.%. Notably, the silver and oxygen content increased while the carbon content decreased on the surface with increasing synthesis temperature (Table 4.4). The higher temperature likely enhanced the solubility of reducing agents such as polyphenols, carbohydrates, and sugars. Concurrently, these elevated temperatures may have led to the protein denaturation and decomposition of metabolites and trace compounds of main constituents (C, H, O, N, S, P and Cl), by weakening the chemical bonds and altering their secondary, ternary and quaternary structures. These two competing processes significantly influenced the kinetics and pathways of redox reactions occurring during the synthesis of nanocomposites [182, 183].

❖ Cytotoxicity analysis of **LE** nanocomposites

Concentration-dependent cytotoxicity of **LE** nanocomposites was confirmed through Live/Dead, LDH, and MTT assays (Figures 4.8–4.12, and Table 4.8). Confocal images of the live/dead assay demonstrated that at lower concentrations, the nanocomposites inhibited cell growth, while at higher concentrations, they induced cell death in both HEK293 and HeLa cell lines (Figure 4.8). The LDH assay performed on HEK293, HeLa, A549, MCF-7, and MDA-MB-231 cells indicated a decrease in LDH activity with increasing concentration of nanocomposites against all cell lines. This suggests that the higher concentration of nanocomposites corresponds to a greater ability to inhibit cell growth (Figure 4.9). Notably, the nanocomposites synthesized at 25(±1) °C (**LE1Ag1**, **LE2Ag1**, and **LE3Ag1**) exhibited a faster rate of cell inhibition as compared to the nanocomposite synthesis at 80(±1) °C (**LE1Ag3**, **LE2Ag3**, and **LE3Ag3**). Additionally, these nanocomposites damaged the cell membrane, resulting in the release of LDH from the cells.

Biocompatibility of **LE** nanocomposites was assessed using the HEK293 cell line, where the nanocomposites demonstrated a range of toxicity towards various cancer cell lines, EC_{50} values obtained from MTT assay showing ranges of 11–35 μg ml^{-1} for HeLa and A549 cells, and 30–70 μg ml^{-1} for MCF-7 and MDA-MB-231 cells (Figure 4.10–4.12, and Table 4.8). Importantly, the nanocomposites synthesized at 80(±1) °C i.e. **LE1Ag3**, **LE2Ag3**, and **LE3Ag3** demonstrated higher biocompatibility towards HEK293 cells compared to those synthesized at 25(±1) °C i.e. **LE1Ag1**, **LE2Ag1**, and **LE3Ag1**.

The toxicity of the nanocomposites was more pronounced in HeLa and A549 cell lines than in MCF-7 and MDA-MB-231 cell lines (Figure 4.10–4.12, and Table 4.8). Although the cell lines analyzed had similar sizes, i.e. 10–15 mm, and shared compositions of nucleic acids, lipids,

proteins, and carbohydrates, variations in cellular responses to the nanocomposites cannot be solely attributed to their physicochemical properties. Factors such as dominant molecular mechanisms, the ability of the cell membrane to resist NP penetration, and the presence of different repair proteins likely contribute to these differential responses [82].

Among the tested nanocomposites, **LE2Ag1** exhibited higher cell death at lower concentrations compared to other nanocomposites, indicating its pronounced toxicity across all cell lines. This heightened cytotoxic effect can be attributed to the higher amounts of smaller-sized silver forms (Ag_{met}, AgCl, and Ag_3PO_4) present in the **LE2Ag1**, as these smaller silver forms being the source for Ag^+ ions, facilitate diffusion through size-specific channels of the membrane. In contrast, the larger silver forms can damage cell membranes, resulting in increased cytotoxicity. Furthermore, the surface of **LE2Ag1** nanocomposite contains oxygen-deficient carbon organic groups, which may weaken electrostatic repulsion between the nanocomposite and the negatively charged cell constituents, thus enhancing the penetration of NPs through the lipophilic membrane barrier. Moreover, the larger surface area of smaller, potentially positively charged NPs could facilitate the adsorption of biomolecules and catalytic processes, leading to membrane damage and disruption of cell organelles. Other nanocomposites showed higher values of EC_{50} in the 2nd phase, indicating lower cytotoxic effects on cancer cells as compared to **LE2Ag1**.

In summary, the **LE** nanocomposites synthesized displayed biocompatibility towards normal HEK293 cell line within the range where they were cytotoxic to HeLa, A549, MCF-7, and MDA-MB-231 cell lines, reflecting a complex two-step cell cytotoxicity mechanism dependent on the concentration of nanocomposites. This concentration-dependent biphasic cytotoxicity indicates the effective concentrations (EC_{50}) deduced using MTT assay for phase I corresponds to inhibition concentration (IC_{50}), and phase II corresponds to lethal concentrations (LC_{50}).

The overall cytotoxicity of the **LE** nanocomposites on the cancer cells decreased with a decrease in the content of smaller-sized silver forms (Ag, AgCl, and Ag_3PO_4), leading to a lower availability of Ag^+ ions, and a higher presence of oxygen-rich surface carbon groups, which impacted the cellular uptake. Corresponding to the different compositions of extracts used for synthesis, the variation in surface chemical properties of nanocomposites, as characterized using XPS, plays a critical role in biological response. Therefore, it is important to study the surface of nanocomposites in-depth to understand and synthesize optimized green nanocomposites for high biocompatibility and cytotoxic effects.

4.5 Conclusions

Nanocomposites with metallic silver as the major phase and AgCl as the minor phase were synthesized using dry leaves of *Malus sylvestris L.* (**LE1)**, *Pinus sylvestris L.* (**LE2)** and *Sorbus aucuparia L.* (**LE3)** extracts. Additionally, the Ag_3PO_4 phase in amounts lower than Ag and AgCl phase was also present in **LE2** nanocomposites synthesized at 25(±1) and 50(±1) °C. Increasing synthesis temperature aided the growth of metallic silver in the composite. The nanocomposites' surface was composed of organic groups present in the leaf extracts. The resulting overlayer thickness was ~ 6–8 nm. The surface of nanocomposites was enriched in oxygen compared to the bulk of nanocomposites. Nanocomposites were biocompatible to normal HEK293 cell line in the concentration range where they were cytotoxic to cancerous cells i.e. 11–35 μg ml^{-1} for HeLa and A549 cells, 36–70 μg ml^{-1} for MCF-7 and 30–53 μg ml^{-1} for MDA-MB-231 cells. Nanocomposites showed concentration-based biphasic anticancer activity towards HeLa, A549, MCF-7, and MDA-MB-231 cell lines. The nanocomposites′ concentration-dependent biphasic phase responses observed were both inhibitory phases. The anticancer activity of **LE2Ag1** nanocomposite synthesized at 25(±1) °C using **LE2** after 2 hours, determined using MTT assay in terms of lethal concentration for HEK293, was found to be 3× higher than for HeLa cells, 2× higher than for A549 cells, and almost similar for MCF-7, and MDA-MB-231 cell lines. The highest anticancer activity was exhibited by **LE2Ag1** nanocomposite due to the higher content of small-sized AgCl and Ag_3PO_4 crystallites providing Ag^+ ions, the presence of phosphorus in the nanocomposite, and the oxygen-deficient surface containing high carbon content.

5. Conclusions and future research

5.1 Major conclusions

The increasing demand for eco-friendly and cost-effective methods for nanoparticle synthesis has driven the shift toward green synthesis approaches. In green synthesis, metal nanoparticles (NPs) are produced using biological sources such as plants, plant extracts, agricultural and industrial wastes, bacteria, and fungi, which serve as natural reducing and capping agents. Among these, plants and plant-based wastes are particularly attractive due to their abundance, low cost, and environmentally friendly nature. In recent years, waste-mediated synthesis of silver and silver-based nanoparticles has gained attention, with studies showing the successful production of biocompatible nanoparticles without the use of toxic chemical reducing agents. However, despite being a major source of organic waste, the brewing industry's waste by-products have been largely overlooked as potential materials for nanoparticle synthesis. With the global production of brewery waste continuously rising, managing this waste has become a growing environmental challenge. Therefore, this study aimed to address two key issues: sustainable waste management and the development of green nanomaterials. By utilizing a large amounts of plant-based materials as reducing and stabilizing agents, this work focused on converting silver salts into silver-based nanocomposites (Ag NPs). Following synthesis and characterization of the obtained nanocomposites, their potential biomedical applications were explored.

In this work, nanocomposites were synthesized using brewery wastes (**BW**) [100, 101] and leaf extracts (**LE**) [175] using a “one-pot” synthesis method. Organic content plays a critical role in determining the reduction mechanism, capping ability of materials, and stabilization processes during nanocomposite synthesis, influencing their physicochemical properties and bioactivity. The **BW** from stages 5 (**BW5**), 7 (**BW7**) and 9 (**BW9**) and beer (**B**) were rich in bioactive compounds like carbohydrates, fermentable sugars, sulphates, nitrogen and phosphorus content whereas extracts from *Malus sylvestris L. denoted as* **LE1** and *Sorbus aucuparia L.* denoted as **LE3** were rich in polyphenols. Importantly, both brewery waste **BW5** and *Pinus sylvestris L.* leaf extract denoted as **LE2** had lower amounts of polyphenols.

The silver nanocomposites synthesized from **BW** primarily exhibited AgCl and Ag_3PO_4 as the dominant crystalline phases, accompanied by a minor fraction of metallic silver [100, 101]. Conversely, **LE**-derived nanocomposites predominantly consisted of metallic silver with trace amounts of AgCl [175]. The differences in composition between **BW** and **LE** nanocomposites are significant, as AgCl and Ag_3PO_4 can act as reservoirs for controlled Ag^+ ion release, while metallic silver exhibits different dissolution kinetics and reactivity. Elemental mapping indicated a homogenous distribution of all constituents within the nanocomposites, ensuring uniform physicochemical characteristics and stability.

X-ray Photoelectron Spectroscopy (XPS) analysis identified silver, carbon, and oxygen as the major elements present on the surfaces of all nanocomposites, with **BW**-based nanocomposites also containing trace quantities of chlorine and phosphorus [100, 101]. The presence of phosphorus and chlorine in **BW** nanocomposites suggests potential synergistic effects in cytotoxicity, as these elements can influence cellular interactions and ion transport mechanisms. A notable trend was observed wherein silver content increased proportionally with synthesis temperature, ranging from 25 to 80 °C for both **BW** and **LE** nanocomposites. This increase in silver content at higher temperatures may enhance nanocomposite stability while potentially reducing the rate of Ag^+ ion release.

Surface composition analysis further revealed that **BW** nanocomposites contained 40–60 wt.% silver, 20–40 wt.% carbon, and 10–15 wt.% oxygen [100, 101]. In contrast, **LE** nanocomposite surfaces were characterized by a predominant carbon content (55–75 wt.%), followed by oxygen (15–25 wt.%) and silver (8–20 wt.%) [175]. The lower silver content in **LE** nanocomposites suggests a more limited availability of Ag^+ ions, which could affect their antimicrobial and anticancer activities compared to **BW** nanocomposites.

Cytotoxicity evaluations demonstrated a dose-dependent response, with selective toxicity toward cancer cells. A biphasic toxicity pattern was observed: at lower concentrations (0–10 μg ml^{-1}), inhibition of cell proliferation was predominant, likely due to oxidative stress and metabolic disruption induced by Ag^+ ions. At higher concentrations (10–70 μg ml^{-1}), direct cytolytic effects occurred following approximately 30–50% inhibition, potentially due to increased membrane damage, mitochondrial dysfunction, and induction of apoptosis or necrosis.

Nanocomposites synthesized at 25(±1) °C exhibited greater cytotoxicity, resulting in enhanced cell death at lower concentrations compared to those synthesized at 80(±1) °C. This observation suggests that lower-temperature synthesis may yield nanocomposites with higher surface reactivity and enhanced Ag^+ ion release, intensifying their biological interactions. Across all tested cancer cell lines, nanocomposites demonstrated higher toxicity against HeLa and A549 cells relative to MCF-7 and MDA-MB-231 cells. The differential cytotoxicity among cell lines may be attributed to variations in cellular uptake mechanisms, intracellular antioxidant defenses, and metabolic responses to silver exposure.

Half maximal inhibition concentrations (IC_{50}s) and half maximal lethal concentrations (LC_{50}s) are usually used to evaluate the suitability and performance of drugs. The lower IC_{50} and LC_{50} values observed for **BW** nanocomposites in comparison to **LE** nanocomposites indicate their superior anticancer efficacy. This enhanced cytotoxic potential is likely attributed to the higher silver content in **BW** nanocomposites, primarily present as AgCl and Ag_3PO_4, which serve as reservoirs for Ag^+ ion release, facilitating improved cellular uptake. Additionally, the presence of phosphorus and chlorine within **BW** nanocomposites may contribute to their heightened cytotoxicity through mechanisms such as oxidative stress amplification, disruption of ion homeostasis, and interference with cellular signaling pathways.

Furthermore, all nanocomposites demonstrated biocompatibility with normal human HEK293 cells within the concentration range that exhibited cytotoxic effects on cancer cells. Synthesis temperature was found to influence nanocomposite interactions with normal cells, with those synthesized at elevated temperatures exhibiting enhanced biocompatibility. This suggests that higher-temperature synthesis may lead to more stable nanostructures with reduced Ag^+ ion leaching, thereby minimizing unintended toxicity toward healthy cells while preserving anticancer activity.

Several publications report the anticancer effect of green extracts and NPs synthesized using the green method on the respective cells. However, till now only a limited number of studies reporting the IC_{50}/EC_{50} values of green Ag NPs as anticancer agents on HEK293, HeLa, A549, MCF-7, and MDA-MB-231 cell lines have been published [184-193]. The IC_{50}/EC_{50} values obtained in the present study for the investigated cell lines were compared with those reported previously in the literature (Table 5.1).

Table 5.1 Comparison of IC_{50}/LC_{50} for **BW5Ag1** and **LE2Ag1** nanocomposites with the literature EC_{50} values. (Notation DOX – **Doxorubicin,** AE – aqueous extract, EE – ethanolic extract, ME – methanolic extract)

Cell line	Anticancer agents	*EC_{50} µg ml^{-1}	IC_{50} µg ml^{-1}	LC_{50} µg ml^{-1}	Reference
HEK293	**BW5Ag1** nanocomposite	-	**0.4**	**13.5**	present work
	LE2Ag1 nanocomposite	-	**0.5**	**32.2**	
	Ag NPs using *Rhizophora apiculata*	0.622†	-		[194]
HeLa	**BW5Ag1** nanocomposite	-	**0.3**	**7.3**	present work
	LE2Ag1 nanocomposite	-	**0.8**	**11.4**	
	C. Gloeosporioides AE	176.20	-		[184]
	Ag NPs using *Rhizophora apiculata*	1.98†			[194]
	Polyvinyl pyrrolidone coated Ag NPs	3.43			[83]
	Ag NPs using *Guignardia mangiferae*	27.54			[93]
	Erythrina abyssinica AE	13.8			[185]
	Gallic acid	13.44			[186]
	Methyl gallate	16.55			
	Cisplatin	8.04			
	Ganoderma resinaceum AE	140			[187]
	DOX	3.64			[185]
A549	**BW5Ag1** nanocomposite	-	**0.7**	**11.3**	present work
	LE2Ag1 nanocomposite	-	**0.8**	**14**	
	Ag NPs using *Avecinnia marina*	50	-		[84]
	Bark of Beilschmiedia kunstleri Gamble AE	44.74			[188]
MCF-7	**BW5Ag1** nanocomposite	-	**0.9**	**17.5**	present work
	LE2Ag1 nanocomposite	-	**0.5**	**36.8**	
	Polyvinyl pyrrolidone coated Ag NPs	3.06	-		[83]
	Ag NPs using *Guignardia mangiferae*	23.84			[93]
	Green ZnO-NPs (20–80 nm)	11.16			[189]
	Abutilon theophrasti EE	505.8			[190]

	Erythrina abyssinica AE	11.4			[185]
	T. Sanguinea AE	36.33			[191]
	Phenolic part of T. Sanguinea AE	11.14			
	DOX	2.97			[185]
MDA-MB-231	**BW5Ag1** nanocomposite	**-**	**0.3**	**13.9**	present work
	LE2Ag1 nanocomposite	**-**	**2.6**	**30.4**	
	Polyvinyl pyrrolidone coated Ag NPs	2.62	-		[83]
	Ag NPs using *Bacillus funiculus*	8.7			[85]
	P. Oxalicum extract AE	260.627			[192]
	Green ZnO-NPs (20–80 nm)	60.08			[189]
	C. Europaea extract AE	43.62			[193]

* Single phase response of a drug to cells were considered as EC_{50} values in literature

† Ag NPs were 3× times more toxic to HEK293 cells as compared to HeLa cells. Hence, they are toxic to humans.

Superior anticancer performance of nanocomposite synthesized at 25 °C using stage 5 brewery waste, **BW5Ag1** was observed compared to all other nanocomposites synthesized using **BW** and **LE**. Furthermore, nanocomposite synthesized at 25 °C using extract of *Pinus sylvestris L.*, **LE2Ag1** showed better efficacy compared to all other **LE** nanocomposites. Therefore, these two nanocomposites have been used for comparison with literature data. **BW5Ag1** nanocomposite is more effective compared to the most nanoparticles except for chemically synthesized polyvinyl pyrrolidone (PVP) coated Ag NPs against all cancer cell lines. **LE2Ag1** efficiency was higher than green extracts. Both nanocomposites exhibited slightly weaker activity than the commercial anticancer drug **Doxorubicin** (DOX). **LE2Ag1** was more effective for MDA-MB-231 cells compared to the green ZnO-NPs. This extensive comparison shows the efficacy of nanocomposites synthesized using **BW** and **LE** can be potential candidates for cancer treatment with some further optimization.

5.2 Future research pathways

Silver nanoparticles have demonstrated a remarkable potential in cancer treatment due to their unique physicochemical properties and anticancer activity. However, to fully harness their therapeutic potential, future research must focus on several key areas. One major challenge is the lack of comprehensive understanding of the mechanisms underlying the selective cytotoxicity of Ag NPs toward cancer cells while sparing healthy tissues. While the current study highlights the cytotoxic effects of nanocomposites on cells, it does not delve deeply into

the mechanistic pathways underlying these effects. Further investigations are necessary to elucidate the qualitative and quantitative mechanisms associated with cell damage and death. Especially, the influence of ROS of nanocomposites has not been explored in this study, although indirect findings suggest a correlation between cytotoxicity and the amount of positively charged silver present in nanocomposites, which facilitates and enhances the formation of bonds with negatively charged hydrolyzed carbon-oxygen forms of biomolecules and their damaged counterparts in cancer cells, leading to further disruption. Further studies will focus on quantifying the contribution of ROS to cell death, which may vary depending on the specific cancer cell type and treatment conditions.

Additionally, the long-term biocompatibility, biodistribution, and potential toxicity of Ag NPs in vivo are not well-established. Extensive in-vivo studies are essential to evaluate the biodistribution, accumulation, and clearance of Ag NPs, as well as their interaction with the immune system and tumor microenvironment. Furthermore, there is a limited research on the interaction of Ag NPs with the tumor microenvironment and their potential to overcome drug resistance. Addressing these gaps is crucial for the successful translation of Ag NP-based therapies from the laboratory to clinical settings.

With regards to the nanomaterials' material chemistry, standardization of synthesis methods, surface functionalization strategies, and dosage optimization are also needed to ensure reproducibility and safety. The size and shape of Ag NPs play a vital role in their cellular uptake, biodistribution, and cytotoxicity. Future research should focus on precisely controlling the morphology of nanoparticles to enhance their interaction with cancer cells and improve penetration into solid tumors. Understanding the intricate balance between reduction mechanisms and the structural changes occurring during synthesis is essential for optimizing these materials for specific applications. Future studies would aim to understand the structural changes during synthesis and their impact on anticancer efficacy. One of the major challenges in Ag NP-based therapy is improving anticancer activity while minimizing toxicity to healthy cells. Functionalizing the surface with biocompatible organic layers, such as polyethylene glycol (PEG) or chitosan, can enhance stability and reduce immunogenicity. Additionally, targeting ligands can be incorporated to improve specificity toward cancer cells. By addressing these critical research gaps, Ag NPs can be developed as a more effective, targeted, and minimally invasive platform for the future cancer treatments.

References

[1] R. Baskar, R. Lee Ka Fau - Yeo, K.-W. Yeo R Fau - Yeoh, K.W. Yeoh, Cancer and radiation therapy: current advances and future directions, (1449-1907 (Electronic)).
[2] C.B. Blackadar, Historical review of the causes of cancer, (2218-4333 (Print)).
[3] G.B. Faguet, A brief history of cancer: Age-old milestones underlying our current knowledge database, International Journal of Cancer 136(9) (2015) 2022-2036.
[4] Cancer Characteristics, Definitions, and Recent Investigations. https://www.cdc.gov/cancer-environment/php/guidelines/characteristics.html. (Accessed June 20, 2023).
[5] G.M. Cooper, The Cell: A Molecular Approach, 2nd edition ed., Sunderland (MA): Sinauer Associates2000.
[6] S.H. Care, What Causes Cancer? https://stanfordhealthcare.org/medical-conditions/cancer/cancer/cancer-causes.html. (Accessed June 25, 2023).
[7] N.C. Institute, Cancer Classification. https://training.seer.cancer.gov/disease/categories/classification.html. (Accessed June 25, 2023).
[8] G. de Pinieux, M. Karanian, F. Le Loarer, S. Le Guellec, S. Chabaud, P. Terrier, C. Bouvier, M. Batistella, A. Neuville, Y.M. Robin, J.F. Emile, A. Moreau, F. Larousserie, A. Leroux, N. Stock, M. Lae, F. Collin, N. Weinbreck, S. Aubert, F. Mishellany, C. Charon-Barra, S. Croce, L. Doucet, I. Quintin-Rouet, M.C. Chateau, C. Bazille, I. Valo, B. Chetaille, N. Ortonne, A. Brouchet, P.A.-O. Rochaix, A. Demuret, J.P. Ghnassia, L. Mescam, N. Macagno, I. Birtwisle-Peyrottes, C. Delfour, E. Angot, I. Pommepuy, D. Ranchere, C. Chemin-Airiau, M. Jean-Denis, Y. Fayet, J.B. Courrèges, N. Mesli, J. Berchoud, M. Toulmonde, A. Italiano, A. Le Cesne, N. Penel, F. Ducimetiere, F. Gouin, J.M. Coindre, J.A.-O.X. Blay, Nationwide incidence of sarcomas and connective tissue tumors of intermediate malignancy over four years using an expert pathology review network, (1932-6203 (Electronic)).
[9] A.A.f.C. Research, Experts Forecast Cancer Research and Treatment Advances in 2023. https://www.aacr.org/blog/2023/01/13/experts-forecast-cancer-research-and-treatment-advances-in-2023/. (Accessed June 30, 2023).
[10] M. Clinic, Cervical cancer. https://www.mayoclinic.org/diseases-conditions/cervical-cancer/symptoms-causes/syc-20352501. (Accessed July 03, 2023).
[11] What Is Cervical Cancer? https://www.cancer.gov/types/cervical. (Accessed July 03, 2023).
[12] U.S.C.f.D.C.a. Prevention, Cervical Cancer Basics. https://www.cdc.gov/cancer/cervical/basic_info/index.htm. (Accessed July 03, 2023).
[13] Wikipedia, HeLa. https://en.wikipedia.org/wiki/HeLa. (Accessed July 03, 2023).
[14] J.H. Medicine, The Legacy of Henrietta Lacks. https://www.hopkinsmedicine.org/henrietta-lacks. (Accessed July 03, 2023).
[15] R. Nott, HeLa Cell Line, Embryo Project Encyclopedia (2020-09-18), Arizona State University. School of Life Sciences. Center for Biology and Society. Embryo Project Encyclopedia.
[16] G. Menon, F.M. Alkabban, T. Ferguson, Breast Cancer, StatPearls [Internet]. Treasure Island (FL): StatPearls Publishing (2024).
[17] N.C.I. (NIH), Introduction to Breast Cancer. https://training.seer.cancer.gov/breast/intro/. (Accessed July 03, 2023).
[18] A.C. Society, Treating Breast Cancer. https://www.cancer.org/cancer/types/breast-cancer/treatment.html. (Accessed July 03, 2023).

[19] C. Gest, U. Joimel, L. Huang, L.-L. Pritchard, A. Petit, C. Dulong, C. Buquet, C.-Q. Hu, P. Mirshahi, M. Laurent, F. Fauvel-Lafève, L. Cazin, J.-P. Vannier, H. Lu, J. Soria, H. Li, R. Varin, C. Soria, Rac3 induces a molecular pathway triggering breast cancer cell aggressiveness: differences in MDA-MB-231 and MCF-7 breast cancer cell lines, BMC Cancer 13(1) (2013) 63.
[20] F. Jokar, J.A. Mahabadi, M. Salimian, A. Taherian, S.M.G. Hayat, A. Sahebkar, M.A. Atlasi, Differential Expression of HSP90β in MDA-MB-231 and MCF-7 Cell Lines after Treatment with Doxorubicin, (2093-6966 (Print)).
[21] T.A. Theodossiou, M. Ali, M. Grigalavicius, B. Grallert, P. Dillard, K.O. Schink, C.E. Olsen, S. Wälchli, E.M. Inderberg, A. Kubin, Q. Peng, K. Berg, Simultaneous defeat of MCF7 and MDA-MB-231 resistances by a hypericin PDT–tamoxifen hybrid therapy, npj Breast Cancer 5(1) (2019) 13.
[22] U.o.R.M.C. Rochester, Lung Cancer: Introduction. https://www.urmc.rochester.edu/encyclopedia/content.aspx?contenttypeid=34&contentid=16333-1. (Accessed July 03, 2023).
[23] H. Lemjabbar-Alaoui, O.U. Hassan, Y.W. Yang, P. Buchanan, Lung cancer: Biology and treatment options, (0006-3002 (Print)).
[24] D.J. Giard, S.A. Aaronson, G.J. Todaro, P. Arnstein, J.H. Kersey, H. Dosik, W.P. Parks, In Vitro Cultivation of Human Tumors: Establishment of Cell Lines Derived From a Series of Solid Tumors2, JNCI: Journal of the National Cancer Institute 51(5) (1973) 1417-1423.
[25] T. Thenrajan, S. Alwarappan, J. Wilson, Molecular Diagnosis and Cancer Prognosis-A Concise Review. LID - 10.3390/diagnostics13040766 [doi] LID - 766, (2075-4418 (Print)).
[26] A. Imran, H.Y. Qamar, Q. Ali, H. Naeem, M. Riaz, S. Amin, N. Kanwal, F. Ali, M.F. Sabar, I.A. Nasir, Role of Molecular Biology in Cancer Treatment: A Review Article, (2251-6085 (Print)).
[27] S. Sethi, S. Ali, P.A. Philip, F.H. Sarkar, Clinical Advances in Molecular Biomarkers for Cancer Diagnosis and Therapy, International Journal of Molecular Sciences 14(7) (2013) 14771-14784.
[28] Cancer Diagnosis Research. https://www.cancer.gov/research/areas/diagnosis. (Accessed June 25, 2023).
[29] S. Chakraborty, T. Rahman, The difficulties in cancer treatment, (1754-6605 (Electronic)).
[30] Treatment Types. https://www.cancer.org/cancer/managing-cancer/treatment-types.html. (Accessed July 2, 2023).
[31] A.R. Bagheri, N. Aramesh, M. Bilal, J. Xiao, H.W. Kim, B. Yan, Carbon nanomaterials as emerging nanotherapeutic platforms to tackle the rising tide of cancer - A review, (1464-3391 (Electronic)).
[32] D.A.-O. Debela, S.G. Muzazu, K.D. Heraro, M.T. Ndalama, B.W. Mesele, D.C. Haile, S.K. Kitui, T.A.-O. Manyazewal, New approaches and procedures for cancer treatment: Current perspectives, (2050-3121 (Print)).
[33] I.F. Tannock, Conventional cancer therapy: promise broken or promise delayed?, (0140-6736 (Print)).
[34] A.R. Bagheri, N. Aramesh, M. Bilal, J. Xiao, H.-W. Kim, B. Yan, Carbon nanomaterials as emerging nanotherapeutic platforms to tackle the rising tide of cancer – A review, Bioorganic & Medicinal Chemistry 51 (2021) 116493.
[35] S. Mosleh-Shirazi, M. Abbasi, M.R. Moaddeli, A. Vaez, M. Shafiee, S.R. Kasaee, A.M. Amani, S. Hatam, Nanotechnology Advances in the Detection and Treatment of Cancer: An Overview, (2206-7418 (Electronic)).
[36] S. Gavas, S. Quazi, T.A.-O. Karpiński, Nanoparticles for Cancer Therapy: Current Progress and Challenges, (1931-7573 (Print)).

[37] M. Overchuk, R.A. Weersink, B.C. Wilson, G. Zheng, Photodynamic and Photothermal Therapies: Synergy Opportunities for Nanomedicine, ACS Nano 17(9) (2023) 7979-8003.
[38] T.A.-O. Pivetta, C.A.-O. Botteon, P.A.-O. Ribeiro, P.D. Marcato, M.A.-O. Raposo, Nanoparticle Systems for Cancer Phototherapy: An Overview. LID - 10.3390/nano11113132 [doi] LID - 3132, (2079-4991 (Print)).
[39] Y.A.-O. Hou, X.A.-O. Yang, R.Q. Liu, D. Zhao, C.X. Guo, A.C. Zhu, M.N. Wen, Z.A.-O. Liu, G.F. Qu, H.A.-O. Meng, Pathological Mechanism of Photodynamic Therapy and Photothermal Therapy Based on Nanoparticles, (1178-2013 (Electronic)).
[40] H.A.-O. Han, K.A.-O. Choi, Advances in Nanomaterial-Mediated Photothermal Cancer Therapies: Toward Clinical Applications. LID - 10.3390/biomedicines9030305 [doi] LID - 305, (2227-9059 (Print)).
[41] J.J. Xu, W.C. Zhang, Y.W. Guo, X.A.-O. Chen, Y.N. Zhang, Metal nanoparticles as a promising technology in targeted cancer treatment, (1521-0464 (Electronic)).
[42] S. Jain, J.M. Hirst Dg Fau - O'Sullivan, J.M. O'Sullivan, Gold nanoparticles as novel agents for cancer therapy, Br J Radiol. 85(1010):101-13(1748-880X (Electronic)).
[43] J. Peng, X. Liang, Progress in research on gold nanoparticles in cancer management, (1536-5964 (Electronic)).
[44] S. Chien, Could gold nanoparticles help treat cancer? https://www.mdanderson.org/cancerwise/could-gold-nanoparticles-help-treat-cancer.h00-159540534.html. (Accessed July 5, 2023).
[45] S.A.-O. Anjum, M. Hashim, S.A. Malik, M. Khan, J.A.-O. Lorenzo, B.A.-O. Abbasi, C.A.-O. Hano, Recent Advances in Zinc Oxide Nanoparticles (ZnO NPs) for Cancer Diagnosis, Target Drug Delivery, and Treatment. LID - 10.3390/cancers13184570 [doi] LID - 4570, (2072-6694 (Print)).
[46] S. Ibraheem, A.A. Kadhim, K.A. Kadhim, I.A. Kadhim, M. Jabir, Zinc Oxide Nanoparticles as Diagnostic Tool for Cancer Cells, International Journal of Biomaterials 2022 (2022) 2807644.
[47] G. Bisht, S. Rayamajhi, ZnO Nanoparticles: A Promising Anticancer Agent, (1849-5435 (Print)).
[48] F. Soetaert, P. Korangath, D. Serantes, S. Fiering, R. Ivkov, Cancer therapy with iron oxide nanoparticles: Agents of thermal and immune therapies, (1872-8294 (Electronic)).
[49] M.V. Shestovskaya, A.L. Luss, O.A. Bezborodova, V.V. Makarov, A.A. Keskinov, Iron Oxide Nanoparticles in Cancer Treatment: Cell Responses and the Potency to Improve Radiosensitivity, Pharmaceutics 15(10) (2023) 2406.
[50] S.A.-O. Çeşmeli, C.A.-O. Biray Avci, Application of titanium dioxide (TiO(2)) nanoparticles in cancer therapies, (1029-2330 (Electronic)).
[51] C. Zarzzeka, J. Goldoni, F. Marafon, W.G. Sganzerla, T. Forster-Carneiro, M.D. Bagatini, L.M.S. Colpini, Use of titanium dioxide nanoparticles for cancertreatment: A comprehensive review and bibliometric analysis, Biocatalysis and Agricultural Biotechnology 50 (2023) 102710.
[52] S. Sargazi, S. Er, S. Sacide Gelen, A. Rahdar, M. Bilal, R. Arshad, N. Ajalli, M. Farhan Ali Khan, S. Pandey, Application of titanium dioxide nanoparticles in photothermal and photodynamic therapy of cancer: An updated and comprehensive review, Journal of Drug Delivery Science and Technology 75 (2022) 103605.
[53] D.A.-O. Kovács, N.A.-O. Igaz, M.K. Gopisetty, M.A.-O. Kiricsi, Cancer Therapy by Silver Nanoparticles: Fiction or Reality? LID - 10.3390/ijms23020839 [doi] LID - 839, (1422-0067 (Electronic)).
[54] H.A.-O. Gomes, C.A.-O. Martins, J.A.-O.X. Prior, Silver Nanoparticles as Carriers of Anticancer Drugs for Efficient Target Treatment of Cancer Cells. LID - 10.3390/nano11040964 [doi] LID - 964, (2079-4991 (Print)).

[55] J.J. Milligan, S. Saha, A Nanoparticle’s Journey to the Tumor: Strategies to Overcome First-Pass Metabolism and Their Limitations, Cancers 14(7) (2022) 1741.
[56] C. Liao, Y. Li, S.C. Tjong, Bactericidal and Cytotoxic Properties of Silver Nanoparticles, Int J Mol Sci 20(2) (2019).
[57] I.L. Hsiao, Y.K. Hsieh, C.F. Wang, I.C. Chen, Y.J. Huang, Trojan-horse mechanism in the cellular uptake of silver nanoparticles verified by direct intra- and extracellular silver speciation analysis, Environ Sci Technol 49(6) (2015) 3813-21.
[58] M.M. Rohde, C.M. Snyder, J. Sloop, S.R. Solst, G.L. Donati, D.R. Spitz, C.M. Furdui, R. Singh, The mechanism of cell death induced by silver nanoparticles is distinct from silver cations, Particle and Fibre Toxicology 18(1) (2021) 37.
[59] A. Kessler, J. Hedberg, E. Blomberg, I. Odnevall, Reactive Oxygen Species Formed by Metal and Metal Oxide Nanoparticles in Physiological Media– A Review of Reactions of Importance to Nanotoxicity and Proposal for Categorization, Nanomaterials 12(11) (2022) 1922.
[60] M. Ahamed, M.S. Alsalhi, M.K. Siddiqui, Silver nanoparticle applications and human health, Clin Chim Acta 411(23-24) (2010) 1841-8.
[61] E.E. Frohlich, E. Frohlich, Cytotoxicity of Nanoparticles Contained in Food on Intestinal Cells and the Gut Microbiota, Int J Mol Sci 17(4) (2016) 509.
[62] P. Sokołowska, K. Białkowska, M. Siatkowska, M. Rosowski, M. Kucińska, P. Komorowski, K. Makowski, B. Walkowiak, Human brain endothelial barrier cells are distinctly less vulnerable to silver nanoparticles toxicity than human blood vessel cells: A cell-specific mechanism of the brain barrier?, Nanomed.: Nanotechnol. Biol. Med. 13(7) (2017) 2127-2130.
[63] L.M. Stabryla, K.A. Johnston, J.E. Millstone, L.M. Gilbertson, Emerging investigator series: it's not all about the ion: support for particle-specific contributions to silver nanoparticle antimicrobial activity, Environmental Science: Nano 5(9) (2018) 2047-2068.
[64] X.F. Zhang, W. Shen, S. Gurunathan, Silver Nanoparticle-Mediated Cellular Responses in Various Cell Lines: An in Vitro Model. LID - 10.3390/ijms17101603 [doi] LID - 1603, (1422-0067 (Electronic)).
[65] S. Gliga Ar Fau - Skoglund, I.O. Skoglund S Fau - Wallinder, B. Wallinder Io Fau - Fadeel, H.L. Fadeel B Fau - Karlsson, H.L. Karlsson, Size-dependent cytotoxicity of silver nanoparticles in human lung cells: the role of cellular uptake, agglomeration and Ag release, (1743-8977 (Electronic)).
[66] <Size-dependent cytotoxicity of silver-imp.pdf>.
[67] R.A.-O. Canaparo, F.A.-O. Foglietta, T.A.-O. Limongi, L.A.-O. Serpe, Biomedical Applications of Reactive Oxygen Species Generation by Metal Nanoparticles. LID - 10.3390/ma14010053 [doi] LID - 53, (1996-1944 (Print)).
[68] H. Malekzad, P.S. Zangabad, H. Mirshekari, M. Karimi, M.R. Hamblin, Noble metal nanoparticles in biosensors: recent studies and applications, (2191-9089 (Print)).
[69] P.K. Jain, X. Huang, I.H. El-Sayed, M.A. El-Sayed, Noble Metals on the Nanoscale: Optical and Photothermal Properties and Some Applications in Imaging, Sensing, Biology, and Medicine, Accounts of Chemical Research 41(12) (2008) 1578-1586.
[70] Y. Qing, L. Cheng, R. Li, G. Liu, Y. Zhang, X. Tang, J. Wang, H. Liu, Y. Qin, Potential antibacterial mechanism of silver nanoparticles and the optimization of orthopedic implants by advanced modification technologies, (1178-2013 (Electronic)).
[71] M.J. Lee, M.B. Yaffe, Protein Regulation in Signal Transduction. LID - 10.1101/cshperspect.a005918 [doi] LID - a005918, (1943-0264 (Electronic)).
[72] O. Kerber, J. Tran, A. Misiaszek, A. Chorążewska, W. Bal, A. Krężel, Zn(II) to Ag(I) Swap in Rad50 Zinc Hook Domain Leads to Interprotein Complex Disruption through the Formation of Highly Stable Agx(Cys)y Cores, Inorganic Chemistry 62(10) (2023) 4076-4087.

[73] M. Akter, M.T. Sikder, M.M. Rahman, A. Ullah, K.F.B. Hossain, S. Banik, T. Hosokawa, T. Saito, M. Kurasaki, A systematic review on silver nanoparticles-induced cytotoxicity: Physicochemical properties and perspectives, (2090-1232 (Print)).
[74] T. Zhang, Q. Wang L Fau - Chen, C. Chen Q Fau - Chen, C. Chen, Cytotoxic potential of silver nanoparticles, (1976-2437 (Electronic)).
[75] K.M. Fahy, M.K. Eiken, K.V. Baumgartner, K.Q. Leung, S.E. Anderson, E. Berggren, E. Bouzos, L.R. Schmitt, P. Asuri, K.E. Wheeler, Silver Nanoparticle Surface Chemistry Determines Interactions with Human Serum Albumin and Cytotoxic Responses in Human Liver Cells, ACS Omega 8(3) (2023) 3310-3318.
[76] A. Alquraini, J. El Khoury, Scavenger receptors, (1879-0445 (Electronic)).
[77] I.A. Zani, S.L. Stephen, N.A. Mughal, D. Russell, S. Homer-Vanniasinkam, S.B. Wheatcroft, S. Ponnambalam, Scavenger receptor structure and function in health and disease, (2073-4409 (Print)).
[78] J. Depciuch, E. Barnaś, J. Skręt-Magierło, A. Skręt, E. Kaznowska, K. Łach, P. Jakubczyk, J. Cebulski, Spectroscopic evaluation of carcinogenesis in endometrial cancer, Sci. Rep. 11(1) (2021) 9079.
[79] C. Liu, Y. Zhang, X. Yan, X. Zhang, C. Li, W. Yang, D. Shi, Infrared absorption of human breast tissues in vitro, J. Lumin. 119-120 (2006) 132-136.
[80] S. Rehman, Z. Movasaghi, A.T. Tucker, S.P. Joel, J.A. Darr, A.V. Ruban, I.U. Rehman, Raman spectroscopic analysis of breast cancer tissues: identifying differences between normal, invasive ductal carcinoma and ductal carcinoma in situ of the breast tissue, J Raman Spectrosc. 38(10) (2007) 1345-1351.
[81] I.P. Santos, C.B. Martins, L.A.E. Batista de Carvalho, M.P.M. Marques, A.L.M. Batista de Carvalho, Who's Who? Discrimination of Human Breast Cancer Cell Lines by Raman and FTIR Microspectroscopy, Cancers (Basel) 14(2) (2022).
[82] A.C. Martínez-Torres, D.G. Zarate-Triviño, H.Y. Lorenzo-Anota, A. Ávila-Ávila, C. Rodríguez-Abrego, C. Rodríguez-Padilla, Chitosan gold nanoparticles induce cell death in HeLa and MCF-7 cells through reactive oxygen species production, Int J Nanomedicine (2018) 3235-3250.
[83] E.G. K Juarez-Moreno, N Giro´n-Vazquez, RA Cha´vez-Santoscoy, JD Mota-Morales, LL Perez-Mozqueda, MR Garcia-Garcia, A Pestryakov, N Bogdanchikova, Comparison of cytotoxicity and genotoxicity effects of silver nanoparticles on human cervix and breast cancer cell lines, Hum Exp Toxicol. 36(9) (2017) 931- 948.
[84] K.S. Shan Tian, Ramzi A. Mothana, Govindan Ramachandran, Govindan Rajivgandhi, Natesan Manoharan, Anti-cancer activity of biosynthesized silver nanoparticles using Avicennia marina against A549 lung cancer cells through ROS/mitochondrial damages, Saudi J. Biol. Sci. 27 (2020) 3018–3024.
[85] J.H. Sangiliyandi Gurunathan, Vasuki Eppakayala, Muniyandi Jeyaraj, Jin-Hoi Kim, Cytotoxicity of Biologically Synthesized Silver Nanoparticles in MDA-MB-231 Human Breast Cancer Cells, Biomed Res Int. 2013:535796 (2013).
[86] M.K. Jadwiga Jodynis-Liebert, Biphasic Dose-Response Induced by Phytochemicals: Experimental Evidence, J. Clin. Med. 9 (2020) 718.
[87] L.F. Ivo Iavicoli, Veruscka Lesoa, Edward J. Calabrese, Hormetic dose–responses in nanotechnology studies, Sci. Total Environ. 47 (2014) 361–374.
[88] V.L. Ivo Iavicoli, Luca Fontana, Edward J. Calabrese, Nanoparticle Exposure and Hormetic Dose–Responses: An Update, Int. J. Mol. Sci. 19 (2018) 805.
[89] E.J.C. Marc A. Nascarella, Barbara D. Beck, Quantifying Hormetic (Biphasic) Dose-Responses in the Assessment of Nanoparticle Toxicology, International Conference on the Environmental Implications and Applications of Nanotechnology, 2009.

[90] J. Shen, L. Li, N.G. Howlett, P.S. Cohen, G. Sun, Application of a Biphasic Mathematical Model of Cancer Cell Drug Response for Formulating Potent and Synergistic Targeted Drug Combinations to Triple Negative Breast Cancer Cells, Cancers (Basel) 12(5) (2020).
[91] Y. Xie, D. Liu, C. Cai, X. Chen, Y. Zhou, L. Wu, Y. Sun, H. Dai, X. Kong, P. Liu, Size-dependent cytotoxicity of Fe3O4 nanoparticles induced by biphasic regulation of oxidative stress in different human hepatoma cells, Int J Nanomedicine 11 (2016) 3557-70.
[92] W. Yang, L. Wang, E.M. Mettenbrink, P.L. DeAngelis, S. Wilhelm, Nanoparticle Toxicology, Annu. Rev. Pharmacol. Toxicol. 61(1) (2021) 269-289.
[93] M.D. Balakumaran, R. Ramachandran, P.T. Kalaichelvan, Exploitation of endophytic fungus, Guignardia mangiferae for extracellular synthesis of silver nanoparticles and their in vitro biological activities, Microbiol Res 178 (2015) 9-17.
[94] E.P. Stater, A.Y. Sonay, C. Hart, J. Grimm, The ancillary effects of nanoparticles and their implications for nanomedicine, Nat. Nanotechnol. 16(11) (2021) 1180-1194.
[95] A.C. Burdusel, Gherasim, O., Grumezescu, A. M., Mogoanta, L., Ficai, A., Andronescu, E., Biomedical Applications of Silver Nanoparticles: An Up-to-Date Overview, Nanomaterials 8(9) (2018).
[96] K.C. Hembram, Kumar, R., Kandha, L., Parhi, P. K., Kundu, C. N., Bindhani, B. K., Therapeutic prospective of plant-induced silver nanoparticles: application as antimicrobial and anticancer agent, Artif Cells Nanomed Biotechnol 46(sup3) (2018) S38-S51.
[97] V. da Silva Ferreira, ConzFerreira, M. E., Lima, L. M., Frases, S., de Souza, W., Sant'Anna, C., Green production of microalgae-based silver chloride nanoparticles with antimicrobial activity against pathogenic bacteria, Enzyme Microb Technol 97 (2017) 114-121.
[98] M. Zhao, Y. Fang, L. Ma, X. Zhu, L. Jiang, M. Li, Q. Han, Synthesis, characterization and in vitro antibacterial mechanism study of two Keggin-type polyoxometalates, J. Inorg. Biochem. 210 (2020) 111131.
[99] S.P. Deshmukh, S.M. Patil, S.B. Mullani, S.D. Delekar, Silver nanoparticles as an effective disinfectant: A review, Mater Sci Eng C Mater Biol Appl 97 (2019) 954-965.
[100] N.V. Rangam, A.J. Sudagar, A. Ruszczak, P. Borowicz, J. Tóth, L. Kövér, D. Michałowska, M. Roszko, K.R. Noworyta, B. Lesiak, Valorizing the Unexplored Filtration Waste of Brewing Industry for Green Silver Nanocomposite Synthesis, Nanomaterials 12(3) (2022).
[101] A.J. Sudagar, N.V. Rangam, A. Ruszczak, P. Borowicz, J. Tóth, L. Kövér, D. Michałowska, M.Ł. Roszko, K.R. Noworyta, B. Lesiak, Valorization of Brewery Wastes for the Synthesis of Silver Nanocomposites Containing Orthophosphate, Nanomaterials 11(10) (2021) 2659.
[102] S.A.-O. Kaabipour, S.A.-O. Hemmati, A review on the green and sustainable synthesis of silver nanoparticles and one-dimensional silver nanostructures, (2190-4286 (Print)).
[103] L. Xu, Y.Y. Wang, J. Huang, C.Y. Chen, Z.X. Wang, H. Xie, Silver nanoparticles: Synthesis, medical applications and biosafety, (1838-7640 (Electronic)).
[104] B. Pucelik, A. Sułek, M. Borkowski, A. Barzowska, M. Kobielusz, J.M. Dąbrowski, Synthesis and Characterization of Size- and Charge-Tunable Silver Nanoparticles for Selective Anticancer and Antibacterial Treatment, ACS Applied Materials & Interfaces 14(13) (2022) 14981-14996.
[105] N.T.K. Thanh, N. Maclean, S. Mahiddine, Mechanisms of Nucleation and Growth of Nanoparticles in Solution, Chemical Reviews 114(15) (2014) 7610-7630.
[106] J. Lee, J. Yang, S.G. Kwon, T. Hyeon, Nonclassical nucleation and growth of inorganic nanoparticles, Nature Reviews Materials 1(8) (2016) 16034.

[107] M. Khan, M.R. Shaik, S.F. Adil, S.T. Khan, A. Al-Warthan, M.R.H. Siddiqui, M.N. Tahir, W. Tremel, Plant extracts as green reductants for the synthesis of silver nanoparticles: lessons from chemical synthesis, Dalton Transactions 47(35) (2018) 11988-12010.
[108] S. Mourdikoudis, L.M. Liz-Marzán, Oleylamine in Nanoparticle Synthesis, Chemistry of Materials 25(9) (2013) 1465-1476.
[109] V. Montes-García, I. Pérez-Juste J Fau - Pastoriza-Santos, L.M. Pastoriza-Santos I Fau - Liz-Marzán, L.M. Liz-Marzán, Metal nanoparticles and supramolecular macrocycles: a tale of synergy, (1521-3765 (Electronic)).
[110] M.R. Chitsazi, H. Korbekandi, G. Asghari, R. Bahri Najafi, A. Badii, S. Iravani, Synthesis of silver nanoparticles using methanol and dichloromethane extracts of Pulicaria gnaphalodes (Vent.) Boiss. aerial parts, (2169-141X (Electronic)).
[111] K. Pal, S. Chakroborty, N. Nath, Limitations of nanomaterials insights in green chemistry sustainable route: Review on novel applications, Green Processing and Synthesis 11(1) (2022) 951-964.
[112] P.C. Ray, P.P. Yu H Fau - Fu, P.P. Fu, Toxicity and environmental risks of nanomaterials: challenges and future needs, (1532-4095 (Electronic)).
[113] M.A. Kakakhel, W. Sajjad, F. Wu, N. Bibi, K. Shah, Z. Yali, W. Wang, Green synthesis of silver nanoparticles and their shortcomings, animal blood a potential source for silver nanoparticles: A review, Journal of Hazardous Materials Advances 1 (2021) 100005.
[114] M. Khoshnamvand, Z. Hao, O.O. Fadare, P. Hanachi, Y. Chen, J. Liu, Toxicity of biosynthesized silver nanoparticles to aquatic organisms of different trophic levels, Chemosphere 258 (2020) 127346.
[115] R. Hamid-Reza, D. Mohsen, Nanoparticle Synthesis, Applications, and Toxicity, in: S. Margarita, Z. Roumen (Eds.), Applications of Nanobiotechnology, IntechOpen, Rijeka, 2019, p. Ch. 1.
[116] P.G. Jamkhande, N.W. Ghule, A.H. Bamer, M.G. Kalaskar, Metal nanoparticles synthesis: An overview on methods of preparation, advantages and disadvantages, and applications, Journal of Drug Delivery Science and Technology 53 (2019) 101174.
[117] P.T. Anastas, J.C. Warner, Green Chemistry: Theory and Practice, Oxford University Press2000.
[118] J. Singh, T. Dutta, K.H. Kim, M. Rawat, P. Samddar, P.A.-O. Kumar, 'Green' synthesis of metals and their oxide nanoparticles: applications for environmental remediation, (1477-3155 (Electronic)).
[119] V.V. Makarov, A.J. Love, O.V. Sinitsyna, S.S. Makarova, I.V. Yaminsky, M.E. Taliansky, N.O. Kalinina, "Green" nanotechnologies: synthesis of metal nanoparticles using plants, (2075-8251 (Print)).
[120] D. Hebbalalu, J. Lalley, M.N. Nadagouda, R.S. Varma, Greener Techniques for the Synthesis of Silver Nanoparticles Using Plant Extracts, Enzymes, Bacteria, Biodegradable Polymers, and Microwaves, ACS Sustainable Chemistry & Engineering 1(7) (2013) 703-712.
[121] L.M. Carrillo-López, R.M. Soto-Hernández, H.A. Zavaleta-Mancera, A.R. Vilchis-Néstor, Study of the Performance of the Organic Extracts of Chenopodium ambrosioides for Ag Nanoparticle Synthesis, Journal of Nanomaterials 2016 (2016) 4714162.
[122] S. Shahzadi, S. Fatima, Q. ul ain, Z. Shafiq, M.R.S.A. Janjua, A review on green synthesis of silver nanoparticles (SNPs) using plant extracts: a multifaceted approach in photocatalysis, environmental remediation, and biomedicine, RSC Advances 15(5) (2025) 3858-3903.
[123] M. Fahim, A. Shahzaib, N. Nishat, A. Jahan, T.A. Bhat, A. Inam, Green synthesis of silver nanoparticles: A comprehensive review of methods, influencing factors, and applications, JCIS Open 16 (2024) 100125.

[124] M.S. Akhter, M.A. Rahman, R.K. Ripon, M. Mubarak, M. Akter, S. Mahbub, F. Al Mamun, M.T. Sikder, A systematic review on green synthesis of silver nanoparticles using plants extract and their bio-medical applications, Heliyon 10(11) (2024) e29766.
[125] H. Agarwal, S. Venkat Kumar, S. Rajeshkumar, A review on green synthesis of zinc oxide nanoparticles – An eco-friendly approach, Resource-Efficient Technologies 3(4) (2017) 406-413.
[126] R. Álvarez-Chimal, V.I. García-Pérez, M.A. Álvarez-Pérez, R. Tavera-Hernández, L. Reyes-Carmona, M. Martínez-Hernández, J.Á. Arenas-Alatorre, Influence of the particle size on the antibacterial activity of green synthesized zinc oxide nanoparticles using Dysphania ambrosioides extract, supported by molecular docking analysis, Arabian Journal of Chemistry 15(6) (2022) 103804.
[127] W. Handayani, A.S. Ningrum, C. Imawan, The Role of pH in Synthesis Silver Nanoparticles Using Pometia pinnata (Matoa) Leaves Extract as Bioreductor, Journal of Physics: Conference Series 1428(1) (2020) 012021.
[128] R.C. de Oliveira, R.A.C. Amoresi, N.L. Marana, M.A. Zaghete, M. Ponce, A.J. Chiquito, J.R. Sambrano, E. Longo, A.Z. Simões, Influence of Synthesis Time on the Morphology and Properties of CeO2 Nanoparticles: An Experimental–Theoretical Study, Crystal Growth & Design 20(8) (2020) 5031-5042.
[129] Beer statistics, 2018.
[130] M. Mosher, K. Trantham, Brewing Science: A Multidisciplinary Approach, Springer International Publishing2021.
[131] A.C. Fărcaş, Socaci, S. A., Mudura, E., Dulf, F. V., Vodnar, D. C., Tofană, M., Salanță, L. C., Exploitation of Brewing Industry Wastes to Produce Functional Ingredients, in: M. Kanauchi (Ed.), Brewing Technology, IntechOpen Book2017.
[132] K.R. Thomas, P.K.S.M. Rahman, Brewery wastes. Strategies for sustainability. A review, Aspects of applied biology 80 (2006).
[133] A. Jaeger, E.K. Arendt, E. Zannini, A.W. Sahin, Brewer's Spent Yeast (BSY), an Underutilized Brewing By-Product, Fermentation 6(4) (2020) 123.
[134] N.P. Cheremisinoff, Handbook of Water and Wastewater Treatment Technologies, Elsevier Science2002.
[135] J.L. Gardea-Torresdey, E. Gomez, J.R. Peralta-Videa, J.G. Parsons, H. Troiani, M. Jose-Yacaman, Alfalfa Sprouts: A Natural Source for the Synthesis of Silver Nanoparticles, Langmuir 19(4) (2003) 1357-1361.
[136] X.F. Zhang, Z.G. Liu, W. Shen, S. Gurunathan, Silver Nanoparticles: Synthesis, Characterization, Properties, Applications, and Therapeutic Approaches. LID - 10.3390/ijms17091534 [doi] LID - 1534, (1422-0067 (Electronic)).
[137] R.F. Egerton, Physical Principles of Electron Microscopy: An Introduction to TEM, SEM, and AEM, Springer International Publishing2016.
[138] Y. Waseda, E. Matsubara, K. Shinoda, X-Ray Diffraction Crystallography: Introduction, Examples and Solved Problems, Springer Berlin Heidelberg2011.
[139] H.H. Perkampus, H.C. Grinter, T.L. Threlfall, UV-VIS Spectroscopy and Its Applications, Springer Berlin Heidelberg2013.
[140] B.C. Smith, Fundamentals of Fourier Transform Infrared Spectroscopy, CRC Press2011.
[141] B.J. Berne, R. Pecora, Dynamic Light Scattering: With Applications to Chemistry, Biology, and Physics, Dover Publications2013.
[142] J.C. Russ, M.A. Frs, R. Kiessling, J. Charles, Fundamentals of Energy Dispersive X-Ray Analysis: Butterworths Monographs in Materials, Elsevier Science2013.
[143] S. Gaisford, V. Kett, P. Haines, Principles of Thermal Analysis and Calorimetry, Royal Society of Chemistry2019.

[144] S. Hüfner, Photoelectron Spectroscopy: Principles and Applications, Springer Berlin Heidelberg2013.
[145] A. Nigam, S. Kala, Optical, structural and XPS studies of Ag nanoparticles prepared via Melia azedarach plant extract, American Institute of Physics Conference Series, 2020, p. 020116.
[146] M. Schnippering, M. Carrara, A. Foelske, R. Kötz, D.J. Fermín, Electronic properties of Ag nanoparticle arrays. A Kelvin probe and high resolution XPS study, Physical chemistry chemical physics : PCCP 9 6 (2007) 725-30.
[147] E.A. Skomorokhova, T.P. Sankova, I.A. Orlov, A.N. Savelev, D.A.-O. Magazenkova, M.G. Pliss, A.N. Skvortsov, I.M. Sosnin, D.A. Kirilenko, I.V. Grishchuk, E.I. Sakhenberg, E.V. Polishchuk, P.N. Brunkov, A.E. Romanov, L.V. Puchkova, E.A.-O. Ilyechova, Size-Dependent Bioactivity of Silver Nanoparticles: Antibacterial Properties, Influence on Copper Status in Mice, and Whole-Body Turnover, (1177-8903 (Print)).
[148] K.S. Siddiqi, Husen, A., Rao, R. A. K., A review on biosynthesis of silver nanoparticles and their biocidal properties, J Nanobiotechnology 16(1) (2018) 14.
[149] General guidelines for the determination of nitrogen by the Kjeldahl method, Food and feed products, 2009, p. 7.
[150] R.J. Grubesic, J. Vukovic, D. Kremer, S. Vladimir-Knezevic, Spectrophotometric method for polyphenols analysis: prevalidation and application on Plantago L. species, J Pharm Biomed Anal 39(3-4) (2005) 837-42.
[151] B.R. Hewitt, Spectrophotometric Determination of Total Carbohydrate, Nature 182(4630) (1958) 246-247.
[152] N. Petkova, R. Vrancheva, P. Denev, I. Ivanov, A. Pavlov, HPLC-RID method for determination of inulin and fructooligosaccharides, Acta nat. sci. 1 (2014) 99-107.
[153] E. Cendejas-Bueno, J.L. Rodriguez-Tudela, M. Cuenca-Estrella, A. Gomez-Lopez, Development and validation of a fast HPLC/photodiode array detection method for the measurement of voriconazole in human serum samples. A reference laboratory experience, Enferm Infecc Microbiol Clin 31(1) (2013) 23-8.
[154] I. Bisutti, Hilke, I., Raessler, M., Determination of total organic carbon – an overview of current methods, TrAC Trends Analyt Chem 23(10-11) (2004) 716-726.
[155] B. Beckhoff, B. Kanngießer, N. Langhoff, R. Wedell, H. Wolff, Handbook of Practical X-Ray Fluorescence Analysis, Springer Berlin Heidelberg2007.
[156] L. Kover, D. Varga, I. Cserny, J. Toth, K. Tokesi, Some applications of high-energy, high-resolution Auger-electron spectroscopy using Bremsstrahlung radiation, Surf. Interface Anal. 19 (1992) 9-15.
[157] S. Tougaard, Background analysis of XPS/AES QUASES Simple Backgrounds, QUASES- Tougaard Inc., Tougaard, S, Odense, Denmark, 1994-2010.
[158] M. Mohai, Multimodel of X-ray photoelectron spectroscopy quantification program for 32-bit Windows, XPSMultiQuant, 1999-2001.
[159] M. Mohai, XPS MultiQuant: multimodel XPS quantification software, Surf. Interface Anal. 36(8) (2004) 828-832.
[160] Calcein, AM, cell-permeant dye Manual. https://www.thermofisher.com/document-connect/document-connect.html?url=https://assets.thermofisher.com/TFS-Assets%2FLSG%2Fmanuals%2FMAN0019058_CalceinAM_UG.pdf. (Accessed 15th July 2021).
[161] Propidium Iodide Nucleic Acid Stain Manual. thermofisher.com/document-connect/document-connect.html?url=https://assets.thermofisher.com/TFS-Assets%2FLSG%2Fmanuals%2Fmp01304.pdf. (Accessed 15th July 2021).
[162] CyQUANT™ LDH Cytotoxicity Assay Manual. https://www.thermofisher.com/document-connect/document-

connect.html?url=https://assets.thermofisher.com/TFS-Assets%2FLSG%2Fmanuals%2FMAN0018500_CyQUANT-LDH-Cytotoxicity-Assay-Kit_PI.pdf. (Accessed 15th July 2021).
[163] CyQUANT™ MTT Cell Viability Assay Manual. https://www.thermofisher.com/document-connect/document-connect.html?url=https://assets.thermofisher.com/TFS-Assets%2FLSG%2Fmanuals%2FMAN0019028_CyQUANT_MTT_CellProliferationAssayKit_PI.pdf. (Accessed 15th July 2021).
[164] OriginLab, 30.1.9 BiDoseResp. https://www.originlab.com/doc/Origin-Help/BiDoseResp-FitFunc. (Accessed 10th May 2019).
[165] J. Ma, X. Niu, J. Wang, J. Wu, Facile synthesis of Ag_3PO_4 with the assistance of N, N-dimethylformamid and urea for high performance photocatalysis, Catal. Commun. 77 (2016) 55-59.
[166] C.R. Hubbard, R.L. Snyder, RIR - measurement and use in quantitative XRD, Powder Diffr. 3(2) (1988) 74-77.
[167] J.H. Scofield, Hartree-Slater subshell photoionization cross-sections at 1254 and 1487 eV, J. Electron Spectrosc. Relat. Phenom. 8 (1976) 129-137.
[168] S. Tanuma, C.J. Powell, D.R. Penn, Calculations of electron inelastic mean free paths. V. Data for 14 organic compounds over the 50–2000 eV range, Surf. Interface Anal. 21 (1993) 165-176.
[169] A.V. Naumkin, A. Kraut-Vass, W. Gaarenstroom, C.J. Powell, NIST X-ray photoelectron spectroscopy Database, NIST SRD 20, version 4.1.
[170] B. Lesiak, L. Kövér, J. Tóth, J. Zemek, P. Jiricek, A. Kromka, N. Rangam, C sp^2/sp^3 hybridisations in carbon nanomaterials – XPS and (X)AES study, Appl. Surf. Sci. 452 (2018) 223-231.
[171] S. Vorobyev, E. Vishnyakova, M. Likhatski, A. Romanchenko, I. Nemtsev, Y. Mikhlin, Reactivity and Chemical Sintering of Carey Lea Silver Nanoparticles, Nanomaterials 9(11) (2019).
[172] QUASES-Tougaard background analysis of XPS/AES Part1-QUASES-Analyze, Tougaard Inc, 1994-2003.
[173] J. Farkasovska, V. Bugarova, J. Godocikova, V. Majtan, J. Majtan, The role of hydrogen peroxide in the antibacterial activity of different floral honeys, European Food Research and Technology 245(12) (2019) 2739-2744.
[174] M. Masoura, P. Passaretti, T.W. Overton, P.A. Lund, K. Gkatzionis, Use of a model to understand the synergies underlying the antibacterial mechanism of H2O2-producing honeys, Scientific Reports 10(1) (2020) 17692.
[175] N. Rangam, A. Sudagar, R. Koronkiewicz, P. Borowicz, J. Tóth, L. Kövér, D. Michałowska, M. Roszko, M. Pilz, K. Kwapiszewska, B. Lesiak-Orłowska, Surface and composition effects on the biphasic cytotoxicity of nanocomposites synthesized using leaf extracts, International Journal of Biological Macromolecules 276 (2024) 133723.
[176] A. Jablonski, J. Zemek, Overlayer thickness determination by XPS using the multiline approach, Surf Interface Anal. 41(3) (2009) 193-204.
[177] A. Barinov, O.B. Malcioğlu, S. Fabris, T. Sun, L. Gregoratti, M. Dalmiglio, M. Kiskinova, Initial Stages of Oxidation on Graphitic Surfaces: Photoemission Study and Density Functional Theory Calculations, J. Phys. Chem. C 113(21) (2009) 9009-9013.
[178] K. Shimizu, A. Shchukarev, J.-F. Boily, X-ray Photoelectron Spectroscopy of Fast-Frozen Hematite Colloids in Aqueous Solutions. 3. Stabilization of Ammonium Species by Surface (Hydr)oxo Groups, J. Phys. Chem. C 115(14) (2011) 6796-6801.
[179] A. Farhana, S.L. Lappin, Biochemistry, Lactate Dehydrogenase, StatPearls [Internet], 2022.

[180] S.J. Oh, H. Kim, Y. Liu, H.K. Han, K. Kwon, K.H. Chang, K. Park, Y. Kim, K. Shim, S.S. An, M.Y. Lee, Incompatibility of silver nanoparticles with lactate dehydrogenase leakage assay for cellular viability test is attributed to protein binding and reactive oxygen species generation, Toxicol. Lett. 225 (2014) 422–432.
[181] G.Y. Di Veroli, C. Fornari, I. Goldlust, G. Mills, S.B. Koh, J.L. Bramhall, F.M. Richards, D.I. Jodrell, An automated fitting procedure and software for dose-response curves with multiphasic features, Sci. Rep. 5(1) (2015) 14701.
[182] C. Antoniou, A. Kyratzis, Y. Rouphael, S. Stylianou, M.C. Kyriacou, Heat- and Ultrasound-Assisted Aqueous Extraction of Soluble Carbohydrates and Phenolics from Carob Kibbles of Variable Size and Source Material, Foods 9(10) (2020) 1364.
[183] A. Antony, M. Farid, Effect of Temperatures on Polyphenols during Extraction, Appl. Sci. 12(4) (2022) 2107.
[184] M.M. Al-Ansari, P. Dhasarathan, A.J.A. Ranjitsingh, L.A. Al-Humaid, Ganoderma lucidum inspired silver nanoparticles and its biomedical applications with special reference to drug resistant Escherichia coli isolates from CAUTI, Saudi J. Biol. Sci. 27(11) (2020) 2993-3002.
[185] M.M. Mohammed, N.A. Ibrahim, N.E. Awad, A.A. Matloub, A.G. Mohamed-Ali, E.E. Barakat, A.E. Mohamed, P.L. Colla, Anti-HIV-1 and cytotoxicity of the alkaloids of Erythrina abyssinica Lam. growing in Sudan, Nat Prod Res 26(17) (2012) 1565-75.
[186] N. Mamat, H. Abdullah, H. Hapidin, N.F. Mokhtar, Gallic Acid and Methyl Gallate Enhance Antiproliferative Effect of Cisplatin on Cervical Cancer (HeLa) Cells, Sains Malays. 49 (2020) 1107-1114.
[187] M. Kozarski, A. Klaus, J. Vunduk, D. Jakovljevic, M. Jadranin, M. Niksic, Health impact of commercially cultivated mushroom Agaricus bisporus and wild-growing mushroom Ganoderma resinaceum - a comparative overview, J. Serb. Chem. Soc. 85 (2019) 129-129.
[188] A. Mollataghi, A.H. Hadi, S.C. Cheah, (-)-Kunstleramide, a new antioxidant and cytotoxic dienamide from the bark of Beilschmiedia kunstleri gamble, Molecules 17(4) (2012) 4197-208.
[189] A.H. Aalami, M. Mesgari, A. Sahebkar, Synthesis and Characterization of Green Zinc Oxide Nanoparticles with Antiproliferative Effects through Apoptosis Induction and MicroRNA Modulation in Breast Cancer Cells, Bioinorg Chem Appl 2020 (2020) 8817110.
[190] N.Z. Mamadalieva, F. Sharopov, J.P. Girault, M. Wink, R. Lafont, Phytochemical analysis and bioactivity of the aerial parts of Abutilon theophrasti (Malvaceae), a medicinal weed, Nat Prod Res 28(20) (2014) 1777-9.
[191] R.F.A. Abdelhameed, S.S. Elhady, A. Sirwi, H. Samir, E.A. Ibrahim, A.K. Thomford, A. El Gindy, G.M. Hadad, J.M. Badr, M.S. Nafie, Thonningia sanguinea Extract: Antioxidant and Cytotoxic Activities Supported by Chemical Composition and Molecular Docking Simulations, Plants 10(10) (2021) 2156.
[192] A. Verma, P. Gupta, N. Rai, R.K. Tiwari, A. Kumar, P. Salvi, S.C. Kamble, S.K. Singh, V. Gautam, Assessment of Biological Activities of Fungal Endophytes Derived Bioactive Compounds Isolated from Amoora rohituka, J Fungi (Basel) 8(3) (2022) 285.
[193] F.E. Amrati, M. Bourhia, M. Slighoua, S. Ibnemoussa, A. Bari, R. Ullah, A. Amaghnouje, F. Di Cristo, M. El Mzibri, A. Calarco, L. Benbacer, D. Bousta, Phytochemical Study on Antioxidant and Antiproliferative Activities of Moroccan Caralluma europaea Extract and Its Bioactive Compound Classes, Evid Based Complement Alternat Med 2020 (2020) 8409718.
[194] Xiongwei Liu, Kuizhong Shan, Xiaxia Shao, Xianqing Shi, Yun He, Zhen Liu, Joe Antony Jacob, L. Deng, Nanotoxic Effects of Silver Nanoparticles on Normal HEK-293 Cells in Comparison to Cancerous HeLa Cell Line, Int J Nanomedicine 16 (2021) 753–761.

Institute of Physical Chemistry
Polish Academy of Sciences

Kasprzaka 44/52
01-224 Warsaw, Poland

www.ichf.edu.pl